

Formation and pathways of dense water in the Nordic Seas



Ailin Brakstad

Thesis for the degree of Philosophiae Doctor (PhD)
University of Bergen, Norway
2023

UNIVERSITY OF BERGEN



Formation and pathways of dense water in the Nordic Seas

Ailin Brakstad



Thesis for the degree of Philosophiae Doctor (PhD)
at the University of Bergen

Date of defense: 20.10.2023

© Copyright Ailin Brakstad

The material in this publication is covered by the provisions of the Copyright Act.

Year: 2023

Title: Formation and pathways of dense water in the Nordic Seas

Name: Ailin Brakstad

Print: Skipnes Kommunikasjon / University of Bergen

Scientific environment

This work was conducted at the Geophysical Institute, University of Bergen and the Bjerknes Centre for Climate Research. My position was funded by the Trond Mohn Foundation under Grant Agreement BFS2016REK01 and the project "Overturning in the Nordic Seas", which was led by my main advisor Kjetil Våge. My co-advisors were Geoffrey Gebbie and Emil Jeansson. In fall 2017, Geoffrey Gebbie kindly hosted me for a three-month research stay at the Woods Hole Oceanographic Institution, USA. I also had a short research stay in spring 2019 at the Alfred Wegener Institute for Polar and Marine Research, Germany, hosted by Wilken-Jon von Appen. These stays were partly funded by the Meltzer foundation at the University of Bergen. Support for this work was also provided by the Office of Naval Research Global through the Northern Ocean Rapid Surface Evolution project (award number N62909-22-1-2023). During my PhD I have been enrolled in the Norwegian Research School on changing climates in the coupled earth system (CHESS).



UNIVERSITY OF BERGEN
Faculty of Mathematics and Natural Sciences

BJERKNES CENTRE
for Climate Research



Research school on changing climates in the coupled earth system

Acknowledgements

Words cannot express my gratitude to everyone who made this exciting work and journey possible. First and foremost, I want to thank my supervisor, Kjetil, for letting me be a part of the OVENS project and for navigating me through the “slightly” longer than expected PhD period. I deeply appreciate all your support, encouragement, and patience. Thank you for always being available for questions and discussions, for always providing thorough and immediate feedback, for your enthusiasm and motivation, and for providing me with many exciting opportunities and adventures. It has been a lot of fun working with you on this intriguing project, including our many shared cruises and travels. I am extremely grateful for having had you as my main advisor and look forward to continue working with you on several new, exciting projects. I would also like to thank my co-supervisors Jake and Emil. Jake, thank you for introducing me to your TMI method and the world of inverse modelling, and for hosting me at WHOI for a three-month research stay in fall 2017. Your support and encouragement in the development of the regional TMI code have been invaluable. Although challenging at times, I have really enjoyed digging into the details of this simple, but yet so complex method. I feel grateful to have worked with such a unique and powerful tool. Emil, thank you for sharing your insights and expertise on water masses, their properties, and mixing in the Nordic Seas, and for reminding me (a physical oceanographer) to also take the chemical aspects into account, which have been invaluable for interpreting the TMI results. Thank you for teaching me how to sample and analyze transient tracers on the IGP cruise in 2018 and for your constant support and enthusiasm - I always left our discussions feeling more motivated. I have learned so much from the three of you and could not have wished for a better set of advisors. Thank you!

There were many more people who made important contributions to my PhD work: Thanks to Wilken and Gereon for providing Kristin and me with the unique hydrographic data set from 10 years of moored profilers in the central Greenland Sea, and to Wilken for hosting us at AWI in spring 2019. Many thanks to Kristin for leading the analysis of these data during your MSc project, and for continuing the work with me to get the beautiful data and results published. I also want to thank all other co-authors for your contributions and constructive feedback on the papers. Thanks to everyone in the OVENS-group, including Stefanie, Lisbeth, and Anna, for many insightful scientific discussions, meetings, and social activities. Stefanie, thanks for the countless days and months we spent together on different research vessels, in Woods Hole, in Bergen, and more. Sharing these adventures with you was a lot of fun and I really enjoyed all our scientific and not-so-scientific discussions. I am extremely grateful for all your feedback and support throughout the PhD journey. I also want to thank Bob and his lab at WHOI, including Astrid, Jie, and Peigen, for many inspiring scientific discussions and meetings at sea, in Woods Hole, on Iceland, and during our THOR scientific retreats in the White Mountains and at Geilo. Mirjam, thank you for the many inspiring and creative hours in the lab, and Øyvind, thanks for your support and for including me in Ocean Outlook. I had a lot of fun making the Ocean Outlook movie together with you, Stefanie, and Frode. Thanks to Lars Henrik for including me in the BCCR Nordic Seas/Arctic Ocean synthesis work, which helped me to zoom out and think about the bigger picture of the

Nordic Seas and Arctic Ocean climate system. I also appreciate several collaborations with Xabier, Are, Siv, Jake, Emil, and Elaine on different aspects of the TMI method and convection in the Greenland Sea. Thanks for the many stimulating discussions that have also helped me placing my PhD work into context. I am excited to continue our development of the transient Nordic Seas TMI version. I feel privileged to have been part of the excellent climate research community in Bergen, including the GFI Physical Oceanography group and the BCCR Polar research group. Thanks to the Norglidiers group for including me as a glider pilot during my PhD and for wanting me to stay afterwards. In particular, thanks to Ilker and Fiona, for your patience over the past two years. I look forward to continuing to work with you with full dedication on all the exciting, new projects now that my thesis is submitted.

A big thanks also to the excellent PhD community for making my journey pleasant, also after office hours. Helene and Elina, I really appreciate all the care and fun adventures you have given me. To my friends and family, thank you for all your support over the years and for taking my mind off work after many hours in the office. A special thanks to my parents, for your constant support and encouragement, for always believing in me, and for always showing interest in my work. Last, but not least, thank you Bjørn Erik, for all your love and patience, and for always being there for me. This journey would not have been possible without you by my side.

Ailin Brakstad
Bergen, June 2023

Abstract

Dense water formed in the Nordic Seas flows southward across the Greenland-Scotland Ridge and sinks to great depths in the North Atlantic to supply the lower limb of the Atlantic Meridional Overturning Circulation. While the exchange flows across the ridge have been monitored for several decades, gaps in our knowledge remain regarding where and how the dense overflow waters are formed and transported to the ridge. Questions also remain regarding the variability in dense-water formation and its implications for the dense-water reservoir and overflows from the Nordic Seas, which are critical to understand the overturning in the Nordic Seas. Based on observational data, this thesis quantifies the origin and upstream pathways of the overflow waters, as well as how and why they have changed over the past 70 years. A particular focus was on the variability in dense-water formation in the Greenland Sea, where a major portion of the overflow waters originate.

In Paper I, we focused on the interannual and long-term changes in dense-water formation in the Greenland Sea based on hydrographic observations from 1986 to 2016 and a one-dimensional mixed-layer model. We found that the period prior to the mid-1990s was particularly fresh and strongly stratified, resulting in predominantly shallow convection (<300 m), despite strong atmospheric forcing. Increased salinity, linked to higher salinity in the Atlantic Water inflow into the Nordic Seas, weakened the water-column stability after the mid-1990s. This transition led to increased convection depths (500–1500 m) and the formation of a new, less dense class of intermediate water that has been the main product of convection in the Greenland Sea until present. Although the volume of the new water mass increased from the 1990s to the 2000s, its vertical extent has been constrained to the upper half of the Greenland Sea water column, above the remnants of the denser Greenland Sea deep water that was the main product of convection prior to the 1980s.

Approximately 60–80% of the heat lost to the atmosphere during winter is related to intense, short-lived events called cold-air outbreaks (CAOs). In Paper II, we utilized a unique 10-year (1999–2009) hydrographic record from moored profilers with 1–2 days temporal resolution to examine, for the first time, the direct impact of CAOs on the mixed-layer development in the Greenland Sea. This revealed that the mixed-layer response depended on when the CAO events occurred and on their intensity. Early in winter (November–January) the response was primarily a cooling of the mixed layer, while later in winter (February–April) the mixed layer mainly deepened. Idealized simulations with a one-dimensional mixed-layer model suggest that the temporal distribution of CAOs impacts the timing of the onset of the deepening phase, while the end-of-winter mixed-layer depth and hydrographic properties are more sensitive to the integrated heat loss over the winter, which is determined by the total number and intensity of CAOs. Considerable variability was observed in the mixed-layer response to CAOs, highlighting the importance of lateral heat and salt fluxes. These were quantified and included in the mixed-layer model, which suggests that their combined effect is a reduction in the end-of-winter mixed-layer depth of up to several hundred meters.

In Paper III we developed a regional high-resolution water-mass inversion for the Nordic Seas to determine the origin and upstream pathways of the two main overflow

plumes passing the Greenland-Scotland Ridge in Denmark Strait and the Faroe Bank Channel. The inversion is based on the geographical distribution of hydrographic and geochemical water properties from observations covering the period 2000–2019 and resolves the pathways that connect the overflow plumes to their origins. The Denmark Strait overflow is mainly composed of water originating in the Greenland Sea ($39\pm 2\%$), the Iceland Sea ($20\pm 3\%$), and in the Atlantic Domain ($19\pm 2\%$) of the Nordic Seas. Dense water from the Greenland Sea propagates southward along two distinct pathways: an outer core of the East Greenland Current and along a previously unknown pathway that crosses the Jan Mayen Ridge into the Iceland Sea just south of Jan Mayen. Both of these pathways feed the North Icelandic Jet that consists of $82\pm 2\%$ dense-water formed in the Greenland Sea. Most of the Faroe Bank Channel overflow originates in the Greenland Sea ($46\pm 8\%$) and the Arctic Ocean ($25\pm 9\%$) and propagates toward the channel with the Iceland-Faroe Slope Jet and along the eastern margin of the Jan Mayen Ridge. The latter pathway turns eastward over to the Norwegian continental slope, which it then follows southward to the Faroe-Shetland Channel. This pathway can account for $24\pm 3\%$ of the Faroe Bank Channel overflow, while the Iceland-Faroe Slope Jet supplies $58\pm 3\%$. These results improve our understanding on the origin and upstream pathways of the overflows, in particular regarding the dense-water pathways from the Greenland Sea and how the overflow water approaches the Faroe-Shetland Channel.

The focus in Paper IV was long-term variability in the Nordic Seas reservoir and overflows using a 70-year long (1950–2019) observational record and the regional water-mass inversion for the two periods 1950–1979 and 2000–2019. The results revealed that the Nordic Seas reservoir has warmed and become less dense due to changes in the Atlantic Water inflow and the cessation of bottom-reaching convection in the Greenland Sea. This has, in turn, impacted the entire density structure in the Nordic Seas. The transition from bottom to intermediate-depth convection has reduced the density and supply from the Greenland Sea to the Faroe Bank Channel overflow, while the contribution of the less dense intermediate water to the overflow through Denmark Strait has increased. Our analyses of the overflow water composition and properties demonstrate that it is important to take both the spatial and temporal variability in dense-water formation into account when examining the long-term changes in the overflows. The Atlantic Water has warmed and become less dense over the past 2-3 decades. If this trend continues in the future, it is expected to further decrease the density of the overturning the Nordic Seas.

Collectively, the four papers in this thesis have significantly advanced our knowledge about the formation and pathways of dense water in the Nordic Seas, their variability, and the contributions to the overflow waters across the Greenland-Scotland Ridge from an observational point of view. As such, the thesis provides an important step forward to understand the overturning in the Nordic Seas and its variability.

Sammendrag

De nordiske hav er viktig for dannelsen av kalde, tette og dype vannmasser som strømmer sørover på tvers av Grønland-Skottland-ryggen og forsyner den dype grenen av omveltningssirkulasjonen i Atlanterhavet. På tross av at størrelsen på dypvannstransporten over ryggen er godt kjent, gjenstår det mange åpne spørsmål angående hvor og hvordan de dype vannmassene dannes og transporteres til ryggen. Det er også stor usikkerhet rundt variasjonene i dypvannsdannelse og hvilke implikasjoner dette har for omveltningssirkulasjonen. I denne oppgaven bruker vi observasjonsdata til å kvantifisere hvor dype vannmasser dannes, hvordan de strømmer mot Grønland-Skottland-ryggen, og hvordan dette har endret seg de siste 70 årene. Oppgaven retter et spesielt fokus mot Grønlandshavet, som er en viktig kilde til dypvannet i de nordiske hav.

I Artikkel I benyttet vi hydrografiske observasjoner fra 1986 til 2016, sammen med en endimensjonal blandalagsmodell, til å undersøke mellomårlig variabilitet og langtidstrender i dypvannsdannelsen i Grønlandshavet. Vi fant at perioden før midten av 1990-tallet var spesielt fersk og sterkt stratifisert, noe som resulterte i grunn konveksjon (<300 m), til tross for sterkt atmosfærisk pådriv. Saltinnholdet i Grønlandshavet økte etter midten av 1990-tallet på grunn av høyere saltholdighet i Atlanterhavsvannet som strømmer nordover inn i de nordiske hav. Dette førte til svekket stratifisering, dypere konveksjon (500–1500 m), og dannelse av en ny klasse dypvann som har vært hovedproduktet av konveksjonen i Grønlandshavet frem til i dag. Denne nye vannmassen er mindre tett enn dypvannet som ble produsert i Grønlandshavet før 1980-tallet. Den vertikale utstrekningen av den nye vannmassen er derfor begrenset til den øvre halvdel av vannsøylen.

Store mengder varme ekstraheres fra de nordiske hav til atmosfæren om vinteren. Omtrent 60–80% av varmen frigjøres under intense, kortvarige kaldluftsutbrudd (heretter omtalt som utbrudd). I Artikkel II brukte vi et unikt 10-årig (1999–2009) hydrografisk datasett fra profilerende instrumenter med 1–2 dagers tidsoppløsning til å kvantifisere, for aller første gang, den direkte påvirkningen av slike utbrudd på blandalaget i Grønlandshavet. Dette viste at responsen i blandalagsegenskapene var avhengig av styrken på utbruddene og når de inntraff. Kaldluftsutbrudd som inntraff tidlig på vinteren (november–januar) førte i hovedsak til en nedkjøling av blandalaget, mens utbrudd som inntraff senere på vinteren (februar–april) førte til en økning i blandalagsdyp. Idealisererte simuleringer med en endimensjonal blandalagsmodell antyder at tidspunktet når dyp konveksjon inntreffer avhenger av fordelingen av utbrudd, mens blandalagsegenskapene mot slutten av vinteren er mer avhengig av styrken og det totale antallet utbrudd gjennom vinteren. Responsen i blandalagsegenskapene var også avhengig av laterale varme- og salt flukser. Disse ble kvantifisert og inkludert i blandalagsmodellen. Resultatene viste at deres kombinerte effekt er en reduksjon i blandalagsdybden på opptil flere hundre meter.

I Artikkel III utviklet vi en inversjonsmodell med høy romlig oppløsning for vannmassene i de nordiske hav. Denne ble brukt til å identifisere opprinnelsen til de to største dypvannsstrømmene som passerer Grønland-Skottland-ryggen i Danmarkstredet og Færøyanalkanalen. Inversjonsmodellen er basert på hydrografiske og geokjemiske vannegenskaper observert i perioden 2000–2019 og viser hvor dypvann dannes og hvor-

dan de strømmer mot ryggen. Dypvannsstrømmen i Danmarkstredet består hovedsakelig av vannmasser fra Grønlandshavet ($39\pm 2\%$), Islandshavet ($20\pm 3\%$) og fra Norskehavet ($19\pm 2\%$). Dypvann dannet i Grønlandshavet beveger seg sørover langs to distinkte strømningsveier: en ytre kjerne av Østgrønlandsstrømmen og en tidligere ukjent strømningsvei som krysser Jan Mayen-ryggen inn mot Islandshavet sør for Jan Mayen. Begge disse strømningsveiene forsyner Nordislandsjeten som består av $82\pm 2\%$ dypvann dannet i Grønlandshavet. Det meste av dypvannsstrømmen i Færøbankkanalen har sin opprinnelse i Grønlandshavet ($46\pm 8\%$) og Polhavet ($25\pm 9\%$). Disse vannmassene strømmer sørover mot kanalen med Island–Færøy-jeten og langs den østlige delen av Jan Mayen-ryggen. Den sistnevnte strømningsveien svinger østover til den norske kontinental-skråningen, som den deretter følger sørover til Færøy-Shetland-kanalen. Denne strømningsveien kan bidra med $24\pm 3\%$ av dypvannet i Færøybankkanalen, mens Island–Færøy-jeten forsyner $58\pm 3\%$. Disse resultatene øker vår forståelse av hvor de dype vannmassene dannes og hvordan de transporteres til Grønland-Skottland-ryggen.

Fokuset i Artikkel IV var langtidsendringer i dypvannet i de nordiske hav. Til å undersøke dette ble observasjonsdata over en 70-års periode (1950–2019) benyttet, sammen med inversjonsmodellen for periodene 1950–1979 og 2000–2019. Resultatene avslørte at dypvannsreservene i de nordiske hav har blitt varmere og mindre tett på grunn av økt temperatur i det innstrømmende Atlanterhavsvannet og opphør av konveksjon til bunnen av Grønlandshavet etter 1980-tallet. Dette har påvirket hele tetthetsstrukturen i de nordiske hav. Den reduserte konveksjonen har ført til en nedgang i tettheten og bidraget fra Grønlandshavet til dypvannsstrømmen gjennom Færøybankkanalen. Derimot har bidraget til Danmarkstredet fra den nye, mindre tette vannmassen i Grønlandshavet økt. Våre analyser av egenskapene og sammensetningen av dypvannsstrømmene på tvers av Grønland-Skottland-ryggen demonstrerer at det er viktig å ta hensyn til både romlige og tidsmessige variasjoner i dypvannsdannelse for å forstå langtidsendringene. Dersom trenden mot varmere og mindre tette dypvannsreserver fortsetter i fremtiden, forventes en tetthetsreduksjon i omveltningssirkulasjonen i de nordiske hav.

Til sammen har de fire artiklene i denne oppgaven økt vår kunnskap om dannelsen, strømningsveiene, og variabiliteten til dypvannet i de nordiske hav i betydelig grad. Denne kunnskapen er kritisk for å kunne bedre forstå dypvannstrømmene på tvers av Grønland-Skottland-ryggen, deres bidrag til omveltningssirkulasjonen i Atlanterhavet og hva vi kan forvente av disse i et framtidig varmere klima.

List of papers

This thesis consists of an introduction and discussion that form the framework for four scientific papers. The motivation and objectives of the thesis is presented in Chapter 1, while Chapter 2 introduces the general scientific background including a description of the different components of the overturning system in the Nordic Seas. An overview of the data sets and methods employed in the thesis is provided in Chapter 3 before a brief summary of the papers is presented in Chapter 4. The papers (listed below, numbers I–IV) are included in Chapter 5. Finally, the conclusions are discussed and set into context in Chapter 6.

- I) **Brakstad, A.**, K. Våge, L. Håvik, and G.W.K. Moore (2019): *Water mass transformation in the Greenland Sea during the period 1986–2016*, Journal of Physical Oceanography, **49**(1), 121–140.
- II) Svingen, K., **A. Brakstad**, K. Våge, W. J. von Appen, and L. Papritz (2023): *The impact of cold-air outbreaks and oceanic lateral fluxes on dense-water formation in the Greenland Sea from a ten-year moored record (1999–2009)*, Journal of Physical Oceanography, **53**(6), 1499–1517.
- III) **Brakstad, A.**, G. Gebbie, K. Våge, E. Jeansson, and S. R. Ólafsdóttir (2023): *Formation and pathways of dense water in the Nordic Seas based on a regional inversion*, Progress in Oceanography, **212**.
- IV) **Brakstad, A.**, K. Våge, M. Árthun, G. Gebbie, and E. Jeansson (in preparation, 2023): *Observed long-term changes in the overturning in the Nordic Seas*.

Additional contributions

- A) Lauvset, S. K., **A. Brakstad**, K. Våge, A. Olsen, E. Jeansson, and K. A. Mork (2018): *Continued warming, salinification and oxygenation of the Greenland Sea gyre*, *Tellus A: Dynamic Meteorology and Oceanography*, **70(1)**, 1–9.
- B) Renfrew, I. A. and 65 other co-authors including **A. Brakstad** (2019): *The Iceland Greenland Seas Project*, *Bulletin of the American Meteorological Society*, **100(9)**, 1795–1817.
- C) Stenseth, N. C., M. R. Payne, E. Bonsdorff, D. J. Dankel, J. M. Durant, L. G. Anderson, C. W. Armstrong, T. Blenckner, **A. Brakstad**, S. Dupont, A. M. Eikeset, A. Goksøyr, S. Jónsson, A. Kuparinen, K. Våge, H. Österblom, and Ø. Paasche (2020): *Attuning to a changing ocean*, *Proceedings of the National Academy of Sciences*, **177(34)**, 20363–20371.
- D) Huang, J., R. S. Pickart, R. X. Huang, P. Lin, **A. Brakstad**, and F. Xu (2020): *Sources and upstream pathways of the densest overflow water in the Nordic Seas*, *Nature Communications*, **11(1)**, 1–9.
- E) Bretones, A., K. H. Nisancioglu, M. F. Jensen, **A. Brakstad**, and S. Yang (2022): *Transient increase in Arctic deep-water formation and ocean circulation under sea ice retreat*, *Journal of Climate*, **35(1)**, 109–124.
- F) Smedsrud, L. H., M. Muilwijk, **A. Brakstad**, E. Madonna, S. K. Lauvset, C. Spensberger, A. Born, T. Eldevik, H. Drange, E. Jeansson, C. Li, A. Olsen, Ø. Skagseth, D. A. Slater, F. Straneo, K. Våge, and M. Årthun (2022): *Nordic Seas heat loss, Atlantic inflow, and Arctic sea ice cover over the last century*, *Reviews of Geophysics*, **60(1)**, e2020RG000725.
- G) Davila, X., G. Gebbie, **A. Brakstad**, S. K. Lauvset, E. L. McDonagh, J. Schwinger, and A. Olsen (2022): *How is the ocean anthropogenic carbon reservoir filled?*, *Global Biogeochemical Cycles*, **36(5)**, e2021GB007055.
- H) Davila, X., A. Olsen, S. K. Lauvset, E. L. McDonagh, **A. Brakstad**, and G. Gebbie (in review, 2023): *Origins of Oxygen Minimum Zones*, *Journal of Geophysical Research: Oceans*.
- I) Langehaug, H. R., **A. Brakstad**, K. Våge, E. Jeansson, M. Ilicak, and C. A. Katsman (in preparation, 2023): *Drivers of surface salinity changes in the Greenland-Iceland Seas on seasonal and interannual time scales - a climate model study*.
- J) Davila, X., G. Gebbie, **A. Brakstad**, S. K. Lauvset, E. L. McDonagh, E. Jeansson, and A. Olsen (in preparation, 2023): *Water-mass ages and ventilation timescales of the Nordic Seas inferred from transient tracers*.
- K) Pou, J. M. H., K. Våge, and **A. Brakstad** (in preparation, 2023): *Detection and evolution of persistent weakly-stratified layers in the Greenland Sea*.

Contents

Scientific environment	i
Acknowledgements	iii
Abstract	v
Sammendrag	vii
List of papers	ix
1 Motivation	1
2 Introduction	3
2.1 Importance of overturning in the Nordic Seas	3
2.2 Overview of the Nordic Seas	4
2.2.1 Geography	4
2.2.2 Large-scale wind and buoyancy forcing	5
2.2.3 Ocean circulation and hydrography	8
2.3 Dense-water formation in the Nordic Seas	10
2.3.1 Water masses	11
2.3.2 Transformation within the boundary current system	13
2.3.3 Open-ocean convection in the interior basins	15
2.3.4 Inflow of dense water from the Arctic Ocean	19
2.3.5 Exchange and mixing between the boundary and the interior	19
2.4 Sources and upstream pathways of dense overflow water	20
2.4.1 Denmark Strait Overflow Water	20
2.4.2 Faroe Bank Channel Overflow Water	22
3 Data and methods	25
3.1 Historical hydrographic and geochemical observations	25
3.2 Moored hydrographic measurements	27
3.3 Atmospheric reanalyses, sea ice, and satellite altimeter data	28
3.4 Mixed-layer estimation	28
3.5 One-dimensional mixed-layer model	29
3.6 Regional water-mass inversion	31
4 Summary of the papers	35
5 Scientific papers	39
Paper I: Water mass transformation in the Greenland Sea during the period 1986–2016	41
Paper II: The impact of cold-air outbreaks and oceanic lateral fluxes on dense-water formation in the Greenland Sea from a ten-year moored record (1999–2009)	63

Paper III: Formation and pathways of dense water in the Nordic Seas based on a regional inversion	85
Paper IV: Observed long-term changes in the overturning in the Nordic Seas .	113
6 Concluding discussion	147
6.1 Surface origin of the overflows and density transformation	147
6.2 Overflow-water pathways	148
6.3 Strengths and weaknesses of the regional water-mass inversion	149
6.4 Contribution from the Greenland Sea to the overflows	150
6.5 Mechanisms governing the variability in Greenland Sea convection	151
6.6 Future perspectives and the impacts of climate change	152
6.7 Summary	153
Bibliography	155

1 Motivation

Although the Nordic Seas only account for 1% of the the World's ocean by area, they impact climate on a global scale. They are a main source of dense water to the lower limb of the Atlantic Meridional Overturning Circulation (AMOC, Section 2.1, *Gebbie and Huybers*, 2011; *Lozier et al.*, 2019; *Chafik and Rossby*, 2019; *Petit et al.*, 2020; *Tsubouchi et al.*, 2021; *Árthun et al.*, 2023), critical for the transport of heat, freshwater, and sea ice between the North Atlantic and Arctic Ocean (*Drange et al.*, 2005; *Haine et al.*, 2015), and supply a significant amount of the global CO₂ inventory (4–8%, *Jeansson et al.*, 2011; *Davila et al.*, 2022; *Smedsrud et al.*, 2022). Warm and saline surface water is transported northward into the Nordic Seas in the upper limb of the AMOC. Within the Nordic Seas, the water is transformed into colder, fresher, and denser water masses by severe heat loss to the atmosphere and interactions with cold and fresh water from river runoff and sea-ice melt. Several distinct processes contribute to the transformation: gradual cooling along the boundary currents, open-ocean convection during winter in the interior basins, mixing between the boundary currents and the interior, and shelf convection in the Arctic Ocean that modifies the dense water masses that flows into the Nordic Seas (Section 2.3, *Swift et al.*, 1980; *Swift and Aagaard*, 1981; *Aagaard et al.*, 1985; *Strass et al.*, 1993; *Mauritzen*, 1996; *Rudels et al.*, 1999; *Eldevik et al.*, 2009; *Spall et al.*, 2021; *Smedsrud et al.*, 2022). The resulting dense water returns southward at depth and supplies the lower limb of the AMOC. The magnitude of the transport of dense water from the Nordic Seas across the Greenland-Scotland Ridge is reasonably well known, but gaps in our knowledge remain regarding where and how the dense overflow waters are formed and transported to the ridge. A better understanding of the origin and pathways of the overflow waters, and their variability, is imperative for our understanding of AMOC's sensitivity to a warming climate.

Both the atmosphere and ocean are warming, which is particularly evident in the Nordic Seas and Arctic Ocean (e.g., *Shu et al.*, 2022). The increased heat content in the Nordic Seas since 2000 can to a large extent be explained by increased ocean heat transport from the North Atlantic (*Tsubouchi et al.*, 2021). The variability and trends in the Atlantic Water inflow to the Nordic Seas have downstream impacts for both the heat and salt content in the Nordic Seas (*Eldevik et al.*, 2009; *Skagseth and Mork*, 2012; *Glessmer et al.*, 2014; *Mork et al.*, 2014a; *Yashayaev and Seidov*, 2015; *Lawvset et al.*, 2018; *Asbjørnsen et al.*, 2019; *Tsubouchi et al.*, 2021; *Smedsrud et al.*, 2022). Combined with a warmer atmosphere, the increased Atlantic Water heat transport has also resulted in a significant retreat of the sea-ice edge (*Onarheim et al.*, 2018; *Selyuzhenok et al.*, 2020), which in turn impacts the ocean-to-atmosphere heat loss (*Moore et al.*, 2015, 2022; *Smedsrud et al.*, 2022). The largest heat fluxes typically occur near the sea-ice edge and are associated with intense, short-lived cold-air outbreaks that advect cold polar air masses from the sea ice over the relatively warmer open ocean (*Papritz and Spengler*, 2017; *Spensberger and Spengler*, 2021). The larger open-ocean area increases the air-sea heat loss, while the general declining temperature difference between the ocean and atmosphere reduces the heat loss. The combined result is a northwestward shift in the region with most intense heat loss, which can have substantial impacts on where and how dense water is formed (*Moore et al.*, 2015; *Våge et al.*, 2018; *Pérez-Hernández et al.*,

2019; Athanase *et al.*, 2020; Moore *et al.*, 2022; Strehl *et al.*, submitted).

Open-ocean convection in the Greenland Sea forms dense water that contributes to the overflows from the Nordic Seas, especially to the densest component (Swift *et al.*, 1980; Swift and Aagaard, 1981; Fogelqvist *et al.*, 2003; Jeansson *et al.*, 2008; Huang *et al.*, 2020). The Greenland Sea convection depth and dense-water properties have changed substantially over the past 70 years (Schlosser *et al.*, 1991; Meincke *et al.*, 1992; Karstensen *et al.*, 2005; Ronski and Budéus, 2005; Latarius and Quadfasel, 2010; Lawset *et al.*, 2018; Somavilla, 2019; Strehl *et al.*, submitted). In particular, the bottom-reaching convection that used to form the cold and dense Greenland Sea Deep Water ceased in the early 1980s, most likely because of anomalously fresh near-surface conditions that increased the stratification, combined with reduced atmospheric forcing and brine release from local sea-ice formation (Meincke *et al.*, 1992; Visbeck *et al.*, 1995; Moore *et al.*, 2015; Somavilla, 2019; Strehl *et al.*, submitted). Although convection has been constrained to intermediate depths since then, the less dense Greenland Sea Arctic Intermediate water formed at present may be more important for the Nordic Seas' overflows (Huang *et al.*, 2020). While the air-sea heat fluxes and the intensity of cold-air outbreaks have decreased over the Greenland Sea gyre the past 50 years (Moore *et al.*, 2015; Somavilla, 2019; Dahlke *et al.*, 2022; Moore *et al.*, 2022), increased salinity since the mid-1990s, associated with higher Atlantic Water salinity, has decreased the water-column stability (Lawset *et al.*, 2018). The combined effect of air-sea heat fluxes and oceanic lateral advection, and their relative importance for the variability in dense-water formation in the Greenland Sea, remain unclear. The direct impact of cold-air outbreaks on convection in the Greenland Sea is also largely unexplored because of sparse temporal data coverage and the short duration of these events (Terpstra *et al.*, 2021).

Understanding what drives the variability and trends in dense-water formation and its implications for the dense-water reservoir and overflows from the Nordic Seas are essential to understand the overturning in the Nordic Seas, to predict its response to a future warming climate, and to appreciate its contribution to the lower limb of the AMOC. In summary, we posed the following overarching research questions that were addressed in Papers I-IV, respectively (Chapter 5):

- I) What determines the interannual and long-term variability in dense-water formation in the Greenland Sea?
- II) How do cold-air outbreaks and lateral fluxes of heat and salt impact dense-water formation in the Greenland Sea?
- III) Where do the overflow waters originate and how do they propagate toward the Greenland-Scotland Ridge?
- IV) How have the dense-water reservoir and the overflows from the Nordic Seas changed over the observational record and why?

To address these questions, we compiled a comprehensive observational database for the Nordic Seas over the period 1950–2019, developed a regional water-mass inversion that connects the various overflow plumes to their origins, utilized a unique 10-year (1999–2009) observational record from moored profiling vehicles in the central Greenland Sea, and employed a one-dimensional mixed-layer model that was tailored to represent and explore Greenland Sea conditions (Chapter 3).

2 Introduction

2.1 Importance of overturning in the Nordic Seas

Meridional ocean transport of heat, salt, carbon, and nutrients is important for maintaining Earth's climate. A large part of the oceanic poleward heat transport is associated with the overturning circulation in the Atlantic, particularly in the northern hemisphere (*Trenberth and Fasullo, 2008; Buckley and Marshall, 2016*). The Atlantic Meridional Overturning Circulation (AMOC) transports warm and saline surface water northward, where heat is released to the atmosphere resulting in increased water density. The cold, dense water sinks to depth forming the North Atlantic Deep Water that returns southward in the lower limb of the AMOC (Figure 2.1). To close the overturning cell, the dense water returns to the surface by wind-driven upwelling in the Southern Ocean and by vertical mixing (*Kuhlbrodt et al., 2007; Marshall and Speer, 2012*). While the upwelling of dense water is essential to sustain the AMOC, the strength and shape of the AMOC is also determined by buoyancy fluxes and the formation of dense water (*Kuhlbrodt et al., 2007*). The transformation from the upper to the lower limb of the AMOC is also important for the vertical transport of anthropogenic heat and carbon (*Buckley and Marshall, 2016; Davila et al., 2022*).

The AMOC variability and strength are measured at several zonal transects throughout the Atlantic Ocean (*Frajka-Williams et al., 2019*) and the overturning in the subpolar North Atlantic has been monitored since 2014 at the OSNAP array both east and west of Greenland (*Lozier et al., 2017*). Results from this array suggest that the bulk of the density transformation and its variability takes place east of Greenland and not in the Labrador Sea which was previously considered one of the key overturning sites (*Lozier et al., 2019*). The overturning transport at OSNAP east was estimated to 15.6 ± 0.8 Sv (where $1 \text{ Sv} \equiv 10^6 \text{ m}^3 \text{ s}^{-1}$, *Lozier et al., 2019*). Although the region south of the Greenland-Scotland Ridge (i.e., the Irminger Sea and Iceland Basin, Figure 2.1) can account for half of the overturning transport, in terms of volume, the largest heat loss occurs in the Nordic Seas (*Chafik and Rossby, 2019; Petit et al., 2020*). This is also where the deepest and densest component of the North Atlantic Deep Water is formed (*Dickson and Brown, 1994*). Dense water from the Nordic Seas spill across the Greenland-Scotland Ridge as overflow plumes that sink to great depths. As the plumes cascade down the ridge, they entrain water masses from the Irminger Sea and Iceland Basin, which together form the headwaters to the lower limb of the AMOC (*Dickson and Brown, 1994; Chafik and Rossby, 2019*). While most models predict a weakened AMOC in the future, the overturning strength in the Nordic Seas and Arctic Ocean is predicted to increase (at least during the 21st century, *Bretones et al., 2022; Árthun et al., 2023*). This suggests that the Nordic Seas (and Arctic Ocean) could become even more important for the lower limb of the AMOC in the future, acting as a stabilizing factor (*Árthun et al., 2023*). As such, it is important to understand what drives the variability in the formation and pathways of dense water in the Nordic Seas, which is the focus of this thesis.

2.2 Overview of the Nordic Seas

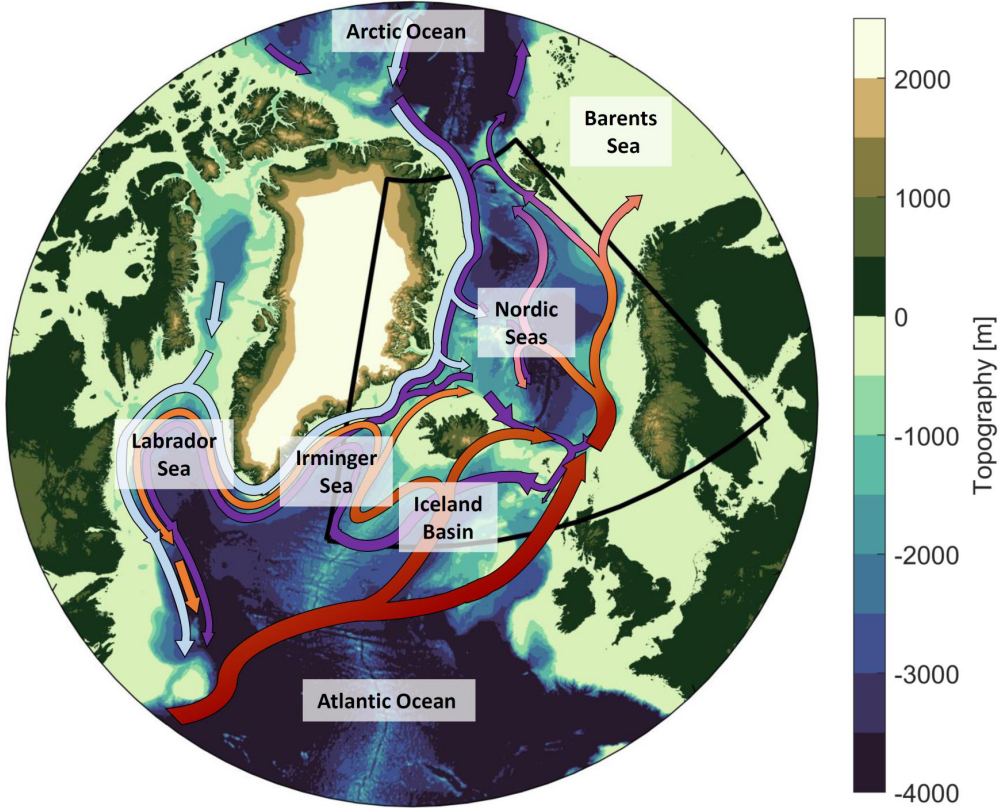


Figure 2.1: Map of the subpolar North Atlantic and the Nordic Seas including schematic circulation of warm and saline surface waters (red), cold and fresh surface waters (light blue), and dense deep waters (dark purple).

2.2.1 Geography

In addition to being an important component of the AMOC, the Nordic Seas comprising the Norwegian, Greenland, and Iceland Seas are the main connection for heat and salt transport between the North Atlantic and the Arctic Ocean (Figure 2.1, *Drange et al.*, 2005). The region is separated from the Arctic Ocean by the 2500-m deep Fram Strait between Svalbard and Greenland (e.g., *Langehaug and Falck*, 2012) and by the 300–400 m shallow Barents Sea. The southern boundary, between the Nordic Seas and North Atlantic, is the Greenland-Scotland Ridge (the red line in Figure 2.2). This submarine ridge consists of four main gaps separated by Iceland, the Faroe Islands, and the Faroe Bank. From northwest to southeast these gaps are: Denmark Strait with a sill depth of 650 m, Iceland-Faroe Ridge which ranges from 300 to 500 m depth, the 840 m deep Faroe Bank Channel, and Wyville-Thompson Ridge which reaches depths of

approximately 600 m. The Faroe Bank Channel, which is a continuation of the Faroe-Shetland Channel, is the deepest passage through the Greenland-Scotland Ridge. Below this depth (840 m) the ridge forms a continuous barrier which constrains exchange of water between the Nordic Seas and the North Atlantic (*Hansen and Østerhus, 2000*).

The bathymetry of the Nordic Seas is rather complex, including several interior basins separated by submarine ridges that have many deep gaps and channels, as well as shallow shelf areas and steep slopes along the margins (Figure 2.2). These bathymetric features guide the oceanic circulation and have major implications for the distribution and transformation of water masses in the Nordic Seas (*Nøst and Isachsen, 2003*).

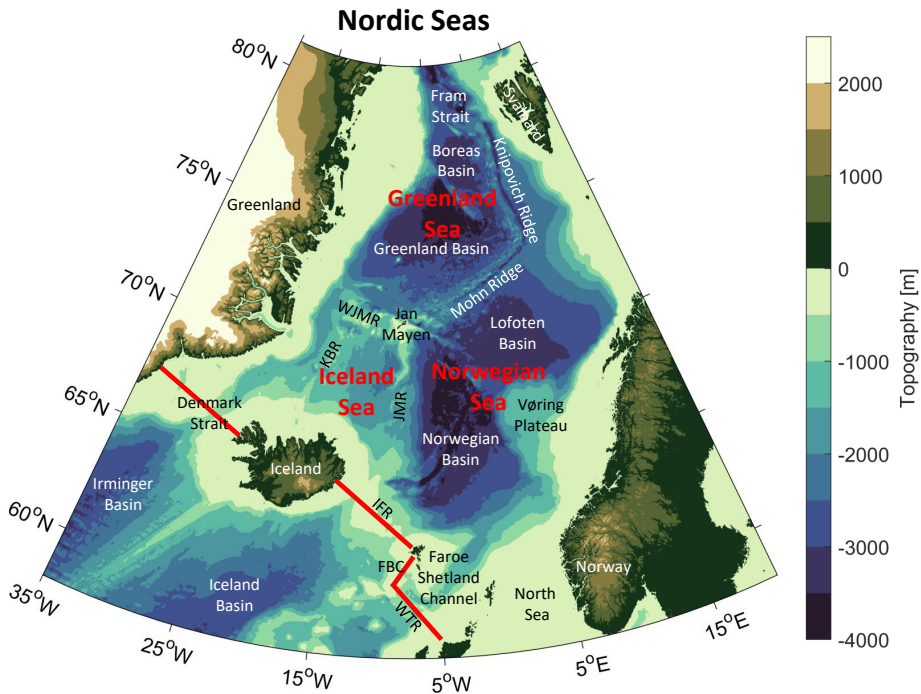


Figure 2.2: Map of the main topographic features in the Nordic Seas (area outlined in black in Figure 2.1). The Greenland-Scotland Ridge is marked by red lines. The abbreviations are: WJMR–West Jan Mayen Ridge, JMR–Jan Mayen Ridge, KBR–Kolbeinsey Ridge, IFR–Iceland-Faroe Ridge, WTR–Wyville-Thompson Ridge, and FBC–Faroe Bank Channel. The topography was obtained from ETOPO1 (*Amante and Eakins, 2009*).

2.2.2 Large-scale wind and buoyancy forcing

The large-scale sea-level pressure over the Nordic Seas is dominated by the northern mode of the North Atlantic Oscillation (NAO), namely the low-pressure system situated southwest of Iceland, as well as a local minimum over the Lofoten Basin (Figure 2.3a, *Furevik and Nilsen, 2005*). These minima, and the high-pressure systems situated over Greenland and Europe, results in a cyclonic wind circulation, with southwesterly winds

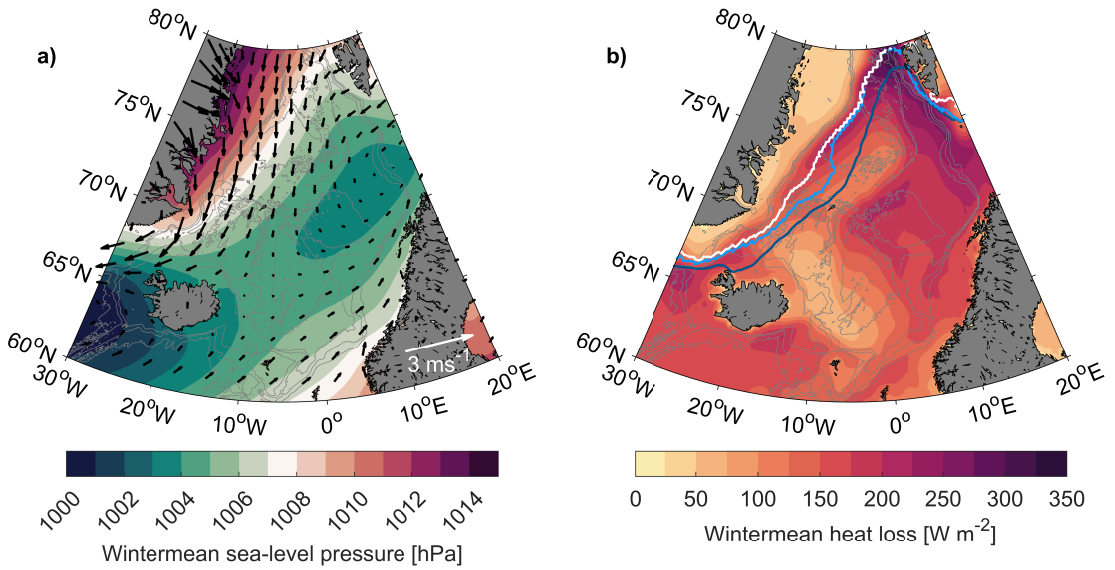


Figure 2.3: Mean winter (November–April) sea-level pressure (a) and ocean-to-atmosphere heat loss (b) during 2000–2019 based on monthly ERA5 reanalysis data (Hersbach et al., 2020). The black arrows (a) indicate 10-m winds, while the gray contours indicate the 500-, 1000-, 1500-, and 3000-m isobaths. Annual mean 20% sea-ice concentration contours (b) during 1950–1979 (dark blue), 1980–1999 (light blue), and 2000–2019 (white) were obtained from Walsh et al. (2017).

along Norway and vigorous northerly winds along Greenland. The associated wind stress creates a divergent Ekman flow in the ocean that contributes to a depression of the sea surface in the interior Nordic Seas, which sustains a large-scale cyclonic ocean circulation in the Nordic Seas (Figure 2.1, *Nøst and Isachsen, 2003; Furevik and Nilsen, 2005*). Here we focus on the winter season (November–April, Figure 2.3a), but the large-scale wind forcing is cyclonic in summer too, although substantially weaker (*Jónsson, 1991*). Thus, variability in large-scale sea-level pressure impacts the strength of the cyclonic ocean circulation in the Nordic Seas. A stronger north-south sea-level pressure gradient (e.g., a more positive phase of the NAO) leads to strengthened cyclonic wind forcing and ocean circulation in the Nordic Seas, including increased northward transports along the continental slope of Norway (*Dickson et al., 2000; Furevik and Nilsen, 2005; Bringedal et al., 2018; Muilwijk et al., 2018; Smedsrud et al., 2022*).

The ocean circulation and transformation of water masses in the Nordic Seas are also driven by a large-scale buoyancy forcing related to oceanic heat loss to the atmosphere and freshwater input from rivers and melting sea ice (e.g., *Serreze et al., 2007; Segtnan et al., 2011; Lambert et al., 2016; Smedsrud et al., 2022*). In the annual mean, the Nordic Seas loses heat to the atmosphere, which cools the ocean, while a warming occurs in the tropics. This uneven air-sea heat exchange drives a northward transport of warm water and a southward transport of cold water. The cooling (negative buoyancy forcing) densifies the northward flowing water, which results in an overturning circulation and a southward flow of dense, cold water at depth (purple arrows in Figure 2.1). The freshwater input from rivers and melting sea ice, on the other hand, results in a positive buoyancy forcing that supports a horizontal estuarine-like circulation, with a cold, fresh,

and light southward flow at the surface (light blue arrows in Figure 2.1). The combined circulation is often referred to as a double estuary circulation (*Eldevik and Nilsen, 2013; Lambert et al., 2016*). The overall buoyancy forcing acts as a “pull” mechanism on the northward flow of Atlantic Water across the Greenland-Scotland Ridge and recent studies indicate that it could be equally important as the wind-driven circulation, which is often referred to as a “push” mechanism (*Timmermans and Marshall, 2020; Smedsrud et al., 2022*). Their relative importance is not fully understood because it likely varies with time and the two forcing mechanisms are also connected to each other (e.g., *Timmermans and Marshall, 2020*).

There is a pronounced seasonal cycle in the air-sea heat exchange in the Nordic Seas, with substantial ocean cooling in winter and warming during the summer season, driven mainly by radiation (*Serreze et al., 2007; Smedsrud et al., 2022*). Strong winds and large temperature contrasts between the ocean and atmosphere in winter result in substantial heat fluxes, exceeding 300 W m^{-2} on average in the northern part of the Nordic Seas between November and April (Figure 2.3b). These large winter heat fluxes are crucial for the formation of dense water masses in the Nordic Seas (e.g., *Moore et al., 2015*). The greatest heat fluxes occur near the sea-ice edge where cold air masses over the sea ice first encounters open water and in the eastern basins of the Nordic Seas where warm Atlantic Water flows northward, resulting in large ocean-atmosphere temperature differences (e.g., *Furevik and Nilsen, 2005; Isachsen et al., 2007; Papritz and Spengler, 2017; Moore et al., 2015; Spensberger and Spengler, 2021; Moore et al., 2022*). Most (60–80%) of the ocean heat loss in winter is associated with strong, short-lived weather events called cold-air outbreaks (CAOs, *Papritz and Spengler, 2017*). These events are excursions of cold, dry polar air advected from the sea ice or cold landmasses over relatively warmer ocean water, leading to intense heat fluxes, particularly near the sea-ice edge (*Papritz and Spengler, 2017; Terpstra et al., 2021; Spensberger and Spengler, 2021*). They typically last for 2-4 days and are often linked to polar lows (*Papritz and Spengler, 2017; Terpstra et al., 2021*).

While much of the variability in ocean heat loss in the Nordic Seas in winter can be linked to the number and intensity of atmospheric polar lows entering the region, which is associated with variability in the North Atlantic storm track, significant long-term changes take place as a result of global warming (e.g., *Moore et al., 2015; Smedsrud et al., 2022; Moore et al., 2022*). Both the atmosphere and the ocean is warming, which has resulted in a general northwestward retreat of the sea-ice edge (Figure 2.3b, *Onarheim et al., 2018; Selyuzhenok et al., 2020*). The sea-ice retreat opens new ocean areas to the atmosphere, which increases the air-sea heat exchange. By contrast, heat fluxes in regions far away from the sea ice are declining, because the atmosphere is warming faster than the ocean, which decreases the air-sea temperature difference (*Moore et al., 2015; Smedsrud et al., 2022; Moore et al., 2022*). This leads to an overall northwestward shift in the region with most intense heat loss, which can have great impacts on the local formation of dense water (*Moore et al., 2015; Våge et al., 2018; Pérez-Hernández et al., 2019; Pope et al., 2020; Athanase et al., 2020; Moore et al., 2022; Strehl et al., submitted*).

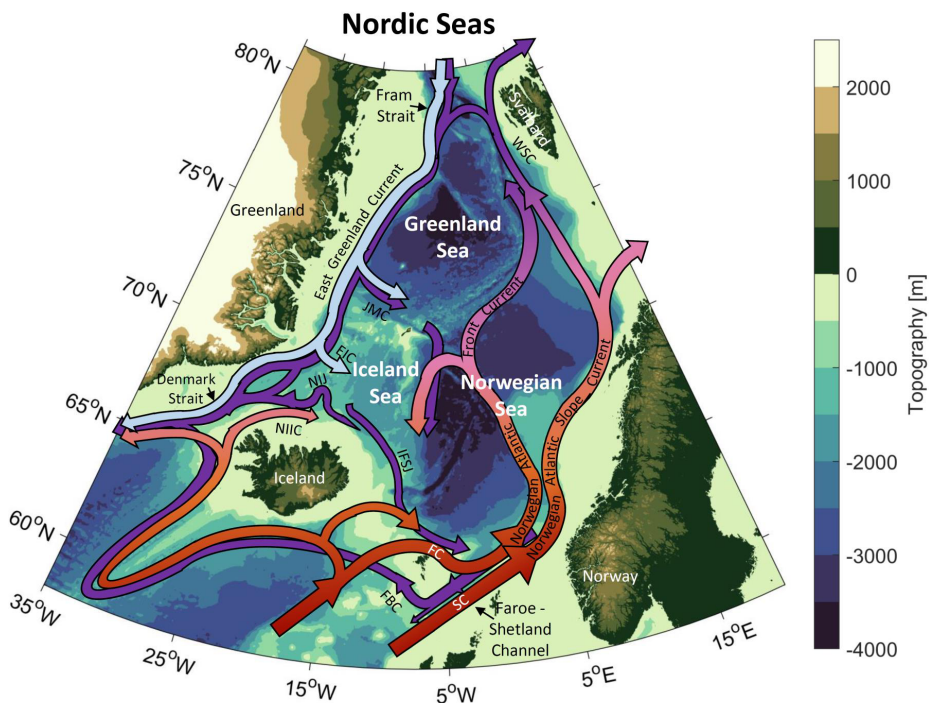


Figure 2.4: Map of the Nordic Seas including schematic circulation with the same color coding as in Figure 2.1. The abbreviations are: FC-Faroe Current, SC-Shetland Current, NIIC-North Icelandic Irminger Current, WSC-West Spitsbergen Current, JMC-Jan Mayen Current, EIC-East Icelandic Current, NIJ-North Icelandic Jet, IFSJ-Iceland-Faroe Slope Jet, and FBC-Faroe Bank Channel.

2.2.3 Ocean circulation and hydrography

Three main branches of warm and saline Atlantic Water (AW) flow northward into the Nordic Seas (Figure 2.4, *Helland-Hansen and Nansen, 1909*). The greatest AW inflow takes place east of Iceland in the Faroe Current across the Iceland-Faroe Ridge (3.8 ± 0.5 Sv, *Hansen et al., 2015; Østerhus et al., 2019*) and in the Shetland Current across the Faroe-Shetland Ridge (2.7 ± 0.5 Sv, accounting for a recirculating component of the Faroe Current, *Hansen and Østerhus, 2000; Berx et al., 2013; Østerhus et al., 2019*). The smallest and most variable AW inflow occurs west of Iceland in the North Icelandic Irminger Current ($0.9\text{--}1.6$ Sv, *Jónsson and Valdimarsson, 2012; Østerhus et al., 2019; Casanova-Masjoan et al., 2020; Semper et al., 2022*). The two main branches east of Iceland continue northward within the Norwegian Sea, which is characterized by warm and saline AW at the surface and typically referred to as the Atlantic Domain of the Nordic Seas (Figure 2.5, *Swift and Aagaard, 1981*). The northward flow consists of the Norwegian Atlantic Slope Current that follows the Norwegian slope along the eastern margin and the Norwegian Atlantic Front Current that veers west at the Vøring Plateau and follows the Mohn and Knipovich ridges northward (Figure 2.4, *Orvik and Niiler, 2002*). A small fraction of the frontal branch enters the Iceland Sea just south of Jan Mayen (*Mork et al., 2014b*), while another fraction recirculates southward as the western edge of the Norwegian Basin gyre (*Poulain et al., 1996*). The relatively fresh water along the Norwegian coast is associated with the Norwegian Coastal Current that flows parallel to the Norwegian Atlantic Slope Current from North Sea into the Barents Sea (Figure 2.5b, e.g., *Mauritzen, 1996*).

In the northern part of the Atlantic Domain the Norwegian Atlantic Slope Current bifurcates. One branch flows through the Barents Sea and into the Arctic Ocean, while the other branch continues northward and merges with the Norwegian Atlantic Front Current to form the West Spitsbergen Current (Figure 2.4). Some of the AW in the West Spitsbergen Current continues northward into the Arctic Ocean through Fram Strait on the eastern side of the strait, while the remainder recirculates and joins the southward-flowing East Greenland Current on the western side of Fram Strait (Mauritzen, 1996). The Arctic Ocean and the Polar Domain of the Nordic Seas (Figure 2.5, Swift and Aagaard, 1981) are covered by fresh, cold, and light Polar Surface Water (PSW) from river runoff and sea-ice melt. When the Atlantic-origin water masses, which have cooled and densified going northward (Section 2.3.2), approach the PSW, they flow beneath it to intermediate depths (e.g., Mauritzen, 1996).

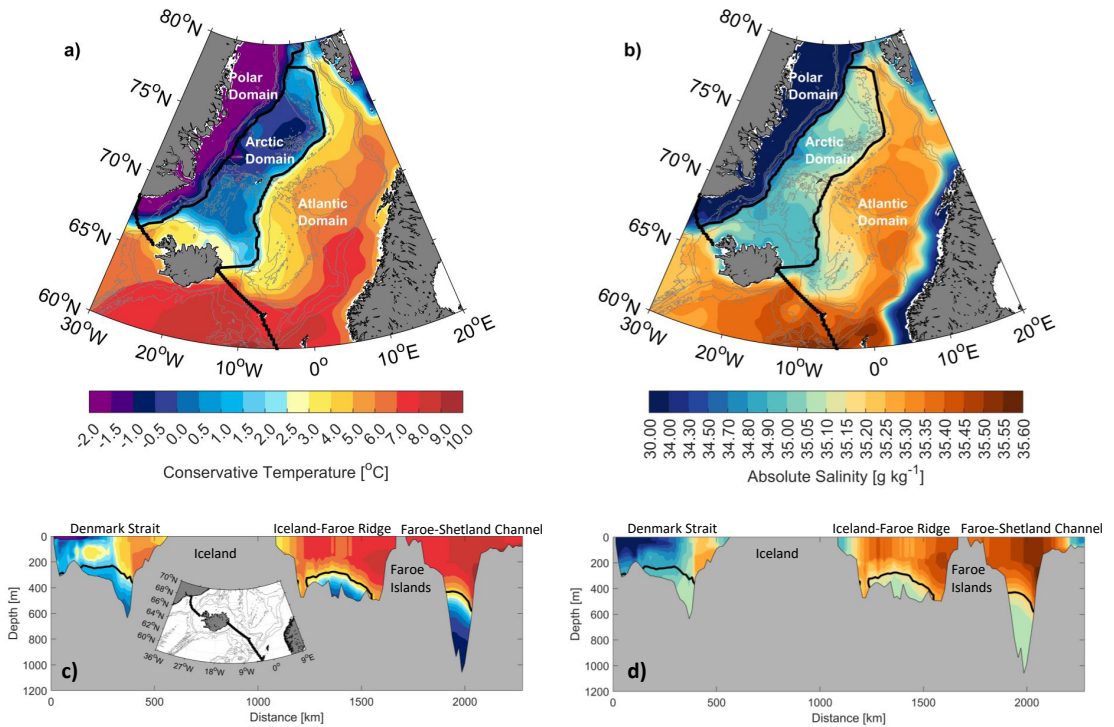


Figure 2.5: Late-winter (February–April) sea-surface temperature (a) and salinity (b) during 2000–2019. The gray contours indicate the 500-, 1000-, 1500-, and 3000-m isobaths. The lower panels show the distribution of temperature (c) and salinity (d) along the Greenland-Scotland Ridge. The location of the ridge is indicated on the inserted map (c). The water masses below the black solid line indicating $\sigma_0 = 27.80 \text{ kg m}^{-3}$ are classified as overflow water (Dickson and Brown, 1994).

The East Greenland Current transports both PSW and dense intermediate water masses along the east Greenland shelf break from Fram Strait to Denmark Strait (Håvik *et al.*, 2017a), and is important also for transporting sea ice from the Arctic Ocean (Haine *et al.*, 2015). The Atlantic-origin water masses advected by the current are both from

the recirculating branch in Fram Strait and from the Fram and Barents Sea branches that have encircled cyclonically around the Arctic Ocean (*Rudels et al.*, 2002). Two currents branch off the East Greenland Current on its way southward (Figure 2.4). These are the Jan Mayen Current north of the West Jan Mayen Ridge (*Bourke et al.*, 1992) and the East Icelandic Current in the Iceland Sea (*Macrander et al.*, 2014; *de Jong et al.*, 2018), which divert fresh surface water into the interior Greenland and Iceland Seas (*Dodd et al.*, 2009; *Spall et al.*, 2021; *Langehaug et al.*, 2022). The East Greenland Current also bifurcates into a shelfbreak and a separated branch, where the separated branch is located offshore of the Greenland shelf break (*Våge et al.*, 2013; *Harden et al.*, 2016; *Håvik et al.*, 2017a). Both of these branches continue through Denmark Strait and close the cyclonic boundary circulation loop of the Nordic Seas.

The interior Iceland and Greenland Seas constitute the Arctic Domain of the Nordic Seas (Figure 2.5, *Swift and Aagaard*, 1981). The Arctic Domain is separated from the Atlantic and Polar domains by pronounced hydrographic fronts (*Helland-Hansen and Nansen*, 1909; *Swift and Aagaard*, 1981). The Arctic Front is located along the Jan Mayen, Mohn, and Knipovich Ridges and separates the Arctic Domain from the warmer and more saline Atlantic Domain. The Polar Front, which forms the border to the colder and fresher Polar Domain, migrates seasonally (*Våge et al.*, 2018; *Spall et al.*, 2021; *Langehaug et al.*, 2022). During winter, the front is located near the Greenland shelf due to strong northerly winds and onshore Ekman transport, while weaker winds in summer results in an offshore migration into the Iceland and Greenland Seas. The Arctic Domain is characterized by weak stratification and substantial heat loss during winter, which results in deep convection and the formation of dense Arctic Intermediate Waters (Section 2.3.3, *Swift et al.*, 1980; *Swift and Aagaard*, 1981). These Arctic Intermediate Waters are transported from north of Iceland toward Denmark Strait by the North Icelandic Jet (*Jónsson and Valdimarsson*, 2004; *Våge et al.*, 2011; *Semper et al.*, 2019) and toward the Faroe-Shetland Channel by the Iceland-Faroe Slope Jet (*Semper et al.*, 2020). More details on the pathways of dense water are given in Section 2.4.1 and 2.4.2.

In total, the outflow across the Greenland-Scotland Ridge consists of 5.8 Sv of dense overflow water (defined as denser than $\sigma_0 = 27.80 \text{ kg m}^{-3}$, *Dickson and Brown*, 1994), while approximately 2.0 Sv is fresh PSW (*Østerhus et al.*, 2019). The outflow of PSW occurs primarily on the east Greenland shelf (*Håvik et al.*, 2017a), while the overflows are confined to the deep gaps in the ridge (Figures 2.5c and d). On average, only 10% of the total overflow water transport takes place across the Wyville-Thompson Ridge and the Iceland-Faroe Ridge, combined (*Østerhus et al.*, 2019). The transports are also intermittent and for the Iceland-Faroe Ridge, not well constrained (*Østerhus et al.*, 2019). The remaining 90% are accounted for by the Denmark Strait and Faroe Bank Channel overflows, which will be introduced further in Section 2.4.1 and 2.4.2, respectively.

2.3 Dense-water formation in the Nordic Seas

Several processes transform and modify water masses in the Nordic Seas. In this thesis, we focus on those mechanisms that impact the formation and properties of dense water that can contribute to the overflows across the Greenland-Scotland Ridge and the lower limb of the AMOC. These include gradual transformation of the AW within the boundary current system (Section 2.3.2), open-ocean convection in the interior basins (Section

2.3.3), transformation in the Arctic Ocean that leads to southward flow of dense water through Fram Strait (Section 2.3.4), and exchange and mixing between the boundary and the interior of the Nordic Seas (Section 2.3.5). A brief overview of the water masses present within the Nordic Seas is given in Section 2.3.1, before going into details about the various processes.

2.3.1 Water masses

The volumetric distributions of temperature, salinity, and oxygen of the water masses present in the Nordic Seas during winter are shown in Figure 2.6. These properties are a result of inflow of various water masses into the region and transformation within the Nordic Seas itself. The water-mass definitions vary in the literature depending on the temporal and spatial region of interest, the research question, and on the data background (i.e., whether both hydrographic and geochemical properties were considered, *Rudels et al.*, 2002, 2005; *Tanhua et al.*, 2005; *Jeansson et al.*, 2008; *Eldevik et al.*, 2009; *Våge et al.*, 2011; *Mastropole et al.*, 2017; *Jeansson et al.*, 2017). Here we introduce the water-mass definitions relevant for our study, which is a simplified version of *Rudels et al.* (2002, 2005) similar to *Våge et al.* (2011) and *Semper* (2020), but including geochemical parameters to distinguish between water masses originating in the Nordic Seas and Arctic Ocean following *Jeansson et al.* (2008, 2017). The goal is to provide a brief introduction to the water masses and where they originate geographically, but we note that the regional water-mass inversion used in this thesis (Paper III and Paper IV) is not sensitive to or dependent on these definitions (Section 3.6). An overview of the hydrographic water-mass definitions are given in Table 2.1.

The surface water masses in the Nordic Seas can be divided into the warm and saline AW, the fresh and cold PSW, and a broad range of relatively fresh and warm water collectively referred to as Surface Water (Figure 2.5, Figure 2.6). The surface

Table 2.1: Overview of the main water masses in the Nordic Seas. Definitions follow *Rudels et al.* (2002, 2005) and *Våge et al.* (2011), but are converted to Conservative Temperature (Θ) and Absolute Salinity (S_A) similar to *Semper* (2020) following the TEOS-10 standard (Section 3.1, *IOC et al.*, 2010)

Water masses	Hydrographic definition
Surface Water (SW)	$\Theta \geq 0 \text{ }^\circ\text{C}$; $S_A < 35.066 \text{ g kg}^{-1}$
Polar Surface Water (PSW)	$\Theta < 0 \text{ }^\circ\text{C}$; $\sigma_0 < 27.70 \text{ kg m}^{-3}$
Atlantic Water (AW)	$\Theta \geq 3 \text{ }^\circ\text{C}$; $S_A \geq 35.066 \text{ g kg}^{-1}$
Atlantic-origin water (Atow): consists of Return Atlantic Water and Arctic Atlantic Water (RAW/AAW)	$0 \leq \Theta < 3 \text{ }^\circ\text{C}$; $\sigma_0 \geq 27.70 \text{ kg m}^{-3}$; $\sigma_{0.5} < 30.44 \text{ kg m}^{-3}$
Arctic-origin water (Arow): consists of Greenland Sea and Iceland Sea Arctic Intermediate Water (GSAIW/ISAIW) The definition overlaps with water masses from the Arctic Ocean, such as the upper Polar Deep Water (uPDW)	$\Theta < 0 \text{ }^\circ\text{C}$; $\sigma_0 \geq 27.70 \text{ kg m}^{-3}$; $\sigma_{0.5} < 30.44 \text{ kg m}^{-3}$ $\Theta < 0 \text{ }^\circ\text{C}$; $\sigma_0 > 27.97 \text{ kg m}^{-3}$; $\sigma_{0.5} < 30.44 \text{ kg m}^{-3}$
Nordic Seas Deep Water (NDW): consists of Greenland Sea and Arctic Ocean Deep Water (GSDW/AODW)	$\sigma_{0.5} \geq 30.44 \text{ kg m}^{-3}$

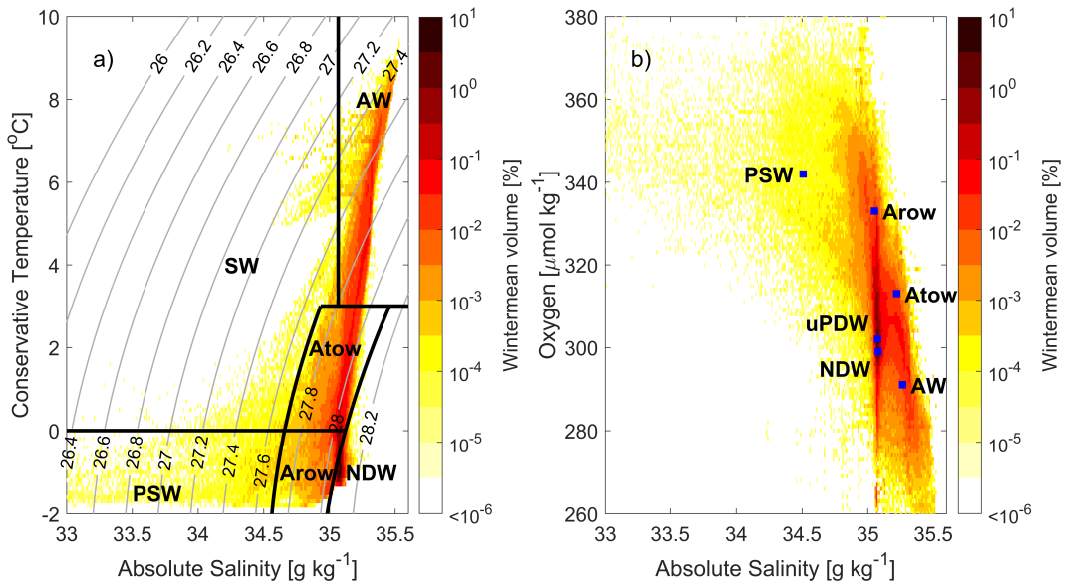


Figure 2.6: Water-mass properties in the Nordic Seas during winter (February–April) based on the hydrographic database compiled in Paper III (1950–2019, Section 3.1). (a): volumetric temperature-salinity diagram, including the water-mass definitions given in Table 2.1. (b): Volumetric oxygen-salinity diagram. The colors indicate the percentage of the total Nordic Seas volume (note the logarithmic scales). The blue squares (b) indicate mean oxygen-salinity properties of the various water masses according to Jeansson et al. (2008): Note that the AW was defined in the inflow west of Iceland, the Atow is representative of the recirculating Atow in Fram Strait, and Arow is from the Greenland Sea gyre.

water masses are typically separated from the intermediate water masses by the $\theta_0 = 27.70 \text{ kg m}^{-3}$ isopycnal (Rudels *et al.*, 2002, 2005). The Atlantic-origin water (Atow) is AW that has been gradually densified along the boundary currents of the Nordic Seas and Arctic Ocean (Mauritzen, 1996). It consists of Return Atlantic Water that is densified AW that recirculates directly in Fram Strait and Arctic-Atlantic Water that has encircled the entire Arctic Ocean (Rudels *et al.*, 2002, 2005). By contrast, the Arctic-origin water (Arow) is mainly formed by open-ocean convection in the Arctic Domain of the Nordic Seas (i.e., within the Iceland and Greenland Seas, Swift *et al.*, 1980; Swift and Aagaard, 1981). The Arow is also often referred to as Arctic Intermediate Water (Rudels *et al.*, 2002, 2005; Jeansson *et al.*, 2008, 2017). The distinction between Atow and Arow is typically defined by the 0°C isotherm (e.g. Våge *et al.*, 2011; Rudels *et al.*, 2002, 2005). Intermediate water masses colder than 0°C are also transported southward from the Arctic Ocean with the East Greenland Current below the Atow. While these water masses overlap with the Arow in terms of hydrography, they generally have lower oxygen and higher nutrient concentrations as it has been a longer time since they were ventilated by the atmosphere (such as the upper Polar Deep Water, Figure 2.6b, Table 2.1, Jeansson *et al.*, 2008, 2017). Finally, we have the Nordic Seas Deep Water (NDW), which fills the deep basins of the entire Nordic Seas and is mainly composed of deep water formed in the Greenland Sea and Arctic Ocean (Aagaard *et al.*, 1985; Swift and Koltermann, 1988). The deep waters are typically separated from the intermediate water masses by the $\theta_{0.5} = 30.44 \text{ kg m}^{-3}$ isopycnal (Rudels *et al.*, 2002, 2005; Jeansson *et al.*, 2008).

2.3.2 Transformation within the boundary current system

The AW is gradually cooled and freshened on its transit with the cyclonic rim current system around the Nordic Seas and Arctic Ocean (Figure 2.7, Mauritzen, 1996; Eldevik *et al.*, 2009; Smedsrud *et al.*, 2022). This implies that it is the cooling that ultimately drives the densification. Most of the cooling takes place in the Atlantic Domain of the Nordic Seas, which is where Isachsen *et al.* (2007) found the greatest buoyancy loss. The overflows are approximately 7°C colder than the AW inflow (Figure 2.7, Smedsrud *et al.*, 2022). Over 60% of this cooling occurs before the AW leaves the surface and flows beneath the PSW in Fram Strait. The densified AW, now classified as Atow, is sufficiently dense to contribute to the overflows across the Greenland-Scotland Ridge.

The majority of the cooling within the Atlantic Domain takes place in the northern part and in the Lofoten Basin (Bosse *et al.*, 2018). Here the AW layer extends well below 500 m depth due to vertical mixing during winter (Mauritzen, 1996; Bosse *et al.*, 2018). The Lofoten Basin is also characterized by strong eddy fields (Köhl, 2007; Raj *et al.*, 2016; Dugstad *et al.*, 2019), where eddies are shed off the Norwegian Atlantic Slope Current and propagate into the centre of the Lofoten Basin sustaining a permanent vortex with a local winter mixed-layer depth exceeding 1000 m (e.g., Köhl, 2007; Bosse *et al.*, 2018; Bosse and Fer, 2019). Huang *et al.* (2023) investigated the role of air-sea heat fluxes and lateral advection on the cooling of the AW in the Atlantic Domain. They found that oceanic lateral heat transfer dominates the temperature change along the Norwegian Atlantic Slope Current, while air-sea heat fluxes account for nearly all the cooling of the Norwegian Atlantic Front Current. The fraction of this western branch that recirculates southward along the western slope of the Norwegian Basin (Section 2.2.3, Poulain *et al.*,

1996) also becomes sufficiently dense to supply the overflow waters (Read and Pollard, 1992; Eldevik *et al.*, 2009).

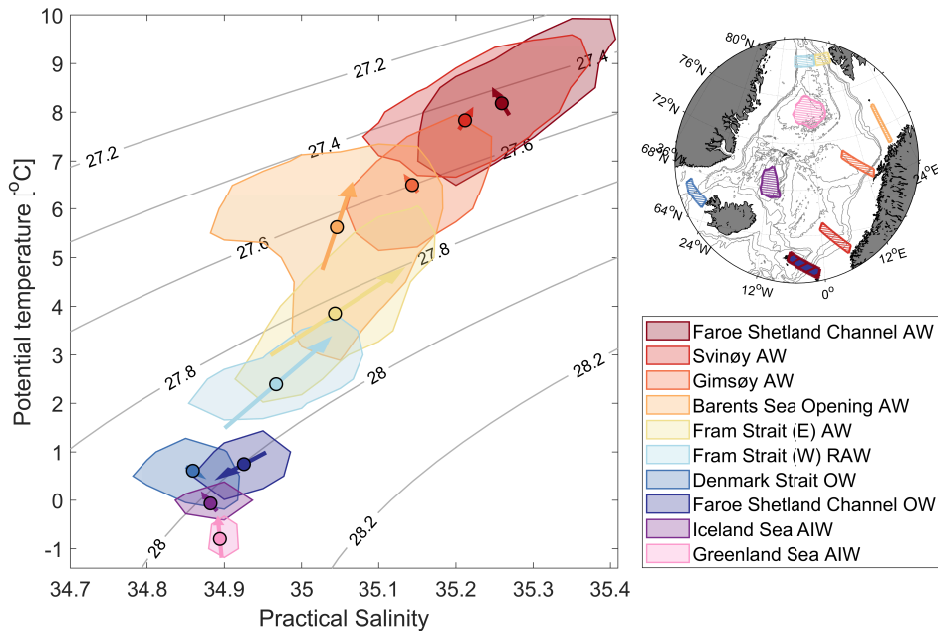


Figure 2.7: Evolution of hydrographic properties in the Nordic Seas from the AW inflow (red) to the overflows (blue), based on observations between 1950 and 2019 (Section 3.1). The figure is a modified version of Figure 6 in Smedsrud *et al.* (2022). The geographical regions are indicated on the map. The colored dots are observed median values of each water mass, while the arrows indicate linear trends over the period 1950–2019. The shading is based on the overall frequency of occurrence and outlines approximately 60% of the observations. The vertical constraints for the water masses were: AW and RAW – the depth of maximum temperature below 100 m (± 50 m); overflow water (OW) – denser than $\sigma_0 = 27.80 \text{ kg m}^{-3}$ and above the sill depths of Denmark Strait (650 m) and the Faroe Bank Channel (840 m); AIW – the typical mixed-layer depths in the Iceland Sea (150–350 m) and in the Greenland Sea (500–1500 m).

Substantial air-sea heat fluxes also occur further north in the Barents Sea, where the AW meets the cold polar air near the sea-ice edge. Some of the water is cooled to below 0°C before it enters the Arctic Ocean (Section 2.3.4, Schauer *et al.*, 2002). The integrated heat loss over the Barents Sea has increased in conjunction with the sea-ice retreat because of the larger open-ocean area (Smedsrud *et al.*, 2022). However, Skagseth *et al.* (2020) indicated that the "Barent Sea cooling machine" (warmer AW inflow, less sea ice, more regional heat loss) has recently reached a state of less efficient cooling due to reduced heat fluxes over the southern Barents Sea as a result of anomalous southerly winds. Moore *et al.* (2022) also showed that the heat fluxes in the southern Barents Sea have decreased as the sea ice retreated northward. This has resulted in a warmer outflow from the Barents Sea into the Arctic Ocean (Skagseth *et al.*, 2020). The water that flows northward through both the Barents Sea and Fram Strait encircle the Arctic Ocean as intermediate water masses and are further modified along the transit (Section 2.3.4,

Rudels et al., 1999, 2004). When returning to the Nordic Seas in the East Greenland Current, the water classified as Atow is typically recognized by maxima in temperature and salinity below the PSW (between 100 and 500 m depth, *Mauritzen*, 1996; *Rudels et al.*, 2002, 2005; *Jeansson et al.*, 2008; *Håvik et al.*, 2017a). Some of the water from the Arctic Ocean has cooled to temperatures below 0°C and are no longer classified as Atow as described in Section 2.3.4.

Most of the East Greenland Current north of Denmark Strait has until recently been covered by sea ice in winter, and further modifications of the Atow has primarily taken place by lateral exchange with water in the Iceland and Greenland Seas (Section 2.3.5). During the last decade, however, large parts of the current has become ice free during winter (*Våge et al.*, 2018; *Moore et al.*, 2022). This has facilitated enhanced transformation of the Atow by air-sea interaction along the East Greenland Current. *Våge et al.* (2018) recently showed evidence of re-ventilation of the Atow in the northwestern Iceland Sea and suggest that this could potentially compensate for some of the reduced heat fluxes observed in regions far away from the sea ice (*Moore et al.*, 2022).

2.3.3 Open-ocean convection in the interior basins

Another important mechanism for dense-water formation in the Nordic Seas is open-ocean convection, a process which is divided into three distinct phases as illustrated in Figure 2.8 (*Marshall and Schott*, 1999). The first phase is preconditioning of the water column such that it becomes sufficiently weakly stratified, prior to winter, for the atmospheric forcing during winter to initiate deep convection. Weak stratification is typically found within the cyclonic gyres in the interior basins of the Nordic Seas. Associated with these gyres is a divergent Ekman transport near the surface that brings dense, weakly-stratified water masses closer to the surface where they are more readily exposed to atmospheric forcing. The doming of dense isopycnals reduces stratification and preconditions the water column for wintertime convection (Figure 2.8a, *Marshall and Schott*, 1999). Even though a region is preconditioned for deep convection, the atmospheric forcing during winter must be sufficiently strong to erode the near-surface stratification to initiate convective overturning (i.e., the second phase of open-ocean convection, Figure 2.8b). During active convection, vertical mixing takes place in numerous plumes and the result is a deep mixed patch that can become more than 100 km in diameter (*Marshall and Schott*, 1999). Although the degree of horizontal homogeneity within a convective region can vary due to small scale plumes and vortices (e.g., *Marshall and Schott*, 1999; *Rudels et al.*, 1989; *Gascard et al.*, 2002; *Wadhams et al.*, 2002), we focus on the resulting mixed patch in the thesis, which accounts for the bulk of the convective region. The nearly vertically homogeneous layer caused by the convective mixing is defined as the mixed layer (Figure 2.8c). The final phase of open-ocean convection is restratification (Figure 2.8d). Lateral exchange between the mixed patch and the ambient water takes place throughout the year and when the atmospheric forcing ceases in spring it results in a restratification of the convective region (*Straneo*, 2006). The well-mixed water mass spreads out at its neutral density level under the influence of gravity and a thin stratified layer develops over the mixed patch.

Deep open-ocean convection is not a process that occurs with certainty and regularity. The timing and strength of the convection depends on a variety of factors. These include the strength of the atmospheric buoyancy and cyclonic wind forcing, the stability of the

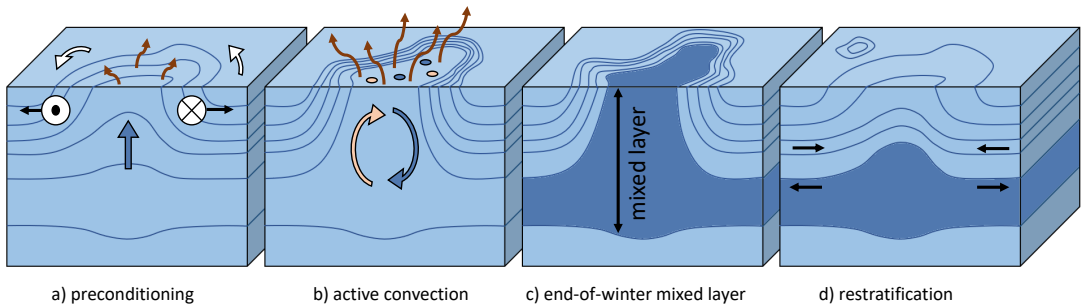


Figure 2.8: Schematic illustration of the three phases of open-ocean convection: (a) preconditioning, (b) active convection which results in a deep (c) end-of-winter mixed layer, and (d) restratification. The density stratification of the water column is indicated by blue contours, while the volume ventilated by convection is shaded dark blue. The red arrows at the surface illustrate heat loss to the atmosphere. The figure is based on Figure 3 in Marshall and Schott (1999).

water column, lateral advection, whether convection occurred during the previous winter (which would impact the water column stability), and sea ice (e.g., Meincke *et al.*, 1992; Malmberg and Jónsson, 1997; Marshall and Schott, 1999). Sea ice influences the depth of convection in various ways. The presence of sea ice has an insulating effect that reduces air-sea interactions, sea-ice formation releases brine that increases the near-surface salinity and density, while sea-ice melting decreases the near-surface salinity and density. As a relatively fresh surface layer is needed for ice to form in the first place, substantial brine release is required to erode the strong near-surface stratification for convection to occur. Another condition to induce deep convection is advection of the locally formed sea ice out of the gyre center leaving an open-ocean region with high surface salinity (Meincke *et al.*, 1992; Marshall and Schott, 1999).

Open-ocean convection in the Lofoten Basin and its interaction with the Norwegian Atlantic Current is crucial for cooling and densification of the AW as it progresses northward in the Atlantic Domain (Section 2.3.2, Bosse *et al.*, 2018). Below we focus on the open-ocean convection that takes place within the Arctic Domain of the Nordic Seas.

The Greenland Sea

The deepest and densest open-ocean convection in the Nordic Seas takes place in the Greenland Sea gyre. Here, convection occasionally extended to the bottom before the early 1980s and formed the cold and dense Greenland Sea Deep Water (GSDW) that used to supply most of the deep water in the entire Nordic Seas and Arctic Ocean (Helland-Hansen and Nansen, 1909; Carmack and Aagaard, 1973; Malmberg, 1983; Aagaard *et al.*, 1985; Schlosser *et al.*, 1991; Bönisch and Schlosser, 1995; Bönisch *et al.*, 1997; Strehl *et al.*, submitted). In the 1980s, however, formation of GSDW ceased and convection has only been observed to intermediate depths after that (Schlosser *et al.*,

1991; *Meincke et al.*, 1992; *Rhein*, 1996; *Meincke et al.*, 1997; *Karstensen et al.*, 2005; *Ronski and Budéus*, 2005; *Latarius and Quadfasel*, 2010; *Somavilla*, 2019; *Strehl et al.*, submitted). Various studies have linked the reduced convection to reduced atmospheric forcing, less sea-ice formation, and increased stratification due to changes in the hydrographic conditions (*Meincke et al.*, 1992; *Somavilla*, 2019; *Strehl et al.*, submitted). The primary reason for the shut down of deep convection in the 1980s was most likely increased near-surface stratification due to a temporary freshening (*Strehl et al.*, submitted).

The main product of convection after the GSDW formation ceased has been the slightly warmer and less dense Greenland Sea Arctic Intermediate Water (GSAIW, *Meincke et al.*, 1992, 1997; *Karstensen et al.*, 2005; *Ronski and Budéus*, 2005; *Latarius and Quadfasel*, 2010; *Lawset et al.*, 2018, Paper I). As a result, a two-layer structure has developed in the Greenland Sea, with a pronounced intermediate stratification maximum separating the GSAIW from the denser GSDW. The distinction between deep and intermediate water masses is typically defined by the potential density anomaly referred to 500 m depth of 30.444 kg m^{-3} (Figure 2.6, Table 2.1, *Rudels et al.*, 2005; *Jensson et al.*, 2008). In the Greenland Sea the depth of this isopycnal coincides with the stratification maximum, which has descended from around 600 m in the late 1980s to between 1500 and 2000 m in the early 2000s (*Karstensen et al.*, 2005; *Ronski and Budéus*, 2005; *Budéus and Ronski*, 2009; *Latarius and Quadfasel*, 2010, Paper I). This is in line with the steady draining of the GSDW since the early 1980s and the gradual replacement of an increasing volume of GSAIW (Paper I, *Somavilla*, 2019). The stratification maximum limits convection to intermediate depths and prevents renewal of GSDW. A stronger warming trend of the GSAIW has further strengthened the stratification maximum (*Strehl et al.*, submitted). The reduced rates of renewal by local convection have in turn been accompanied by an increased input of saline deep water from the Arctic Ocean (*Meincke et al.*, 1997; *Somavilla et al.*, 2013) which has been observed to affect also other deep waters in the Nordic Seas (*Østerhus and Gammelsrød*, 1999).

While *Strehl et al.* (submitted) found that the total ocean to atmosphere heat loss over the Greenland Sea has increased since 1950 due to sea-ice retreat and a larger open-ocean area, *Moore et al.* (2015) found a 20% reduction in the magnitude of the heat fluxes over the Greenland Sea gyre since the end of the 1970s. The reduced heat fluxes over the gyre were primarily a result of increased distance to the sea-ice edge and decreased winter air-sea temperature differences (Section 2.2.2, *Moore et al.*, 2015). These changes have also resulted in reduced intensity of cold-air outbreaks (i.e., the strongest heat-flux events, *Somavilla*, 2019; *Dahlke et al.*, 2022; *Strehl et al.*, submitted). According to *Moore et al.* (2015, 2022), the trend toward weaker atmospheric heat fluxes over the Greenland Sea is expected to continue in a warming climate with continued sea-ice retreat, which could have substantial ramifications for the water-mass transformation there. However, the depth of convection also depends on the hydrographic conditions prior to the convective season, which in turn, depends on the lateral advection from the surrounding water masses (*Latarius and Quadfasel*, 2016; *Lawset et al.*, 2018, Paper II). Except for the cold and fresh PSW to the west of the gyre, any lateral exchange with surrounding water masses will increase the temperature and salinity of the water column in the Greenland Sea gyre. *Lawset et al.* (2018) argued that increased salinity in the northward-propagating AW has increased the salinity and thereby decreased the stability of the upper 1500 m of the Greenland Sea water column since the early 2000s,

which in turn has resulted in a tendency for deeper convection.

In Paper I (*Brakstad et al.*, 2019), we explored the interannual variability in convection and dense-water formation in the Greenland Sea over the period 1986–2016. We focused particularly on the evolution of GSAIW and used a combination of hydrographic observations and a one-dimensional mixed-layer model to determine its sensitivity to changes in the atmospheric forcing and hydrographic conditions. This is crucial to better understand how the convective activity in the Greenland Sea will respond to changing conditions in the future. A unique hydrographic data set, with high temporal resolution, from three profiling moorings in the central Greenland Sea between 1999 and 2009 (Section 3.2) was utilized in Paper II (*Svingen et al.*, 2023) in combination with the one-dimensional mixed-layer model to investigate how the wintertime mixed layer develops through the winter. We focused particularly on the impact of cold-air outbreaks (their frequency, intensity, and timing), which has not previously been studied in the Greenland Sea because of sparse data coverage. The mooring data and model were also used to estimate the effect of lateral heat and salt fluxes from surrounding water masses. While the overall magnitudes of heat and salt fluxes into the Greenland Sea gyre were estimated by *Moore et al.* (2015), *Latarius and Quadfasel* (2016), and in Paper I based on budget calculations, uncertainties remain regarding their vertical distributions and where the heat and salt enter the gyre.

The Iceland Sea

Open-ocean convection in the central Iceland Sea typically extends to 150–250 m depth and forms slightly less dense Arctic-origin water than the Greenland Sea (*Swift and Aagaard*, 1981; *Våge et al.*, 2015, 2022). Based on hydrographic observations, *Våge et al.* (2022) quantified the water-mass transformation in the central Iceland Sea and how it has changed over the four decades from winter 1974–1975, which was originally investigated by *Swift and Aagaard* (1981), to 2015–2016. They found that the locally formed water was warmer and less dense in 2015–2016 and that the entire water column of the central Iceland Sea has decreased in density. The water masses presently formed are warmer than 0°C, which implies that the traditional distinction between Arctic-origin and Atlantic-origin water masses at the 0°C isotherm (Table 2.1, Figure 2.6, *Swift and Aagaard*, 1981; *Rudels et al.*, 2005; *Våge et al.*, 2011) is no longer representative (*Våge et al.*, 2022).

The changes in the central Iceland Sea have occurred in concert with diminished ocean-to-atmosphere heat fluxes due to the retreating sea-ice edge (*Våge et al.*, 2022; *Moore et al.*, 2022). However, the sea-ice retreat has also resulted in an ice free western Iceland Sea, where convection has been observed to ventilate the Atlantic-origin layer of the East Greenland Current (*Våge et al.*, 2018). *Våge et al.* (2018) found mixed-layer depths exceeding 400 m in the northwestern part of the Iceland Sea near the sea-ice edge, which aligns well with the notion that the deepest and densest convection in the Iceland Sea actually occurs in the northwestern part on the outskirts of the gyre (*Våge et al.*, 2015). This is different from the Greenland Sea where convection within the gyre dominates (Paper I).

2.3.4 Inflow of dense water from the Arctic Ocean

In addition to PSW and Atow, several dense intermediate and deep water masses colder than 0°C are also transported southward through Fram Strait from the Arctic Ocean by the East Greenland Current (*Rudels et al.*, 2005; *Jeansson et al.*, 2008, 2017). These dense water masses are located below the warmer Atow and are composed of AW that has been cooled substantially by wintertime convection in the Barents Sea, dense plumes formed on the Arctic shelves, and NDW originally formed in the Greenland Sea that flows into the Arctic Ocean with the West Spitsbergen Current (*Aagaard et al.*, 1985; *Rudels et al.*, 1999; *Langehaug and Falck*, 2012). The dense plumes are formed by convection on the Arctic shelves (including the Barent Sea, e.g., *Ivanov et al.*, 2004). Here air-sea heat fluxes cool the water column such that sea ice forms. The sea-ice formation releases saline brine that sinks and accumulates near the bottom. The cold, brine-enriched water spills across the shelf break as dense plumes that cascade down the continental slope toward deeper isobaths (*Aagaard et al.*, 1985; *Ivanov et al.*, 2004). The plumes cascade as rotating gravity currents until they reach neutral density. On the way, they entrain ambient water, and can modify intermediate and deep water masses of the Arctic Ocean (*Aagaard et al.*, 1985; *Bauch et al.*, 1995). This process is often referred to as shelf or slope convection, and is most efficient in regions where the locally formed sea ice is constantly removed by winds (i.e., polynyas, *Backhaus et al.*, 1997).

The relative contributions of shelf convection, water formed in the Barents Sea, and water originally sourced from the Greenland Sea to the water masses that flow southward across Fram Strait are not well known. Because of their long transit through the Arctic Ocean before entering the Nordic Seas, their geochemical properties are distinct from the water occupying the same density range in the Nordic Seas (*Jeansson et al.*, 2008, 2017). One example is the upper Polar Deep Water (uPDW), which has a generally lower oxygen and higher nutrient concentration than the Arow formed in the Iceland and Greenland Seas (e.g., Figure 2.6b). The Arctic Ocean Deep Water (AODW) is also warmer and more saline than the GSDW. After the GSDW formation ceased, the inflow of AODW to the Nordic Seas has resulted in a general warming of the deep water masses of the Nordic Seas (*Meincke and Rudels*, 1996; *Østerhus and Gammelsrød*, 1999; *Somavilla et al.*, 2013).

2.3.5 Exchange and mixing between the boundary and the interior

In addition to a few direct currents, such as the Jan Mayen Current and the East Icelandic Current (Figure 2.4, *Bourke et al.*, 1992; *Macrandar et al.*, 2014), exchange between the boundary and the interior basins of the Nordic Seas takes place through lateral mixing and eddy fluxes driven by baroclinic instabilities (e.g., *Strass et al.*, 1993; *Spall*, 2010; *Segtnan et al.*, 2011; *Våge et al.*, 2013; *Håvik et al.*, 2017b; *Ypma et al.*, 2020; *Fer et al.*, 2020; *Spall et al.*, 2021). The Lofoten Basin is known for being particularly eddy-rich (*Köhl*, 2007; *Raj et al.*, 2016; *Dugstad et al.*, 2019). At the eastern boundary of the basin the steep continental slope destabilizes the Norwegian Atlantic Slope Current, which results in baroclinic instabilities and eddies that shed into the interior (*Köhl*, 2007; *Spall*, 2010; *Fer et al.*, 2020). Observations and models also indicate that heat and salt from the Norwegian Atlantic Front Current crosses the Mohn and Knipovich ridges into the central Greenland Sea (*van Aken et al.*, 1995; *Spall*, 2010; *Segtnan et al.*, 2011; *Bosse*

and Fer, 2019; Ypma et al., 2020). However, Huang et al. (2023) recently showed that lateral exchange is less important for the cooling of the front current, compared to the slope current. Nearly all the cooling of the front current can be explained by air-sea heat exchange (Huang et al., 2023). Farther north, eddies in Fram Strait are responsible for a major part of the recirculating AW from the West Spitsbergen Current (e.g., Hattermann et al., 2016).

In the western Nordic Seas, the East Greenland Current mixes with the interior Greenland and Iceland Seas, which results in a reduced Atow temperature (Håvik et al., 2019) and can have important implications for the open-ocean convection in the interior basins (Lauvset et al., 2018, Paper I, Paper II). Because of similar densities, isopycnal mixing between the GSAIW and cold water masses originating in the Arctic Ocean, such as the uPDW, is commonly observed (Strass et al., 1993; Rudels et al., 2002, 2005; Jeansson et al., 2008; Håvik et al., 2017a). Farther south in the Iceland Sea at approximately 69°N, a local maximum in eddy activity is thought to contribute to the bifurcation of the East Greenland Current into the separated and shelf break branches (Våge et al., 2013; Håvik et al., 2017a). The East Greenland Current also transports a substantial amount of sea ice and fresh PSW that may be diverted into the interior basins across the Polar Front (Dodd et al., 2009; Spall et al., 2021; Langehaug et al., 2022). While this can have substantial impacts for the local convection in the Iceland and Greenland Seas, Glessmer et al. (2014) suggested that freshwater from the East Greenland Current only accounts for 20% of the variability in the Nordic Seas freshwater storage. More important is the salinity variability in the AW inflow (Glessmer et al., 2014; Lauvset et al., 2018). In the Atlantic Domain the Norwegian Coastal Current partly mixes with the Norwegian Atlantic Slope Current, which freshens the AW as it propagates northward (Figure 2.7, Mauritzen, 1996).

2.4 Sources and upstream pathways of dense overflow water

Overflow water is typically referred to as water denser than $\sigma_0 = 27.80 \text{ kg m}^{-3}$ (Dickson and Brown, 1994) that spills southward across the Greenland-Scotland Ridge into the North Atlantic. Approximately 90% of the overflow water emanating from the Nordic Seas passes through Denmark Strait or the Faroe Bank Channel (Østerhus et al., 2019). The overflow transport through these passages have been monitored since the mid-1990s and are estimated to $3.2 \pm 0.5 \text{ Sv}$ and $2.0 \pm 0.3 \text{ Sv}$ on average for the Denmark Strait and Faroe Bank Channel, respectively (Hansen et al., 2016; Jochumsen et al., 2017; Østerhus et al., 2019). This implies that over half of the total overflow water transport from the Nordic Seas passes through Denmark Strait, while the Faroe Bank Channel overflow accounts for approximately 1/3. While the overflow water transport is well known, questions remain regarding their upstream sources and pathways as described in the following sections.

2.4.1 Denmark Strait Overflow Water

The origin of the largest overflow plume, which passes through Denmark Strait on the western side of Iceland (Jochumsen et al., 2017; Østerhus et al., 2019), has been debated in the literature for several decades. Initially, the primary source of Denmark Strait Overflow Water (DSOW) was thought to be Arow formed by open-ocean convection in

the Iceland and Greenland Seas (Section 2.3.3, *Swift et al.*, 1980; *Swift and Aagaard*, 1981; *Strass et al.*, 1993). As no direct current from the interior basins to the Denmark Strait was known at this time, the transport of dense water from the gyres was assumed to primarily occur by isopycnal mixing with the boundary currents. *Mauritzen* (1996) later argued that this process is too slow to account for the overflow transport through Denmark Strait and proposed instead that Arow transported with the East Greenland Current is the main source. In this scenario, the formation occurs through gradual densification of AW along the boundary current system of the Nordic Seas and the Arctic Ocean (Section 2.3.2). This scenario was the commonly accepted view for more than a decade, supported by observations (*Eldevik et al.*, 2009) and numerical simulations (*Köhl*, 2007). Although observational water-mass analyses supported this view, they showed that substantial mixing between the East Greenland Current and the interior basins also takes place (*Rudels et al.*, 2002; *Tanhua et al.*, 2005; *Jeansson et al.*, 2008).

The scheme proposed by *Mauritzen* (1996) was modified by the discovery of the North Icelandic Jet (NIJ) flowing along the slope north of Iceland toward Denmark Strait (*Jónsson*, 1999; *Jónsson and Valdimarsson*, 2004; *Våge et al.*, 2011). This current provides a pathway for overflow water distinct from the East Greenland Current, and supplies the densest portion of the DSOW (*Våge et al.*, 2011; *Mastropole et al.*, 2017). According to *Harden et al.* (2016) the East Greenland Current supplies approximately 2/3 of the DSOW, while the NIJ supplies the remaining 1/3. Recent work by *Semper et al.* (2019) suggests that the NIJ transport could account for nearly half of the DSOW.

Våge et al. (2011) hypothesized that the NIJ is the deep branch of a local overturning loop in the Iceland Sea that involves the inflowing NIIC shedding warm and saline eddies into the Iceland Sea and water mass transformation within the interior Iceland Sea. They suggested that densified water sinks near the slope and is advected by the NIJ back to Denmark Strait. Later studies show, however, that convection in the interior Iceland Sea may not produce sufficiently dense water (*Våge et al.*, 2015, 2022). The bulk of the NIJ transport is associated with dense Arow centered around the $\sigma_{\Theta}=28.05 \text{ kg m}^{-3}$ isopycnal (*Semper et al.*, 2019), which is denser than the water presently formed in the central Iceland Sea (*Våge et al.*, 2015, 2022). In Paper I and II, we show that sufficiently dense water is regularly produced in the central Greenland Sea (*Brakstad et al.*, 2019; *Svingen et al.*, 2023), which corroborates the results of *Huang et al.* (2020) who identified the Greenland Sea as a main source of the water masses in the NIJ. This is also supported by *Messias et al.* (2008), who suggested based on a tracer release experiment that took place in 1996 that Arow from the Greenland Sea gyre enters the Iceland Sea and may supply the overflows.

Another current that has recently received increased attention in relation to the DSOW, is the northward flowing NIIC. A fraction of this current recirculates north of Denmark Strait (*Casanova-Masjoan et al.*, 2020) and has densified sufficiently to contribute to the lightest components of the overflow (*Mastropole et al.*, 2017; *Saberi et al.*, 2020; *Garcia-Quintana et al.*, 2021). While *Garcia-Quintana et al.* (2021) suggested, based on numerical simulations, that dense-water formation within the NIIC on the north-west Iceland shelf may contribute significantly to the NIJ, observations show that formation of such dense waters on the Iceland shelf north of Denmark Strait is rare (*Semper et al.*, 2022).

Although our understanding about the origin and upstream pathways of the DSOW has improved substantially over the last few decades, questions still remain regarding the

export of dense water from the Greenland Sea and the final composition of the DSOW plume (i.e., the relative contributions of the different dense-water sources). Several water-mass studies have examined the DSOW composition (e.g., *Tanhua et al.*, 2005; *Jeansson et al.*, 2008; *Eldevik et al.*, 2009; *Mastropole et al.*, 2017; *Lin et al.*, 2020), but their results differ depending on the dense-water sources considered, their specified properties, and whether geochemical data were included or not. The properties are typically defined based on the available observations used in each study and are sensitive to both temporal and spatial variability. In Paper III (*Brakstad et al.*, 2023), we developed a regional high-resolution water-mass inversion based on *Gebbie and Huybers* (2010) and *Gebbie* (2014), which is not dependent on a few pre-defined source waters and accounts for spatial water-mass variability (Section 3.6, Paper III). This facilitated a detailed analysis of the DSOW origin and composition, including how the various dense-water sources flow and mix along their pathways toward Denmark Strait. Results from the inversion confirms the importance of both Atow and Arow for the DSOW, and shows how the NIJ is supplied by dense Arow from the central Greenland Sea (Paper III). Two inversions, one for 1950–1979 and one for 2000–2019 were compared in Paper IV to examine the impact of temporal variability in dense-water formation (particularly the effect of the changes observed in the central Greenland Sea, Section 2.3.3).

2.4.2 Faroe Bank Channel Overflow Water

The deepest and densest overflow plume passes the Greenland-Scotland Ridge through the Faroe Bank Channel. The Faroe Bank Channel Overflow Water (FBCOW) consists of approximately equal parts intermediate and deep water masses (*Fogelqvist et al.*, 2003; *McKenna et al.*, 2016). The intermediate-water component is composed of Arow formed by open-ocean convection in the Iceland and Greenland Seas, uPDW from the Arctic Ocean, and a smaller fraction of Atow primarily densified in the Norwegian Basin (*Hansen and Østerhus*, 2000; *Fogelqvist et al.*, 2003; *Olsson et al.*, 2005; *Eldevik et al.*, 2009; *Jeansson et al.*, 2017). The deep-water component, on the other hand, is a mixture of old GSDW that used to form in the central Greenland Sea until the 1980s and deep water masses flowing southward from the Arctic Ocean (*Aagaard et al.*, 1985; *Swift and Koltermann*, 1988; *Hansen and Østerhus*, 2000). Several studies indicate that these deep water masses enter the Norwegian Sea through deep gaps in the Mohn Ridge north of Jan Mayen (*Swift and Koltermann*, 1988; *Østerhus and Gammelsrød*, 1999; *Hansen and Østerhus*, 2000; *Somavilla*, 2019; *Shao et al.*, 2019; *Wang et al.*, 2021). They are then transported southward along the eastern boundary of the Jan Mayen Ridge along with Arow from the Greenland Sea (*Olsson et al.*, 2005; *Messias et al.*, 2008; *Huang et al.*, 2020). Although the Jan Mayen Ridge boundary current is identified in both observations and models (*Voet et al.*, 2010; *Serra et al.*, 2010; *Köhl*, 2010; *Huang et al.*, 2020; *Hátún et al.*, 2021), it is still unclear how much it contributes to the FBCOW.

The pathways transporting overflow water toward the Faroe Bank Channel has only recently received enhanced attention. *Semper et al.* (2020) documented the existence of a current flowing along the slope north of Iceland to the Faroe Islands. The current was named the Iceland-Faroe Slope Jet (IFSJ) and its transport may account for half of the FBCOW. The hydrographic properties of the water transported by the IFSJ are similar to the NIJ, which suggests that they could be supplied from a common source (*Semper et al.*, 2020). Both currents transport dense Arow and *Huang et al.* (2020) suggested

that this Arow primarily originates in the central Greenland Sea. They also found evidence of several southward pathways along the submarine ridge system surrounding the central Iceland Sea. Where and how the dense water exits the Greenland Sea and to what extent these potential pathways feed the NIJ and IFSJ remain unclear. Another pathway, transporting overflow water from the eastern margin along the Norwegian slope toward the Faroe-Shetland Channel (upstream of the Faroe Bank Channel, Figure 2.2) was identified by *Chafik et al.* (2020). The upstream sources of this water, however, are not known. The upstream sources and pathways of the FBCOW were examined in Paper III using the high-resolution regional water-mass inversion (Section 3.6). This showed that most of the FBCOW originates in the Greenland Sea and Arctic Ocean. It also revealed unprecedented details on how dense water from these source regions flow toward the Faroe Bank Channel.

3 Data and methods

A comprehensive database of hydrographic and geochemical observations between 1950 and 2019 was prepared in this thesis and utilized to improve our understanding of the overturning system in the Nordic Seas. This data set, combined with 10 years of moored hydrographic observations from the central Greenland Sea, provided insight into how dense-water formation in the Nordic Seas has varied on time scales ranging from seasonal to multidecadal. To better understand the mechanisms governing the observed variability, we employed several ancillary data sets and methods. These include atmospheric reanalyses, sea-ice observations, and a one-dimensional mixed-layer model. Dense water formed in the Nordic Seas returns southward in the Greenland-Scotland Ridge overflows. A high-resolution regional water-mass inversion based on observations was developed to examine the origin and upstream pathways of these overflows. The data sets and primary methods used in this thesis are introduced in the following sections.

3.1 Historical hydrographic and geochemical observations

Vertical profiles of temperature, salinity, oxygen, nitrate, and phosphate from shipboard conductivity, temperature, and depth (CTD) instruments and water samples, autonomous profiling floats, and instrumented seals were collected from a wide range of archives over the period 1950–2019 (Figure 3.1). The data sources and archives are listed in Paper I (Section 2a) and Paper III (Table 1), while an overview of the temporal and spatial data distributions are given in Paper I (Figure 2) and Paper III (Figure 2). The temporal data coverage was generally lower prior to the 1980's when most observations were collected by water samples. After 1980, the use of shipboard CTD instruments became more common, which led to a considerable increase in the number of profiles collected per year, as well as their vertical resolution. However, difficult weather conditions and sea ice during winter resulted in a bias toward summer data. The seasonal coverage was significantly improved after 2001, when the Argo program and deployments of autonomous profiling floats started in the Nordic Seas. The Argo floats typically measure a vertical profile from 2000 m to the surface every 10 days (Figure 3.1d), and can operate autonomously also throughout the winter when dense water masses primarily form (Våge *et al.*, 2015; Marnela *et al.*, 2016). We note that although there has been a large technological development in oceanographic measurement techniques, water samples are still crucial for obtaining geochemical measurements and for calibration purposes.

In Paper I, we utilized hydrographic observations from the Greenland Sea between 1986–2016 to examine what determined the inter-annual variability in the end-of-winter mixed layer and dense-water product. In this paper, we also used the CTD data collected by the instrumented seals during 2007–2008 (Isachsen *et al.*, 2014) to obtain better data coverage along the Greenland shelf, where data from other sources are sparse. These profiles were acquired over a relatively small geographical area at much higher temporal resolution than the other observations. Hence, they were not included in the combined 1950–2019 hydrographic and geochemical data product compiled in Paper III as they would dominate the late-winter climatologies created and employed in Paper III and IV to investigate dense-water formation in the Nordic Seas on longer time scales. For the same reason, we excluded observations collected by moored installations and underwater

gliders. One way to remove the resolution bias would be to include average profiles from these measurement techniques, which should be considered in future work.

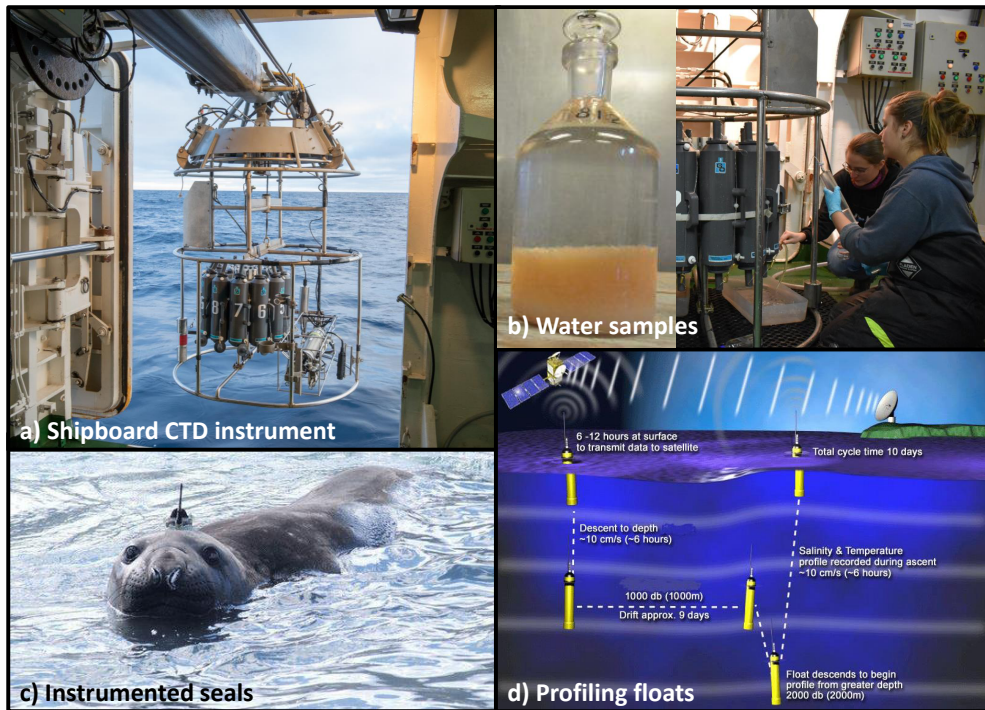


Figure 3.1: Photos of a shipboard CTD rosette (a) with Niskin bottles used to collect water samples (b), a seal instrumented with a CTD sensor (c), and a schematic illustration of the profiling cycle of an autonomous Argo float (d). The photos were taken by Sindre Skrede, NRK - the Norwegian Broadcasting Corporation (a), Mirjam Glessmer, University of Bergen (b, left), Chris Barrell, University of East Anglia (b, right), and Lars Boehme, University of St. Andrews (c). The schematic illustration (d) was obtained from the Argo Program (<https://www.argo.ucsd.edu>).

All observations collected in Paper I and in Paper III were combined into single data sets and quality controlled according to *Skagseth and Mork (2012)* and *Våge et al. (2013, 2015)*. The procedure involved removing duplicates between various archives, erroneous profiles, density inversions, and outliers. Details are provided in the respective papers. For the historical 1950–2019 data product we separated the observations into three periods (1950–1979, 1980–1999, and 2000–2019) and inspected them for outliers separately. These three periods were also used to investigate long-term variability in the dense-water reservoir in the Nordic Seas in Paper IV.

Throughout the thesis we follow the Thermodynamic Equation Of Seawater - 2010 standard (TEOS-10, *IOC et al., 2010*) and use Conservative Temperature and Absolute Salinity instead of potential temperature and practical salinity (EOS-80, Equation of State of Seawater - 1980, *ICES et al., 1981*). One exception is Paper I, where the EOS-80 standard was used.

3.2 Moored hydrographic measurements

In Paper II, we used 10 years (1999–2009) of hydrographic observations from three moored profiling vehicles in the central Greenland Sea, where the deepest and densest convection occurs (Paper I). These vehicles measured vertical profiles of temperature, salinity, and pressure from approximately 100 m depth to the sea floor at 3700 m (Figure 3.2). The vertical motion of the profilers was mechanically driven, by adding and removing lead weights to change the vehicles’ buoyancy. Lead weights were added from a basket at the top of the moorings and released into a net near the bottom. The vehicles themselves were buoyant, while the lead weight added at the top caused them to sink. Further technical details about the moorings are provided in Paper II and in *Budéus et al.* (2005).

The three moored profilers were deployed and recovered annually over the 10-year period. Vertical profiles from each vehicle were acquired every second day on average, except for periods with technical issues (Paper II). Another exception was the final year of the deployment period (2008–2009), when daily profiles were collected (*Budéus*, 2009). In this final year, another supplementary mooring that covered the upper 130 m of the water column was deployed to obtain complete surface to bottom profiles (*Budéus*, 2009). An overview of the mooring locations and temporal data coverage after post processing is provided in Paper II (Figure 2).

The high temporal resolution and long duration of these data facilitated a detailed analysis of the development of the wintertime mixed layer in the Greenland Sea (Paper II). In particular, we quantified the direct impact of cold-air outbreaks and how the mixed layer responded to different timing and intensity of such events, using a statistical approach. This has not previously been possible due to sparse data coverage and the short duration of these events (Section 2.2.2, *Terpstra et al.*, 2021).

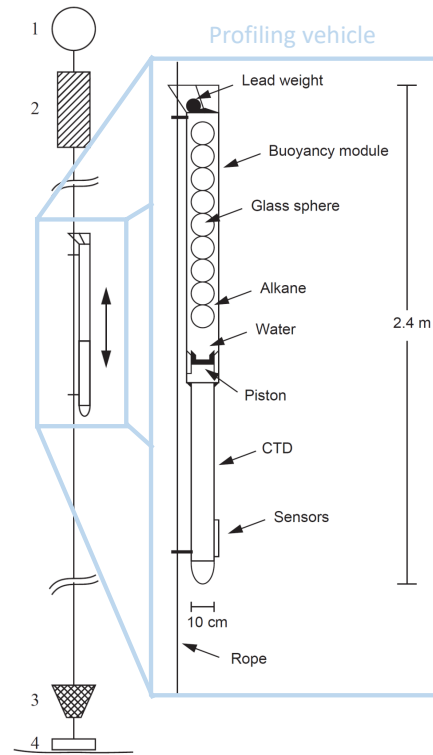


Figure 3.2: Illustration of the moored hydrographic profilers from *Budéus et al.* (2005). The left part shows a complete mooring, including a buoyancy sphere at approximately 70 m depth (1), a control unit with a basket of lead weights (2), the profiling vehicle (in the middle), a net collecting the dropped lead weights (3), and a ground anchor at the bottom (4). Details of the profiling vehicle with CTD sensor are shown to the right.

3.3 Atmospheric reanalyses, sea ice, and satellite altimeter data

Atmospheric reanalyses from the European Centre for Medium-Range Weather Forecast were used in Papers I, II, and IV to assess the impact of atmospheric forcing on dense-water formation in the Nordic Seas on various temporal and spatial scales. In Paper I, we employed 6-hourly air-sea fluxes of heat, freshwater, and momentum, as well as sea-ice concentration from the ERA-Interim product (*Dee et al.*, 2011). These were averaged over the area of the Greenland Sea gyre and used to examine the atmospheric impact on winter mixed-layer variability on inter-annual time scales. We used the new high-resolution product ERA5 in Papers II and IV (*Hersbach et al.*, 2020). This product was not available when the analysis in Paper I was conducted. In Paper II, we employed hourly air-sea fluxes of heat, freshwater, and momentum, as well as potential temperature at 900 hPa, surface skin temperature, surface pressure, and sea-ice concentration. These were used to assess the impact of cold-air outbreaks and heat fluxes on scales from days to multi-year. The parameters were averaged over a small geographical area enclosing the locations of the moored profiling vehicles in the central Greenland Sea (Section 3.2, Figure 2 in Paper II). In Paper IV, we focused on the Nordic Seas dense-water reservoir and overflows on multi-decadal and longer time scales. Hence, we employed monthly mean fields of air-sea heat and momentum fluxes from the ERA-5 product. In addition, we utilized sea-ice observations from the National Snow and Ice data Center in Papers III and IV. These observations have been interpolated onto a regular 0.25° grid with monthly resolution (*Walsh et al.*, 2015, 2017).

To set up the regional water-mass inversion (Section 3.6, Papers III and IV) we used surface geostrophic velocity fields from satellite altimeter data from the Copernicus Marine Environmental Monitoring Service (<http://marine.copernicus.eu>). These fields have a regular spatial resolution of 0.25° and cover the period 1993 to present. They were combined with relative geostrophic velocities estimated from hydrographic observations to obtain absolute geostrophic velocities for the entire Nordic Seas (Paper III and IV).

3.4 Mixed-layer estimation

Throughout the thesis we investigated changes in mixed-layer depths and hydrographic properties, which are measures of the extent of convection and its dense-water product (e.g., Figure 2.8). To determine the vertical extent of the mixed layer, we applied a robust procedure that is built on two independent automated routines and a manual routine involving visual inspection of each hydrographic profile (*Våge et al.*, 2015). The automated routines identify the base of the mixed layer from a density-difference criterion with respect to the measured surface temperature and salinity (*de Boyer Montégut et al.*, 2004; *Nilsen and Falck*, 2006) and as the shallowest extremum in the curvature of the temperature profile (*Lorbacher et al.*, 2006). If neither of the automated routines accurately identified the mixed-layer depth, which was subjectively verified by the visual inspection, it was determined manually following the routine of *Pickart et al.* (2002). A detailed description of the three routines is provided in Paper I (Appendix A). The manual routine was used for 39% of the historical hydrographic profiles in the Greenland Sea between 1986 and 2016 (Paper I) and for approximately half of the mixed layers detected by the moored profilers in the central Greenland Sea between 1999 and 2009 (Paper II). Because of shallow summer mixed layers, most of the mixed layers detected by the moored profilers took place during winter when the automated routines were

less accurate because of the weak water-column stratification (Våge *et al.*, 2015, Paper I, Paper II). The manual routine was also used for multiple stacked mixed layers and mixed layers isolated from the surface, which is often observed during periods of active convection (Våge *et al.*, 2009, 2015; Pickart *et al.*, 2002, Paper I).

In papers III and IV, we focused on late-winter (February–April) mixed layers in the entire Nordic Seas over the period 1950–2019. For the Iceland and Greenland Seas we updated existing mixed-layer databases (Våge *et al.*, 2015; Strehl *et al.*, submitted, Paper I) to cover the entire 1950–2019 period in a consistent manner. For the rest of the Nordic Seas, where the density gradient below the base of the mixed layer was more pronounced than in the Iceland and Greenland Seas, the automated routines generally perform well (e.g., de Boyer Montégut *et al.*, 2004; Nilsen and Falck, 2006). Hence, we employed the automated density-difference criterion to identify the late-winter mixed-layer depths in the remaining areas of the Nordic Seas from 2000 to 2019 (Paper III) and from 1950 to 1999 (Paper IV). The corresponding mixed-layer hydrographic and geochemical properties were estimated as the mean values over the extent of each identified mixed layer.

3.5 One-dimensional mixed-layer model

To better understand the observed mixed-layer variability in the Greenland Sea and its sensitivity to various hydrographic and atmospheric forcing conditions (Papers I and II), we employed a one-dimensional mixed-layer model called Price-Weller-Pinkel (PWP) after Price *et al.* (1986). We used the version modified by Moore *et al.* (2015), and improved it further as described below, to better represent winter conditions within the Greenland Sea gyre. A schematic illustration of the model is shown in Figure 3.3. The model was initialized with fall (October–November) hydrographic profiles and integrated through winter (November–April) with atmospheric forcing, oceanic lateral advection of heat and salt, sea-ice formation, and vertical mixing. The output from the model was the simulated development of the mixed-layer depth and hydrographic properties of the water column.

The atmospheric forcing in the model included air-sea fluxes of heat, freshwater, and momentum (Section 3.3), which were imposed at the surface at each model time step (Price *et al.*, 1986). To balance the annual-mean heat budget for the Greenland Sea gyre, a substantial amount of oceanic heat advection is required (Moore *et al.*, 2015; Latarius and Quadfasel, 2016). Moore *et al.* (2015) used this information to parameterize lateral advection of heat in the model. The vertical distribution was based on the temperature differences across the gyre boundary and is illustrated by the ΔT profile in Figure 3.3. The same principle was used to parameterize lateral advection of salt in Paper I to obtain a balanced salt budget. As in Moore *et al.* (2015), we assumed constant rates of advection throughout the year to determine the added heat and salt in each time step of the model (Appendix B, Paper I). The parameterized heat and salt advection was updated in Paper II based on observations from the moored profilers. Here, we estimated changes in temperature and salinity below the surface mixed layer and assumed that these were primarily caused by oceanic advection of heat and salt. The rates of temperature and salinity changes were similar in magnitude to those estimated from the annual-mean heat and salt budgets, but provided more details regarding the vertical distributions (Section 6, Paper II). To realistically simulate the mixed-layer evolution in the Greenland Sea gyre, it was essential to include lateral advection of both heat and salt (Moore *et al.*,

2015, Paper I, Paper II).

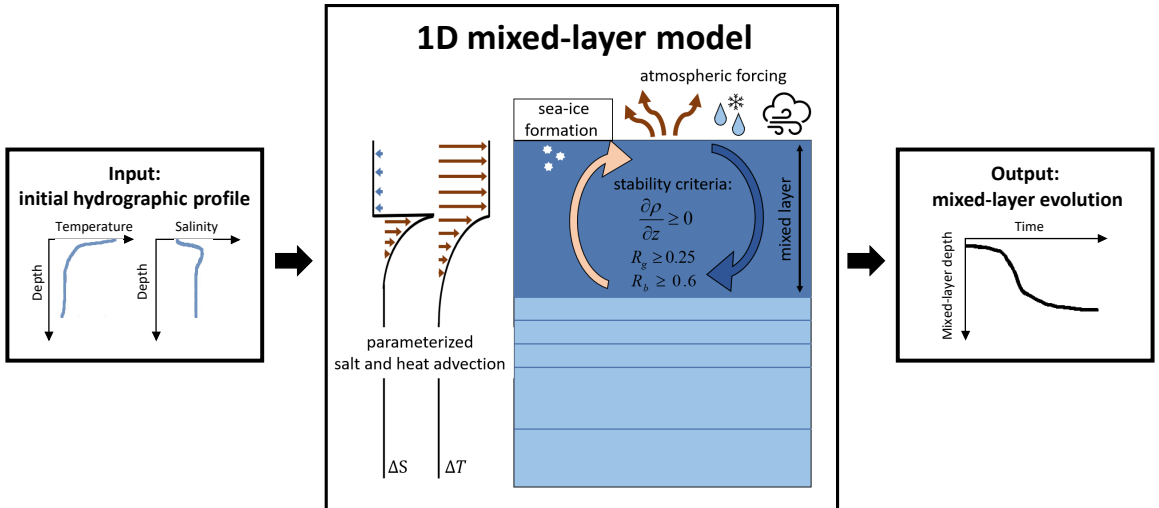


Figure 3.3: Schematic illustration of the one-dimensional mixed-layer model.

We also added salt fluxes representing brine release from sea-ice formation (Paper I), since this has been considered one important driver for deep convection in the Greenland Sea (e.g., *Visbeck et al.*, 1995; *Marshall and Schott*, 1999). When the simulated sea-surface temperature reached the freezing point, we assumed that further heat loss was used to form sea ice following *Pickart et al.* (2016). The resulting salt flux (*Cavaliere and Martin*, 1994) was added to the uppermost grid cell in the model. The effect of increasing ice thickness and sea-ice melt were not included. We also note that sea ice was only present within the gyre in a few of the winters considered in Papers I and II, and was not a main driver for the mixed-layer development in this time period.

All of the processes mentioned above impact the stability of the water column, and vertical mixing and deepening of the mixed layer occurs in the model until three stability criteria are satisfied (Figure 3.3, *Price et al.*, 1986). The first and most important is static stability ($\delta\rho/\delta z \geq 0$, where ρ and z are the water density and depth, respectively), which simulates convection driven by buoyancy loss. When static stability is achieved, the mixed layer is further adjusted by constraining the bulk and gradient Richardson numbers ($R_b \geq 0.6$ and $R_g \geq 0.25$, Figure 3.3). These represent mixed-layer stability by entrainment and shear-flow stability through stirring (*Price et al.*, 1986). On the spatial and temporal scales considered here, these had only minor effects on the mixed-layer development.

The focus in Paper I was to determine the governing mechanisms behind the inter-annual mixed-layer variability in the Greenland Sea, while in Paper II we focused more on shorter time scales and the impact of cold-air outbreaks, in particular, how the timing of such events impacted the mixed-layer development through the winter. To isolate the effect of the temporal distribution of cold-air outbreaks, we used idealized atmospheric

forcing with the equal integrated heat loss over the winter in all simulations. Three different cases were considered: one with all events concentrated early in winter, one with all events concentrated late in winter, and one with events evenly distributed throughout the winter (Section 2e and 7, Paper II).

3.6 Regional water-mass inversion

In Paper III, we developed a regional, high-resolution version of the global, inverse water-mass decomposition method called Total Matrix Intercomparison (TMI, *Gebbie and Huybers, 2010; Gebbie, 2014*) to examine the origin, pathways, and final composition of the overflows from the Nordic Seas. To understand how the TMI method works, we start by describing how a water mass can be decomposed into its constituents based on conservation of water properties and mass. Let us consider the hydrographic properties of the water masses in the Nordic Seas (Figure 2.6a), which all fall within the triangle created by the following end members: warm and saline AW, cold and dense deep water (DW), and cold and fresh PSW. The temperature (T) and salinity (S) of any water mass i within this mixing triangle, can be expressed as a linear combination of the end-member properties, assuming they are conserved. That is:

$$T_i = T_{AW}m_{AW} + T_{DW}m_{DW} + T_{PSW}m_{PSW}, \quad (3.1)$$

$$S_i = S_{AW}m_{AW} + S_{DW}m_{DW} + S_{PSW}m_{PSW}, \quad (3.2)$$

$$1 = m_{AW} + m_{DW} + m_{PSW}, \quad (3.3)$$

where m_{AW} , m_{DW} , and m_{PSW} are the mass fractions from each of the three end members, which add up to 1 to conserve mass. If all temperatures and salinities are known, we can solve for the fractional contribution of each of the three end members. Several studies (e.g., *Eldevik et al., 2009; Mastropole et al., 2017; Lin et al., 2020*) have used this method to determine the origin and upstream sources of the overflows. However, since these studies only consider hydrography properties, they could only solve for three upstream sources, which is not sufficient to describe the composition of the overflows (Section 2.3.1). Additional end members can be accounted for by including geochemical parameters such as oxygen and nutrients (e.g., *Tanhua et al., 2005; Jeansson et al., 2008, 2017*). This is particularly important for water masses originating in the Arctic Ocean, which have similar hydrographic properties to water formed in the Nordic Seas, but different geochemical properties (Figure 2.6a, Section 2.3.1). An inverse modelling technique called Optimum Multiparameter analysis (OMP, *Tomczak and Large, 1989; Karstensen and Tomczak, 1998; Poole and Tomczak, 1999*), is commonly used to solve the system of linear conservation equations (e.g., *Tanhua et al., 2005; Jeansson et al., 2008, 2017*). To solve for the end-member mass fractions, the OMP method minimizes, in a least-squares sense, the misfits to observations of each water-mass property. Remineralization of nutrients and the resulting change in oxygen, which are related to each other through stoichiometric ratios (*Redfield et al., 1963; Anderson and Sarmiento, 1994*), are accounted for by including an interior source term in the corresponding conservation equations (*Karstensen and Tomczak, 1998*).

A major weakness of these traditional water-mass decomposition methods is their sensitivity to the number of end-members included in the analysis and their specified properties, which can vary substantially both in time and space. The inverse method used in this thesis is also based on water-mass decomposition and conservation of hydrographic

and geochemical parameters, but the method is not dependent on a few pre-defined end members (*Gebbie and Huybers, 2010; Gebbie, 2014*). Instead, it is based on the three-dimensional distribution of water-mass properties and solves the conservation equations for each grid cell and its neighbors simultaneously. This geometrically connects all water masses and the resulting distribution of mass fractions m can be used to trace water masses (i.e., the overflows) back to their surface origin. Hence, all surface locations are considered potential end-members or sources of the overflows. The global TMI versions available have a regular horizontal resolution of 4° (*Gebbie and Huybers, 2010; Gebbie, 2014*) and 2° (*Gebbie and Huybers, 2012*), which are not sufficient to resolve the overflow water pathways in the Nordic Seas. Hence, we developed a regional version covering the domain $58.5\text{--}84^\circ\text{N}$ and $45^\circ\text{W}\text{--}45^\circ\text{E}$ that has the resolution $1/3^\circ$ longitude, $1/8^\circ$ latitude, and 46 vertical levels (Paper III). This resolution resulted in 851422 oceanic grid cells, where 49489 of them are considered sources at the surface and lateral boundaries. The inclusion of lateral-boundary sources in the regional TMI version required substantial modifications to the original global TMI code.

The TMI inversion is based on observations of temperature, salinity, oxygen, nitrate, and phosphate (Section 3.1) and the conservation equations for each parameter are combined into a matrix equation following *Gebbie and Huybers (2010)* and *Gebbie (2014)*:

$$\mathbf{A}\mathbf{c} = \mathbf{d}, \quad (3.4)$$

where the vector \mathbf{c} contains information about the three-dimensional distribution of each water-mass property and vector \mathbf{d} contains the interior source term and the surface and lateral boundary properties. The matrix \mathbf{A} quantifies the mass fractions m between each grid cell and its neighbors, which represents the net effect of advection and diffusion on the distribution of water masses (*Gebbie and Huybers, 2010*). The overall goal is to find the solution of \mathbf{A} and \mathbf{d} that minimizes the difference between the water-mass distributions \mathbf{c} and the observations, weighted by the observational uncertainty. The optimized matrix \mathbf{A} can be used to diagnose water-mass composition and pathways (*Gebbie and Huybers, 2010, 2011, Paper III*), where the pathways represent the steady-state circulation that best fits the observations. In Paper III, we created a late-winter climatology for the period 2000–2019 to constrain the inversion, while two inversions (one for 2000–2019 and one for 1950–1979) was performed in Paper IV to investigate long-term changes in the origin and composition of the overflows. Details are provided in Papers III and IV, respectively. The corresponding observational uncertainty, which represent temporal variability within each period, was estimated based on the number of observations included in each grid cell and their variance (Paper III).

A schematic illustration of the TMI workflow is shown in Figure 3.4. Initial surface and lateral boundary properties were obtained from the late-winter climatology of each period. The interior source term was assumed to be negligible ($10^{-3} \mu\text{mol kg}^{-1}$ everywhere, *Gebbie, 2014*) as a first guess. It was enforced to be positive and constrained such that larger values only occur if the observations demanded it. The first guess of the mass fractions (\mathbf{A}) was constructed based on the assumption that water mainly flows and mixes along geostrophic streamlines and isopycnals (*Nøst and Isachsen, 2003, Paper III*), which is more realistic than the isotropic first guess used in previous TMI versions (*Gebbie and Huybers, 2010; Gebbie, 2014*). Potential density and absolute geostrophic velocity fields were derived from the observational climatologies combined with surface geostrophic velocity fields from satellite (Section 3.3). To determine the first guess of the mass fractions in the pathway matrix \mathbf{A} , we estimated and combined gradients in density

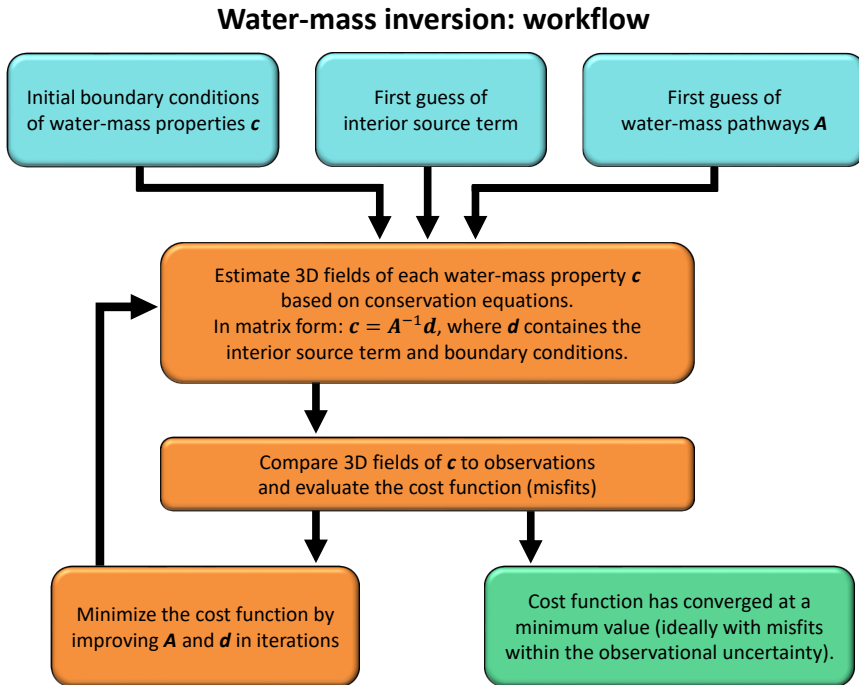


Figure 3.4: Schematic illustration of the workflow in the regional water-mass inversion.

and in the geostrophic stream function. In general, larger gradients lead to smaller mass fractions, implying reduced exchange of water between neighboring grid cells (Appendix D, Paper III).

Based on the initial conditions, the first guess of the interior source term, and the first guess of \mathbf{A} , the inversion estimates the three-dimensional distribution of each water-mass property \mathbf{c} (Equation 3.4, Figure 3.4). The optimized solution of \mathbf{A} and \mathbf{d} are then found by minimizing, in a least-squares sense, the inversion-to-observational misfits in iterations using the method of Lagrange multipliers (Schlitzer, 2007; Gebbie, 2014). The Lagrangian cost function to be minimized must satisfy the conservation equations and contains, in addition to the misfits, other non-observational constraints such as a stably stratified water column, temperatures above freezing, and non-negative values for salinity and the geochemical parameters (Gebbie, 2014). The optimization stops when the cost function has converged at a minimum value, but there is no guarantee that the solution arrives at the overall minimum of the cost function (Köhl and Willebrand, 2002). One way to quantify how well the steady-state pathways fit the observations is to compare the TMI and observed property distributions. By construction, the field should compare well, and in all our runs we find that approximately 80% of the inversion-to-observational misfits are within the observational uncertainty, which indicates a slight overfit (Paper III, Paper IV). A detailed discussion about the strengths and weaknesses of the TMI method, in particular the steady-state assumption, is provided in Section 6.3.

4 Summary of the papers

Paper I: Water mass transformation in the Greenland Sea during the period 1986–2016

Brakstad, A., K. Våge, L. Håvik, and G.W.K. Moore (2019), Journal of Physical Oceanography, 49(1)

In Paper I, we examined the spatial and temporal variability in open-ocean convection in the Greenland Sea based on hydrographic measurements from shipboard CTDs, Argo floats, and instrumented seals over the period 1986–2016. We found that the deepest and densest convection took place late in winter between February and April, and that it was located within the Greenland Sea gyre. Although the late-winter mixed layer was confined to intermediate depths (<1600 m) throughout the record, substantial interannual variability was observed in both the depth and properties of the mixed layer. Particularly evident was a transition from predominantly shallow (<300 m) convection during 1988–1993 to relatively deep convection (500–1000 m) in winters 1994–1996. This transition resulted in the formation of a new class of GSAIW, which has been the main dense-water product in the Greenland Sea since the mid-1990s and is sufficiently dense to contribute to the overflow water transported by the NIJ and IFSJ. A one-dimensional mixed-layer model, updated with lateral advection and sea-ice formation to better represent the conditions in the central Greenland Sea, was used to examine the driving mechanisms for the observed mixed-layer variability. Results from the model suggest that convection was inhibited in 1988–1993 by anomalously fresh near-surface conditions that increased the stability of the upper part of the water column as the atmospheric forcing was relatively strong during these winters. The deeper convection after 1993 was associated with increased near-surface salinity and reduced water column stability that preconditioned the gyre for deeper convection. The weaker stratification along with sufficiently strong atmospheric forcing resulted in mixed-layer depths exceeding 500 m and the production of the new class of GSAIW. Brine release from local sea-ice formation was not an important driver of convection in the Greenland Sea during the 1986–2016 period. Our analysis further shows that there has been a tendency toward deeper convection after 2000, which has led to an increased GSAIW volume. Based on changes in GSAIW volume from fall to spring, we estimated an annual mean production rate of 0.6 ± 0.5 Sv from 1994 to 2014. This rate is likely an underestimate as wintertime export of GSAIW was not accounted for. Neither was formation of dense water in the areas surrounding the Greenland Sea gyre. The average summertime export of GSAIW was estimated to 0.9 ± 0.7 Sv, although rates in excess of 1.5 Sv occurred in summers following winters with deep convection.

Note on author contribution: The basis for Paper I was developed as part of my MSc thesis (*Brakstad, 2016*). During the PhD period, I refined and extended the analysis, and wrote the paper. In particular, all analyses and developments related to the one-dimensional mixed-layer model were performed during the PhD period.

Paper II: The impact of cold-air outbreaks and oceanic lateral fluxes on dense-water formation in the Greenland Sea from a ten-year moored record (1999–2009)

Svingen, K., A. Brakstad, K. Våge, W. J. von Appen, and L. Papritz (2023), Journal of Physical Oceanography, 53(6)

A 10-year (1999–2009) hydrographic record from moored profilers was utilized in Paper II to examine the variability in wintertime convection in the Greenland Sea gyre, with a particular focus on the impact of CAOs and lateral fluxes of heat and salt. Corroborating previous studies, we found that approximately 60–80% of the heat lost to the atmosphere during winter occurred during CAOs. Winters with a high CAO frequency were associated with the largest turbulent heat fluxes and deepest convection. One exception was winter 2006–2007, which had particularly strong intermediate stratification. The high (1–2 days) temporal resolution and long duration of this unique data record facilitated for the first time a statistical quantification of the direct impact of CAOs on the mixed layer in the Greenland Sea. The mixed-layer development can be divided into two phases: a cooling phase that typically occurred between November and January and a deepening phase between February and April. The mixed-layer response to CAOs depended on which phase the events occurred in and their intensity. During the cooling phase, CAOs cooled the mixed layer by up to 0.08 K per day, while the mixed-layer depth remained nearly constant. During the deepening phase, CAOs deepened the mixed layer by up to 38 m per day, with only minor changes in mixed-layer temperature. Idealized simulations with a one-dimensional mixed-layer model suggest that the temporal distribution of CAOs are important for the timing of the onset of the deepening phase (i.e., more CAOs early in winter results in an earlier start of the deepening phase), while the end-of-winter mixed-layer depth and hydrographic properties are more sensitive to the integrated heat loss over the winter. Considerable variability was observed in the mixed-layer response to CAOs, indicating that lateral fluxes of heat and salt were also important. The magnitude and vertical distributions of these fluxes were quantified based on temporal changes in temperature and salinity below the mixed layer. These were then included in the one-dimensional mixed-layer model, which suggests that their combined effect is a reduction in the mixed-layer depth at the end of winter of up to several hundred meters. We compared the hydrographic properties within the gyre to its surroundings using shipboard CTD and Argo float profiles. This indicated that lateral exchange with the East Greenland Current may be particularly important for the input of heat and salt into the gyre, but further investigations are needed to confirm this.

Note on author contribution: Paper II is partly based on the MSc thesis of Kristin Svingen (*Svingen, 2019*), who I co-supervised. During the PhD period, I extended the analysis using the one-dimensional mixed-layer model. I was also responsible for the analysis related to lateral advection of heat and salt. Kristin and I contributed equally to the paper and should be considered joint first authors.

Paper III: Formation and pathways of dense water in the Nordic Seas based on a regional inversion

Brakstad, A., G. Gebbie, K. Våge, E. Jeansson, and S. R. Ólafsdóttir (2023), Progress in Oceanography, 212

A regional high-resolution water-mass inversion for the Nordic Seas during the period 2000–2019 was developed in Paper III to determine the origin, pathways, and final composition of the overflow water in Denmark Strait and the Faroe Bank Channel. The inversion is based on both hydrographic and geochemical observations, as well as their geographical distributions, which is a major advantage compared to traditional water-mass decomposition methods as it resolves also the pathways connecting the overflow plumes to their origins. All surface and lateral boundary locations are considered potential overflow water sources. As such, the inversion is not dependent on a few pre-defined end-members. The DSOW is mainly composed of water originating in the Greenland Sea ($39\pm 2\%$), the Iceland Sea ($20\pm 3\%$), and in the Atlantic Domain ($19\pm 2\%$) of the Nordic Seas. Consistent with previous studies, we found that dense water from these source regions approaches Denmark Strait in the East Greenland Current and the North Icelandic Jet. The East Greenland Current transports warm and saline water from Fram Strait to Denmark Strait, but substantial mixing occurs with the interior Greenland and Iceland Seas along the path. The dense water supplied by the North Icelandic Jet primarily originates in the Greenland Sea ($82\pm 2\%$) and flows southward to the Iceland Sea along two distinct pathways: an outer core of the East Greenland Current and a previously unknown pathway crossing the Jan Mayen Ridge into the Iceland Sea. The latter pathway follows the cyclonic gyre within the Iceland Sea, which leads to a southward flow along Kolbeinsey Ridge to the slope north of Iceland. Although the upstream sources of the DSOW are in broad agreement with previous studies, we find a substantially lower contribution from the Arctic Ocean than indicated by previous studies including both hydrographic and geochemical properties. The discrepancy is likely a result of temporal variability in the observations as neither studies properly account for this. The FBCOW is primarily fed by dense water originating in the Greenland Sea ($46\pm 8\%$) and the Arctic Ocean ($25\pm 9\%$). These regions also supply the densest part of the overflow, while the less dense components stem from the Iceland Sea ($10\pm 1\%$), the Atlantic Domain ($11\pm 1\%$), and the North Atlantic ($9\pm 0\%$). Dense water formed in the Greenland Sea and Arctic Ocean approaches the Faroe-Shetland Channel in the Iceland-Faroe Slope Jet and along the eastern boundary of the Jan Mayen Ridge. The pathway along the Jan Mayen Ridge turns east and crosses over to the Norwegian continental slope, where it follows the eastern margin southwards to the channel. In total, this pathway accounts for $24\pm 3\%$ of the FBCOW, while the IFSJ supplies $58\pm 3\%$. The remaining portion is AW that is densified in the Faroe Current and recirculates around the Faroe Islands ($18\pm 1\%$). The inversion reveals unprecedented details on the upstream sources and pathways of the overflows, which have not previously been obtained using observations.

Paper IV: Observed long-term changes in the overturning in the Nordic Seas

Brakstad, A., K. Våge, M. Årthun, G. Gebbie, and E. Jeansson (manuscript in preparation)

In Paper IV we utilized the 70-year long (1950–2019) observational record to quantify the long-term variability in heat, salt, and dense-water inventory in the Nordic Seas. This revealed that the Nordic Seas reservoir has warmed and become less dense, primarily because of changes in the northward-flowing Atlantic Water and the cessation of GSDW formation in the Greenland Sea. In particular, the volume classified as deep water (DW) has decreased by 20% from 1950–1979 to 2000–2019, while the less dense intermediate water (IW) component has increased in volume. This has, in turn, impacted the overall density structure in the Nordic Seas. Long-term hydrographic timeseries, combined with the regional water-mass inversion were used to examine the impact on the dense overflow waters passing the Greenland-Scotland Ridge in Denmark Strait and the Faroe Bank Channel. We performed and compared two inversions: one constrained by observations from 1950–1979 and one from 2000–2019. These two periods capture the pronounced transition from GSDW to GSAIW formation in the Greenland Sea. Results from the inversions show that the density and supply from the Greenland Sea to the FBCOW has decreased, which led to a 19% reduction in the FBCOW volume classified as DW. However, because of a concurrent reduction in the lightest components of the FBCOW, primarily caused by reduced contributions from the Atlantic Domain of the Nordic Seas, the median overflow density has only had a small negative density trend over the 70-year record. This implies that the FBCOW plume has become more homogeneous. At present, 12% of the FBCOW is still classified as DW. This fraction is expected to diminish as the draining of the DW reservoir continues and the upper level of the DW deepens. By contrast, the Denmark Strait Overflow is mainly fed by less dense IW, which has increased in volume over the 70-year record. The increased IW formation in the Greenland Sea has resulted in increased contributions from the Greenland Sea to the DSOW, from 20% in 1950–1979 to 35% in 2000–2019. Associated with this increase was a reduced supply from nearly all other dense-water sources, except from the Iceland Sea, where the DSOW contribution has remained constant in terms of volume fraction. Our analyses of the overflow water composition and properties demonstrate that it is important to take both the spatial and temporal variability in dense-water formation into account when examining the long-term changes in the overflows. This is particularly important as new regions become ice free and can potentially contribute to production of overflow water. The convection in the Greenland Sea as well as the volume and composition of the Nordic Seas dense-water reservoir are tightly linked to the Atlantic Water inflow, which has warmed and become less dense since 2000. If this trend continues in the future as expected, the overturning in the Nordic Seas will become less dense.

5 Scientific papers

Paper I

Water mass transformation in the Greenland Sea during the period 1986–2016

Brakstad, A., K. Våge, L. Håvik, and G.W.K. Moore
Journal of Physical Oceanography, 49/1 (2019)

Water Mass Transformation in the Greenland Sea during the Period 1986–2016

AILIN BRAKSTAD, KJETIL VÅGE, AND LISBETH HÅVIK

Geophysical Institute, University of Bergen, and Bjerknnes Centre for Climate Research, Bergen, Norway

G. W. K. MOORE

Department of Physics, University of Toronto, Toronto, Ontario, Canada

(Manuscript received 23 December 2017, in final form 27 October 2018)


ABSTRACT

Hydrographic measurements from ships, autonomous profiling floats, and instrumented seals over the period 1986–2016 are used to examine the temporal variability in open-ocean convection in the Greenland Sea during winter. This process replenishes the deep ocean with oxygen and is central to maintaining its thermohaline properties. The deepest and densest mixed layers in the Greenland Sea were located within its cyclonic gyre and exhibited large interannual variability. Beginning in winter 1994, a transition to deeper (>500 m) mixed layers took place. This resulted in the formation of a new, less dense class of intermediate water that has since become the main product of convection in the Greenland Sea. In the preceding winters, convection was limited to <300-m depth, despite strong atmospheric forcing. Sensitivity studies, performed with a one-dimensional mixed layer model, suggest that the deeper convection was primarily the result of reduced water-column stability. While anomalously fresh conditions that increased the stability of the upper part of the water column had previously inhibited convection, the transition to deeper mixed layers was associated with increased near-surface salinities. Our analysis further suggests that the volume of the new class of intermediate water has expanded in line with generally increased depths of convection over the past 10–15 years. The mean export of this water mass from the Greenland Sea gyre from 1994 to present was estimated to be $0.9 \pm 0.7 \text{ Sv}$ ($1 \text{ Sv} \equiv 10^6 \text{ m}^3 \text{ s}^{-1}$), although rates in excess of 1.5 Sv occurred in summers following winters with deep convection.

1. Introduction

The Nordic seas (Fig. 1) are a key region for dense water formation that impacts climate on a global scale (e.g., Gebbie and Huybers 2010). Warm Atlantic water (AW) flows northward into the Nordic seas, releases heat to the atmosphere, and transforms into cold and dense waters that spill across gaps in the Greenland–Scotland Ridge as overflow plumes that feed the lower limb of the Atlantic meridional overturning circulation (AMOC). To better understand the overturning in the Nordic seas and the sensitivity of the AMOC to climate change, we need to understand where these dense water masses are formed and how they are delivered to the various overflow regions.

The origin of the largest overflow plume, which passes through the Denmark Strait on the western side of Iceland (e.g., Jochumsen et al. 2017), has been debated for several decades. While the primary source of the Denmark Strait Overflow Water (DSOW) was initially thought to be dense water formed by open-ocean convection in the Iceland and Greenland Sea gyres (Swift et al. 1980; Swift and Aagaard 1981; Strass et al. 1993), later studies argued that modified AW transported by the East Greenland Current (EGC) is the main source (Mauritzen 1996; Eldevik et al. 2009). In the latter scenario, the warm AW gradually cools and densifies as it follows the cyclonic circulation around the rim of the Nordic seas, and the two interior gyres contribute only to a limited extent. The Iceland Sea regained focus as a possible source of DSOW with the discovery of a

 Denotes content that is immediately available upon publication as open access.

Corresponding author: Ailin Brakstad, ailin.brakstad@uib.no



This article is licensed under a Creative Commons Attribution 4.0 license (<http://creativecommons.org/licenses/by/4.0/>).

DOI: 10.1175/JPO-D-17-0273.1

© 2018 American Meteorological Society

Brought to you by UNIVERSITETSBIBLIOTEKET I | Unauthenticated | Downloaded 06/19/23 05:59 AM UTC

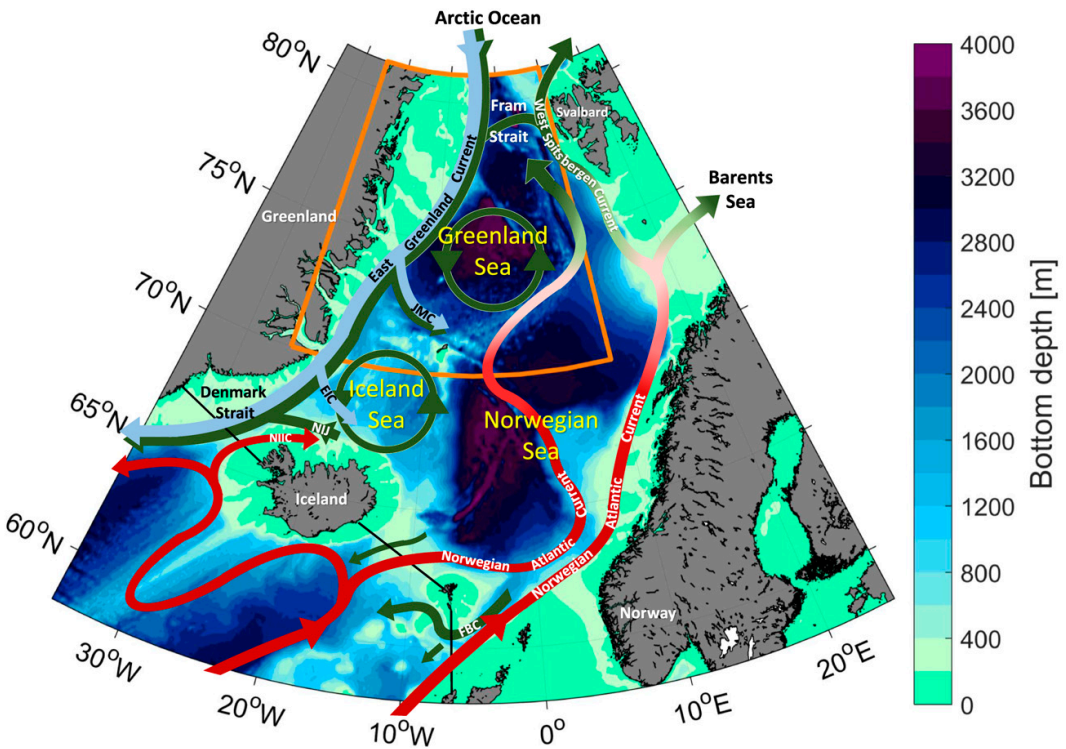


FIG. 1. Bathymetry and schematic circulation of the Nordic seas. Red arrows represent warm Atlantic water while dark green arrows indicate cold and dense waters. Fresh polar water is shown in light blue. The acronyms are the North Icelandic Irminger Current (NIIC), the North Icelandic Jet (NIJ), the East Icelandic Current (EIC), the Jan Mayen Current (JMC), and the Faeroe Bank Channel (FBC) overflow. The crest of the Greenland–Scotland Ridge is indicated by the black line. The orange box outlines the region of interest in this study.

current flowing along the continental slope north of Iceland toward the Denmark Strait, called the North Icelandic Jet (NIJ; [Jónsson and Valdimarsson 2004](#)). Recent estimates suggest that the NIJ supplies almost one-third of the DSW and nearly all of the densest portion (with a potential density anomaly, referred to as potential density, larger than 28.03 kg m^{-3} ; [Våge et al. 2011](#)), while the EGC accounts for the remaining part ([Harden et al. 2016](#)). [Våge et al. \(2011\)](#) hypothesized that the NIJ is the deep branch of a local overturning loop in the Iceland Sea that involves the boundary current system north of Iceland and water mass transformation in the interior Iceland Sea. However, [Våge et al. \(2015\)](#) and [Pickart et al. \(2017\)](#) later found that local convection in the Iceland Sea gyre may not be sufficient to provide all of the densest portion transported by the NIJ. They suggest instead that this dense water originates from the northwestern part of the Iceland Sea, where the deepest and densest

convection occurs, as well as from farther north in the Greenland Sea. A possible source in the Greenland Sea is supported by results from a tracer release experiment that demonstrate rapid communication of dense water from the Greenland Sea into the central Iceland Sea ([Messias et al. 2008](#)).

The largest overflow on the eastern side of Iceland, which passes through the Faeroe Bank Channel (FBC), accounts for approximately one-third of the total overflow water across the Greenland–Scotland Ridge ([Østerhus et al. 2008](#); [Hansen et al. 2016](#)). According to [Eldevik et al. \(2009\)](#), more than 60% of the FBC overflow water originates from the Greenland and Iceland Seas. [Fogelqvist et al. \(2003\)](#) examined the composition of the FBC overflow using geochemical tracers. They concluded that the overflow water in the FBC is a mixture of about equal parts intermediate and deep water masses from the Norwegian Sea, and that the intermediate portion [Norwegian Sea Arctic

Intermediate Water (NSAIW)] is largely a product of wintertime convection in the Greenland Sea. By examining the evolution of the NSAIW, Jeansson et al. (2017) confirmed the importance of the Greenland and Iceland Seas, but they also revealed that a contribution from another, older water mass (upper Polar Deep Water formed in the Arctic Ocean) was required in order to explain the NSAIW properties. Although they argued that this water mass may be the largest source of the NSAIW, they also found that the proportion of intermediate waters formed in the Greenland Sea is increasing. The results of Jeansson et al. (2017) indicate a total supply from the Greenland Sea to the NSAIW of approximately 20%, but the contribution from the Greenland Sea at potential densities greater than 28.04 kg m^{-3} was estimated to 50%. Thus, there is evidence that convection in the Greenland Sea may be important for the overflows both east and west of Iceland, in particular for waters denser than 28.03 kg m^{-3} , although the preferred pathways of the dense water are not fully known.

The convective activity in the Greenland Sea has changed extensively over the past decades. Early studies suggested that wintertime convection extended almost to the bottom, forming very cold and dense Greenland Sea Deep Water (GSDW; Helland-Hansen and Nansen 1909; Carmack and Aagaard 1973; Malmberg 1983; Aagaard et al. 1985). In winter 1971, Malmberg (1983) observed an oxygen-rich, nearly homogeneous layer extending from the surface to 3500 m in the center of the Greenland Sea, indicating convection nearly to the bottom. Since the late 1970s, however, convection has only been observed to intermediate (<2000 m) depths, forming the slightly warmer and less dense Greenland Sea Arctic Intermediate Water (GSAIW; Meincke et al. 1992, 1997; Karstensen et al. 2005; Ronski and Budéus 2005; Latarius and Quadfasel 2010; Jeansson et al. 2017). Meincke et al. (1992) attributed the cessation of very deep convection to a combination of decreased cyclonic wind stress curl and reduced sea ice formation resulting in less brine release. The decreased wind forcing led to a weaker gyre circulation and increased intermediate stratification that isolated the cold GSDW dome from the surface. Recently, Moore et al. (2015) found that the magnitude of the atmospheric heat fluxes over the Greenland Sea have decreased by 20% since the end of the 1970s. They further suggested that if this trend continues, the mixed layer depth could be limited in the future such that only shallow convection occurs, which in turn could impact the production of dense water. However, the depth of convection also depends on the hydrographic conditions prior to the convective season. Lauvset et al. (2018) argued that increased salinity in the

northward-propagating AW has increased the salinity and thereby decreased the stability of the upper 1500 m of the Greenland Sea water column since the early 2000s, which in turn has resulted in a tendency for deeper convection.

It is crucial to determine how various factors influence the depth of convection to fully understand the observed changes in the convective activity in the Greenland Sea and, furthermore, to shed light on its sensitivity to different conditions in the future. The main focus of the present study is to examine the interannual variability of convection and dense water formation in the Greenland Sea. Using a combination of hydrographic observations and a one-dimensional mixed layer model, we document the evolution of the convective product for the period 1986–2016 and explore its sensitivity to changes in hydrographic and atmospheric forcing conditions. In particular, we find that a new class of intermediate water started forming in the Greenland Sea gyre during the mid-1990s. We follow the evolution of this water mass and identify the main factors responsible for its development.

2. Data and methods

a. Hydrographic data

The hydrographic dataset used in this study includes measurements collected by shipboard conductivity, temperature, and pressure (CTD) instruments, autonomous profiling floats, and instrumented seals within the area outlined in orange in Fig. 1 over the time period 1986–2016. The shipboard CTD data were obtained from the archives of the Marine and Freshwater Research Institute of Iceland, the International Council for the Exploration of the Sea (ICES), the World Ocean Database, and the Norwegian Iceland Seas Experiment (NISE) database (Nilsen et al. 2008). Measurements from the autonomous profiling floats, which were first deployed in the Greenland Sea in 2001, were obtained from the archives of the international Argo program. We used delayed mode profiles that have been corrected for drift in salinity (by calibrating the float measurements against historical hydrography; Wong et al. 2003). The accuracy of the corrected float salinities are generally better than 0.01 (we use practical salinity throughout this study, which is nondimensional), while the temperature and pressure errors are less than 0.005°C and 2.4 dbar, respectively. The CTD profiles measured by instrumented hooded seals were postcalibrated against nearby Argo data [see Isachsen et al. (2014) for details on the data and calibration procedures]. The calibrated salinities have errors within the range 0.02–0.1, while the temperature measurements have an uncertainty of 0.03°C .

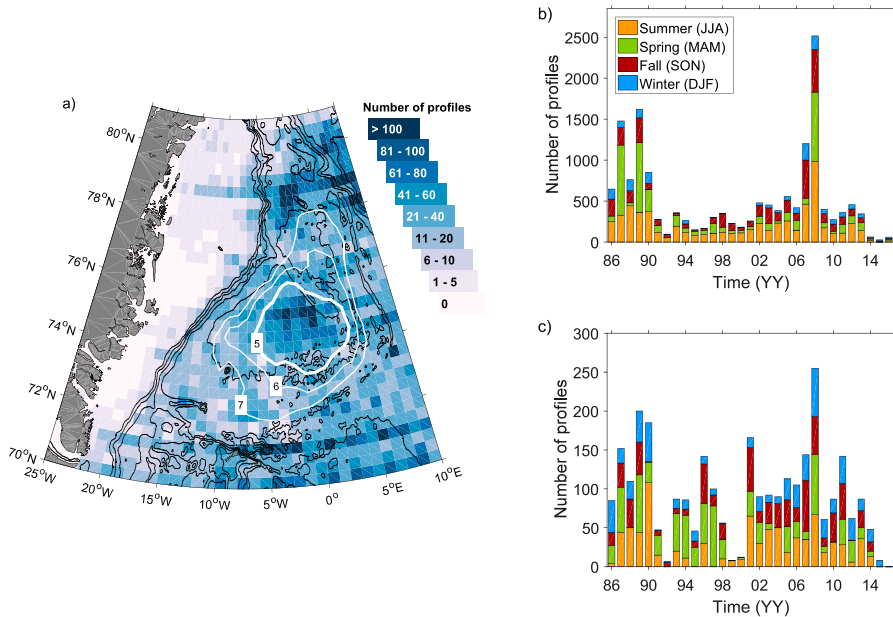


FIG. 2. (a) Total number of profiles per 1° longitude \times $1/3^\circ$ latitude bin, and number of hydrographic profiles per year, color coded by season, (b) for the entire domain and (c) inside the Greenland Sea gyre. The white contours in (a) indicate dynamic topography of the sea surface relative to 500-m depth (dynamic cm), and the thick white contour outlines the Greenland Sea gyre. The 500-, 1000-, 1500-, 2000-, 3000-, and 4000-m isobaths are marked in black.

Data from the various sources were combined into a single historical hydrographic dataset and quality controlled according to Skagseth and Mork (2012) and Våge et al. (2013, 2015). The procedure discards duplicates, erroneous profiles, and outliers. Measurements with temperature and salinity values outside the expected range in the Nordic seas of $[-2^\circ, 20^\circ\text{C}]$ and $[20, 36]$, respectively, were not included. Neither were profiles with density inversions exceeding 0.05 kg m^{-3} except when the inversion was a single data spike, in which case the spike was removed. Outliers were identified by comparing each profile to all other profiles within an effective radius of 110 km (Davis 1998; Våge et al. 2013). The effective radius was increased along isobaths, resulting in an anisotropic area of comparison where the magnitude of the elongation was set by the difference in bottom depth across the topography. This procedure was used because currents in the Nordic seas tend to follow the topography, resulting in smaller variations in hydrography along than across topographic gradients (e.g., Nøst and Isachsen 2003). All profiles within the effective radius were interpolated onto a common vertical coordinate at 5-m intervals and the profile in question was considered an outlier if it

contained data points that differed from the mean temperature and salinity, at any depth, by more than six standard deviations.

The spatial and temporal distributions of the data are shown in Fig. 2. The thick white contour in Fig. 2a outlines the cyclonic gyre in the Greenland Sea defined according to Moore et al. (2015) by the dynamic topography of the sea surface relative to 500-m depth. The center of the cyclonic gyre was identified by the minimum in dynamic topography. A closed contour around this minimum was then chosen as the gyre boundary such that a sufficiently large number of homogeneous profiles were included. While the geographical data coverage is quite good, apart from the Greenland shelf, there are temporal biases (Figs. 2b,c). Wintertime observations are generally scarce because of harsh weather conditions and the presence of sea ice. The deepest convection occurs at the end of winter (February–April; Våge et al. 2015; Marnela et al. 2016). However, less than 20% of the profiles were obtained at this time of the year. We also note that most of the data from the Greenland Sea gyre were obtained by Argo floats, which results in a denser coverage after 2001. The majority of the CTD data collected by the instrumented

seals are located along the Greenland shelf, where data from other sources are sparse. All of these profiles were obtained during 2007–2008. The vertical resolution of the hydrographic profiles differs for each data source, measurement method, and with time, but is generally within the range 1–50 m.

b. Mixed layer depths

The depths and hydrographic properties of the mixed layer were determined following a robust procedure used by Våge et al. (2015) for the Iceland Sea that involves visual inspection of each hydrographic profile. Two independent automated routines, one based on a density-difference criterion (Nilsen and Falck 2006) and one based on the curvature of the temperature profile (Lorbacher et al. 2006), were used to estimate the vertical extent of the mixed layer (see appendix A for further details). By visual inspection, we found that at least one of the two automated routines accurately determined the mixed layer depth for 61% of the profiles. A manual routine developed by Pickart et al. (2002) was employed for the remaining profiles (appendix A).

The automated routines were less accurate for profiles with small density gradients between the mixed layer and the deeper part of the water column, which is typical for wintertime profiles in the Greenland Sea. Several profiles also had a mixed layer that was separated from the surface, because of early stages of restratification in the surface layer or in the form of multiple stacked mixed layers, that the automated routines were not able to identify. Such isolated mixed layers have also been observed during periods of active convection in the Irminger, Iceland, and Labrador Seas (Våge et al. 2009, 2015; Pickart et al. 2002).

c. Gridding of the hydrographic data

To investigate the lateral distribution of a given property, the data were interpolated onto a regular 0.5° longitude × 0.2° latitude grid. The value of each grid point was found from the average (weighted by the inverse distance) of all measurements within an effective radius $r = 50$ km, which was increased along isobaths to account for the greater correlation length scales along topography (Skagseth and Mork 2012; Våge et al. 2013). To study the temporal evolution of the water column in the central Greenland Sea, we interpolated profiles within the gyre onto a regular time versus depth grid of 14 days by 50 m. All data points within the gyre were first assigned to their nearest grid point and, if several data points were allocated to the same grid point, an average value was estimated. Interpolation was then performed by fitting a Laplacian-spline surface to this new partly gridded dataset (Pickart and Smethie 1998). The resulting

gridded product was finally smoothed by convolution with a Gaussian window of 42 days by 150-m depth.

d. Atmospheric forcing

Atmospheric fluxes were obtained from ERA-Interim (ERA-I herein), which covers the period from 1979 to the present (Dee et al. 2011). The parameters included in this study are the 6-hourly air–sea fluxes of heat, freshwater, and momentum, as well as the sea ice concentration. The ERA-I longwave radiative heat flux from the ocean to the atmosphere is known to be underestimated at high latitudes by approximately 20–30 W m^{−2} because of biases in the cloud parameterization (Walsh et al. 2009; Chaudhuri et al. 2014). To account for this underestimation, we followed Moore et al. (2015) and added a constant offset of 25 W m^{−2} to the longwave heat flux. The atmospheric fluxes were averaged over the area of the Greenland Sea gyre outlined in Fig. 2a. When sea ice was present in the gyre, we estimated the ocean–atmosphere turbulent heat flux $Q_{\text{thf}}^{\text{ocean}}$ (latent and sensible heat fluxes) according to Moore et al. (2015) as

$$Q_{\text{thf}}^{\text{ocean}} = \frac{Q_{\text{thf}} - A Q_{\text{thf}}^{\text{ice}}}{1 - A} \approx \frac{Q_{\text{thf}}}{1 - A}, \quad (1)$$

where Q_{thf} is the total turbulent heat flux obtained from ERA-I and A is the mean sea ice concentration over the gyre. It is assumed that the total turbulent heat flux over the ice-covered region $Q_{\text{thf}}^{\text{ice}}$, which is typically an order of magnitude lower than over open water, can be neglected.

e. One-dimensional mixed layer model

The so-called Price–Weller–Pinkel (PWP) one-dimensional mixed layer model (Price et al. 1986) was employed in order to investigate the sensitivity of the mixed layer development in the Greenland Sea to various hydrographic and atmospheric forcing conditions (see appendix B for details). As atmospheric forcing, we applied the ERA-I heat, freshwater, and momentum fluxes averaged over the area of the Greenland Sea gyre, and as initial conditions, we used mean fall (October–November) hydrographic profiles. The model was set up with a vertical resolution of 2 m and with 6-hourly time steps.

Moore et al. (2015) recently modified the PWP model for the Greenland Sea gyre to include lateral advection of heat, which is necessary in order to balance the annual heat budget. We further parameterized lateral advection of salt in the present model version to obtain balanced freshwater budgets. A detailed description of the parameterization is given in appendix Bb. Production of sea ice was also included in the present model version because brine release

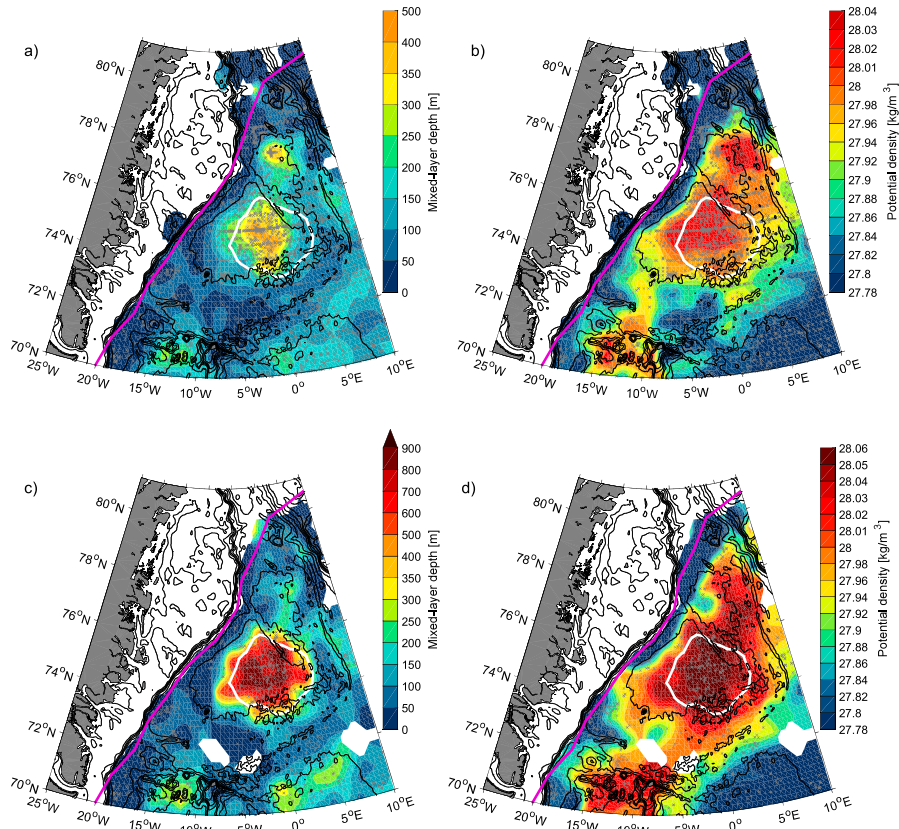


FIG. 3. Mean late-winter (February–April) (a) mixed layer depth and (b) potential density from 1986 to 2016 and the (c),(d) corresponding maps for winters with mean convection depth exceeding the 70th percentile. The locations of data points are indicated by gray crosses. The 200-, 400-, 600-, 800-, 1000-, 1400-, 2000-, 3000-, and 4000-m isobaths are shown as thin black lines. The white contour outlines the Greenland Sea gyre and the magenta curve denotes the mean 50% sea ice concentration contour during November–April.

by sea ice formation has been considered one of the main drivers for deep convection in the Greenland Sea (e.g., [Visbeck et al. 1995](#); [Marshall and Schott 1999](#)). Estimation of sea ice production and the resulting salt flux are described in appendix Bc. We note, however, that there was hardly sea ice within the gyre during the time period covered here [except the winters between 1986 and 1990 and in 1997–98; see Fig. 2b in [Moore et al. \(2015\)](#)].

3. Greenland Sea mean late-winter mixed layer properties

Mean late-winter (February–April) mixed layer depth and potential density from 1986 to 2016 are shown in [Figs. 3a and 3b](#). The deepest and densest mixed layers were located near the center of the

Greenland Sea gyre where the cyclonic circulation weakens the stratification, preconditioning the gyre for deep convection compared to the more stratified surrounding waters ([Marshall and Schott 1999](#)). A region of relatively deep convection is visible also in the Boreas Basin near 78°N where another, smaller cyclonic gyre has been observed ([Quadfasel and Meincke 1987](#)). However, as the majority of the measurements in this area were obtained in winter 1993/94, it is difficult to say whether this local maximum is a recurring feature.

Regions with high mixed layer density (above 28.01 kg m^{-3}) were observed both in the central Greenland Basin and in the Boreas Basin as well as farther south in the Iceland Sea. [Våge et al. \(2015\)](#) found that the deepest and densest mixed layers in the

Iceland Sea are located in the northwest corner, on the outskirts of the gyre, even though the center of the gyre is more preconditioned for convection. They argue that this is due to the stronger atmospheric fluxes near the ice edge. While stronger heat fluxes also occur close to the ice edge in the Greenland Sea (Papritz and Spengler 2017), the deepest mixed layers there are largely confined to the area of the cyclonic gyre. This difference could be a result of the weaker stratification or the generally higher heat fluxes in the Greenland Sea gyre compared to the Iceland Sea gyre (Marshall and Schott 1999; Moore et al. 2015). According to Moore et al. (2015) the winter-mean turbulent heat flux within the Iceland Sea gyre ranged from 50 to 100 W m⁻², while the heat flux in the central Greenland Sea has been within the range 100–150 W m⁻² over the time period 1986–2015 (Fig. 4d).

The mean depth of the late winter mixed layer in the Greenland Sea gyre is approximately 500 m (Fig. 3a). However, the interannual variability of both the mixed layer depth and properties is substantial. By including only winters of deep convection (in which the mixed layer depth within the gyre exceeded the 70th-percentile value; Figs. 3c,d), we found that the mean mixed layer in the center of the gyre exceeded 800 m. During these winters, mixed layer densities greater than $\sigma_\theta = 28.03 \text{ kg m}^{-3}$ were observed over a considerably larger area.

4. Temporal variability of the mixed layer in the central Greenland Sea

The temporal variability of the mixed layer was examined in detail within the Greenland Sea gyre (hereafter referred to as the Greenland Sea), where the deepest and densest convection occurs. The evolution of mean late-winter mixed layer depth and density from 1986 to 2016 are shown in Fig. 4 (only the 50% deepest mixed layers were included in order to exclude restratified profiles and profiles that were obtained before the onset of deep convection). Apart from one winter prior to 1993 (1988/89), the average mixed layer did not extend deeper than 200–300 m. In this period, the coldest, least saline, and least dense mixed layers were observed (mixed layer temperature and salinity are not shown). After 1993, mixed layer depths have in general exceeded 500 m with few exceptions, while sufficiently dense water ($\sigma_\theta > 28.03 \text{ kg m}^{-3}$) to supply the densest portion of the NIJ, and hence also of the DSOW (Våge et al. 2011; Mastropole et al. 2017) has regularly been produced in the center of the Greenland Sea. Such dense waters are probably not formed in large amounts in the Iceland Sea (Våge et al. 2015).

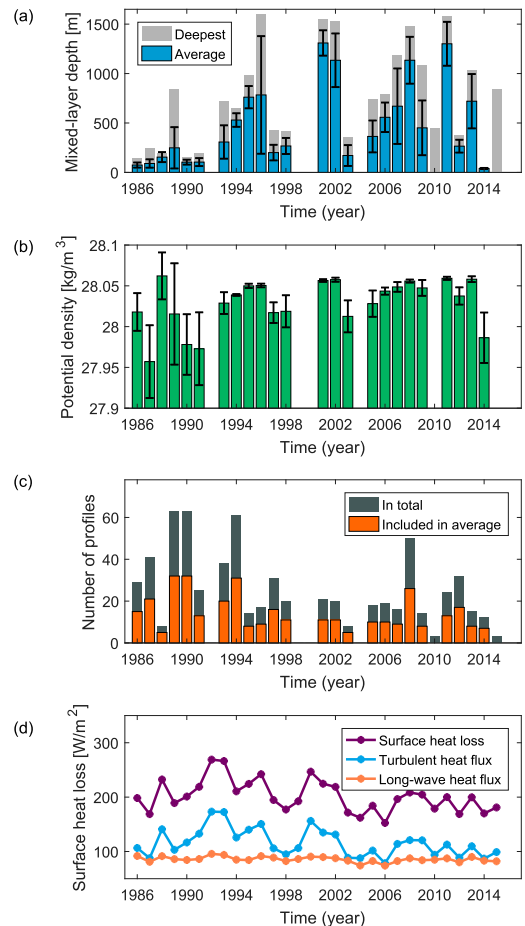


FIG. 4. Mean late-winter (February–April) (a) mixed layer depth and (b) potential density in the Greenland Sea from 1986 to 2016 (colored bars). The black error bars indicate one standard deviation. Average values were excluded for winters with fewer than five profiles (2010 and 2015). The deepest mixed layer observed each winter (light gray bars) is also shown in (a). (c) The total number of profiles each winter (gray) and the number of profiles included in each average (orange). (d) The winter-mean (November–April) surface heat loss (sum of turbulent and longwave heat fluxes). Positive values denote heat loss to the atmosphere.

The temporal evolution of the hydrographic properties of the upper 2000 m of the Greenland Sea are shown in Fig. 5. The upper 500 m of the water column are largely dominated by the seasonal cycle. Several salinity minima are, in addition, visible close to the surface. The two prominent minima that took place in the time periods 1986–93 and 1996–98 coincide with the Great Salinity Anomalies reported by Belkin et al. (1998)

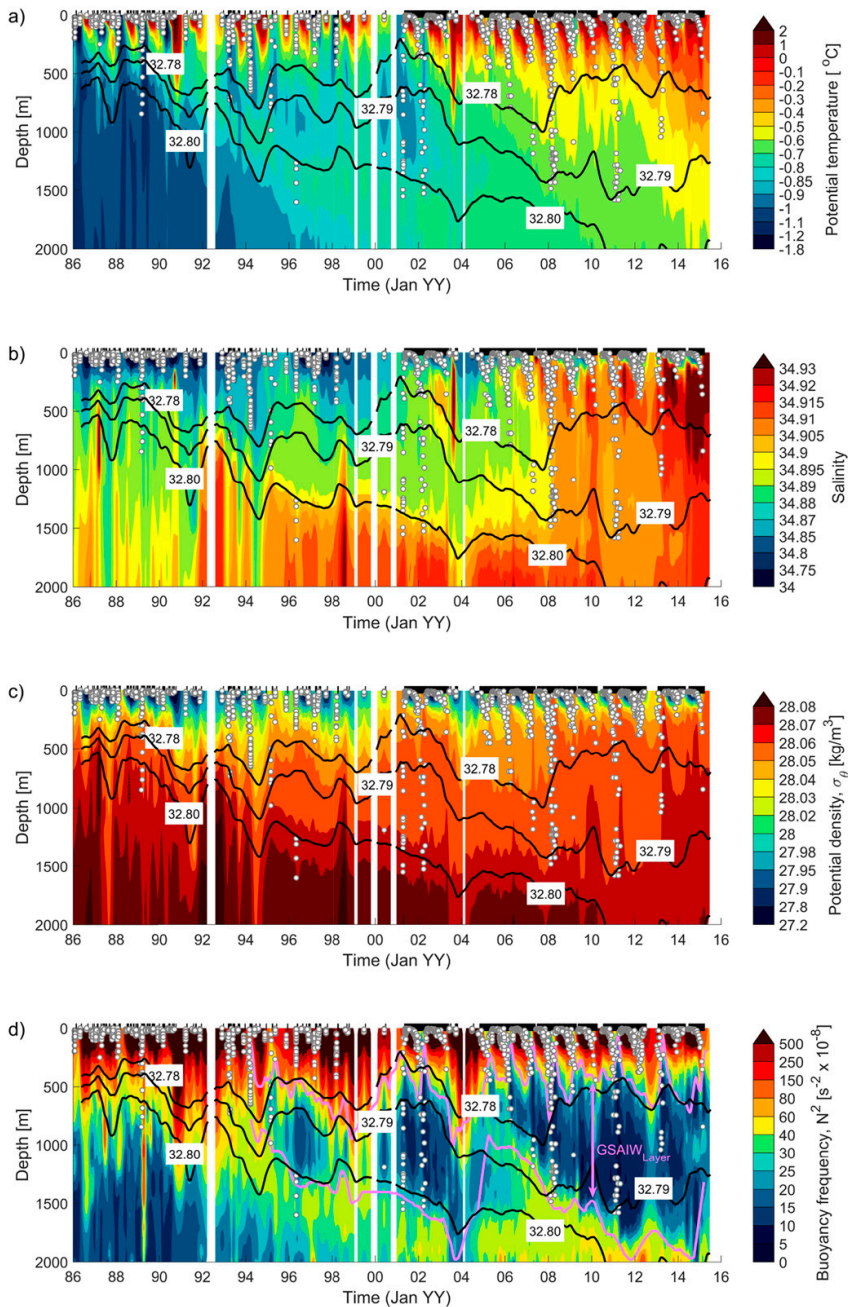


FIG. 5. Evolution of (a) potential temperature, (b) salinity, (c) potential density, and (d) buoyancy frequency within the upper 2000 m of the Greenland Sea gyre from 1986 to 2016. The white dots show the mixed layer depth for each in situ profile, and the black bars along the top of the figures indicate the time of each profile. The black contours represent σ_1 levels equal to 32.78, 32.79, and 32.80 kg m^{-3} . The magenta contours in (d) illustrate the extent of the GSAIW layer.

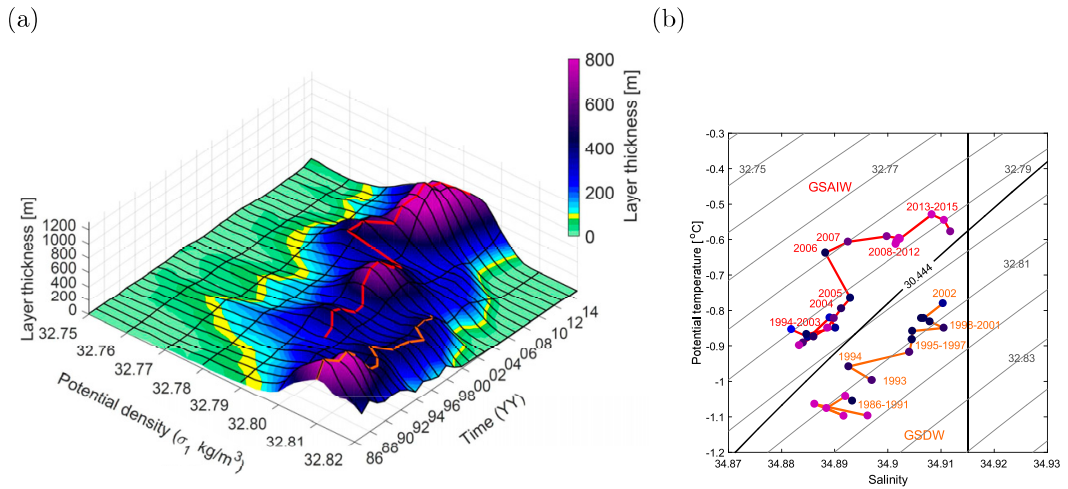


FIG. 6. (a) Temporal evolution of annual-mean thickness of $\Delta\sigma_1 = 0.01 \text{ kg m}^{-3}$ layers within the upper 2000 m of the Greenland Sea from 1986 to 2015. The marked σ_1 values are the center values for each density layer. For the construction of this plot, σ_1 layers overlapping by 0.002 kg m^{-3} have been used. The red and orange lines follow the maximum layer thickness associated with the GSAIW and GSDW, respectively. (b) The corresponding annual-mean potential temperature and salinity characteristics of the GSAIW and GSDW. The colors of the dots correspond to the layer thickness in (a), and the gray lines are σ_1 contours. Following Rudels et al. (2005), we define GSDW by $\sigma_{0.5} \geq 30.444 \text{ kg m}^{-3}$ and salinity $S \leq 34.915$ (marked by the black lines), and GSAIW by $\sigma_{\theta} \geq 27.97 \text{ kg m}^{-3}$, $\sigma_{0.5} \leq 30.444 \text{ kg m}^{-3}$, and potential temperature $\theta \leq 0^{\circ}\text{C}$.

and Belkin (2004), respectively. Another less pronounced freshwater anomaly occurred between 2003 and 2005.

The hydrographic variability below 500 m is characterized by interannual changes in wintertime convection and by long-term trends. A substantial warming and salinification of the upper 1500 m of the water column has taken place over the past three decades (Figs. 5a,b). The salinity increase has been particularly strong over the last 15 years. This corroborates the results of Lauvset et al. (2018), who further argue that the increasing salinity has decreased the stratification of the upper 2000 m and thereby preconditioned the Greenland Sea for deeper convection compared to the 1990s. In the early 1990s, at around 400–600-m depth, we can see the development of the intermediate temperature and stratification maxima documented by, for example, Karstensen et al. (2005) and Latarius and Quadfasel (2010). Both maxima gradually descended until 2004 (following the isopycnal $\sigma_1 = 32.80 \text{ kg m}^{-3}$; see Figs. 5a,d). Thereafter, the temperature maximum vanished, while another intermediate stability maximum [also noted by Marnela et al. (2016)] occurred between 2004 and 2008. The deepening of the stability maxima is associated with periods of strong wintertime convection, which results in an increased volume of weakly stratified water (Fig. 5d). In the following sections, we investigate

the evolution of these weakly stratified waters in order to better understand the water mass transformation that takes place in the central Greenland Sea.

5. A new class of GSAIW

The evolution of the water masses formed within the central Greenland Sea was examined using a volumetric approach (e.g., Yashayaev et al. 2007). Annual mean density profiles were first calculated for each year in order to remove the seasonal cycle and focus on interannual and longer-term changes. For each profile, we then estimated the thickness of different potential density layers ($\Delta\sigma_1 = 0.01 \text{ kg m}^{-3}$) overlapping by 0.002 kg m^{-3} . We used the potential density anomaly referenced to 1000 m (i.e., σ_1) since it better resolves the density changes where the intermediate water masses that are the main product of convection are located. The distance between the various σ_1 isopycnals closely follows the development of the weakly stratified layers as shown by the black contours in Fig. 5d (increases in layer thickness correspond to periods of enhanced dense water production).

The resulting distribution of layer thickness (Fig. 6a) illustrates the evolution of the various classes of water formed in the Greenland Sea. The maximum in layer thickness present before 1990 at a potential density of approximately 32.81 kg m^{-3} indicates the cold and

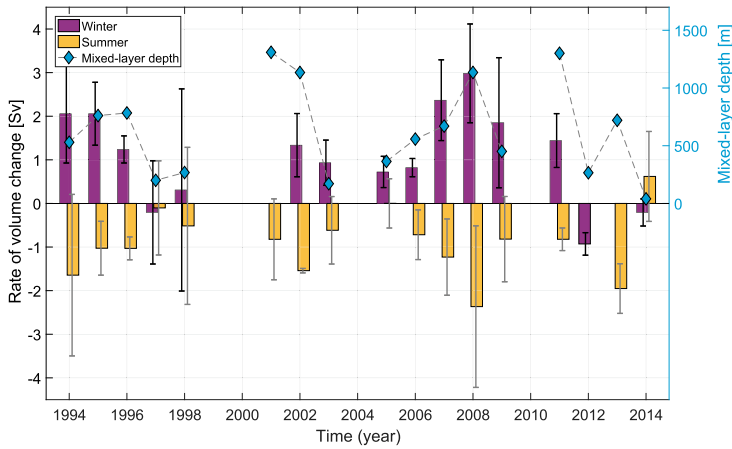


FIG. 7. Average rate of volume change of the GSAIW layer through each winter (purple bars) and summer (yellow bars) since 1994. The winter rates were estimated based on the change in volume over the 6-month period from fall (September–November) to spring (March–May), while the summer rates were based on the change in volume from spring to fall. Average values were excluded for winters/summers with fewer than five profiles in fall or spring. The error bars indicate one standard deviation, and the light blue diamonds mark the mean late-winter (February–April) mixed layer depth.

relatively fresh GSDW that occupied most of the water column below 500 m. The volume of GSDW then gradually decreased until 2002 because of limited ventilation before it vanished from the upper 2000 m of the water column. In 1994/95, another less pronounced maximum appeared, corresponding to the development of a new, less dense class of intermediate water. These years were also the first, since the beginning of this record, with mean late-winter mixed layer depths exceeding 500 m (Fig. 4a). Although the new class of intermediate water (GSAIW) started forming while remnants of the GSDW were still present in the upper 2000 m of the water column, they were separated by the intermediate temperature and stability maxima (Figs. 5a,d). The amount of GSAIW formed after 1994 varied significantly from year to year depending on the depth and intensity of convection. Substantial formation took place in years with relatively deep convection, such as 2002, 2008, and 2011. Periods of limited renewal coincided with the shallow convective years of 1996–98 and 2003–05. The overall proportion of the water column occupied by the homogeneous GSAIW has increased since 1994. It is presently the dominant water mass of the upper 2000 m of the Greenland Sea. The red and orange lines in Fig. 6a follow the maximum layer thicknesses associated with the GSAIW and GSDW, respectively. The corresponding temperature and salinity time series shown in θ - S space in Fig. 6b demonstrate that

the temperature and salinity of both water masses have increased through the record. In terms of density, however, the overall effect is small, as the temperature and salinity changes largely compensate.

We have shown that the volume of GSAIW has increased substantially since the new class first started forming in winter 1994. To examine the rate of production and export each year, we estimated seasonal changes in the volume of the GSAIW layer following the method of Yashayaev and Loder (2016). The mean volume of GSAIW was first estimated each fall (September–November) and spring (March–May). Then we calculated the volume change through each winter and summer and divided by 6 months (assuming constant rate of change through each period). The average rates of volume change (including one standard deviation) from 1994 to 2014 are shown in Fig. 7. Positive values mean that the volume of the GSAIW increased. The definition of the GSAIW layer (illustrated in Fig. 5d) was based on the center σ_1 value ($\pm 0.01 \text{ kg m}^{-3}$) of the density layer with maximum layer thickness at the end of each winter (April–May). The development of this layer captures the evolution of the main water mass produced inside and exported out of the Greenland Sea gyre each year. More than 87% of the profiles that indicate ventilation of the GSAIW layer were located within the Greenland Sea gyre. We note, however, that this definition does not include all waters ventilated in the Greenland Sea that are sufficiently dense

($\sigma_\theta > 27.8 \text{ kg m}^{-3}$) to potentially contribute to the overflow waters. In particular, it excludes the least dense waters in this range that are also formed in areas surrounding the gyre (see Figs. 3b,d).

The average rate of volume change of the GSAIW layer through winter, over the 6-month period from fall to spring (purple bars in Fig. 7), is larger during winters of deep convection as more GSAIW is produced. These GSAIW production estimates are biased low because of the unaccounted export that also takes place throughout winter. For some of the shallow convective winters, the rate of change is negative. This simply means that the export of GSAIW exceeds the production. The minimum rate of wintertime production required to explain the observed volume changes (which would be zero for the shallow convective winters with negative rates) is $1.2 \pm 0.9 \text{ Sv}$ ($1 \text{ Sv} \equiv 10^6 \text{ m}^3 \text{ s}^{-1}$) averaged over the time period 1994–2014. This equals an annual production of $0.6 \pm 0.5 \text{ Sv}$ if we assume zero formation in summer.

The rates of volume change through summer (over the 6 months from spring to fall, shown by the yellow bars in Fig. 7) may be interpreted as the net export (sum of total import and export) out of the Greenland Sea gyre during summer. Since the net export includes possible import into the gyre, it must be less than the total export of GSAIW. The positive rate in 2014 is most likely an artifact of spatial differences within the gyre. That year there were relatively few observations, and all March–May profiles were clustered in the southwest corner of the gyre, while almost every September–November profile was located in the northern part of the gyre. The average summer net export, excluding 2014, is $0.9 \pm 0.7 \text{ Sv}$. This is within the transport range (0.2–0.9 Sv) presented by Karstensen et al. (2003) for the 1990s. Our estimate is lower than the value found by Messias et al. (2008), who inferred an export rate of 1–1.85 Sv from a tracer study. A reason for this discrepancy may be that their estimate was based on data surrounding the central Greenland Sea in the time period 1998–2002, during which we have only a limited amount of data from within the gyre. The rates of export and production are also highly variable. The largest summertime exports generally follow winters with deep convection. Because of this large variability, we have not made an attempt at estimating wintertime and annual export rates.

6. Mechanisms controlling the interannual variability of the Greenland Sea water mass transformation

To investigate the variability of the water mass transformation in the Greenland Sea and to explore why the new class of intermediate water started

TABLE 1. Mean atmospheric forcing (November–April) from 1986 to 2015 used in the PWP model simulations. The turbulent heat flux (latent and sensible heat fluxes) used in the various model simulations span the range 30–880 W m^{-2} , while the overall winter-mean turbulent heat flux was 125 W m^{-2} . Positive fluxes are directed out of the ocean.

Term	Value
Atmospheric freshwater flux	$2.7 \times 10^{-9} \text{ m s}^{-1}$
Surface solar radiation	-27 W m^{-2}
Surface thermal radiation	112 W m^{-2}
Latent heat flux	59 W m^{-2}
Sensible heat flux	66 W m^{-2}
Wind stress τ_x	0.01 N m^{-2}
Wind stress τ_y	0.08 N m^{-2}

forming in 1994/95, we employed the PWP mixed layer model described in section 2e (details are given in appendix B). Idealized model runs were conducted for a range of initial and atmospheric forcing conditions to shed light on the most important factors regulating the observed mixed layer variability in the Greenland Sea. Lateral advection of heat and salt are also important for setting the properties of the mixed layer. They were parameterized as described in appendix B (section b) and assumed constant in all model runs.

The influence of the various atmospheric forcing components on the mixed layer development was explored by sensitivity studies using the PWP model. As expected from previous work (e.g., Våge et al. 2008; Moore et al. 2015), we found that the most important component was the turbulent heat flux (not shown). The remaining air–sea fluxes were therefore kept constant in all model runs equal to the overall winter-mean values from 1986 to 2015 (Table 1). We applied constant forcing through winter from November to April in each simulation, and the span of winter-mean turbulent heat fluxes explored was based on the range of observed values over the 1986–2015 period. We ran the model for winter-mean turbulent heat fluxes equal to every 5th percentile of all winter values. To generate idealized initial conditions, we estimated the convection resistance (CR) of every hydrographic profile in fall (October–November). CR is an integral measure of the density stratification and was computed following Frajka-Williams et al. (2014) as

$$CR(h) = \int_{-h}^0 \sigma_1(S, \theta, z) dz - h\sigma_1(S, \theta, h), \quad (2)$$

where S , θ , z , and σ_1 are the salinity, potential temperature, depth, and the potential density anomaly referenced to 1000 m, respectively. We chose $h = 1000\text{-m}$

depth since this is where the core of the GSAIW is located. The fall profiles were then sorted according to CR and initial conditions were determined as the mean over every 5th percentile.

The resulting end-of-winter mixed layer depths as a function of convection resistance and surface heat loss (sum of turbulent and longwave heat fluxes) are shown by the background color in Fig. 8a. The colored dots indicate the observed mean late-winter mixed layer depths each winter. Although the model underestimates the mixed layer depth slightly, the observations are generally in good agreement with the model results, with deeper mixed layers occurring when heat loss is high and stratification is weak. The contribution of brine release by sea ice formation to the mixed layer deepening is illustrated in Fig. 8b. Conditions required to form sea ice (strong stratification and high surface heat loss) were absent during most of the time period covered by our study. Sea ice formation contributed to a deepening of the mixed layer in 1988, 1989, 1992, and 1993, but the effect was not sufficiently large to result in convection exceeding 400 m.

From 1993 to 1994, a remarkable decrease in stratification took place. The concurrent decrease in heat loss suggests that the change in stability was the primary factor leading to the deeper mixed layers and the formation of the new class of intermediate water in winter 1993/94. A further decrease in stratification resulted in continued ventilation of the new GSAIW until 1996 (the evolution is marked by the black dashed line in Fig. 8a).

To determine the cause of the remarkable decrease in stratification from 1993 to 1996, we examined the evolution of the hydrographic properties in the upper 50 m of the water column. Interannual variability in mixed layer density and, in turn, depth were generally dominated by changes in mixed layer salinity. Shallow convection was associated with cold and fresh mixed layers, while deep convection coincided with warmer and more saline mixed layers (not shown). Earlier studies have also noted the connection between the near-surface salinity and the depth of the mixed layer (e.g., Ronski and Budéus 2005; Latarius and Quadfasel 2010). Examining the 1986–2016 period, we find that when the near-surface salinity in summer was lower than the mean value of 34.71, and the late winter mixed layer depths generally did not exceed 300 m (negative anomalies in Fig. 9). Thus, it appears that there is a threshold beneath which the fresh surface layer will inhibit convection, regardless of the magnitude of the surface heat loss (shown in colors). A similar example from the Labrador Sea is the shallow convection (100–200 m) observed during the Great Salinity Anomaly between 1969 and 1971 (Lazier 1980). In this case, the shutdown of

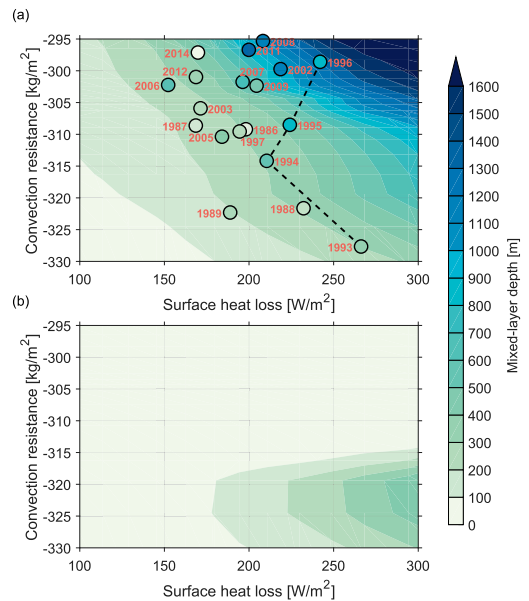


FIG. 8. (a) Simulated end-of-winter mixed layer depth (background color) as a function of winter-mean surface heat loss (turbulent and longwave heat fluxes) and convection resistance. Convection resistance is a measure of the mean fall (October–November) stratification. More-negative values indicate stronger stratification. The colored circles show observed mean late-winter (February–April) mixed layer depths and the black dashed line indicates the change in stratification over the time period 1993–96 prior to and during the formation of the new class of GSAIW. (b) The contribution from sea ice formation to the deepening of the mixed layer, that is, the difference between simulated mixed layer depths using the full model and simulations excluding brine release by sea ice formation.

deep convection resulted from a combination of low near-surface salinity and weak atmospheric forcing (Gelderloos et al. 2012). The shallow convective winters 1988–93 in the Greenland Sea were, however, among the most severe winters in terms of atmospheric heat loss (see Figs. 8, 9). The winter-mean buoyancy flux between 1988 and 1993 (estimated following Gelderloos et al. 2012) was also 1.15 times larger than the winter-mean buoyancy flux in 1994–96 when the new class of intermediate water started forming. This suggests that the low-salinity layer stratifying the upper part of the water column was the main reason for the shallow convection prior to 1993. The effect of sea ice formation was too weak to compensate for the strong stratification generated by the fresh surface layer.

The decrease in water-column stability from 1993 to 1996 resulted from a substantial increase in salinity (black dashed line in Fig. 9). The weaker stratification

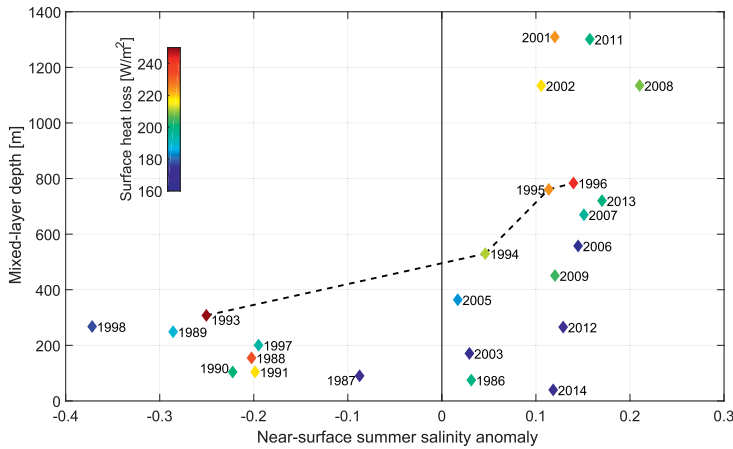


FIG. 9. Mean late-winter (February–April) mixed layer depths vs mean summer (June–October) near-surface (0–50 m) salinity anomalies from 1985 to 2015. The mean near-surface salinity over the entire time period was approximately 34.71 (indicated by the vertical black line). Winter-mean surface heat loss (turbulent and longwave heat fluxes) is shown in color. The black dashed line marks the evolution from 1993 to 1996 when the new class of GSAIW started forming.

along with sufficiently strong atmospheric forcing set the stage for the formation of the new class of intermediate water. The near-surface salinity anomaly has remained positive after 1994 (except for the 1997–98 period), which is required for the continued ventilation of the intermediate water mass. The winters with deepest convection were characterized by both high near-surface salinities in fall and strong atmospheric heat loss through winter.

7. Concluding remarks

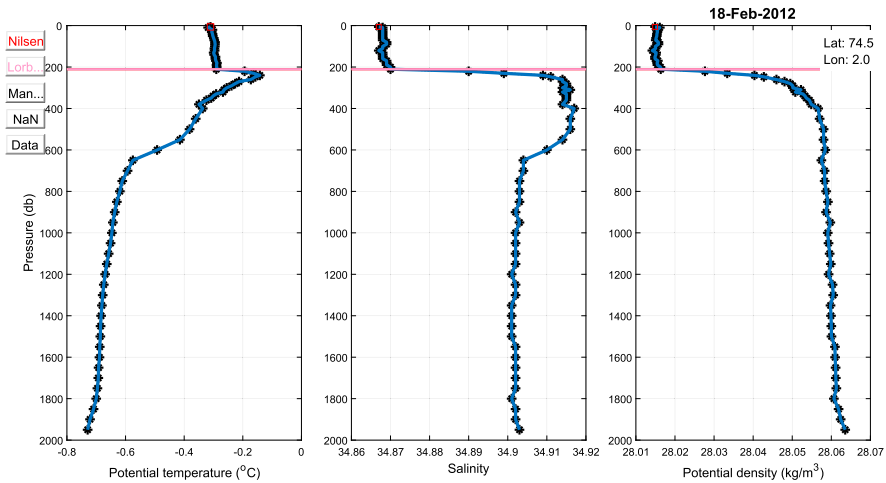
We utilized hydrographic data from several archives including measurements from ships, autonomous profiling floats, and instrumented seals to examine the convective activity in the Greenland Sea over the period 1986–2016. By estimating the mixed layer depth for each hydrographic profile, using a robust procedure involving visual inspection, we found that the deepest and densest mixed layers in the Greenland Sea took place in late winter (February–April) and were located within the cyclonic gyre. Although convection was confined to intermediate depths (<2000 m) during the entire period, the late winter mixed layer depth and the resulting dense water product exhibited large interannual variability. Particularly interesting was the transition from predominantly shallow convection (<300 m) in 1988–93 to the relatively deep convection (500–1000 m) observed in winters 1994–96. This transition marked the beginning of the formation

of a new, less dense class of intermediate water, which since 1994 has been the main product of convection in the Greenland Sea.

The relative importance for this transition of various factors such as sea ice formation, atmospheric heat loss, and stability of the water column were explored using a one-dimensional mixed layer model within a parameter space representative for the Greenland Sea. Sea ice formation contributed to a slight deepening of the mixed layer in four winters in the late 1980s and early 1990s, but was not a main forcing mechanism for the convective activity in the Greenland Sea during the time period covered by our study (1986–2016). The shallow convection in 1988–93 resulted from a near-surface freshening that increased the stability of the upper part of the water column. These winters were also accompanied by strong atmospheric forcing, which suggests that the main factor limiting convection was the increased near-surface freshwater content.

Possible sources of freshwater to the Greenland Sea are precipitation and inflow of ice and low-salinity water from the EGC. Aagaard and Carmack (1989) estimated the excess precipitation to account for only 9% of the annual freshwater addition to the Greenland Sea, and Latarius and Quadfasel (2016) found, from budget calculations, that the atmospheric freshwater flux is around two orders of magnitude lower than the lateral input. This implies that freshwater input from the EGC is the dominant source of freshwater to the Greenland Sea. The amount of freshwater transported southward from

(a)



(b)

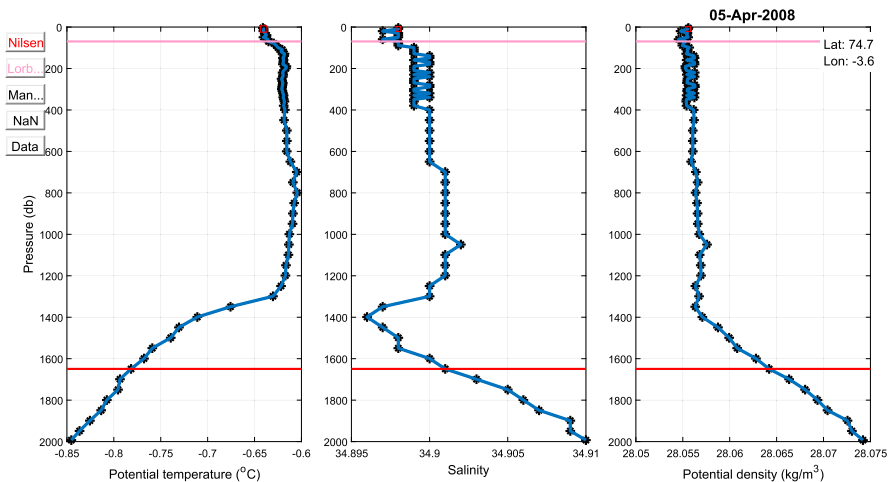


FIG. A1. Examples of two hydrographic profiles from the Greenland Sea gyre, (a) one from February 2012 and (b) one from April 2008. The red and magenta lines indicate the mixed layer depths identified by the density-difference routine and the curvature routine, respectively.

Fram Strait by the EGC was anomalously high during the Great Salinity Anomalies in the late 1980s and late 1990s (Belkin et al. 1998; Belkin 2004), which could be a reason for the low salinities and shallow mixed layers observed in the Greenland Sea during those time periods. The diversion of freshwater into the Greenland Sea is also regulated by the strength of the cyclonic wind stress curl (Malmberg and Jónsson 1997). That is,

shallow convection could also be a result of decreased cyclonic wind forcing that would reduce the cyclonic gyre circulation and, in turn, weaken the polar front between the Greenland Sea and the EGC.

After 1993, a multiyear increase in near-surface salinity lowered the water-column stability in the Greenland Sea. Weaker stratification along with sufficiently strong atmospheric forcing resulted in convection exceeding

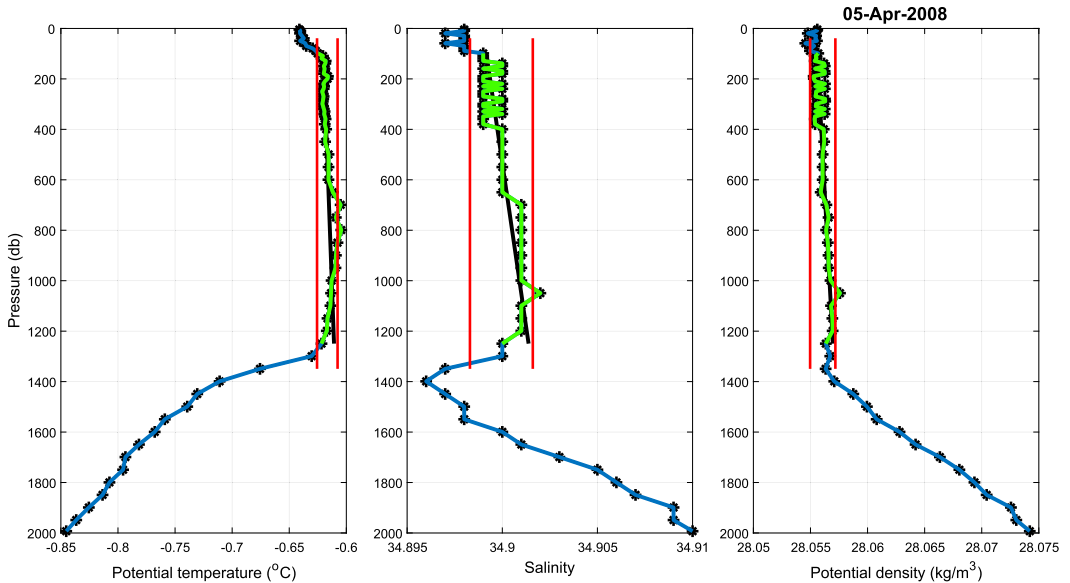


FIG. A2. Illustration of the manual procedure developed by Pickart et al. (2002) for the same hydrographic profile shown in Fig. A1b. The extent of the mixed layer is illustrated in light green, while the vertical red lines indicate plus and minus one standard deviation of the mixed layer properties.

500 m and formation of the new class of GSAIW. Our analysis further suggests that there has been a tendency toward deeper mixed layers during the past 10–15 years. Deeper convection is evident also in the increased volume of GSAIW over the same time period. Hence, there is no indication of predominantly more shallow convection predicted by Moore et al. (2015) if the decreasing trend in atmospheric forcing continues, at least not thus far. The primary reason for this, as suggested by Lauvset et al. (2018), is the weaker stratification within the gyre caused by increased salinities in the upper 1500 m of the water column. Based on a strong cross correlation (0.8, with a 3-yr time lag), they argue that this increase in salinity stems from higher salinities in the Atlantic water that enters the Nordic seas.

The annual mean production of GSAIW from 1994 to 2014 was estimated to 0.6 ± 0.5 Sv and is sufficient to account for roughly 20% of both the NIJ (1.0 ± 0.2 Sv; Harden et al. 2016) and the FBC-overflow (2.2 Sv; Hansen et al. 2016). The contribution may be particularly important for the densest component of the overflow waters ($>28.03 \text{ kg m}^{-3}$; Våge et al. 2015; Pickart et al. 2017; Jeansson et al. 2017). We emphasize that the production rate is a minimal estimate as wintertime export of GSAIW was not accounted for. Potential overflow waters formed in areas surrounding the Greenland Sea gyre were also not included in this

estimate. The average summertime export of GSAIW was estimated to 0.9 ± 0.7 Sv. Although tracer release experiments (e.g., Messias et al. 2008) clearly demonstrate export of intermediate water from the Greenland Sea gyre to the surrounding basins in the Nordic seas, further investigations are required in order to determine how and where this export takes place. One possible mechanism that has been suggested is isopycnal mixing with boundary currents such as the EGC (Strass et al. 1993), but whether this mechanism is sufficient to account for the entire export is not clear. If future convection is reduced, either as a result of decreased heat fluxes (e.g., Moore et al. 2015) or because of enhanced near-surface freshwater content (e.g., from increased ice melt), it could impact the overflows both east and west of Iceland and limit the supply of the densest water to the lower limb of the AMOC.

Acknowledgments. Support for this work was provided by the Bergen Research Foundation under Grant Agreement BFS2016REK01 (AB and KV), the Norwegian Research Council under Grant Agreement 231647 (KV and LH), and the Natural Sciences and Engineering Research Council of Canada (GWKM). Data from ICES and WOD are publicly available (downloaded from <http://ocean.ices.dk/HydChem/HydChem.aspx> and www.noaa.gov/cgi-bin/OS5/SELECT/builder.pl, respectively). The Argo float measurements were obtained

from www.argodatamgt.org/Access-to-data/Argo-data-selection. Data from the instrumented seals were collected as a part of the MEOP program supported by the Norwegian Research Council (Grant 176477) and by the Norwegian Polar Institute (Kit Kovacs and Christian Lydersen). Calibration of the seal data was performed by Pål Erik Isachsen. The authors thank Robert Pickart and Wilken-Jon von Appen for valuable feedback during an early stage of this work.

APPENDIX A

Mixed Layer Depths

The vertical extent of the mixed layer was estimated for each hydrographic profile by two independent automated routines. The first routine (used by [Nilsen and Falck 2006](#)) was based on a density-difference criterion. The base of the mixed layer was identified as the depth where the increase in potential density reached $\Delta\rho = \rho(T_0 - \Delta T, S_0) - \rho(T_0, S_0)$ where T_0 and S_0 are the measured surface temperature and salinity, respectively, and $\Delta T = 0.2^\circ\text{C}$. As [Nilsen and Falck \(2006\)](#), we used a varying $\Delta\rho$ to better account for seasonal changes in the vertical density structure. While [Nilsen and Falck \(2006\)](#) used a temperature difference of $\Delta T = 0.8^\circ\text{C}$ in the Norwegian Sea, [Våge et al. \(2015\)](#) found that $\Delta T = 0.2^\circ\text{C}$ gave better results for the Iceland Sea due to the weaker stratification there. This applies also to the Greenland Sea; hence, we adopt the same temperature-difference criterion. The second routine [developed by [Lorbacher et al. \(2006\)](#)] identified the base of the mixed layer as the shallowest extremum in the curvature of the temperature profile.

The mixed layer depths estimated by the two automated routines were quality controlled (subjectively) by performing a visual inspection of each hydrographic profile. Examples of two wintertime profiles from the Greenland Sea gyre are shown in [Fig. A1](#). The first example (from February 2012; [Fig. A1a](#)) shows a typical profile where both routines successfully estimated the depth of the mixed layer. The profile has a well-defined surface mixed layer down to 210 m that is separated from the deeper part of the water column by a strong density gradient. A typical profile where neither of the two automated routines successfully identified the base of the mixed layer is shown in the second example (from April 2008; [Fig. A1b](#)). The weak density gradient between the mixed layer and the deeper part of the water column led to an overestimation by the density-difference routine, while the separation of the mixed layer from the surface caused the curvature routine to underestimate the mixed layer depth. In cases like this,

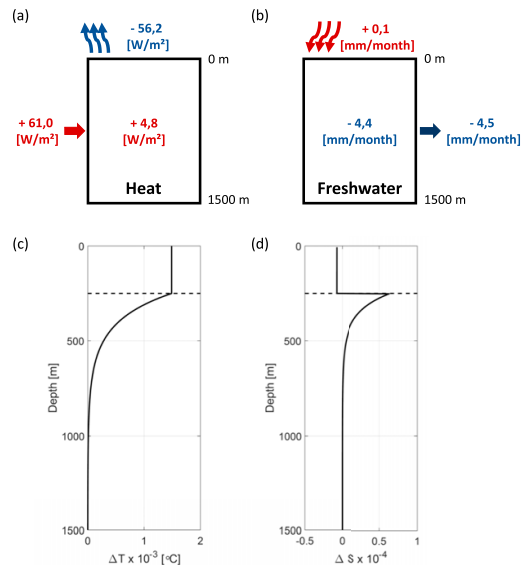


FIG. B1. Annual-mean (a) heat and (b) freshwater budgets for the upper 1500 m of the Greenland Sea gyre. The numbers above each box are the atmospheric fluxes, while the interior changes are shown within each box. The lateral fluxes needed to balance the budgets are indicated by arrows on the sides. The depth distributions of lateral advection of heat and salt, as parameterized in the PWP model, are illustrated by an example of the (c) temperature ΔT and (d) salinity ΔS added for a time step in the model where the mixed layer depth was 500 m. The black dashed lines mark the depth of the mixed layer divided by 2.

we employed a manual procedure developed by [Pickart et al. \(2002\)](#) as illustrated in [Fig. A2](#). The extent of the mixed layer was first estimated visually. Then envelopes of two standard deviations width of the mixed layer temperature, salinity, and density calculated over that depth range were overlaid on the original profiles (vertical red lines in [Fig. A2](#)). The vertical limits of the mixed layer were determined as the locations where any one of the profiles last entered the envelope (upper bound) and first exited the envelope (lower bound). The resulting mixed layer extent is marked in light green in the figure.

APPENDIX B

One-Dimensional Mixed Layer Model

a. Vertical mixing

Atmospheric heat, freshwater, and momentum fluxes are imposed at the surface at each time step in the model ([Price et al. 1986](#)). Vertical mixing and deepening of the

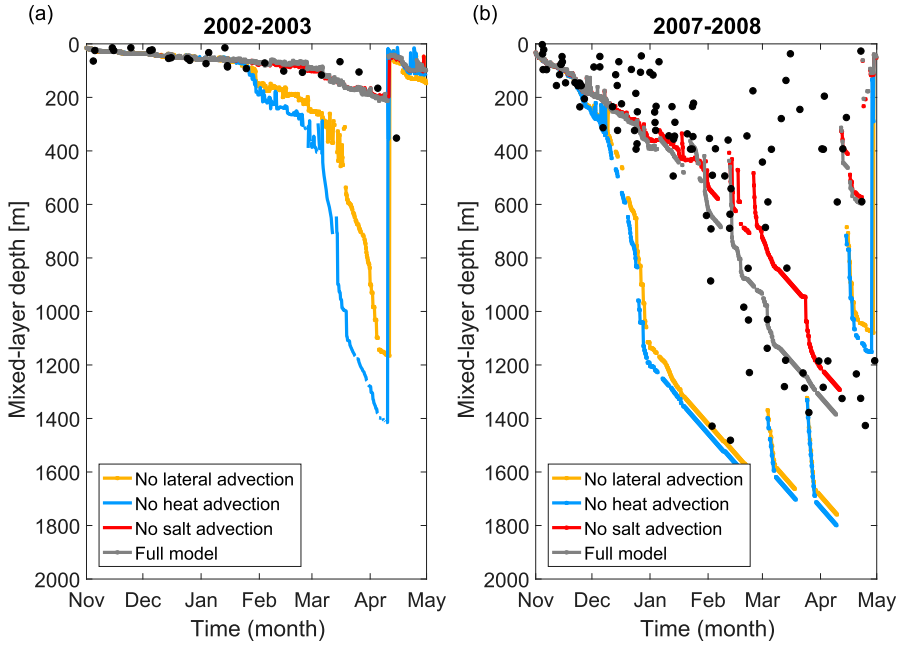


FIG. B2. Seasonal evolution of the mixed layer for (a) a shallow (2002/03) and (b) a deep (2007/08) convective winter. The black dots indicate observed mixed layer depths, while the colored lines show the depth of the mixed layer simulated by the PWP model for four different lateral advection scenarios (see legends).

mixed layer then occur until three different stability criteria are satisfied. The first and most important is the static stability constraint that simulates convection driven by buoyancy loss:

$$\frac{\partial \rho}{\partial z} \geq 0, \tag{B1}$$

where ρ and z are the water density and depth, respectively. When static stability is achieved, the mixed layer is further adjusted by constraining the bulk R_b and gradient R_g Richardson numbers. Mixed layer stability is attained by entrainment when

$$R_b = \frac{g\Delta\rho h}{\rho_0(\Delta V)^2} \geq 0.6, \tag{B2}$$

where h is the mixed layer depth, V is the velocity (which is driven entirely by wind stress induced momentum), ρ_0 is the reference density, and g is the acceleration due to gravity. In the case of shear flow stability, stirring and deepening take place until

$$R_g = \frac{g \frac{\partial \rho}{\partial z}}{\rho_0 \left(\frac{\partial V}{\partial z} \right)^2} \geq 0.25. \tag{B3}$$

This mixing process is likely to occur across sharp gradients typically found at the base of the mixed layer. Results from sensitivity studies suggest that convection driven by buoyancy loss dominates the mixed layer evolution in the Greenland Sea (not shown).

b. Lateral advection

Annual-mean heat and freshwater budgets for the upper 1500 m of the Greenland Sea gyre from 1986 to 2015 were used to estimate the heat and salt advections (see Figs. B1a,b). To balance the budgets, a lateral heat input to the gyre of 61 W m^{-2} , which is close to the value used by Moore et al. (2015), and a freshwater removal from the gyre of $4.5 \text{ mm month}^{-1}$ were required. We assumed constant rates of advection throughout the year. The depth distributions of the heat and salt advections were then determined such that they reflected the temperature and salinity differences across the gyre boundary. For temperature, we used a similar distribution as Moore et al. (2015) as shown in Fig. B1c for a mixed layer depth of 500 m. The distribution of salt is illustrated in Fig. B1d. Salt was removed in the upper half of the mixed layer to account for the input of fresh polar surface water and added below as the surroundings are more saline than the gyre itself. The vertical

distribution of salt advection agrees with the freshwater budgets presented in [Latarius and Quadfasel \(2016\)](#).

We compared the observed and simulated mixed layer depths and properties for each winter. Two winters, one with shallow and one with deep convection, are shown in [Fig. B2](#). Four different simulations are displayed for each winter to illustrate the effect of lateral advection in the model. The exchange of both heat and salt across the gyre boundary must be included in the model in order to realistically simulate the wintertime evolution of the mixed layer. Without advection of heat (blue and yellow curves), the mixed layer depth was greatly overestimated, while the exchange of salt modified the stratification of the water column resulting in moderately deeper mixed layers (cf. the red and gray curves in [Fig. B2b](#)). The simulated mixed layers in our fully parameterized model version (gray) were generally in good agreement with the observations.

c. Sea ice formation

When the simulated sea surface temperature reached the freezing point, we assumed that the net surface heat loss Q_{net} (turbulent and longwave heat fluxes) was used to form sea ice at a rate P following [Pickart et al. \(2016\)](#):

$$P = \frac{Q_{\text{net}}}{\rho_{\text{ice}} L_n}, \quad (\text{B4})$$

where the latent heat of fusion L_n and sea ice density ρ_{ice} were set to 300 kJ kg^{-1} and 920 kg m^{-3} , respectively. This is an upper estimate of P since the effect of increasing ice thickness is neglected. That is, the model simulates polynya-like conditions where newly formed sea ice is exported out of the region directly after formation. Wind-driven export of locally formed sea ice was, according to [Visbeck et al. \(1995\)](#), a key process for the evolution of the mixed layer in the Greenland Sea in the late 1980s. The resulting salt flux F_s from brine release was estimated as

$$F_s = \rho_{\text{ice}} P (S_w - S_{\text{ice}}), \quad (\text{B5})$$

where S_w is the sea surface salinity and $S_{\text{ice}} = 0.31S_w$ is the salinity of the newly formed sea ice ([Cavaliere and Martin 1994](#)). This salt input was added to the upper grid cell at each time step and mixed down in the water column until the stability criteria [Eqs. (B1)–(B3)] were satisfied.

REFERENCES

- Aagaard, K., and E. C. Carmack, 1989: The role of sea ice and other fresh water in the Arctic circulation. *J. Geophys. Res.*, **94**, 14 485–14 498, <https://doi.org/10.1029/JC094iC10p14485>.
- , J. H. Swift, and E. C. Carmack, 1985: Thermohaline circulation in the Arctic Mediterranean Seas. *J. Geophys. Res.*, **90**, 4833–4846, <https://doi.org/10.1029/JC090iC03p04833>.
- Belkin, I. M., 2004: Propagation of the “Great Salinity Anomaly” of the 1990s around the northern North Atlantic. *Geophys. Res. Lett.*, **31**, L08306, <https://doi.org/10.1029/2003GL019334>.
- , S. Levitus, J. Antonov, and S.-A. Malmberg, 1998: “Great Salinity Anomalies” in the North Atlantic. *Prog. Oceanogr.*, **41**, 1–68, [https://doi.org/10.1016/S0079-6611\(98\)00015-9](https://doi.org/10.1016/S0079-6611(98)00015-9).
- Carmack, E., and K. Aagaard, 1973: On the deep water of the Greenland Sea. *Deep-Sea Res. Oceanogr. Abstr.*, **20**, 687–715, [https://doi.org/10.1016/0011-7471\(73\)90086-7](https://doi.org/10.1016/0011-7471(73)90086-7).
- Cavaliere, D. J., and S. Martin, 1994: The contribution of Alaskan, Siberian, and Canadian coastal polynyas to the cold halocline layer of the Arctic Ocean. *J. Geophys. Res.*, **99**, 18 343–18 362, <https://doi.org/10.1029/94JC01169>.
- Chaudhuri, A. H., R. M. Ponte, and A. T. Nguyen, 2014: A comparison of atmospheric reanalysis products for the Arctic Ocean and implications for uncertainties in air–sea fluxes. *J. Climate*, **27**, 5411–5421, <https://doi.org/10.1175/JCLI-D-13-00424.1>.
- Davis, R. E., 1998: Preliminary results from directly measuring middepth circulation in the tropical and South Pacific. *J. Geophys. Res.*, **103**, 24 619–24 639, <https://doi.org/10.1029/98JC01913>.
- Dee, D. P., and Coauthors, 2011: The ERA-Interim reanalysis: Configuration and performance of the data assimilation system. *Quart. J. Roy. Meteor. Soc.*, **137**, 553–597, <https://doi.org/10.1002/qj.828>.
- Eldevik, T., J. E. Ø. Nilsen, D. Iovino, K. A. Olsson, A. B. Sandø, and H. Drange, 2009: Observed sources and variability of Nordic seas overflow. *Nat. Geosci.*, **2**, 406–409, <https://doi.org/10.1038/ngeo518>.
- Fogelqvist, E., J. Blindheim, T. Tanhua, S. Østerhus, E. Buch, and F. Rey, 2003: Greenland–Scotland overflow studied by hydrochemical multivariate analysis. *Deep-Sea Res. I*, **50**, 73–102, [https://doi.org/10.1016/S0967-0637\(02\)00131-0](https://doi.org/10.1016/S0967-0637(02)00131-0).
- Frajka-Williams, E., P. B. Rhines, and C. C. Eriksen, 2014: Horizontal stratification during deep convection in the Labrador Sea. *J. Phys. Oceanogr.*, **44**, 220–228, <https://doi.org/10.1175/JPO-D-13-069.1>.
- Gebbie, G., and P. Huybers, 2010: Total matrix intercomparison: A method for determining the geometry of water-mass pathways. *J. Phys. Oceanogr.*, **40**, 1710–1728, <https://doi.org/10.1175/2010JPO4272.1>.
- Gelderloos, R., F. Straneo, and C. A. Katsman, 2012: Mechanisms behind the temporary shutdown of deep convection in the Labrador Sea: Lessons from the Great Salinity Anomaly years 1968–71. *J. Climate*, **25**, 6743–6755, <https://doi.org/10.1175/JCLI-D-11-00549.1>.
- Hansen, B., K. M. H. Larsen, H. Hátún, and S. Østerhus, 2016: A stable Faroe Bank Channel overflow 1995–2015. *Ocean Sci.*, **12**, 1205–1220, <https://doi.org/10.5194/os-12-1205-2016>.
- Harden, B. E., and Coauthors, 2016: Upstream sources of the Denmark Strait Overflow: Observations from a high-resolution mooring array. *Deep-Sea Res. I*, **112**, 94–112, <https://doi.org/10.1016/j.dsr.2016.02.007>.
- Helland-Hansen, B., and F. Nansen, 1909: The Norwegian Sea: Its physical oceanography based upon the Norwegian researches 1900–1904. Norwegian Fishery and Marine Investigations Rep. Vol. 2, Part 1, No. 2, 390 pp.

- Isachsen, P. E., S. R. Sørli, C. Mauritzen, C. Lydersen, P. Dodd, and K. M. Kovacs, 2014: Upper-ocean hydrography of the Nordic seas during the International Polar Year (2007–2008) as observed by instrumented seals and Argo floats. *Deep-Sea Res. I*, **93**, 41–59, <https://doi.org/10.1016/j.dsr.2014.06.012>.
- Jeansson, E., A. Olsen, and S. Jutterström, 2017: Arctic Intermediate Water in the Nordic seas, 1991–2009. *Deep-Sea Res. I*, **128**, 82–97, <https://doi.org/10.1016/j.dsr.2017.08.013>.
- Jochumsen, K., M. Moritz, N. Nunes, D. Quadfasel, K. M. H. Larsen, B. Hansen, H. Valdimarsson, and S. Jonsson, 2017: Revised transport estimates of the Denmark Strait overflow. *J. Geophys. Res. Oceans*, **122**, 3434–3450, <https://doi.org/10.1002/2017JC012803>.
- Jonsson, S., and H. Valdimarsson, 2004: A new path for the Denmark Strait overflow water from the Iceland Sea to Denmark Strait. *Geophys. Res. Lett.*, **31**, L03305, <https://doi.org/10.1029/2003GL019214>.
- Karstensen, J., P. Schlosser, J. Blindheim, J. Bullister, and D. Wallace, 2003: Formation of intermediate water in the Greenland Sea during the 1990s. *ICES Mar. Sci. Symp.*, **219**, 375–377.
- , —, D. W. R. Wallace, J. L. Bullister, and J. Blindheim, 2005: Water mass transformation in the Greenland Sea during the 1990s. *J. Geophys. Res.*, **110**, C07022, <https://doi.org/10.1029/2004JC002510>.
- Latarius, K., and D. Quadfasel, 2010: Seasonal to inter-annual variability of temperature and salinity in the Greenland Sea gyre: Heat and freshwater budgets. *Tellus*, **62A**, 497–515, <https://doi.org/10.1111/j.1600-0870.2009.00453.x>.
- , and —, 2016: Water mass transformation in the deep basins of the Nordic seas: Analyses of heat and freshwater budgets. *Deep-Sea Res. I*, **114**, 23–42, <https://doi.org/10.1016/j.dsr.2016.04.012>.
- Lauvset, S. K., A. Brakstad, K. Våge, A. Olsen, E. Jeansson, and K. A. Mork, 2018: Continued warming, salinification and oxygenation of the Greenland Sea gyre. *Tellus*, **70A**, 1–9, <https://doi.org/10.1080/16000870.2018.1476434>.
- Lazier, J. R. N., 1980: Oceanographic conditions at ocean weather ship *Bravo*, 1964–1974. *Atmos.–Ocean*, **18**, 227–238, <https://doi.org/10.1080/07055900.1980.9649089>.
- Lorbacher, K., D. Dommenget, P. P. Niiler, and A. Köhl, 2006: Ocean mixed layer depth: A subsurface proxy of ocean-atmosphere variability. *J. Geophys. Res.*, **111**, C07010, <https://doi.org/10.1029/2003JC002157>.
- Malmberg, S.-A., 1983: Hydrographic investigations in the Iceland and Greenland seas in late winter 1971—“Deep water project.” *Jökull*, **33**, 133–140.
- , and S. Jónsson, 1997: Timing of deep convection in the Greenland and Iceland Seas. *ICES J. Mar. Sci.*, **54**, 300–309, <https://doi.org/10.1006/jmsc.1997.0221>.
- Marnela, M., B. Rudels, I. Goszczko, A. Bieszczynska-Möller, and U. Schauer, 2016: Fram Strait and Greenland Sea transports, water masses, and water mass transformations 1999–2010 (and beyond). *J. Geophys. Res. Oceans*, **121**, 2314–2346, <https://doi.org/10.1002/2015JC011312>.
- Marshall, J., and F. Schott, 1999: Open-ocean convection: Observations, theory, and models. *Rev. Geophys.*, **37**, 1–64, <https://doi.org/10.1029/98RG02739>.
- Mastropole, D., R. S. Pickart, H. Valdimarsson, K. Våge, K. Jochumsen, and J. Girtton, 2017: On the hydrography of Denmark Strait. *J. Geophys. Res. Oceans*, **122**, 306–321, <https://doi.org/10.1002/2016JC012007>.
- Mauritzen, C., 1996: Production of dense overflow waters feeding the North Atlantic across the Greenland-Scotland Ridge. Part 1: Evidence for a revised circulation scheme. *Deep-Sea Res. I*, **43**, 769–806, [https://doi.org/10.1016/0967-0637\(96\)00037-4](https://doi.org/10.1016/0967-0637(96)00037-4).
- Meincke, J., S. Jónsson, and J. H. Swift, 1992: Variability of convective conditions in the Greenland Sea. *ICES Mar. Sci. Symp.*, **195**, 32–39.
- , B. Rudels, and H. J. Friedrich, 1997: The Arctic Ocean–Nordic seas thermohaline system. *ICES J. Mar. Sci.*, **54**, 283–299, <https://doi.org/10.1006/jmsc.1997.0229>.
- Messias, M.-J., and Coauthors, 2008: The Greenland Sea tracer experiment 1996–2002: Horizontal mixing and transport of Greenland Sea Intermediate Water. *Prog. Oceanogr.*, **78**, 85–105, <https://doi.org/10.1016/j.pocean.2007.06.005>.
- Moore, G. W. K., K. Våge, R. S. Pickart, and I. A. Renfrew, 2015: Decreasing intensity of open-ocean convection in the Greenland and Iceland seas. *Nat. Climate Change*, **5**, 877–882, <https://doi.org/10.1038/nclimate2688>.
- Nilsen, J. E. Ø., and E. Falck, 2006: Variations of mixed layer properties in the Norwegian Sea for the period 1948–1999. *Prog. Oceanogr.*, **70**, 58–90, <https://doi.org/10.1016/j.pocean.2006.03.014>.
- , H. Hátún, K. A. Mork, and H. Valdimarsson, 2008: The NISE dataset. Faroese Fisheries Laboratory Tech. Rep. 08-01, 20 pp.
- Nøst, O. A., and P. E. Isachsen, 2003: The large-scale time-mean ocean circulation in the Nordic seas and Arctic Ocean estimated from simplified dynamics. *J. Mar. Res.*, **61**, 175–210, <https://doi.org/10.1357/00224003322005069>.
- Østerhus, S., T. Sherwin, D. Quadfasel, and B. Hansen, 2008: The overflow transport east of Iceland. *Arctic–Subarctic Ocean Fluxes*, R. R. Dickson, J. Meincke, and P. Rhines, Eds., Springer, 427–441, https://doi.org/10.1007/978-1-4020-6774-7_19.
- Papritz, L., and T. Spengler, 2017: A Lagrangian climatology of wintertime cold air outbreaks in the Irminger and Nordic seas and their role in shaping air–sea heat fluxes. *J. Climate*, **30**, 2717–2737, <https://doi.org/10.1175/JCLI-D-16-0605.1>.
- Pickart, R. S., and W. M. Smethie, 1998: Temporal evolution of the deep western boundary current where it enters the subtropical domain. *Deep-Sea Res. I*, **45**, 1053–1083, [https://doi.org/10.1016/S0967-0637\(97\)00084-8](https://doi.org/10.1016/S0967-0637(97)00084-8).
- , D. J. Torres, and R. A. Clarke, 2002: Hydrography of the Labrador Sea during active convection. *J. Phys. Oceanogr.*, **32**, 428–457, [https://doi.org/10.1175/1520-0485\(2002\)032<0428:HOTLSD>2.0.CO;2](https://doi.org/10.1175/1520-0485(2002)032<0428:HOTLSD>2.0.CO;2).
- , G. W. K. Moore, C. Mao, F. Bahr, C. Nobre, and T. J. Weingartner, 2016: Circulation of winter water on the Chukchi shelf in early summer. *Deep-Sea Res. II*, **130**, 56–75, <https://doi.org/10.1016/j.dsr.2.2016.05.001>.
- , and Coauthors, 2017: The north Icelandic jet and its relationship to the North Icelandic Irminger Current. *J. Mar. Res.*, **75**, 605–639, <https://doi.org/10.1357/00224017822109505>.
- Price, J. F., R. A. Weller, and R. Pinkel, 1986: Diurnal cycling: Observations and models of the upper-ocean response to diurnal heating, cooling, and wind mixing. *J. Geophys. Res.*, **91**, 8411–8427, <https://doi.org/10.1029/JC091iC07p08411>.
- Quadfasel, D., and J. Meincke, 1987: Note on the thermal structure of the Greenland Sea gyres. *Deep-Sea Res.*, **34A**, 1883–1888, [https://doi.org/10.1016/0198-0149\(87\)90061-6](https://doi.org/10.1016/0198-0149(87)90061-6).
- Ronski, S., and G. Budéus, 2005: Time series of winter convection in the Greenland Sea. *J. Geophys. Res.*, **110**, C04015, <https://doi.org/10.1029/2004JC002318>.
- Rudels, B., G. Björk, J. Nilsson, P. Winsor, I. Lake, and C. Nohr, 2005: The interaction between waters from the Arctic Ocean and the Nordic seas north of Fram Strait and along the East

- Greenland Current: Results from the Arctic Ocean-02 Oden expedition. *J. Mar. Syst.*, **55**, 1–30, <https://doi.org/10.1016/j.jmarsys.2004.06.008>.
- Skagseth, Ø., and K. A. Mork, 2012: Heat content in the Norwegian Sea, 1995–2010. *ICES J. Mar. Sci.*, **69**, 826–832, <https://doi.org/10.1093/icesjms/fss026>.
- Strass, V. H., E. Fahrbach, U. Schauer, and L. Sellmann, 1993: Formation of Denmark Strait overflow water by mixing in the East Greenland Current. *J. Geophys. Res.*, **98**, 6907–6919, <https://doi.org/10.1029/92JC02732>.
- Swift, J. H., and K. Aagaard, 1981: Seasonal transitions and water mass formation in the Iceland and Greenland seas. *Deep-Sea Res.*, **28A**, 1107–1129, [https://doi.org/10.1016/0198-0149\(81\)90050-9](https://doi.org/10.1016/0198-0149(81)90050-9).
- , —, and S.-A. Malmberg, 1980: The contribution of the Denmark Strait overflow to the deep North Atlantic. *Deep-Sea Res.*, **27A**, 29–42, [https://doi.org/10.1016/0198-0149\(80\)90070-9](https://doi.org/10.1016/0198-0149(80)90070-9).
- Våge, K., R. S. Pickart, G. W. K. Moore, and M. H. Ribergaard, 2008: Winter mixed-layer development in the central Irminger Sea: The effect of strong, intermittent wind events. *J. Phys. Oceanogr.*, **38**, 541–565, <https://doi.org/10.1175/2007JPO3678.1>.
- , and Coauthors, 2009: Surprising return of deep convection to the subpolar North Atlantic Ocean in winter 2007–2008. *Nat. Geosci.*, **2**, 67–72, <https://doi.org/10.1038/ngeo382>.
- , R. S. Pickart, M. A. Spall, H. Valdimarsson, S. Jónsson, D. J. Torres, S. Østerhus, and T. Eldevik, 2011: Significant role of the north Icelandic jet in the formation of Denmark Strait overflow water. *Nat. Geosci.*, **4**, 723–727, <https://doi.org/10.1038/ngeo1234>.
- , —, —, G. W. K. Moore, H. Valdimarsson, D. J. Torres, S. Y. Erofeeva, and J. E. Ø. Nilsen, 2013: Revised circulation scheme north of the Denmark Strait. *Deep-Sea Res. I*, **79**, 20–39, <https://doi.org/10.1016/j.dsr.2013.05.007>.
- , G. W. K. Moore, S. Jónsson, and H. Valdimarsson, 2015: Water mass transformation in the Iceland Sea. *Deep-Sea Res. I*, **101**, 98–109, <https://doi.org/10.1016/j.dsr.2015.04.001>.
- Visbeck, M., J. Fischer, and F. Schott, 1995: Preconditioning the Greenland Sea for deep convection: Ice formation and ice drift. *J. Geophys. Res.*, **100**, 18 489–18 502, <https://doi.org/10.1029/95JC01611>.
- Walsh, J. E., W. L. Chapman, and D. H. Portis, 2009: Arctic cloud fraction and radiative fluxes in atmospheric reanalyses. *J. Climate*, **22**, 2316–2334, <https://doi.org/10.1175/2008JCLI2213.1>.
- Wong, A. P. S., G. C. Johnson, and W. B. Owens, 2003: Delayed-mode calibration of autonomous CTD profiling float salinity data by θ -S climatology. *J. Atmos. Oceanic Technol.*, **20**, 308–318, [https://doi.org/10.1175/1520-0426\(2003\)020<0308:DMCOAC>2.0.CO;2](https://doi.org/10.1175/1520-0426(2003)020<0308:DMCOAC>2.0.CO;2).
- Yashayaev, I., and J. W. Loder, 2016: Recurrent replenishment of Labrador Sea Water and associated decadal-scale variability. *J. Geophys. Res. Oceans*, **121**, 8095–8114, <https://doi.org/10.1002/2016JC012046>.
- , M. Bersch, and H. M. van Aken, 2007: Spreading of the Labrador Sea Water to the Irminger and Iceland basins. *Geophys. Res. Lett.*, **34**, L10602, <https://doi.org/10.1029/2006GL028999>.

Paper II

The impact of cold-air outbreaks and oceanic lateral fluxes on dense-water formation in the Greenland Sea from a ten-year moored record (1999–2009)

Svingen, K., A. Brakstad, K. Våge, W. J. von Appen, and L. Papritz
Journal of Physical Oceanography, **53/6** (2023)

The Impact of Cold-Air Outbreaks and Oceanic Lateral Fluxes on Dense-Water Formation in the Greenland Sea from a 10-Year Moored Record (1999–2009)

KRISTIN SVINGEN,^{a,b} AILIN BRAKSTAD,^{a,b} KJETIL VÅGE,^{a,b} WILKEN-JON VON APPEN,^c AND LUKAS PAPRITZ^d

^a *Geophysical Institute, University of Bergen, Bergen, Norway*

^b *Bjerknes Centre for Climate Research, Bergen, Norway*

^c *Alfred Wegener Institute, Helmholtz Centre for Polar and Marine Research, Bremerhaven, Germany*

^d *Institute of Atmospheric and Climate Science, Department of Environmental System Science, ETH Zurich, Zurich, Switzerland*

(Manuscript received 29 July 2022, in final form 1 March 2023, accepted 5 March 2023)

ABSTRACT: The Greenland Sea produces a significant portion of the dense water from the Nordic seas that supplies the lower limb of the Atlantic meridional overturning circulation. Here, we use a continuous 10-yr hydrographic record from moored profilers to examine dense-water formation in the central Greenland Sea between 1999 and 2009. Of primary importance for dense-water formation is air–sea heat exchange, and 60%–80% of the heat lost to the atmosphere during winter occurs during intense, short-lived events called cold-air outbreaks (CAOs). The long duration and high temporal resolution of the moored record has for the first time facilitated a statistical quantification of the direct impact of CAOs on the wintertime mixed layer in the Greenland Sea. The mixed layer development can be divided into two phases: a cooling phase and a deepening phase. During the cooling phase (typically between November and January), CAOs cooled the mixed layer by up to 0.08 K day^{-1} , depending on the intensity of the events, while the mixed layer depth remained nearly constant. Later in winter (February–April), heat fluxes during CAOs primarily led to mixed layer deepening of up to 38 m day^{-1} . Considerable variability was observed in the mixed layer response, indicating that lateral fluxes of heat and salt were also important. The magnitude and vertical distributions of these fluxes were quantified, and idealized mixed layer simulations suggest that their combined effect is a reduction in the mixed layer depth at the end of winter of up to several hundred meters.

KEYWORDS: Arctic; In situ oceanic observations; Deep convection; Oceanic mixed layer; Air–sea interaction; Cold air surges

1. Introduction

The Atlantic meridional overturning circulation plays a crucial role in global climate. Warm and saline Atlantic Water (AW) is transported from the equator toward higher latitudes by the upper branch of the circulation. On its way poleward, heat is lost to the atmosphere. This transforms the water into colder and denser water masses that return equatorward at depth. The majority of the overturning takes place east of Greenland (Lozier et al. 2019; Petit et al. 2020). The densest component is formed in the Nordic seas (comprising the Greenland, Iceland, and Norwegian Seas, Fig. 1) and spills across the Greenland–Scotland Ridge into the deep North Atlantic. While descending, the overflow plumes entrain surrounding water masses, which together supply the lower branch of the overturning circulation (Chafik and Rossby 2019).

One important mechanism of dense-water formation in the Nordic seas is open-ocean convection. This takes place within the cyclonic Greenland Sea Gyre, where doming of dense isopycnals reduces stratification and preconditions the water

column for wintertime convection (e.g., Marshall and Schott 1999). The Greenland Sea Gyre also experiences severe heat loss to the atmosphere during winter (Moore et al. 2015). The cooling and densification of the surface layer initiates convective overturning and the production of dense water. Approximately 60%–80% of the total heat lost to the atmosphere in this region during winter occurs during intense, short-lived cold-air outbreaks (CAOs; Papritz and Spengler 2017). Marine CAOs occur when cold polar air masses over land and ice are advected over relatively warm water, leading to large ocean to atmosphere heat fluxes near the sea-ice edge. Over the past 50 years the sea-ice edge has retreated toward Greenland, which has led to a reduced intensity of CAOs and an overall decline in winter heat loss over the gyre (Moore et al. 2015; Somavilla 2019; Dahlke et al. 2022; Moore et al. 2022). This has, and is projected to continue having, substantial ramifications for water-mass transformation in the central Greenland Sea.

Prior to 1980, deep-reaching convection in the central Greenland Sea produced cold and dense Greenland Sea Deep Water (GSDW), which was considered the main source of deep water in the Nordic seas (Helland-Hansen and Nansen 1909; Malmberg 1983; Aagaard et al. 1985). There is no evidence of significant renewal of GSDW after the early 1980s, and the main product of convection since then has been the warmer, saltier, and less dense Greenland Sea Arctic Intermediate Water (GSAIW; Meincke et al. 1990, 1997; Karstensen et al. 2005; Ronski and Budéus 2005; Latarius and Quadfasel 2010; Brakstad et al. 2019). Convection has been limited to

Denotes content that is immediately available upon publication as open access.

Kristin Svingen and Ailin Brakstad contributed equally to this paper and should be considered co-first authors.

Corresponding author: Ailin Brakstad, ailin.brakstad@uib.no

DOI: 10.1175/JPO-D-22-0160.1

© 2023 American Meteorological Society. For information regarding reuse of this content and general copyright information, consult the AMS Copyright Policy (www.ametsoc.org/PUBSReuseLicenses).

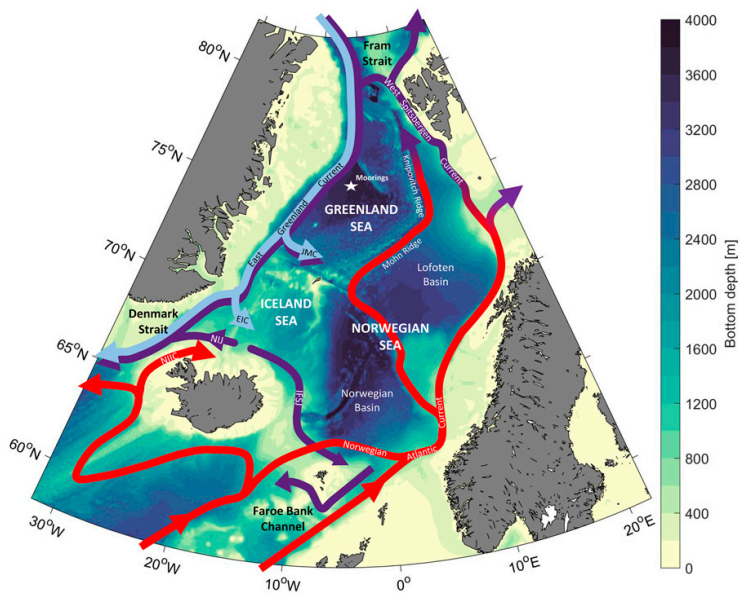


FIG. 1. Schematic circulation in the Nordic seas. The red arrows indicate inflow of warm Atlantic Water, the dark purple arrows mark the flow of dense water, and the light blue arrows show the flow of Polar Surface Water. The location of the moorings is indicated by the white star. The acronyms are the North Icelandic Irminger Current (NIIC), the North Icelandic Jet (NIJ), the Iceland–Faroe Slope Jet (IFSJ), the East Icelandic Current (EIC), and the Jan Mayen Current (JMC).

less than 2000-m depth, and an intermediate stratification maximum (that has further isolated the GSDW from the surface) has developed. The formation of GSDW ceased as a result of reduced atmospheric forcing, combined with temporary freshening that enhanced the stability of the gyre and less local sea-ice formation (Meincke et al. 1992; Visbeck et al. 1995; Somavilla 2019). According to Moore et al. (2015, 2022), the trend toward weaker atmospheric heat fluxes over the Greenland Sea is expected to continue in a warming climate with continued sea-ice retreat. This has not yet limited GSAIW formation, primarily due to increased salt advection into the Greenland Sea since the mid-1990s, resulting in higher densities and a tendency for deeper convection (Lauvset et al. 2018; Brakstad et al. 2019). The overall magnitudes of heat (57 W m^{-2}) and freshwater ($-21 \text{ mm month}^{-1}$) fluxes into the central Greenland Sea were estimated by Latarius and Quadfasel (2016) based on budget calculations. However, uncertainties remain regarding their vertical distributions and where the heat and salt enter the gyre.

While wintertime convection in the Greenland Sea presently produces only intermediate water, this water mass can more directly contribute to the dense overflow waters spilling across the Greenland–Scotland Ridge from the Nordic seas into the deep North Atlantic. Roughly 90% of the dense water emanating from the Nordic seas passes the ridge through either Denmark Strait or the Faroe Bank Channel (FBC; Østerhus et al. 2019). Two main currents supply the Denmark

Strait overflow: the East Greenland Current (EGC) and the North Icelandic Jet (NIJ; Harden et al. 2016; Våge et al. 2011). The overflow water transported with the EGC is mainly Atlantic-origin water that has been gradually cooled and densified along its path around the rim of the Nordic seas and Arctic Ocean (Mauritzen 1996; Eldevik et al. 2009; Våge et al. 2018; Håvik et al. 2019), but also a nonnegligible portion of water formed in the Greenland Sea (Strass et al. 1993; Jeansson et al. 2008). The NIJ, on the other hand, transports water formed primarily in the Greenland Sea (Semper et al. 2019; Huang et al. 2020; Våge et al. 2022; Brakstad et al. 2023). The total contribution from the Greenland Sea to the Denmark Strait overflow is $39\% \pm 2\%$ (Brakstad et al. 2023). The Greenland Sea is also an important source of the Iceland–Faroe Slope Jet that, together with dense water flowing southward along the Jan Mayen Ridge, supply overflow water to the FBC (Semper et al. 2020; Huang et al. 2020; Chafik et al. 2020; Brakstad et al. 2023). In total, $46\% \pm 8\%$ of the FBC overflow originates in the Greenland Sea, while the other main source is the Arctic Ocean (Brakstad et al. 2023). This is in line with Jeansson et al. (2017), who focused on the origin of the intermediate water in the Norwegian Sea upstream of the FBC. The Greenland Sea is thus an important source of overflow water both east and west of Iceland.

Even though water-mass transformation in the Greenland Sea has been an active topic of investigation for several decades (e.g., Meincke et al. 1990, 1992; Ronski and Budéus 2005;

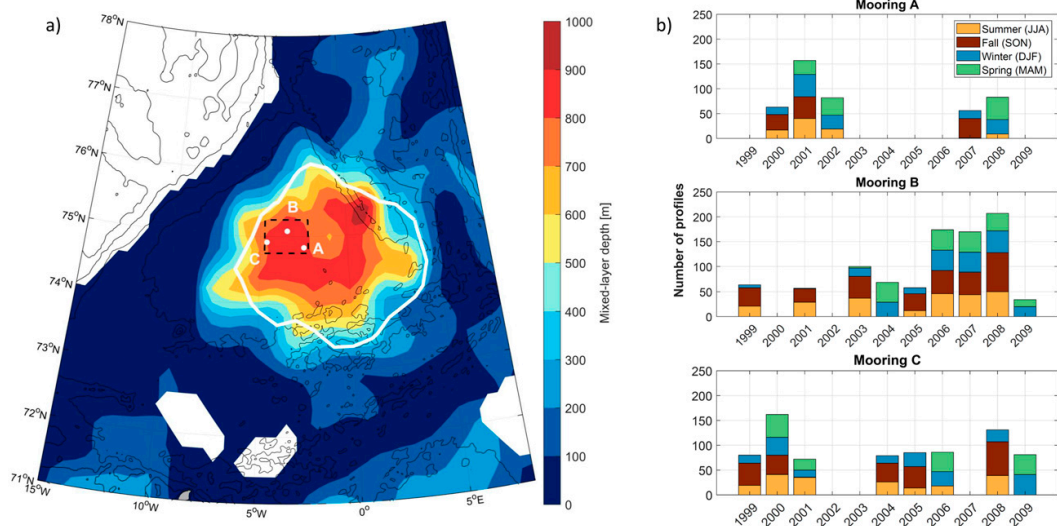


FIG. 2. (a) The locations of moorings A, B, and C. The colors show mean late-winter (February–April) mixed layer depth from the winters with the 30% deepest convection depths between 1986 and 2016 (based on Fig. 3c in Brakstad et al. 2019). The black contours show the 250-, 500-, 1000-, 2000-, and 3000-m isobaths. The outline of the Greenland Sea Gyre as defined by Moore et al. (2015) using dynamic topography of the sea surface relative to 500-m depth is indicated by the white contour. The black dashed line outlines the area over which ERA5 data were averaged. (b) The number of hydrographic profiles each year sorted by mooring and season.

Latarius and Quadfasel 2010; Brakstad et al. 2019; Somavilla 2019), most studies have focused on interannual and long-term variability. Here we use a set of three profiling moorings that were deployed within the Greenland Sea Gyre from 1999 to 2009 to investigate the wintertime evolution of the mixed layer. The profilers measured temperature, salinity, and pressure nearly from the surface to the bottom on average every second day (daily between 2008 and 2009). Due to the long duration and high temporal resolution of the data, we could quantify the direct impact of CAOs on the wintertime mixed layer using a statistical approach, and, in particular, how the response depended on the timing and intensity of the events. This has not previously been possible due to sparse data coverage and the short duration of CAOs (Terpstra et al. 2021). In addition to the impact of atmospheric forcing, previous studies have highlighted the importance of lateral heat and salt fluxes (e.g., Latarius and Quadfasel 2016; Lauvset et al. 2018; Brakstad et al. 2019). We determined the vertical distribution of the lateral heat and salt fluxes into the central Greenland Sea, and used that information in idealized numerical simulations to investigate their impact on the wintertime development of the mixed layer.

2. Data and methods

a. Hydrographic data

Our analysis is primarily based on 10 years (1999–2009) of hydrographic measurements from three moored profilers in the central Greenland Sea. The moorings, hereafter referred to as moorings A (74°50′N, 2°30′W), B (75°05′N, 3°27′W),

and C (74°55′N, 4°37′W), were all located within the cyclonic Greenland Sea Gyre (Fig. 2a), where Brakstad et al. (2019) found the deepest and densest wintertime mixed layers.

Each moored profiler was recovered and redeployed every summer. They were equipped with Sea-Bird Electronics SBE19 Seacats that measured conductivity, temperature, and pressure from approximately 100 m below the sea surface to a few meters above the sea floor at ~3700 m every second day. It requires a large amount of power to operate a profiling vehicle over a year. To overcome challenges related to energy consumption, the vertical motion of the profiler was driven by changes in buoyancy by adding and removing lead weights from the vehicle. The lead weights were kept in a basket mounted at the top of the mooring. The profiler itself was buoyant, and for each cycle the profiler was ballasted by a lead weight from the basket. The additional weight decreased the buoyancy of the vehicle and caused it to sink to the sea floor. At the bottom of the mooring, the lead weight was unloaded and the vehicle returned to the surface driven by its own positive buoyancy. Measurements were only taken during the dive, when the profiler reached a downward velocity of 0.8–1.0 m s⁻¹ (Budéus et al. 2005). Temperature and conductivity were measured at a frequency of 1 Hz, which corresponds to a vertical resolution of approximately 1 m, while pressure was recorded every 120 s. The initial accuracy of the instrument was 0.005°C for temperature and 0.0005 S m⁻¹ for conductivity. For the temperatures in the Greenland Sea, this corresponds to a salinity accuracy better than 0.01 g kg⁻¹. Additional technical details regarding the mooring configuration and performance can be found in Budéus et al. (2005).

The postprocessing included calibration of the mooring data against shipboard CTD measurements collected from the annual mooring turnaround cruises, smoothing of the profiles with a 10-m median filter, and interpolation of the data to integer pressure values. Values outside the expected range of temperature and salinity in the Nordic seas of $[-2, 20]^{\circ}\text{C}$ and $[20, 36] \text{ g kg}^{-1}$, respectively (e.g., Våge et al. 2013) were excluded. The total coverage of quality-controlled data from each mooring is shown in Fig. 2b. Vertical profiles were generally obtained every second day, except during 2008–09 when daily profiles were collected. However, due to technical issues the profilers were at times parked at a constant depth. This was caused either by problems with the loading/unloading of the lead weights that on 11 occasions lasted for the entire deployment, or shorter periods when profiling was prevented by strong currents (Budéus et al. 2005; Budéus 2009). Measurements taken during these periods were not considered.

Data from all three moorings were combined in order to obtain one complete time series from 1999 to 2009 with the minimal number of gaps due to missing data. Before combining the data, mixed layer depths and hydrographic properties, as well as hydrographic properties at depth (2000 m), were compared between moorings that had collected data simultaneously (not shown). Both the end-of-winter mixed layer depths and the monthly mean mixed layer properties agreed well between the different mooring locations. The largest differences in monthly mean mixed layer depth occurred in late winter (March and April), mainly caused by variations in the onset of restratification at the different mooring locations. The differences between monthly mean hydrographic properties at 2000-m depth were negligible. The mooring locations are hereafter used interchangeably to represent the general conditions within the Greenland Sea Gyre. Data from mooring B were used as the basis for the combined time series. Data gaps were filled using data from the other two moorings.

The delicate construction of the buoyant profiler inhibited measurements close to the surface (Budéus et al. 2005; Budéus 2009). The shallowest depths of the profiles varied between deployments, from 95 to 185 m. In the final year of the deployment period (2008–09) a supplementary mooring was deployed to cover the upper part of the water column, from the surface to 130 m. This mooring was located 1.8 km away from mooring C. To overcome the influence of surface waves, this profiler had much greater positive buoyancy than the deep profilers. The surface profiler was equipped with a Sea-Bird Electronics SBE41, which has an initial accuracy of 0.002°C and 0.002 g kg^{-1} for temperature and salinity, respectively. Measurements from moorings B and C were combined with surface measurements from the supplementary mooring to form surface to bottom profiles. The transition between the upper and lower datasets was not smoothed and the profiles from 2008 to 2009 have a distinct joint at 130 m. Further details about the 2008–09 deployment can be found in a technical report (Budéus 2009).

In addition to the mooring data, we used hydrographic profiles from 1999 to 2012 from a database collected by Brakstad et al. (2023). This database consists of profiles from various archives over the period 1950–2019 covering the domain $50^{\circ}\text{--}90^{\circ}\text{N}$ and $45^{\circ}\text{W--}65^{\circ}\text{E}$. The majority of the data collected

in the Greenland Sea during this period was obtained from the Unified Database for Arctic and Subarctic Hydrography (UDASH; Behrendt et al. 2018) and consists of shipboard hydrographic measurements and Argo float profiles.

Following the new standard of the International Thermodynamic Equation Of Seawater-2010 (TEOS-10; IOC et al. 2010) Conservative Temperature and Absolute Salinity (hereafter referred to as temperature and salinity, respectively) were calculated from all hydrographic data and used throughout the analysis.

b. Mixed layer depths

Apart from the 2008–09 deployment, the moored profilers did not measure the upper 100 m of the water column. Hence, only mixed layers extending well below this depth could be identified. In total, mixed layers were identified in 49% of the profiles. The remaining profiles were mainly from summer when the mixed layer was too shallow to be detected.

Depth and properties of the mixed layer were determined using a robust procedure previously applied by Våge et al. (2015) and Brakstad et al. (2019). The mixed layer depth was first estimated by two automated routines, one based on the curvature of the temperature profile (Lorbacher et al. 2006) and the other based on a density difference criterion (Nilsen and Falck 2006). Each profile and the corresponding mixed layer depth estimates were then visually inspected. One or both of the automated routines accurately determined the mixed layer depth for approximately half of the profiles where the mixed layer was sufficiently deep to reach the moorings. For the remaining profiles, a manual procedure developed by Pickart et al. (2002) was applied. The extent of the mixed layer was first estimated visually, and the means and standard deviations of the mixed layer temperature, salinity, and density were calculated over this depth range. Finally, the top and bottom of the mixed layer were determined as the depths where either the temperature, salinity, or density profile permanently exceeded two standard deviations from the mean.

The manual procedure was also used for the majority of the combined profiles from 2008 to 2009 because of the distinct joint at 130 m. The small shift in hydrographic properties between the deep and the shallow profilers was due to their lateral displacement. When the mixed layer extended beneath the shallow moored profiler, the manual procedure was used to set the upper limit of the mixed layer below the joint, even though the mixed layer extended to the surface. This ensured that mixed layer properties were estimated based on data only from the deep profiler. When the mixed layer was shallower than 130 m and fully in the range of the shallow profiler, the automated routines generally performed well.

c. Atmospheric data

Hourly atmospheric fields were obtained from the ERA5 reanalysis, which is the fifth-generation reanalysis produced by the European Centre for Medium-Range Weather Forecasts (Hersbach et al. 2020). The reanalysis data have first been interpolated to a 0.25° latitude–longitude grid and then averaged over a box enclosing all three moorings ($74.75^{\circ}\text{--}75.25^{\circ}\text{N}$ and $2.25^{\circ}\text{--}4.75^{\circ}\text{W}$; Fig. 2a). We used analyzed fields

of potential temperature at 900 hPa, surface skin temperature, surface pressure, and sea-ice concentration, as well as short-range forecasts of wind stress, surface sensible and latent turbulent heat fluxes, evaporation, precipitation, and long- and shortwave radiation.

d. Cold-air outbreaks

To identify CAO events, we followed previous works (e.g., Bracegirdle and Gray 2008; Kolstad 2011; Papritz et al. 2015; Fletcher et al. 2016; Papritz and Spengler 2017; Terpstra et al. 2021) by using a CAO index defined as the difference between potential skin water temperature (θ_{SKT}) and potential air temperature at 900 hPa ($\theta_{900\text{hPa}}$), i.e., $\theta_{\text{SKT}} - \theta_{900\text{hPa}}$. Papritz and Spengler (2017) found that CAOs with a CAO index in excess of 4 K are closely associated with enhanced upward turbulent heat fluxes and are, therefore, most relevant for dense-water formation in the western Nordic seas. Consequently, time steps with a CAO index below 4 K were not considered. From the CAO index time series, the cold-air outbreaks each winter were identified on an event by event basis as follows: The peak of the first event was defined as the maximum CAO index. Every neighboring data point with a CAO index higher than 4 K was then assigned to that event. The start and end of the event were set to the first and last data points where the CAO index was higher than 4 K. Further events were then identified iteratively following the same procedure by considering only data points that were not yet attributed to another event. In the end all events with peak values exceeding 4 K were identified, and all data points with a CAO index higher than 4 K were assigned to a particular event. Following Papritz and Spengler (2017), each event was classified as either moderate ($4\text{ K} < \theta_{\text{SKT}} - \theta_{900\text{hPa}} \leq 8\text{ K}$), strong ($8\text{ K} < \theta_{\text{SKT}} - \theta_{900\text{hPa}} \leq 12\text{ K}$), or very strong ($12\text{ K} < \theta_{\text{SKT}} - \theta_{900\text{hPa}}$) according to the peak value of the CAO index. The temporal distribution of turbulent heat fluxes during the events (centered at the peak CAO index) is shown in Fig. 3 for each intensity class. Both the length of the event and the peak turbulent heat flux increase with CAO intensity.

Terpstra et al. (2021) found that the median duration of a CAO in this region is 2.5 days, with lower and upper quartiles of 1.8 and 4.1 days. To quantify the direct impact of CAOs on the wintertime mixed layer we therefore investigated profile-to-profile changes in mixed layer depth and temperature between all profiles obtained 4 days or less apart. Profiles where the mixed layer was not detected by the moorings were excluded from the analysis. The changes were calculated separately at each of the three mooring locations and divided by the time span between the profiles to estimate a daily rate of change. Each of these differences in mixed layer properties were grouped according to the CAO intensity classification above by the median value of the CAO index between the profiles.

e. Idealized mixed layer model

To investigate how the timing of CAOs and oceanic lateral advection impact the mixed layer development, we employed a one-dimensional mixed layer model known as the Price–Weller–

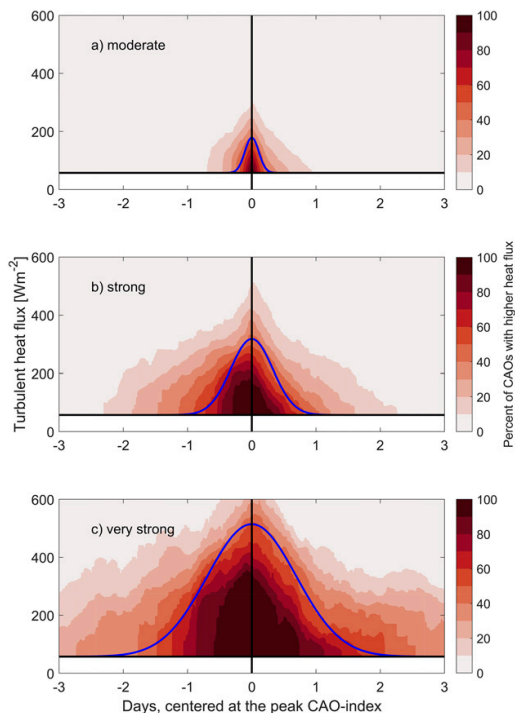


FIG. 3. Temporal distribution of turbulent heat fluxes during (a) moderate, (b) strong, and (c) very strong CAOs. All CAOs were centered at the peak CAO index. The color indicates the percentage of CAO events exceeding the turbulent heat flux value on the y axis. The black horizontal lines mark the winter mean background turbulent heat flux when no CAO was present (57 W m^{-2}). The blue curves are idealized CAOs with a Gaussian distribution (section 2e).

Pinkel (PWP) model after Price et al. (1986). A modified version of this model, including lateral fluxes of heat and salt, was developed by Moore et al. (2015) and Brakstad et al. (2019) to better represent the conditions in the central Greenland Sea. Lateral advection of heat was parameterized by Moore et al. (2015) based on the annual-mean heat budget for the Greenland Sea Gyre and reflects the vertical profile of the temperature difference across the gyre boundary. The same principle was used to parameterize lateral advection of salt by Brakstad et al. (2019), who also included salt fluxes from formation of sea ice. In this study, we updated the PWP model setup for the Greenland Sea with our improved estimates of lateral heat and salt fluxes (section 6). The importance of lateral advection was examined by comparing two sets of PWP runs for each winter (one with and one without lateral advection) to the observed mixed layer evolution. The initial hydrographic conditions were based on the first November profile where the mixed layer was detected by the moorings. The model was then integrated to the end of April with realistic atmospheric forcing based on hourly heat,

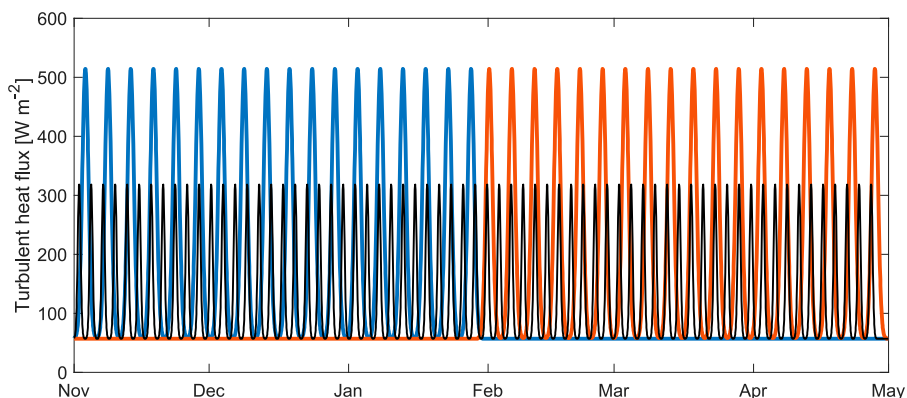


FIG. 4. Time series of turbulent heat fluxes for idealized CAOs concentrated early in winter (blue), late in winter (orange), and evenly distributed throughout winter (black). These were constructed based on the idealized heat-flux distributions for single CAOs (blue curves, Fig. 3) as described in the text. The integrated November–April heat loss equals the 1999–2009 mean for all three time series, while the background heat flux without CAOs is 57 W m^{-2} .

freshwater, and momentum fluxes from ERA5 (section 2c). We note that sea surface temperatures below the freezing point were nearly absent during the time period considered here. Hence, the effect of salt fluxes from sea-ice formation was negligible. The model has a vertical resolution of 2 m and a time step of 1 h.

The same setup, but with idealized atmospheric forcing, was used to examine how the timing of CAOs impacts the mixed layer development. To isolate the effect of the temporal CAO distribution, we required that the integrated turbulent heat loss from November to April was equal to the 1999–2009 mean in all simulations. Three different cases were then considered: one with all CAOs concentrated early in winter, one with all CAOs concentrated late in winter, and one with CAOs evenly distributed throughout the winter. The corresponding time series of turbulent heat fluxes (Fig. 4) were constructed based on idealized heat-flux distributions of single CAOs (blue curves in Fig. 3). The idealized CAOs have Gaussian distributions with peak turbulent heat fluxes (181, 318, and 515 W m^{-2}) and durations (0.7, 2.7, and 5.0 days) equal to the means of the moderate, strong, and very strong events, respectively (section 2d). The background turbulent heat flux when the CAO index was below 4 K was 57 W m^{-2} on average (black horizontal lines in Fig. 3), this was used as the background also in the simulations. Idealized CAOs were then added to the background turbulent heat flux until the integrated November–April heat loss reached the 1999–2009 mean. As several strong and very strong CAO events typically occur every winter, too many moderate events were required to obtain the required integrated heat loss. Hence, the three idealized time series were only constructed based on strong and very strong events: either 18 very strong events early in winter, 18 very strong events late in winter, or 67 strong events distributed evenly throughout the winter (Fig. 4). The remaining atmospheric forcing components were constant, equal to the November–April mean between 1999 and 2009.

3. Evolution of hydrographic properties in the Greenland Sea Gyre

By combining data from all three moorings (section 2a), we obtained near-surface to bottom hydrographic time series in the Greenland Sea Gyre covering the entire 1999–2009 period with only three major data gaps (Fig. 5). Throughout the deployment, the entire water column became warmer and more saline (Figs. 5a,b). This development is consistent with Lauvset et al. (2018) and Brakstad et al. (2019), who documented warming and salinification in the upper 2000 m between 1986 and 2016. Lauvset et al. (2018) attributed this change in properties to the increased temperature and salinity of the AW entering the Nordic seas during the same period (e.g., Holliday et al. 2008; Tsubouchi et al. 2021). AW is advected into the Nordic seas by the Norwegian Atlantic Current, which flows northward to the east of the Greenland Sea Gyre, and densified Atlantic-origin water is returned to the south by the EGC on the western side of the gyre (Fig. 1). The Atlantic-origin water is warmer and more saline than the ambient water in the Greenland Sea, and heat and salt continuously penetrate the gyre between 50- and 1500-m depth (Latarius and Quadfasel 2016).

Lauvset et al. (2018) and Brakstad et al. (2019) only considered data above 2000-m depth, which corresponds to the depth range where the evolution of the Greenland Sea properties can be explained by eddy fluxes from surrounding water masses (Latarius and Quadfasel 2016). Below 2000 m, the water column consists of GSDW that has not been ventilated since deep-reaching convection ceased in the early 1980s (e.g., Meincke et al. 1992; Karstensen et al. 2005; Brakstad et al. 2019). After the GSDW was isolated from the surface, it has only been modified by mixing with deep water masses from the Arctic Ocean through Fram Strait (Somavilla et al. 2013) and from the Norwegian Sea through the Jan Mayen Channel (Østerhus and Gammelsrød 1999). These deep waters are

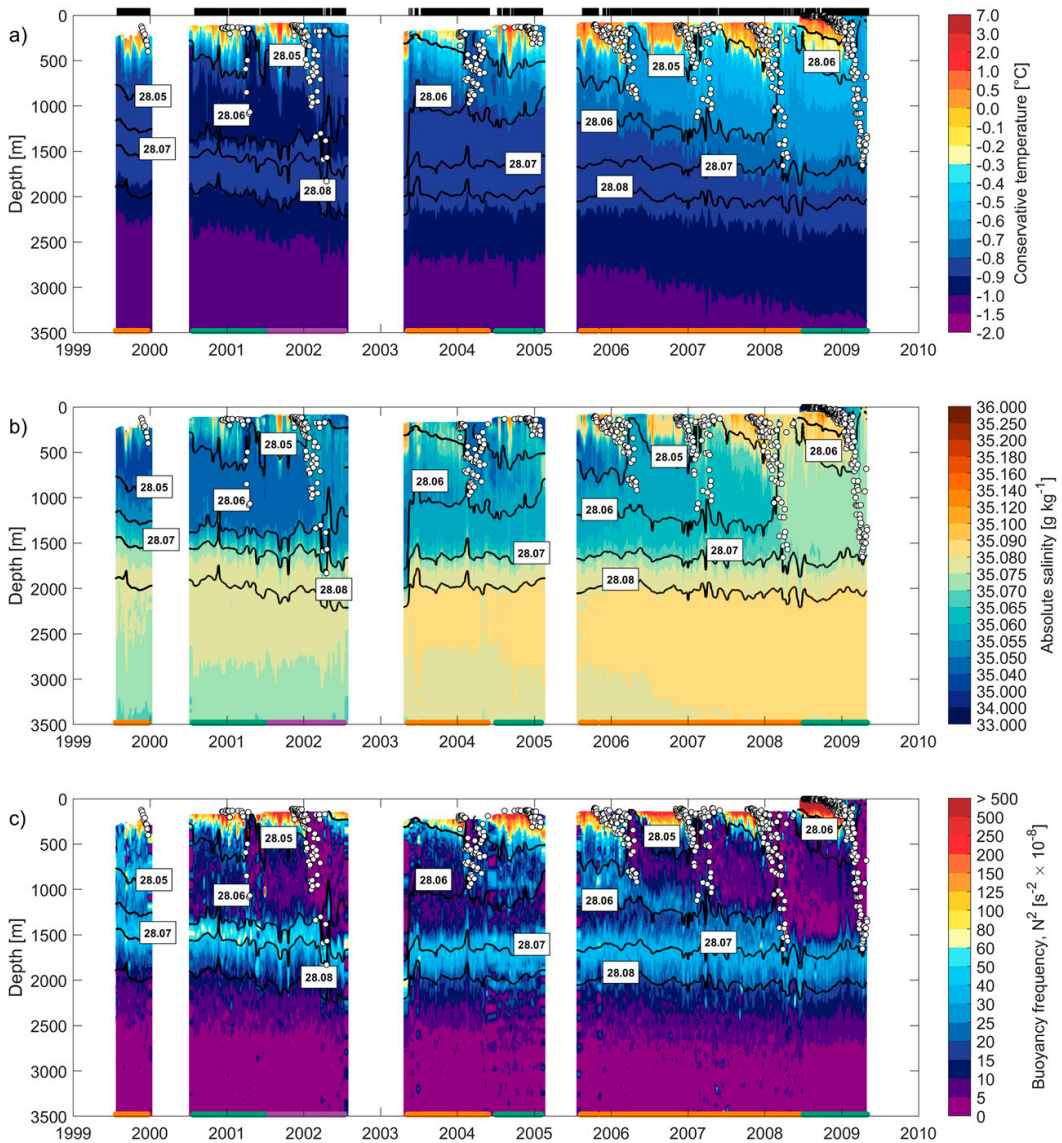


FIG. 5. (a) Temperature, (b) salinity, and (c) buoyancy frequency in the Greenland Sea Gyre between 1999 and 2009. The black lines show potential density contours. Mixed layer depths are marked by white dots. The colors at the bottom of each figure indicate which mooring the data originate from (purple for mooring A, orange for mooring B, and green for mooring C). The x axes indicate the start of each year, while the black bars at the top of the figure mark when profiles were obtained. Note the nonlinear color bars.

warmer and more saline than the GSDW, hence a warming and salinification are observed also at depth (Østerhus and Gammelsrød 1999; Somavilla et al. 2013).

While long-term warming and salinification took place at all depths, the hydrographic properties in the upper half (above 2000 m) of the water column were primarily modified

by local convection in winter. The $\sigma_\theta = 28.05 \text{ kg m}^{-3}$ isopycnal was ventilated every winter, while the $\sigma_\theta = 28.06 \text{ kg m}^{-3}$ isopycnal outcropped during the last two winters (2007/08 and 2008/09, Fig. 5). Thus, convection in the Greenland Sea produced water masses that can supply the densest portion of the overflow water each winter throughout the entire 1999–2009

period (e.g., [Huang et al. 2020](#)). However, the interannual variability in the stratification as indicated by the buoyancy frequency in [Fig. 5c](#) was pronounced. This variability primarily stems from changes in convection depth (indicated by the white dots). Winters of deep convection (such as 2001/02 and 2007/08) were followed by summers of reduced stratification at intermediate depths. The intimate link between convection depth and intermediate stratification was in particular evident in the stepwise increase of convection depth and concurrent decrease in stratification between 2006 and 2009. [Ronski and Budéus \(2005\)](#) used, among other criteria, the change in water column stratification to estimate the depth of wintertime convection by comparing profiles from the Greenland Sea from two subsequent summers. Although we have no measurements from winter 1999/2000, convection to about 1300 m can be inferred from the weakly stratified intermediate layer that appeared in summer 2000. This decrease in stratification from fall 1999 to summer 2000 was caused by convection in winter 1999/2000.

The pronounced stability maximum between 1500- and 2000-m depth separates the GSAIW from the deeper GSDW ([Fig. 5c](#)). This maximum developed following an intermediate temperature maximum around 500 m in the early 1990s (e.g., [Budéus et al. 1998](#); [Karstensen et al. 2005](#)). Since then, the maxima have gradually descended as the overlying GSAIW was ventilated by convection and increased in volume while the GSDW remained isolated from the surface. Even though the temperature maximum disappeared after 2002, the stability maximum persisted around 1500-m depth. Another pronounced intermediate layer of high stratification was evident between 2004 and 2008 (also noted by [Brakstad et al. 2019](#)). This maximum arose around 1000-m depth in 2004 as a result of relatively shallow convection combined with continuous restratification from lateral advection across the gyre boundary. Increased convection depths the following winters gradually eroded this stratification maximum until 2008, when it reached 1500-m depth and disappeared.

4. Wintertime mixed layer evolution

Since hydrographic profiles were obtained every second day, it was possible to examine the mixed layer evolution through winter and its response to atmospheric forcing on short time scales. Throughout the record, brief near-surface temperature increases occurred. These events must stem from warmer water masses advected past the moorings as the total heat flux during winter was always directed from the ocean to the atmosphere, hence cooling the ocean. To focus our analysis on the direct impact of the atmospheric forcing on the mixed layer, all profiles with warm near-surface anomalies were excluded from the analysis.

Substantial interannual variability was observed in the end-of-winter mixed layer depths ([Fig. 6a](#)). More than 1000 m separated the shallowest (2005/06) and deepest (2001/02) convection depths. Nevertheless, the mixed layer evolution each winter had a similar pattern both in depth and in temperature ([Figs. 6a,b](#)), which can be divided into two distinct phases. In the first phase (approximately November–January), the shallow mixed layer cooled substantially, even when the heat loss was

only modest, while the change in mixed layer depth was minor ([Fig. 6c](#)). When the mixed layer became sufficiently dense to erode the near-surface stratification that had accumulated through summer, the second phase commenced and the mixed layer deepened rapidly. In the second phase (approximately February–April), the heat loss was distributed over an increasingly deep mixed layer, which led to reduced cooling (i.e., less reduction in temperature); this, however, was not necessarily related to reduced heat fluxes. A similar pattern was noted by [Pawlowicz \(1995\)](#), who investigated the seasonal cycle of temperature and salinity in the upper waters of the Greenland Sea Gyre prior to the 1990s. Hereafter, we refer to the first phase as the cooling phase and the second phase as the deepening phase.

For each winter the transition between the two phases was identified by the inflection point of the 30-day running mean mixed layer depth. The deepening phase commenced when the second derivative had a minimum after mid-December, i.e., when the slope of the mixed layer depth increased the most (marked with diamonds in [Fig. 6a](#)). The transition from the cooling to the deepening phase generally occurred between late December and early February. The winter of 2000/01, when the deepening phase was delayed until mid-March, was an exception. Unlike the other winters, the moorings were covered by sea ice throughout most of January and February. The sea-ice cover insulated the sea surface from the atmosphere, which kept the mixed layer shallow. When the ice edge retreated in March, the water column was exposed to the atmosphere and the deepening phase began shortly thereafter. While the moorings were covered by sea ice, the mixed layer was mostly too shallow to be detected (note the few mixed layers detected between January and February in [Fig. 6a](#)). These under-ice profiles that were not directly exposed to the atmosphere are not included in the analysis.

5. The impact of cold-air outbreaks on the mixed layer

The CAO frequency in winter ranges between 20% and 50% ([Fig. 7](#)). Winters with a high CAO frequency generally have a higher winter mean turbulent heat flux from the ocean to the atmosphere. Corroborating the results of [Paprutz and Spengler \(2017\)](#), CAOs accounted for 60%–80% of the total turbulent heat loss each winter. Winter 2001/02 was an exception, then the CAO contribution exceeded 80%, thereby strongly exceeding the range of CAO frequencies (20%–50%, [Fig. 7](#)). Even during winter 2005/06, when the CAO frequency was only 22%, the events were responsible for 60% of the total heat loss. Consistent with the few CAOs this winter, the mean turbulent heat flux was particularly low (107 W m^{-2}), and convection did not exceed 1000 m. There is a clear connection between the winter mean turbulent heat flux and the maximum convection depth each winter, with the deepest mixed layer depths occurring in winters with the strongest atmospheric forcing, hence the incidence of CAOs is important for dense-water formation in the Greenland Sea. Winter 2006/07 breaks the general pattern in [Fig. 7](#). This winter was characterized by strong intermediate stratification in fall ([Fig. 5c](#)), which

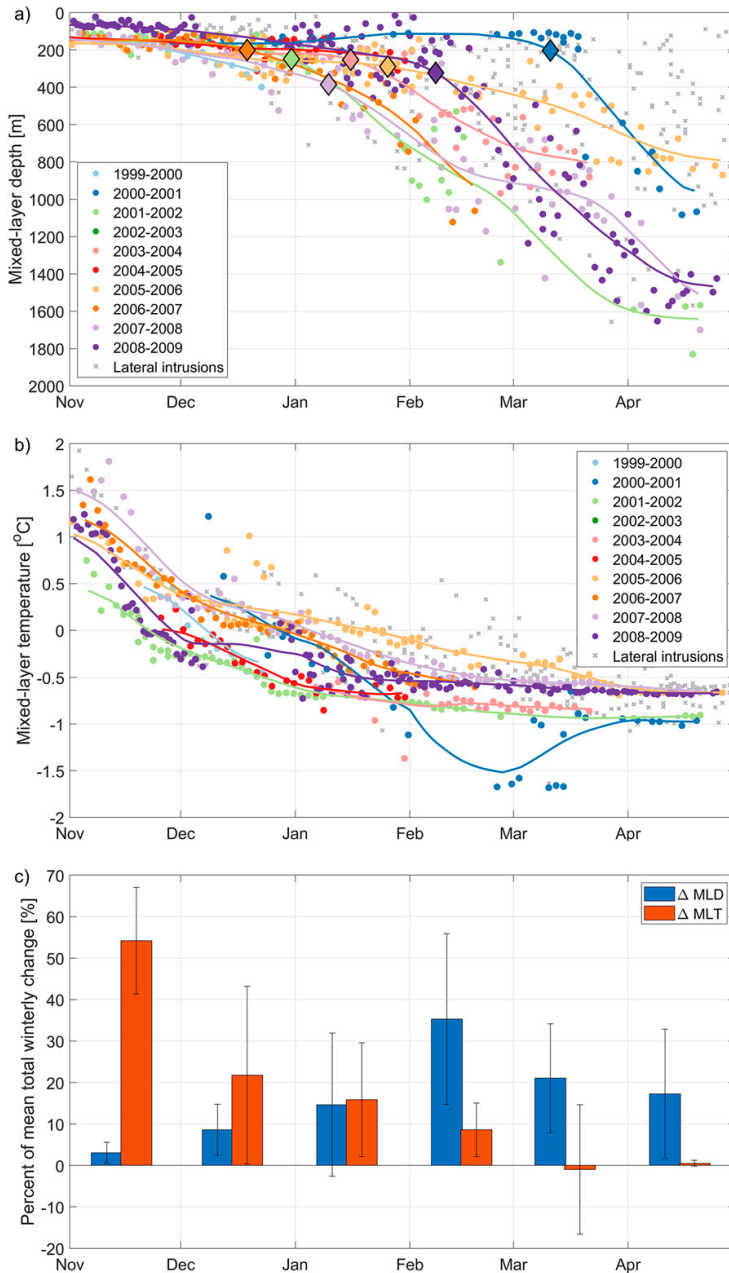


FIG. 6. Wintertime evolution of mixed layer (a) depth and (b) temperature, where each color indicates different winters. The lines are 30-day running means. The gray crosses represent mixed layers that were excluded from the analysis because of lateral intrusions near the surface. The diamonds in (a) indicate the inflection point of the 30-day running mean mixed layer depths (i.e., the transition between the first and the second phases of convection). (c) Mean monthly change in mixed layer depth (MLD) and temperature (MLT), shown as the percentage of the mean (1999–2009) total change from November to April.

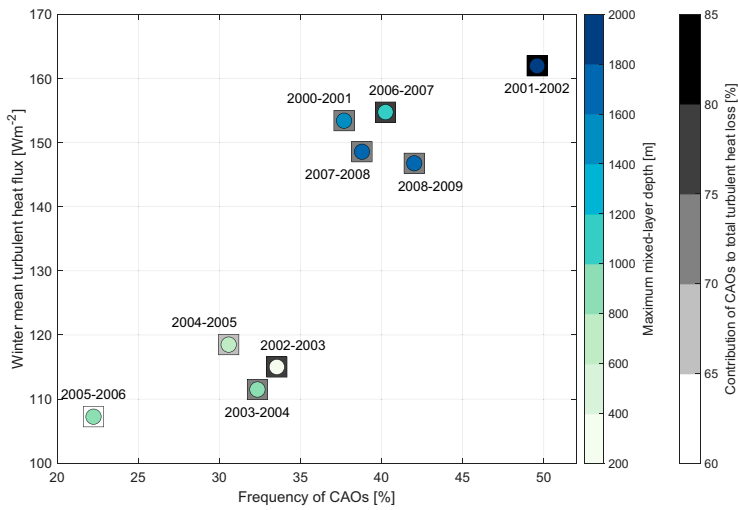


FIG. 7. Winter mean turbulent heat flux plotted as a function of CAO frequency each winter. The maximum convection depth each winter, determined using data from the profiling moorings and from Brakstad et al. (2019), is shown as colored circles, while the contribution of CAOs to the total turbulent heat loss each winter is shown as filled grayscale squares.

constrained the mixed layer to shallower depths than other winters with comparable total heat loss.

Because of sparse temporal data coverage, the direct impact of CAOs on wintertime convection in the Greenland Sea has previously not been quantifiable. Such an analysis is further complicated by the fact that the evolution of the mixed layer through winter is also affected by other factors, such as lateral advection. A recent study from the Iceland Sea investigating the oceanic impact of a single well-observed CAO event, found that the mixed layer response varied spatially depending on the importance of lateral advection (Renfrew et al. 2023). Lateral advection of heat and salt may also vary with time. This implies that the impact of single CAOs on the mixed layer development in the central Greenland Sea may not be representative. However, from our 10-yr moored record with relatively high temporal resolution, a statistical approach yields significant results. The profile-to-profile changes in mixed layer depth and temperature were grouped according to the median value of the CAO index between the profiles (section 2d) and according to the phase they occurred in (Fig. 8). Within each phase and CAO intensity class, outliers that were more than three standard deviations away from the mean were removed.

The impact of a CAO on the mixed layer properties depended on when the event occurred. In the cooling phase, the increase in mixed layer depth was small, even during the strongest CAO events. Regardless of the strength of the CAO, the average deepening rate did not exceed 6 m day^{-1} . In the deepening phase, the rate of increase in mixed layer depth was substantially higher. The deepening also increased with intensifying CAOs, apart from very strong events. Since only three profile-to-profile changes were assigned to very strong CAOs during the deepening phase, this result is not considered statistically

significant. The same analysis was performed using instead the maximum CAO index in the time period between the profiles (not shown). Although the number of data points increased, the mixed layer response was similar to that of strong events. On average, the CAO index exceeded 12 K only 2% of the deepening phase (typically between February and April). The average deepening during strong CAO events was 38 m day^{-1} .

In periods when no CAOs were registered, the mixed layer shoaled. In addition to being cooled by the atmosphere, the water column in the Greenland Sea Gyre is continuously affected by substantial lateral fluxes of heat and salt from surrounding water masses (e.g., Latarius and Quadfasel 2016). The shoaling of the mixed layer indicates that to deepen or maintain the mixed layer, substantial atmospheric forcing is required. During periods characterized by weak atmospheric heat fluxes, lateral fluxes dominate and cause temporary restratification and shoaling mixed layers.

While the greatest changes in mixed layer depth occurred in the deepening phase, the mixed layer temperature cooled comparatively little (Fig. 8b). The average change in mixed layer temperature was -0.02 K day^{-1} during strong events. During the cooling phase, on the other hand, changes in the mixed layer temperature were substantial. For strong and very strong CAOs, the mixed layer cooled by $0.07\text{--}0.08 \text{ K day}^{-1}$ on average (due to large standard errors, these two classes were not significantly different).

To summarize, the strong and very strong CAOs that occurred early in winter primarily cooled the mixed layer until the near-surface stratification was eroded and the second phase of convection commenced. In the second phase, the strong atmospheric cooling during CAOs primarily led to a deepening of the mixed layer, while the temperature remained

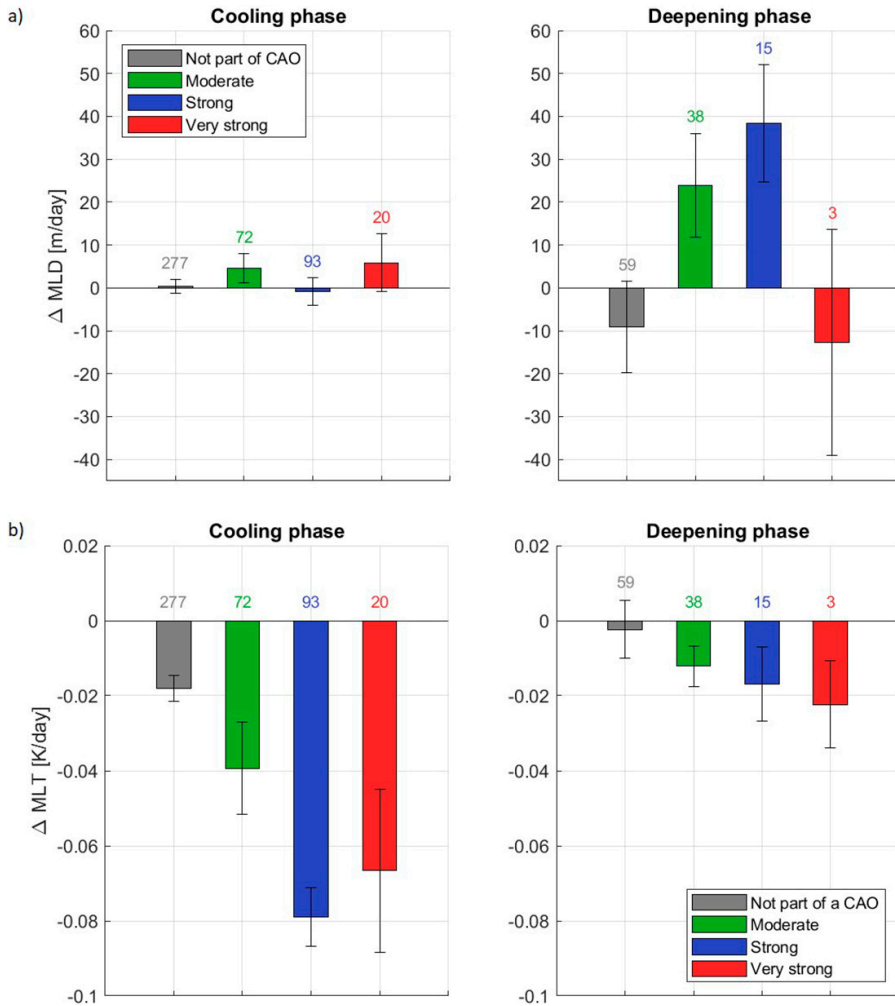


FIG. 8. Daily change in mixed layer (a) depth and (b) temperature calculated from profile-to-profile differences. The changes are grouped by the phase in which they occurred and assigned to a CAO intensity according to the median value of the CAO index in the time period between the profiles (indicated by different colored bars in the figure). The bars mark the average values within each phase and CAO intensity class. The error bars indicate one standard error of the mean, and the number of data points available are written over each bar.

relatively constant. This distinction, in mixed layer response between the two phases, is statistically robust over ten winters.

6. Lateral heat and salt fluxes into the Greenland Sea Gyre

For all CAO-intensity classes, we observed substantial variability in the mixed layer depth and temperature responses as indicated by the large standard errors in Fig. 8. In some cases, the mixed layer shoaled and warmed, even when subject to persistent cooling by the atmosphere. This indicates that

lateral fluxes of heat and salt are also important for the development of the mixed layer. Previous studies have quantified an overall flux of warm and saline water into the Greenland Sea Gyre (Moore et al. 2015; Latarius and Quadfasel 2016; Brakstad et al. 2019), but uncertainties remain regarding the vertical distribution of these fluxes and their origin.

To quantify the lateral heat and salt advection we estimated profile-to-profile differences in temperature and salinity based on the gridded fields shown in Fig. 5. The means over the entire 1999–2009 period were then estimated at each depth level and converted to annual mean rates of change as shown by

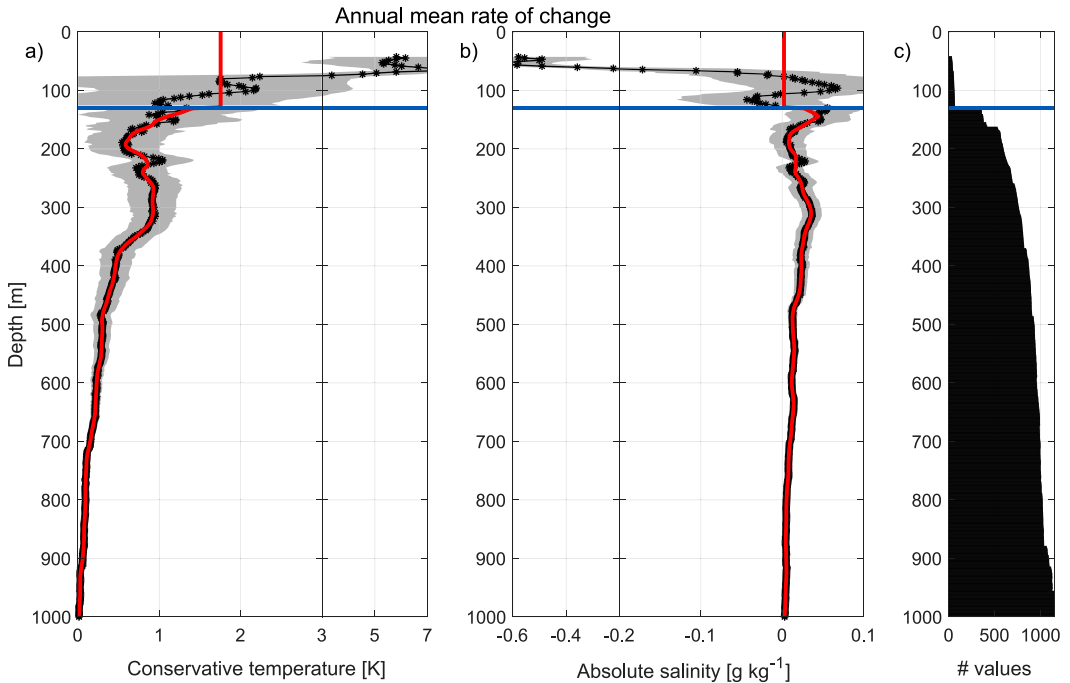


FIG. 9. Annual mean rate of change in (a) temperature and (b) salinity below the surface mixed layer (black profiles). The gray shaded areas indicate one standard error. (c) The number of estimates included in the mean at each depth level. The horizontal blue lines mark 130-m depth. The changes above this depth were estimated based on the shallow profiler only (2008/09) and represent changes observed between May and October since the mixed layer exceeded 130-m depth during winter (November–April). The thick red lines are 30-m running means, and constant from 130 m to the surface (equal to the 70–130-m median values). Note the changing intervals on the x axes.

the black profiles in Fig. 9. All measurements taken within the surface mixed layer were removed to exclude impacts of atmospheric forcing. That is, we assume that any changes in temperature and salinity below the surface mixed layer are caused by lateral advection of heat and salt. The changes above 130 m were estimated based on data from the single deployment of the shallow profiler. These changes are mainly based on summer data (May–October), as the mixed layer depth exceeded 130 m most of the winter.

Atmospheric forcing ignored, the lateral heat flux into the Greenland Sea Gyre (Fig. 9a) would lead to an annual temperature increase of 6 K near the surface, which decreases exponentially toward 0 K at approximately 1000-m depth. Only 4% of the heat added by lateral advection takes place below this depth. In addition to the exponential decrease of the lateral heat fluxes, an intermediate maximum is centered near 300 m. At the same depth level we also observe a maximum in the salt advection (Fig. 9b). The annual change in salinity is generally positive below 130-m depth, while the most prominent signal is the freshening due to inflow of Polar Surface Water in the upper 70 m of the water column.

Relatively warm and saline water is present both east and west of the Greenland Sea Gyre (Fig. 10). The upper part of

the water column in the Norwegian Atlantic Front Current (NAFC) that flows northward along the Mohn Ridge on the eastern side of the gyre contains warm and saline AW. Densified Atlantic-origin water is returned to the south by the EGC on the western side of the gyre and is associated with subsurface maxima in temperature and salinity. Apart from the fresh Polar Surface Water in the west, any lateral exchange between the gyre and its surroundings will lead to an influx of heat and salt into the gyre. Both observations and models indicate that part of the heat and salt in the NAFC crosses the Mohn Ridge into the central Greenland Sea (Spall 2010; Segtnan et al. 2011; Bosse and Fer 2019; Ypma et al. 2020). This could account for the large near-surface heat flux into the gyre, but we do not observe the same surface intensification in salinity (Fig. 9). Instead, the upper part of the gyre is freshened by inflow of Polar Surface Water from the west. The depth of the EGC's subsurface temperature and salinity maxima coincides with the 300-m peaks in annual mean temperature and salinity change within the gyre, suggesting that exchange across the western gyre boundary is the primary source of at least these intermediate maxima. In Fig. 10b, we also see a tongue of saline water reaching the mooring locations from the west.

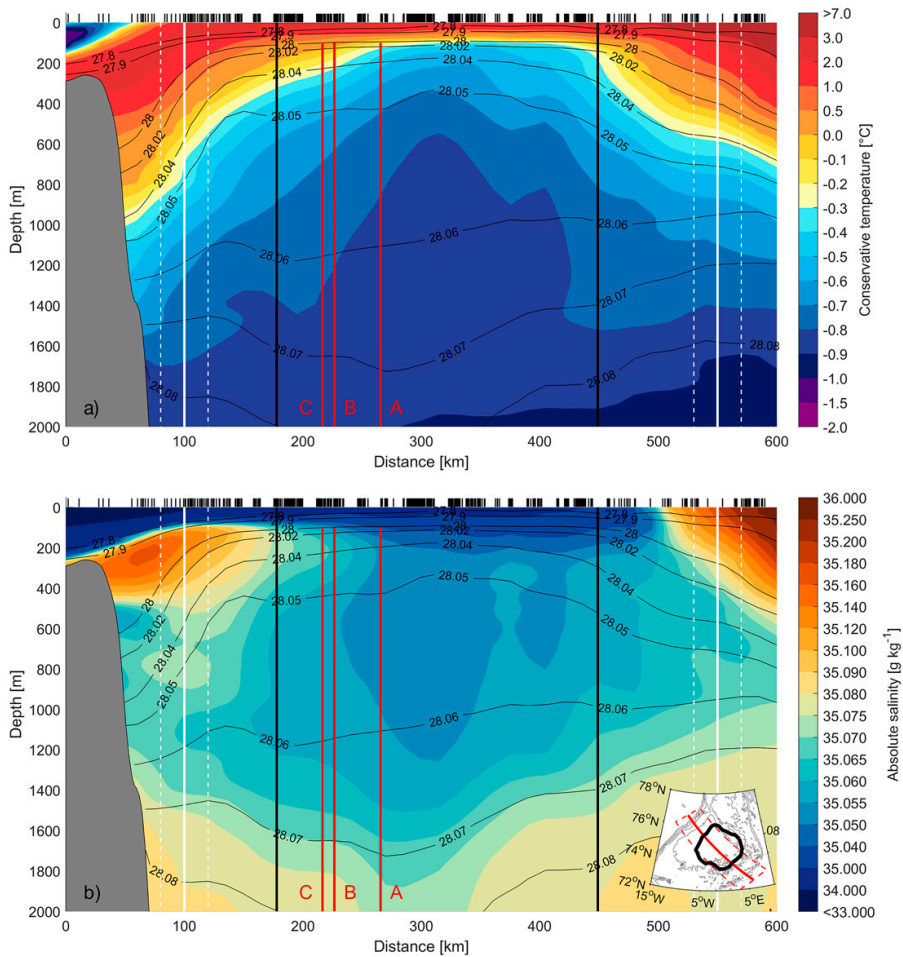


FIG. 10. (a) Temperature and (b) salinity across the Greenland Sea based on shipboard hydrographic measurements and Argo float data from May to October 1999–2012. The black contours indicate potential density. The red solid line in the inserted map in (b) marks the location of the section relative to the gyre (thick black contour). All available observations between the two red dashed lines were included and projected onto the section. The data coverage is indicated by the black bars at the top of each panel, and the x axes show the distance along the section starting from the Greenland shelf. The red vertical lines mark the mooring locations, while the black vertical lines indicate the boundaries of the gyre. Average hydrographic profiles east and west of the gyre were estimated from data within the white dashed lines.

The average temperature and salinity profiles east and west of the Greenland Sea Gyre, as well as the mean hydrography within the gyre, are shown in Fig. 11. The typical density range in the central Greenland Sea between 70- and 500-m depth, where most of the heat and salt are added, is 27.97–28.05 kg m⁻³. In this density range, when comparing the eastern and western profiles along isopycnals, the temperature and salinity are in fact higher to the west in the EGC. If we assume that exchange of heat and salt primarily

occur along isopycnals, we also see that the gyre is warmer and more saline than the eastern profile in the range 28.02–28.05 kg m⁻³. Another indication that the exchange across the western gyre boundary dominates is the steepness of the isopycnals, which determines the stability of the frontal boundaries (Spall 2010). The isopycnal steepness is higher on the western side (Fig. 10), which implies that the front is more unstable, and the potential for exchange of heat and salt may be greater.

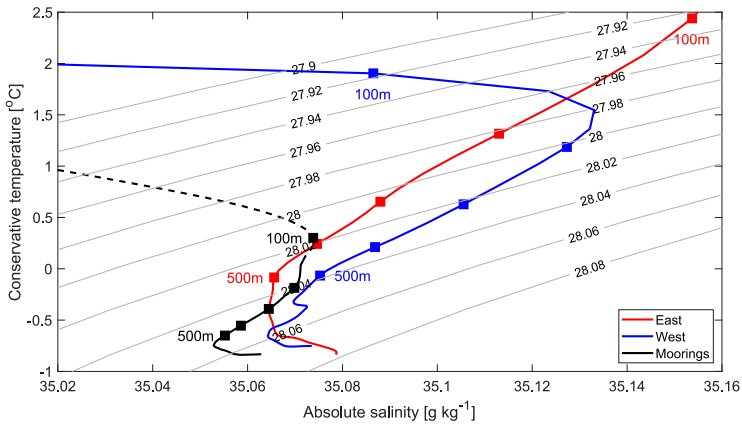


FIG. 11. Average temperature and salinity profiles east (red) and west (blue) of the Greenland Sea Gyre from Fig. 10. The May–October mean temperature and salinity profile within the gyre (black) is based on mooring data between 1999 and 2009. Note that the upper 130 m is from the single deployment of the shallow profiler in 2008–09 (black dashed line). Only data above 1500 m are included in the figure, and every 100-m depth down to 500 m are indicated by colored squares. The gray contours indicate potential density.

7. The impact of lateral advection and the distribution of cold-air outbreaks on the wintertime mixed layer evolution

To determine the impact of lateral advection on the wintertime evolution of the mixed layer, we used the one-dimensional PWP mixed layer model described in section 2e with lateral heat and salt fluxes parameterized. The annual mean rates of temperature and salinity changes (Fig. 9) were converted into rates of changes per model time step of 1 h. These were then added to the simulated temperature and salinity profiles at each time step to represent constant fluxes of heat and salt. No deep convection took place in the simulations with lateral advection parameterized based on the black profiles in Fig. 9 due to the high heat and freshwater fluxes near the surface. The upper 130 m primarily contain summer data, where substantial seasonal variability in lateral advection is expected due to an east–west migration of the Polar Front (Våge et al. 2018; Spall et al. 2021). During fall and winter, the fresh Polar Surface Water is pushed toward the Greenland shelf by westerly Ekman transport induced by strong northerly winds. Hence, we expect a reduced freshwater flux into the central Greenland Sea in winter. To account for this, constant values for rate of change in temperature and salinity (equal to the 70–130-m median values, below the strong freshening signal) were used throughout the upper 130 m as indicated by the red profiles in Fig. 9. The resulting rate of change in depth-integrated heat content corresponds to an influx of 72 W per horizontal square meter, which is approximately 10 W m^{-2} larger than previous gyre-mean estimates (Moore et al. 2015; Latarius and Quadfasel 2016).

For each winter we ran two sets of simulations: one including parameterized lateral heat and salt fluxes and one without lateral advection. Both sets of simulations were initialized using

November hydrographic conditions and forced by ERA5 fluxes from the corresponding winter (section 2e). The simulated development of the mixed layer depth in each run was then compared to observations (i.e., the 30-day running means shown in Fig. 6a). For consistency, we also estimated the 30-day running mean mixed layer depth in each simulation. The mean difference in mixed layer depth between the two sets of simulations and the observations are shown in Fig. 12. The simulations with no lateral advection (the blue dashed line in Fig. 12) always overestimated the mixed layer depth. The seasonal cycle in model error, approaching 800 m in the beginning of March, was due to the timing of the transition between the cooling and deepening phases, which occurred earlier in the model than in the observations. The resulting end-of-winter mixed layer depth was overestimated by 300 m on average when lateral advection was not accounted for. The simulations including advection of heat and salt (the red dashed line in Fig. 12) also overestimated the mixed layer depth, but to a much lesser extent. The deeper mixed layers were mainly caused by an earlier onset of deep convection in the model, which could be explained by the lack of seasonality in the parameterized lateral fluxes. In the mean, the simulated end-of-winter mixed layer depth was underestimated by slightly less than 100 m. Comparing the two sets of simulations, we see that lateral fluxes (of heat, in particular) act to reduce the mixed layer depth in the central Greenland Sea by approximately 400 m on average. That is, the idealized simulations indicate that lateral fluxes are important for the development of the mixed layer in the central Greenland Sea.

The PWP model was also used to investigate the impact of the distribution of CAOs. Three idealized time series of turbulent heat fluxes were created as described in section 2e (Fig. 4), while the remaining atmospheric forcing was kept constant, equal to the winter mean values over the entire 1999–2009

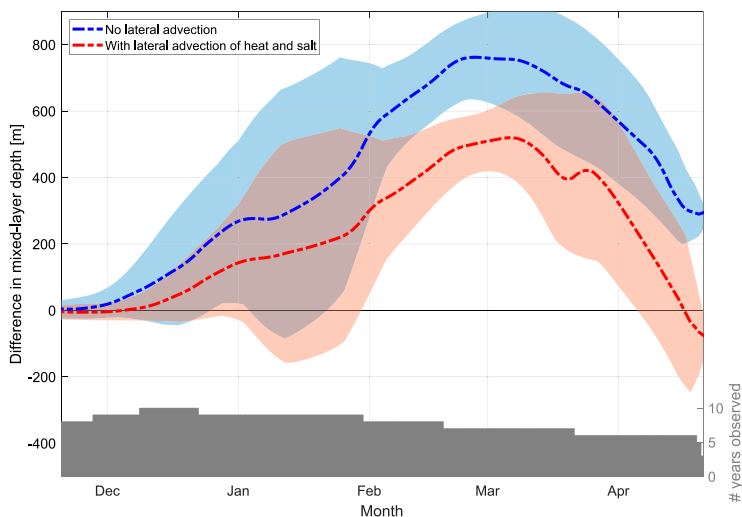


FIG. 12. Simulated minus observed mixed layer depth (30-day running means). The blue dashed line indicates the mean difference for simulations without lateral advection, while the red dashed line is the difference with both heat and salt advection included. The shading, indicating one standard error, represents the variability between the different winters. The gray bars at the bottom of the figure mark the number of years with observations that are compared to the simulations.

period. The turbulent heat flux was either constructed from 1) very strong CAOs concentrated early in the winter, 2) very strong CAOs concentrated late in winter, or 3) strong CAOs evenly distributed over the winter. The integrated turbulent heat losses over the entire winter (November–April) were equal in all three cases, to isolate the effect of the temporal distribution. Simulations were then performed for each winter and set of idealized atmospheric forcing time series, with and without lateral advection.

The simulations suggest that changes in the temporal distribution of CAOs only slightly modify the maximum mixed layer depth and hydrographic properties (Figs. 13a–c). Focusing on the maximum mixed layer depth, we see that very strong CAOs late in winter tend to result in deeper convection than when the events occurred early in winter. However, the difference is only on the order of 100 m. More important are the integrated heat loss over the winter and oceanic lateral advection. The initial hydrographic conditions are also important as indicated by the relatively large winter-to-winter variability (Fig. 13a). The onset of the deepening phase, on the other hand, is greatly influenced by the CAO distribution (Fig. 13d). As expected, more heat loss early in winter leads to an earlier onset of the deepening phase, while the inclusion of lateral advection tends to delay the onset of deep convection.

8. Summary and conclusions

We used a 10-yr (1999–2009) hydrographic record from moored profilers to examine dense-water formation in the Greenland Sea Gyre, with particular focus on the impact of CAOs and lateral fluxes of heat and salt. Although the

moorings were located in the western part of the gyre, the long-term evolution of the mixed layer depth and hydrographic properties were representative for the entire gyre. Consistent with Lauvset et al. (2018) and Brakstad et al. (2019), we observed a general warming and salinification of the entire water column. Intermediate (500–1500 m) convection was observed regularly, and water sufficiently dense ($\sigma_\theta = 28.05 \text{ kg m}^{-3}$) to supply the densest component of the overflow waters was produced every winter (Huang et al. 2020).

In agreement with Papritz and Spengler (2017), we found that between 60% and 80% of the heat lost to the atmosphere during winter occurs during CAOs. Winters with a high frequency of CAOs had the largest winter mean turbulent heat flux and the deepest end-of-winter mixed layer, apart from winter 2006/07 when the intermediate stratification was particularly strong. Our results suggest that the mixed layer development during winter can be divided into two phases: a cooling phase and a deepening phase. The oceanic response to CAOs is highly dependent on which phase the events occur in. Early in winter, the CAOs primarily cooled the mixed layer, while the mixed layer depth remained nearly constant. The magnitude of the cooling depended on the intensity of the events, with the largest cooling ($0.07\text{--}0.08 \text{ K day}^{-1}$) taking place during strong and very strong CAOs. Later in winter, typically between February and April, CAOs mainly deepened the mixed layer. The greatest rate of deepening (up to 38 m day^{-1}) occurred during strong CAOs. Very strong CAOs (with CAO indices above 12 K) rarely occurred in the deepening phase during the 1999–2009 period. It was therefore not possible to obtain statistically meaningful numbers for these events during the deepening phase. The end-of-winter mixed layer depth and hydrographic

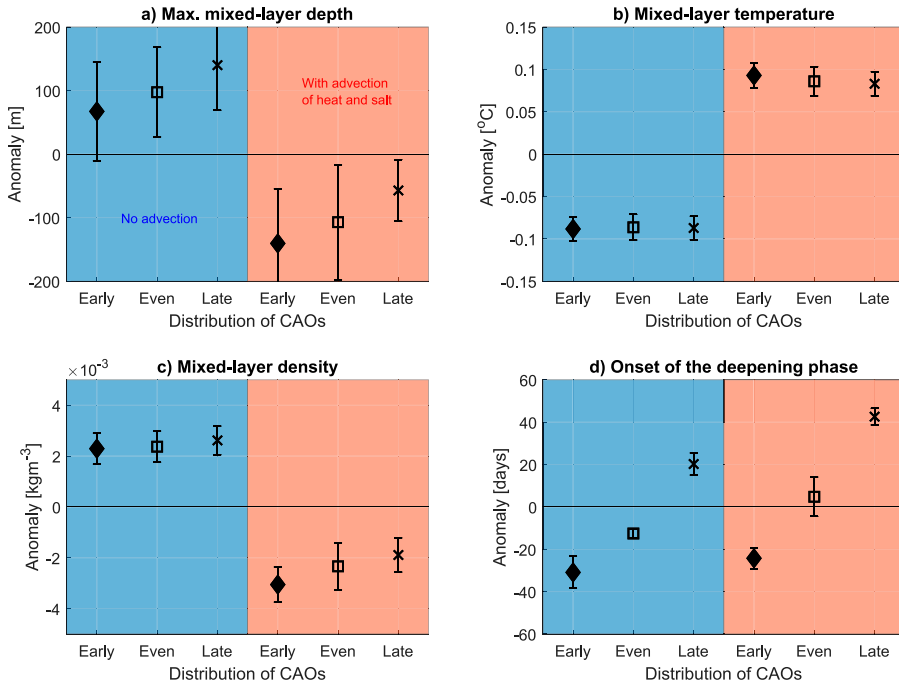


FIG. 13. Anomalies in simulated (a) maximum mixed layer depth, (b) temperature, (c) density, and (d) the onset of the deepening phase, relative to the mean of all simulations each winter. The temporal distribution of CAOs in each simulation is indicated on the x axes, while the background color shows whether lateral advection was included (red) or not (blue). The standard deviations indicate winter-to-winter variability due to different initial hydrographic conditions.

properties are dependent on the integrated heat loss over the winter, but idealized numerical simulations suggest that they are not sensitive to changes in the temporal distribution. The onset of the deepening phase, on the other hand, largely follows the temporal distribution of CAOs: more CAOs early in winter results in an earlier onset of the deepening phase.

A shortcoming of the moored measurements, when considering the atmospheric impact on the mixed layer, is that the profilers did not reach the surface (only to around 100 m depth). The final year of the deployment (2008–09) was an exception. Then a separate moored profiler to sample the upper 130 m of the water column was deployed in addition to the deep profilers. For the remaining years we have only considered the months when the mixed layer exceeded 100-m depth (typically between November and April). When the upper part of the moorings measured a homogeneous layer, we assumed that it was in direct contact with the atmosphere. However, we observed shorter periods of increased temperature near the top of the moorings, even though the atmospheric re-analysis product indicated ocean-to-atmosphere heat loss. Profiles containing such warm-water intrusions were excluded from the statistical analyses, but undetected intrusions above 100-m depth likely occurred. This could account for some of the observed variability in the mixed layer response to CAOs.

The considerable variability in the mixed layer response to CAOs is also in part due to the influx of heat and salt from surrounding water masses. We considered temporal changes in temperature and salinity below the mixed layer to quantify the magnitude and vertical distributions of these fluxes. Our estimated annual mean depth-integrated lateral heat flux of 72 W m^{-2} is comparable to, but approximately 10 W m^{-2} higher than, previous estimates (Moore et al. 2015; Latarius and Quadfasel 2016). This could stem from a lack of wintertime data in our estimate since we excluded measurements taken within the mixed layer, or because we only have one year of near-surface measurements. Unlike Moore et al. (2015) and Latarius and Quadfasel (2016), we included depths below 1500 m in our estimate. However, this is not a main reason for the discrepancy, as less than 4% of the heat added by lateral advection occurs below this depth.

While the largest lateral heat fluxes occur near the surface, we also identified a subsurface maximum near 300-m depth. This maximum corresponds to the depth of the Atlantic-origin water in the East Greenland Current (Håvik et al. 2017), suggesting that it primarily originates from exchange across the western boundary of the gyre. The density structure across the Greenland Sea, based on shipboard hydrographic measurements and Argo float data, also indicate that the western front is more unstable

than the front associated with the Norwegian Atlantic Front Current over the Mohn Ridge. However, the magnitudes of the relative contributions from the regions surrounding the Greenland Sea Gyre remain unknown. Dedicated velocity and turbulence measurements are needed to investigate this further.

The magnitude and vertical distribution of lateral heat and salt fluxes were used in an idealized mixed layer model to determine the impact of lateral advection on the wintertime mixed layer development. The two fluxes have competing effects on the density and depth of the mixed layer. While the lateral heat flux restratifies the water column (leading to a shallower mixed layer), the salt flux preconditions the water column for deeper convection. The combined effect is a reduction in the end-of-winter mixed layer depth by approximately 400 m in the mean relative to simulations without lateral fluxes. Apart from the inflow of fresh Polar Surface Water, the salt flux is positive over the rest of the water column. [Lauvset et al. \(2018\)](#) and [Brakstad et al. \(2019\)](#) found that increased salt advection since the mid-1990s has led to increased mixed layer depths and sustained the formation of GSAIW, even though the atmospheric heat fluxes declined ([Moore et al. 2015](#)). The trend in AW salinity has recently reversed ([Mork et al. 2019](#)), and convection in the Greenland Sea could become increasingly vulnerable to changes in the atmospheric forcing.

The hydrographic measurements from the moored profilers provide a unique dataset, both in terms of high temporal resolution and the long duration, which are both necessary to quantify the direct impact of CAOs on the wintertime mixed layer. This study provides a first demonstration that winter-to-winter variability in CAO frequency has a profound impact on the ocean mixed layer and on dense-water formation in the Greenland Sea. Through a well-established link between variability in seasonal CAO frequency and the frequency of extratropical cyclones ([Fletcher et al. 2016](#); [Papritz and Grams 2018](#)), our results provide an avenue for understanding how seasonal variability in the configuration of the North Atlantic storm track feeds back on dense-water formation in the central Greenland Sea. Our analysis also highlights the importance of the interplay between atmospheric forcing and oceanic lateral advection for the Greenland Sea mixed layer development.

Acknowledgments. This work was funded by the Trond Mohn Foundation under Grant Agreement BFS2016REK01 (KS, AB, and KV), the Bjerknes Centre for Climate Research (KS), the Office of Naval Research Global (Award N62909-22-1-2023, AB and KV), and the Helmholtz Infrastructure Initiative FRAM (WJvA). The authors would also like to thank Dr. Gereon Budéus (Alfred Wegener Institute for Polar and Marine Research) for providing post processed data and for help with the technical description. The mooring time series were funded by the IPY-legacy project LOTEVA-GS.

Data availability statement. The hydrographic data from the moored autonomous profilers, obtained by the Alfred Wegener Institute, are available at <https://doi.pangaea.de/10.1594/PANGAEA.9111001> ([Budéus et al. 2020](#)). The hydrographic

dataset from [Brakstad et al. \(2023\)](#) consists of observations from several archives that can be accessed as listed in their Table 1. The combined hydrographic dataset is available at the Norwegian Marine Data Centre (<https://doi.org/10.21335/NMDC-1271328906>). The ERA5 reanalysis can be downloaded from the Copernicus Climate Service (<https://climate.copernicus.eu/climate-reanalysis>).

REFERENCES

- Aagaard, K., J. H. Swift, and E. C. Carmack, 1985: Thermohaline circulation in the Arctic Mediterranean Seas. *J. Geophys. Res.*, **90**, 4833–4846, <https://doi.org/10.1029/JC090iC03p04833>.
- Behrendt, A., H. Sumata, B. Rabe, and U. Schauer, 2018: UDASH - Unified Database for Arctic and Subarctic Hydrography. *Earth Syst. Sci. Data*, **10**, 1119–1138, <https://doi.org/10.5194/essd-10-1119-2018>.
- Bosse, A., and I. Fer, 2019: Mean structure and seasonality of the Norwegian Atlantic Front current along the Mohn Ridge from repeated glider transects. *Geophys. Res. Lett.*, **46**, 13 170–13 179, <https://doi.org/10.1029/2019GL084723>.
- Bracegirdle, T. J., and S. L. Gray, 2008: An objective climatology of the dynamical forcing of polar lows in the Nordic seas. *Int. J. Climatol.*, **28**, 1903–1919, <https://doi.org/10.1002/joc.1686>.
- Brakstad, A., K. Våge, L. Håvik, and G. W. K. Moore, 2019: Water mass transformation in the Greenland Sea during the period 1986–2016. *J. Phys. Oceanogr.*, **49**, 121–140, <https://doi.org/10.1175/JPO-D-17-0273.1>.
- , G. Gebbie, K. Våge, E. Jeansson, and S. R. Ólafsdóttir, 2023: Formation and pathways of dense water in the Nordic seas based on a regional inversion. *Prog. Oceanogr.*, **212**, 102981, <https://doi.org/10.1016/j.pocan.2023.102981>.
- Budéus, G., 2009: Autonomous daily CTD profiles between 3,700 meters and the ocean surface. *Sea Technol.*, **10**, 45–48.
- , W. Schneider, and G. Krause, 1998: Winter convective events and bottom water warming in the Greenland Sea. *J. Geophys. Res.*, **103**, 18 513–18 527, <https://doi.org/10.1029/98JC01563>.
- , K. Ohm, M. Damm, and R. Plügge, 2005: The externally powered, compressibility compensated Jojo mooring: A mechanical solution to autonomous deep sea profiling. *Deep-Sea Res. I*, **52**, 1964–1973, <https://doi.org/10.1016/j.dsr.2005.05.005>.
- , A. Brakstad, K. Svingen, K. Våge, and W.-J. von Appen, 2020: Physical oceanography data from moorings J008-J034 and JP31/JP34 in the Greenland Sea, 1999–2009. PANGAEA, <https://doi.org/10.1594/PANGAEA.910907>.
- Chafik, L., and T. Rossby, 2019: Volume, heat, and freshwater divergences in the subpolar North Atlantic suggest the Nordic seas as key to the state of the meridional overturning circulation. *Geophys. Res. Lett.*, **46**, 4799–4808, <https://doi.org/10.1029/2019GL082110>.
- , H. Hátún, J. Kjellsson, K. M. H. Larsen, T. Rossby, and B. Berx, 2020: Discovery of an unrecognized pathway carrying overflow waters toward the Faroe Bank Channel. *Nat. Commun.*, **11**, 3721, <https://doi.org/10.1038/s41467-020-17426-8>.
- Dahlke, S., A. Solbès, and M. Maturilli, 2022: Cold air outbreaks in Fram Strait: Climatology, trends, and observations during an extreme season in 2020. *J. Geophys. Res. Atmos.*, **127**, e2021JD035741, <https://doi.org/10.1029/2021JD035741>.
- Eldevik, T., J. E. Ø. Nilsen, D. Iovino, K. A. Olsson, A. B. Sandø, and H. Drange, 2009: Observed sources and variability of Nordic seas overflow. *Nat. Geosci.*, **2**, 406–410, <https://doi.org/10.1038/ngeo518>.

- Fletcher, J., S. Mason, and C. Jakob, 2016: The climatology, meteorology, and boundary layer structure of marine cold air out-breaks in both hemispheres. *J. Climate*, **29**, 1999–2014, <https://doi.org/10.1175/JCLI-D-15-0268.1>.
- Harden, B. E., and Coauthors, 2016: Upstream sources of the Denmark Strait overflow: Observations from a high-resolution mooring array. *Deep-Sea Res. I*, **112**, 94–112, <https://doi.org/10.1016/j.dsr.2016.02.007>.
- Håvik, L., R. S. Pickart, K. Våge, D. J. Torres, A. M. Thurnherr, A. Beszczynska-Möller, W. Walczowski, and W.-J. von Appen, 2017: Evolution of the East Greenland current from Fram Strait to Denmark Strait: Synoptic measurements from summer 2012. *J. Geophys. Res. Oceans*, **122**, 1974–1994, <https://doi.org/10.1002/2016JC002228>.
- , M. Almansí, K. Våge, and T. W. N. Haine, 2019: Atlantic-origin overflow water in the East Greenland current. *J. Phys. Oceanogr.*, **49**, 2255–2269, <https://doi.org/10.1175/JPO-D-18-0216.1>.
- Helland-Hansen, B., and F. Nansen, 1909: The Norwegian Sea: Its physical oceanography based upon the Norwegian researches, 1900–1904. Norwegian Fishery and Marine Investigations Rep., Vol. 2, 390 pp., <https://hdl.handle.net/11250/114874>.
- Hersbach, H., and Coauthors, 2020: The ERA5 global reanalysis. *Quart. J. Roy. Meteor. Soc.*, **146**, 1999–2049, <https://doi.org/10.1002/qj.3803>.
- Holliday, N. P., and Coauthors, 2008: Reversal of the 1960s to 1990s freshening trend in the northeast North Atlantic and Nordic seas. *Geophys. Res. Lett.*, **35**, L03614, <https://doi.org/10.1029/2007GL032675>.
- Huang, J., R. S. Pickart, R. X. Huang, P. Lin, A. Brakstad, and F. Xu, 2020: Sources and upstream pathways of the densest overflow water in the Nordic seas. *Nat. Commun.*, **11**, 5389, <https://doi.org/10.1038/s41467-020-19050-y>.
- IOC, SCOR, and IAPSO, 2010: The international thermodynamic equation of seawater 2010: Calculation and use of thermodynamic properties. Intergovernmental Oceanographic Commission, Manuals and Guides No. 56, UNESCO, 218 pp., https://www.teos-10.org/pubs/TEOS-10_Manual.pdf.
- Jeansson, E., S. Jutterström, B. Rudels, L. G. Anderson, K. Anders Olsson, E. P. Jones, W. M. Smethie, and J. H. Swift, 2008: Sources to the East Greenland current and its contribution to the Denmark Strait overflow. *Prog. Oceanogr.*, **78**, 12–28, <https://doi.org/10.1016/j.pocean.2007.08.031>.
- , A. Olsen, and S. Jutterström, 2017: Arctic intermediate water in the Nordic seas, 1991–2009. *Deep-Sea Res. I*, **128**, 82–97, <https://doi.org/10.1016/j.dsr.2017.08.013>.
- Karstensen, J., P. Schlosser, D. W. Wallace, J. L. Bullister, and J. Blindheim, 2005: Water mass transformation in the Greenland Sea during the 1990s. *J. Geophys. Res.*, **110**, C07022, <https://doi.org/10.1029/2004JC002510>.
- Kolstad, E. W., 2011: A global climatology of favourable conditions for polar lows. *Quart. J. Roy. Meteor. Soc.*, **137**, 1749–1761, <https://doi.org/10.1002/qj.888>.
- Latarius, K., and D. Quadfasel, 2010: Seasonal to inter-annual variability of temperature and salinity in the Greenland Sea Gyre: Heat and freshwater budgets. *Tellus*, **62A**, 497–515, <https://doi.org/10.1111/j.1600-0870.2010.00453.x>.
- , and —, 2016: Water mass transformation in the deep basins of the Nordic seas: Analyses of heat and freshwater budgets. *Deep-Sea Res. I*, **114**, 23–42, <https://doi.org/10.1016/j.dsr.2016.04.012>.
- Lauvset, S. K., A. Brakstad, K. Våge, A. Olsen, E. Jeansson, and K. A. Mork, 2018: Continued warming, salinification and oxygenation of the Greenland Sea gyre. *Tellus*, **70A**, 1–9, <https://doi.org/10.1080/16000870.2018.1476434>.
- Lorbacher, K., D. Dommenges, P. P. Niiler, and A. Köhl, 2006: Ocean mixed layer depth: A subsurface proxy of ocean-atmosphere variability. *J. Geophys. Res.*, **111**, C07010, <https://doi.org/10.1029/2003JC002157>.
- Lozier, M. S., and Coauthors, 2019: A sea change in our view of overturning in the subpolar North Atlantic. *Science*, **363**, 516–521, <https://doi.org/10.1126/science.aau6592>.
- Malmberg, S. A., 1983: Hydrographic investigations in the Iceland and Greenland Seas in late winter 1971. *Jokull*, **33**, 133–140.
- Marshall, J., and F. Schott, 1999: Open-ocean convection: Observations, theory and models. *Rev. Geophys.*, **37**, 1–64, <https://doi.org/10.1029/98RG02739>.
- Mauritzen, C., 1996: Production of dense overflow waters feeding the North Atlantic across the Greenland-Scotland Ridge. Part 1: Evidence for a revised circulation scheme. *Deep-Sea Res. I*, **43**, 769–806, [https://doi.org/10.1016/0967-0637\(96\)00037-4](https://doi.org/10.1016/0967-0637(96)00037-4).
- Meincke, J., and Coauthors, 1990: Greenland Sea Project: A venture toward improved understanding of the oceans' role in climate. *Eos, Trans. Amer. Geophys. Union*, **71**, 750–756, <https://doi.org/10.1029/90EO00208>.
- , S. Jónsson, and J. H. Swift, 1992: Variability of convective conditions in the Greenland Sea. *ICES Mar. Sci. Symp.*, **195**, 32–39.
- , B. Rudels, and H. J. Friedrich, 1997: The Arctic Ocean-Nordic seas thermohaline system. *ICES J. Mar. Sci.*, **54**, 283–299, <https://doi.org/10.1006/jmsc.1997.0229>.
- Moore, G. W. K., K. Våge, R. S. Pickart, and I. A. Renfrew, 2015: Decreasing intensity of open-ocean convection in the Greenland and Iceland Seas. *Nat. Climate Change*, **5**, 877–882, <https://doi.org/10.1038/nclimate2688>.
- , I. A. Renfrew, and R. S. Pickart, 2022: Sea-ice retreat suggests re-organization of water mass transformation in the Nordic and Barents Seas. *Nat. Commun.*, **13**, 67, <https://doi.org/10.1038/s41467-021-27641-6>.
- Mork, K. A., Ø. Skagseth, and H. Sjøland, 2019: Recent warming and freshening of the Norwegian Sea observed by Argo data. *J. Climate*, **32**, 3695–3705, <https://doi.org/10.1175/JCLI-D-18-0591.1>.
- Nilsen, J. E. Ø., and E. Falck, 2006: Variations of mixed layer properties in the Norwegian Sea for the period 1948–1999. *Prog. Oceanogr.*, **70**, 58–90, <https://doi.org/10.1016/j.pocean.2006.03.014>.
- Østerhus, S., and T. Gammelsrød, 1999: The abyss of the Nordic seas is warming. *J. Climate*, **12**, 3297–3304, [https://doi.org/10.1175/1520-0442\(1999\)012<3297:TAOTNS>2.0.CO;2](https://doi.org/10.1175/1520-0442(1999)012<3297:TAOTNS>2.0.CO;2).
- , and Coauthors, 2019: Arctic Mediterranean exchanges: A consistent volume budget and trends in transports from two decades of observations. *Ocean Sci.*, **15**, 379–399, <https://doi.org/10.5194/os-15-379-2019>.
- Papritz, L., and T. Spengler, 2017: A Lagrangian climatology of wintertime cold air outbreaks in the Irminger and Nordic seas and their role in shaping air-sea heat fluxes. *J. Climate*, **30**, 2717–2737, <https://doi.org/10.1175/JCLI-D-16-0605.1>.
- , and C. M. Grams, 2018: Linking low-frequency large-scale circulation patterns to cold air outbreak formation in the north-eastern North Atlantic. *Geophys. Res. Lett.*, **45**, 2542–2553, <https://doi.org/10.1002/2017GL076921>.
- , S. Pfahl, H. Sodemann, and H. Wernli, 2015: A climatology of cold air outbreaks and their impact on air-sea heat fluxes in the high-latitude South Pacific. *J. Climate*, **28**, 342–364, <https://doi.org/10.1175/JCLI-D-14-00482.1>.

- Pawlowicz, R., 1995: A note on seasonal cycles of temperature and salinity in the upper waters of the Greenland Sea Gyre from historical data. *J. Geophys. Res.*, **100**, 4715–4726, <https://doi.org/10.1029/94JC02014>.
- Petit, T., M. S. Lozier, S. A. Josey, and S. A. Cunningham, 2020: Atlantic deep water formation occurs primarily in the Iceland Basin and Irminger Sea by local buoyancy forcing. *Geophys. Res. Lett.*, **47**, e2020GL091028, <https://doi.org/10.1029/2020GL091028>.
- Pickart, R. S., D. J. Torres, and R. A. Clarke, 2002: Hydrography of the Labrador Sea during active convection. *J. Phys. Oceanogr.*, **32**, 428–457, [https://doi.org/10.1175/1520-0485\(2002\)032<0428:HOTLSD>2.0.CO;2](https://doi.org/10.1175/1520-0485(2002)032<0428:HOTLSD>2.0.CO;2).
- Price, J. F., R. A. Weller, and R. Pinkel, 1986: Diurnal cycling: Observations and models of the upper ocean response to diurnal heating, cooling, and wind mixing. *J. Geophys. Res.*, **91**, 8411–8427, <https://doi.org/10.1029/JC091iC07p08411>.
- Renfrew, I. A., and Coauthors, 2023: Coupled atmosphere-ocean observations of a cold air outbreak and its impact on the Iceland Sea. *Quart. J. Roy. Meteor. Soc.*, **149**, 472–493, <https://doi.org/10.1002/qj.4418>.
- Ronski, S., and G. Budéus, 2005: Time series of winter convection in the Greenland Sea. *J. Geophys. Res.*, **110**, C04015, <https://doi.org/10.1029/2004JC002318>.
- Segtnan, O. H., T. Furevik, and A. D. Jenkins, 2011: Heat and freshwater budgets of the Nordic seas computed from atmospheric reanalysis and ocean observations. *J. Geophys. Res.*, **116**, C11003, <https://doi.org/10.1029/2011JC006939>.
- Semper, S., K. Våge, R. S. Pickart, H. Valdimarsson, D. J. Torres, and S. Jónsson, 2019: The emergence of the North Icelandic Jet and its evolution from northeast Iceland to Denmark Strait. *J. Phys. Oceanogr.*, **49**, 2499–2521, <https://doi.org/10.1175/JPO-D-19-0088.1>.
- , R. S. Pickart, K. Våge, K. M. H. Larsen, B. Hansen, and H. Hátún, 2020: The Iceland-Faroe slope jet: A conduit for dense water toward the Faroe Bank Channel overflow. *Nat. Commun.*, **11** 5390, <https://doi.org/10.1038/s41467-020-19049-5>.
- Somavilla, R., 2019: Draining and upwelling of Greenland Sea deep waters. *J. Geophys. Res. Oceans*, **124**, 2842–2860, <https://doi.org/10.1029/2018JC014249>.
- , U. Schauer, and G. Budéus, 2013: Increasing amount of Arctic Ocean deep waters in the Greenland Sea. *Geophys. Res. Lett.*, **40**, 4361–4366, <https://doi.org/10.1002/grl.50775>.
- Spall, M. A., 2010: Non-local topographic influences on deep convection: An idealized model for the Nordic seas. *Ocean Modell.*, **32**, 72–85, <https://doi.org/10.1016/j.ocemod.2009.10.009>.
- , M. Almansi, J. Huang, T. W. Haine, and R. S. Pickart, 2021: Lateral redistribution of heat and salt in the Nordic seas. *Prog. Oceanogr.*, **196**, 102609, <https://doi.org/10.1016/j.pcean.2021.102609>.
- Strass, V. H., E. Fahrbach, U. Schauer, and L. Sellmann, 1993: Formation of Denmark Strait overflow water by mixing in the East Greenland current. *J. Geophys. Res.*, **98**, 6907–6919, <https://doi.org/10.1029/92JC02732>.
- Terpstra, A., I. A. Renfrew, and D. E. Sergeev, 2021: Characteristics of cold-air outbreak events and associated polar meso-scale cyclogenesis over the North Atlantic region. *J. Climate*, **34**, 4567–4584, <https://doi.org/10.1175/JCLI-D-20-0595.1>.
- Tsubouchi, T., K. Våge, B. Hansen, K. M. H. Larsen, S. Østerhus, C. Johnson, S. Jónsson, and H. Valdimarsson, 2021: Increased ocean heat transport into the Nordic seas and Arctic Ocean over the period 1993–2016. *Nat. Climate Change*, **11**, 21–26, <https://doi.org/10.1038/s41558-020-00941-3>.
- Våge, K., R. S. Pickart, M. A. Spall, H. Valdimarsson, S. Jónsson, D. J. Torres, S. Østerhus, and T. Eldevik, 2011: Significant role of the North Icelandic Jet in the formation of Denmark Strait overflow water. *Nat. Geosci.*, **4**, 723–727, <https://doi.org/10.1038/ngeo1234>.
- , —, —, G. W. K. Moore, H. Valdimarsson, D. J. Torres, S. Y. Erofeeva, and J. E. Ø. Nilsen, 2013: Revised circulation scheme north of the Denmark Strait. *Deep-Sea Res. I*, **79**, 20–39, <https://doi.org/10.1016/j.dsr.2013.05.007>.
- , G. W. Moore, S. Jónsson, and H. Valdimarsson, 2015: Water mass transformation in the Iceland Sea. *Deep-Sea Res. I*, **101**, 98–109, <https://doi.org/10.1016/j.dsr.2015.04.001>.
- , L. Papritz, L. Håvik, M. A. Spall, and G. W. K. Moore, 2018: Ocean convection linked to the recent ice edge retreat along East Greenland. *Nat. Commun.*, **9**, 1287, <https://doi.org/10.1038/s41467-018-03468-6>.
- , S. Semper, H. Valdimarsson, S. Jónsson, R. S. Pickart, and G. W. K. Moore, 2022: Water mass transformation in the Iceland Sea: Contrasting two winters separated by four decades. *Deep-Sea Res. I*, **186**, 103824, <https://doi.org/10.1016/j.dsr.2022.103824>.
- Visbeck, M., J. Fischer, and F. Schott, 1995: Preconditioning the Greenland Sea for deep convection: Ice formation and ice drift. *J. Geophys. Res.*, **100**, 18489–18502, <https://doi.org/10.1029/95JC01611>.
- Ypma, S. L., S. Georgiou, J. S. Dugstad, J. D. Pietrzak, and C. A. Katsman, 2020: Pathways and water mass transformation along and across the Mohn-Knipovich ridge in the Nordic seas. *J. Geophys. Res. Oceans*, **125**, e2020JC016075, <https://doi.org/10.1029/2020JC016075>.

Paper III

Formation and pathways of dense water in the Nordic Seas based on a regional inversion

Brakstad, A., G. Gebbie, K. Våge, E. Jeansson, and S. R. Ólafsdóttir
Progress in Oceanography, **212** (2023)



Contents lists available at ScienceDirect

Progress in Oceanography

journal homepage: www.elsevier.com/locate/pocean

Formation and pathways of dense water in the Nordic Seas based on a regional inversion

Ailin Brakstad^{a,b,*}, Geoffrey Gebbie^c, Kjetil Våge^{a,b}, Emil Jeansson^{d,b}, Sólveig Rósa Ólafsdóttir^e

^a Geophysical Institute, University of Bergen, Norway

^b Bjerknes Centre for Climate Research, Bergen, Norway

^c Woods Hole Oceanographic Institution, Woods Hole, USA

^d NORCE Norwegian Research Centre, Bergen, Norway

^e Marine and Freshwater Research Institute, Reykjavík, Iceland

ARTICLE INFO

Dataset link: <https://doi.org/10.21335/NMDC-1271328906>, <http://marine.copernicus.eu>

Keywords:

Nordic Seas
Overturning
Dense-water formation
Water masses
Observations

ABSTRACT

Dense waters formed in the Nordic Seas spill across gaps in the Greenland-Scotland Ridge into the abyss of the North Atlantic to feed the lower limb of the Atlantic Meridional Overturning Circulation. The overflow water transport is well known, but open questions remain regarding where and how the dense overflow waters are formed and transported to the ridge. Here we develop a regional high-resolution version of an inverse method called Total Matrix Intercomparison, which combines hydrographic and geochemical tracer observations between 2000 and 2019 to resolve the pathways that connect the overflows to their origins. Consistent with previous studies we find two main pathways feeding the Denmark Strait Overflow Water (DSOW): the East Greenland Current and the North Icelandic Jet. Most of the water supplied by the North Icelandic Jet originates in the Greenland Sea ($82 \pm 2\%$) and flows southward along an outer core of the East Greenland Current, as well as along a previously unknown pathway crossing the Jan Mayen Ridge into the Iceland Sea. In total, $39 \pm 2\%$ of the DSOW originates in the Greenland Sea, while the Iceland Sea and the Atlantic Domain of the Nordic Seas account for $20 \pm 3\%$ and $19 \pm 2\%$, respectively. The majority of the Faroe Bank Channel Overflow Water originates in the Greenland Sea ($46 \pm 8\%$) and the Arctic Ocean ($25 \pm 9\%$). These dense waters approach the sill in the Iceland-Faroe Slope Jet and along the eastern side of the Jan Mayen Ridge. The inversion reveals unprecedented details on the upstream sources and pathways of the overflows, which have not previously been obtained using observations.

1. Introduction

The overflows from the Nordic Seas are a main source of dense water to the lower limb of the Atlantic Meridional Overturning Circulation (AMOC, Lozier et al., 2019; Chafik and Rossby, 2019; Tsubouchi et al., 2021). Warm and saline Atlantic Water flows northwards into the Nordic Seas (Fig. 1), where intense heat loss in winter transforms the water into colder and denser water masses that return southwards through gaps in the Greenland-Scotland Ridge (GSR) as overflow plumes. The largest overflow plume passes through Denmark Strait between Greenland and Iceland (3.2 Sv , $1 \text{ Sv} \equiv 10^6 \text{ m}^3 \text{ s}^{-1}$), while most of the overflow east of Iceland (2.0 Sv) flows southwards through the Faroe Bank Channel (Østerhus et al., 2019). The overflow through these two passages combine to approximately 90% of the total overflow water, generally defined as water denser than $\sigma_\theta = 27.8 \text{ kg m}^{-3}$ (Dickson and Brown, 1994). The sources and upstream pathways of the dense

water masses feeding these two overflows are not as well known as the transports across the ridge, although both are of key importance for better understanding the sensitivity of the AMOC to a warming climate.

Dense waters are formed in the Nordic Seas by several mechanisms. One is the gradual cooling of the Atlantic Water (AW) along the boundary current system around the Nordic Seas and Arctic Ocean (Mauritzen, 1996; Eldevik et al., 2009). Most of the cooling takes place in the Norwegian Sea (Fig. 1, Isachsen et al., 2007), known as the Atlantic Domain of the Nordic Seas because it is characterized by warm and saline AW at the surface (Swift and Aagaard, 1981). The AW branches that flow northwards through the Barents Sea and Fram Strait encircle the Arctic Ocean, and are further cooled and modified during transit (Rudels et al., 1999, 2005). In Fram Strait the branches transporting densified AW, now referred to as Atlantic-origin water (Våge

* Corresponding author at: Geophysical Institute, University of Bergen, Norway.

E-mail address: Ailin.Brakstad@uib.no (A. Brakstad).

<https://doi.org/10.1016/j.pocean.2023.102981>

Received 15 October 2022; Received in revised form 11 January 2023; Accepted 24 January 2023

Available online 28 January 2023

0079-6611/© 2023 The Authors. Published by Elsevier Ltd. This is an open access article under the CC BY license (<http://creativecommons.org/licenses/by/4.0/>).

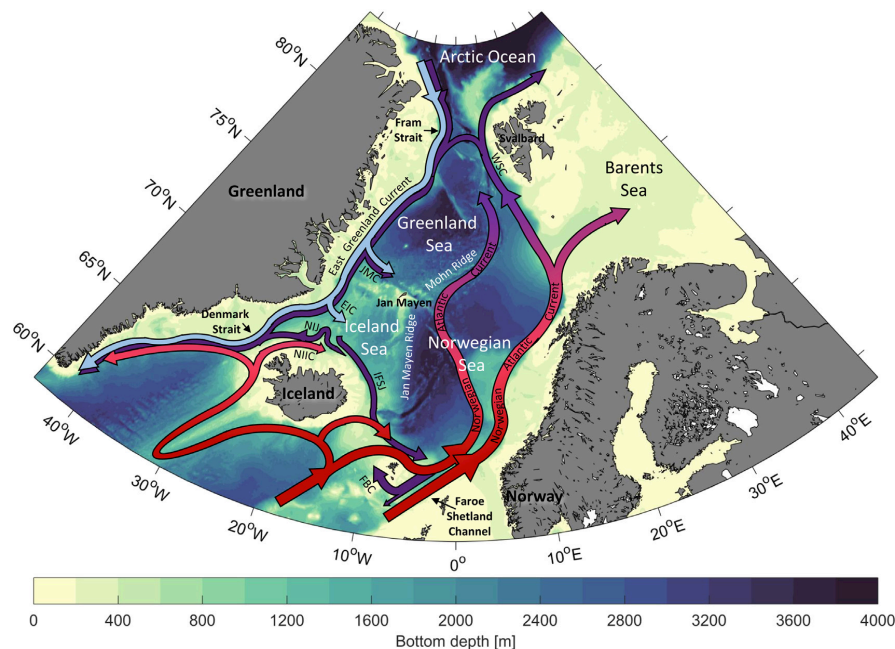


Fig. 1. Schematic circulation in the Nordic Seas. The inflow of warm Atlantic Water is indicated by red arrows, pathways of dense waters are illustrated by dark purple arrows, and southward transport of fresh Polar Surface Water with the East Greenland Current is shown in light blue arrows. The acronyms are: NIIC=North Icelandic Irminger Current; NIJ=North Icelandic Jet; IFSJ=Iceland-Faroe Slope Jet; EIC=East Icelandic Current; JMC=Jan Mayen Current; WSC=West Spitsbergen Current; FBC=Faroe Bank Channel. The background color is the bathymetry from ETOPO1 (Amante and Eakins, 2009).

et al., 2011) merge and return southwards with the East Greenland Current as an intermediate water mass with overflow-water density and a temperature between 0 and 3 °C (Rudels et al., 2005; Håvik et al., 2019). Above the Atlantic-origin water is the cold and fresh Polar Surface Water (PSW), which dominates the entire Greenland shelf along the western Nordic Seas (referred to as the Polar Domain, Swift and Aagaard, 1981). The PSW is too light to contribute directly to the overflows, but gradual mixing with the underlying Atlantic-origin water modifies the upper part of the Denmark Strait overflow plume (e.g., Tanhua et al., 2005; Jeansson et al., 2008; Mastropole et al., 2017).

Another mechanism of dense-water formation is open-ocean convection in the interior Iceland and Greenland Seas (Fig. 1, Swift et al., 1980; Swift and Aagaard, 1981; Marshall and Schott, 1999). These interior seas constitute the Arctic Domain of the Nordic Seas and are separated from the Atlantic and Polar domains by pronounced hydrographic fronts (Helland-Hansen and Nansen, 1909; Swift and Aagaard, 1981). The surface waters in the Arctic Domain are colder and fresher than the AW to the east, but warmer and more saline than the PSW to the west. The region is characterized by weak stratification and substantial heat loss during winter, which results in deep convection and the formation of dense Arctic Intermediate Waters (Swift et al., 1980; Swift and Aagaard, 1981). While these Arctic-origin waters are typically defined as water colder than 0 °C (e.g., Rudels et al., 2005; Jeansson et al., 2008; Våge et al., 2011; Mastropole et al., 2017), intermediate water masses warmer than 0 °C currently form in the central Iceland Sea (Våge et al., 2022).

The densest Arctic-origin water is formed in the Greenland Sea, where wintertime convection at present reaches depths of approximately 500–1500 m (Latarius and Quadfasel, 2010; Lauvset et al., 2018; Brakstad et al., 2019). However, both the depth of convection and the resulting water-mass product have changed substantially over the last 50 years (e.g., Schlosser et al., 1991; Meincke et al., 1992;

Karstensen et al., 2005; Brakstad et al., 2019). Prior to the late 1970s convection occasionally extended to the bottom and produced very cold and dense Greenland Sea Deep Water (GSDW), which was considered the main source of deep water to the entire Nordic Seas (along with deep water from the Arctic Ocean, Helland-Hansen and Nansen, 1909; Malmberg, 1983; Aagaard et al., 1985; Schlosser et al., 1991). There is no evidence of significant renewal of GSDW after 1980, and the main product of convection since the mid-1990s has been the lighter Greenland Sea Arctic Intermediate Water (Karstensen et al., 2005; Ronski and Budéus, 2005; Latarius and Quadfasel, 2010; Brakstad et al., 2019). As a result, a two-layer structure has developed in the Greenland Sea, with a pronounced stratification maximum preventing renewal of GSDW. The distinction between deep and intermediate water masses is typically defined by the potential density anomaly referred to 500 m depth of $\sigma_{0,5} = 30.444 \text{ kg m}^{-3}$ (e.g., Rudels et al., 2005; Jeansson et al., 2008). In the Greenland Sea the depth of this isopycnal coincides with the stratification maximum, which has been located between 1500 and 2000 m depth since the early 2000s (Brakstad et al., 2019).

Dense intermediate and deep waters colder than 0 °C are also supplied to the Nordic Seas from the Arctic Ocean via the East Greenland Current (Rudels et al., 2005; Jeansson et al., 2008, 2017). These water masses are located below the warmer Atlantic-origin water and are mainly a product of AW that has been substantially modified by wintertime convection in the Barents Sea, dense plumes formed on the Arctic shelves, and dense water originally formed in the Nordic Seas that entered the Arctic Ocean in the West Spitsbergen Current (Aagaard et al., 1985; Rudels et al., 1999; Langehaug and Falck, 2012). The fraction of water originally sourced from the Nordic Seas is not well known, but by the time these Arctic Ocean water masses flow southwards through Fram Strait their geochemical properties are distinct from the water occupying the same density range in the Nordic Seas (Jeansson et al., 2008, 2017). The Arctic Ocean deep waters are also warmer and

Table 1

List of data sources, time periods, and parameters included in our analysis, including references. T = temperature, S = salinity, O = oxygen, N = nitrate, and P = phosphate.

Data source	Year(s)	Parameters	Reference
Unified Database for Arctic and Subarctic Hydrography (UDASH)	1980–2015	T and S	Behrendt et al. (2018), https://doi.pangaea.de/10.1594/PANGAEA.872931
International Council for the Exploration of the Seas (ICES)	1950–2019	T, S, O, N, and P	http://ocean.ices.dk/HydChem/HydChem.aspx
Marine Freshwater and Research Institute of Iceland	1950–2018	T, S, O, N, and P	https://sjora.hafro.is
World Ocean Database (WOD)	1966–2018	T, S, O, N, and P	www.noaa.gov/cgi-bin/OS5/SELECT/builder.pl
Global Ocean Data Analysis Project version 2 (GLODAPv2) - 2019	1972–2017	T, S, O, N, and P	Olsen et al. (2016, 2019), https://doi.org/10.25921/xnme-wr20
Argo program	2001–2019	T and S	https://doi.org/10.17882/42182
Norwegian Iceland Seas Experiment database (NISE)	1950–2009	T and S	Nilsen et al. (2008)
Institute of Marine Research (Norwegian Marine Data Centre)	1967–2018	T, S, O, N, and P	https://www.hi.no/en/hi/forskning/research-data-1
Shipboard measurements along the continental slope north of Iceland	2004–2018	T and S	Semper et al. (2019), https://doi.pangaea.de/10.1594/PANGAEA.903535
Iceland-Greenland Seas Project	2018	T, S, O, N, and P	Renfrew et al. (2019)

more saline than the GSDW. After the GSDW formation ceased, the inflow of Arctic Ocean deep waters to the Nordic Seas has thus resulted in a general warming at depth (Meincke and Rudels, 1996; Østerhus and Gammelsrød, 1999; Somavilla et al., 2013).

The deep water in the Nordic Seas is located well below the Denmark Strait sill depth (650 m), while intermediate water masses can contribute more directly to the overflow plume. About 2/3 of the Denmark Strait Overflow Water (DSOW) is supplied by the East Greenland Current (Harden et al., 2016). This current mainly transports overflow water of Atlantic origin (Håvik et al., 2019), but also a substantial portion of dense water from the interior basins (Strass et al., 1993; Rudels et al., 2002; Jeansson et al., 2008). The remaining 1/3 of the DSOW, or perhaps closer to 1/2 according to recent work by Semper et al. (2019), is supplied by the North Icelandic Jet (NIJ) that flows along the slope north of Iceland. The NIJ supplies the densest portion of the DSOW (Våge et al., 2011; Mastropole et al., 2017). While (Våge et al., 2011) hypothesized that the NIJ is part of a local overturning loop in the Iceland Sea, later studies suggest that convection in the interior Iceland Sea may not produce sufficiently dense water (Våge et al., 2015, 2022). Based on several shipboard surveys, Semper et al. (2019) found that the bulk of the NIJ transport is associated with a narrow potential density range centered around $\sigma_{\theta} = 28.05 \text{ kg m}^{-3}$ (referred to as the NIJ transport mode). Such dense water is presently not formed in the central Iceland Sea, but it is regularly produced farther north in the Greenland Sea (Brakstad et al., 2019; Huang et al., 2020).

The Faroe Bank Channel Overflow Water (FBCOW) is supplied by intermediate and deep water masses from the Norwegian Sea (Fogelqvist et al., 2003; McKenna et al., 2016). However, most of these water masses are not locally formed. The Norwegian Sea Intermediate Water is composed of Arctic-origin water formed in the Iceland and Greenland Seas, Atlantic-origin water, and intermediate waters from the Arctic Ocean (Eldevik et al., 2009; Jeansson et al., 2017). The Norwegian Sea Deep Water is a mixture of deep water from the Greenland Sea and the Arctic Ocean that enters the Norwegian Basin through deep gaps in the Mohn Ridge north of Jan Mayen (Swift and Koltermann, 1988; Hansen and Østerhus, 2000; Somavilla, 2019; Shao et al., 2019; Wang et al., 2021). Olsson et al. (2005) suggested that intermediate Arctic-origin water from the Greenland Sea also enters the Norwegian Basin north of Jan Mayen, and then follows the eastern side of the Jan Mayen Ridge southwards. This southward-flowing current is supported by other observational and numerical studies (e.g., Voet et al., 2010; Serra et al., 2010; Köhl, 2010; Huang et al., 2020; Hátún et al., 2021),

but questions remain regarding the contribution from the current to the FBCOW. The existence of another current flowing from north of Iceland to the Faroe Islands was recently documented by Semper et al. (2020). This current, named the Iceland-Faroe Slope Jet (IFSJ), may account for approximately half of the FBCOW. The water masses transported by the IFSJ have similar hydrographic properties as the NIJ transport mode, which suggests that they have a common source (Semper et al., 2020). Huang et al. (2020) argued that the primary source region for both the NIJ and the IFSJ is the central Greenland Sea. They also found evidence of several southward pathways along the submarine ridge system surrounding the central Iceland Sea. Where and how the dense water exits the Greenland Sea and to what extent these potential pathways feed the NIJ and IFSJ remain unclear. Chafik et al. (2020) suggested that some overflow water may approach the Faroe-Shetland Channel (upstream of the Faroe Bank Channel, Fig. 1) from the eastern margin along the Norwegian slope, but the upstream sources of this water mass are not known.

The relative contributions of the water masses constituting the Denmark Strait and Faroe Bank Channel overflow plumes are also uncertain. The main reason is that traditional decomposition methods are very sensitive to the number of end-members included in the analysis and their specified properties, which can vary substantially in time and space. Here a regional version of the inverse water-mass decomposition method called Total Matrix Intercomparison (TMI, Gebbie and Huybers, 2010; Gebbie, 2014) was developed to investigate the upstream sources of the Nordic Seas dense water. Our focus is particularly on the origin, pathways, and final composition of the overflow water that passes over the GSR in Denmark Strait and the Faroe Bank Channel. The TMI method is not dependent on a few pre-defined source water masses. Instead, every surface location is considered a potential source of overflow water. By combining hydrographic and geochemical tracer observations between 2000 and 2019, the TMI method geometrically connects the water masses constituting the overflow plumes to their origins, which is a major advantage compared to traditional decomposition methods. With the regional high-resolution inversion we could identify the upstream pathways of the overflows and how water from various source regions contributed and mixed along the pathways.

2. Hydrographic and geochemical observations

2.1. Data sources and quality control

Vertical profiles of temperature (T), salinity (S), oxygen (O), nitrate (N), and phosphate (P) were collected from a range of archives (listed in Table 1) over the period 1950–2019 within the domain 58.5–84°N and

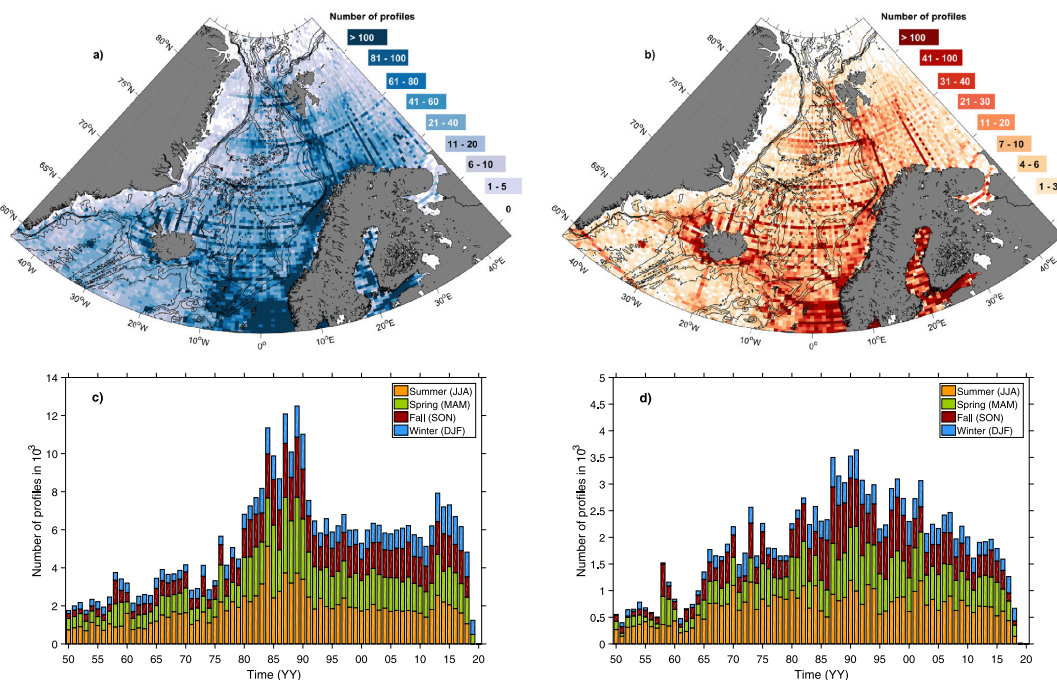


Fig. 2. Distribution of temperature/salinity profiles (a and c) and oxygen/nutrient profiles (b and d). The upper panels show the total number of profiles per $2/3^\circ$ longitude \times $1/4^\circ$ latitude bin since 1950. The bin size is twice the size of the TMI grid cells. The lower panels indicate the number of profiles per year, color coded by season. Note the different color schemes (a and b) and vertical axes (c and d) for the hydrographic and geochemical data distributions.

45°W – 45°E . All observations were combined into a single data set and quality controlled. The quality control involves removing duplicates, erroneous profiles, density inversions, and outliers (details are provided in Appendix A). We followed the TEOS-10 standard (IOC et al., 2010) and used Conservative Temperature and Absolute Salinity, hereafter referred to as temperature and salinity, throughout the analysis. The spatial and temporal data distributions of the final quality-controlled data set are shown in Fig. 2. While the spatial variability in water-mass properties is accounted for in the TMI, it is based on the assumption that the observations represent a steady ocean state. Hence, we restricted our analysis to the period 2000–2019. This time period is considered sufficiently stable in terms of dense-water formation and water column structure (i.e. Brakstad et al., 2019; Somavilla, 2019) and is characterized by a generally warmer and more saline water column than the 1980s and 1990s (Skagseth and Mork, 2012; Mork et al., 2014b; Lauvset et al., 2018). The period also contains a sufficient number of observations to adequately constrain the inversion (Fig. 2).

2.2. 2000–2019 climatology of late-winter conditions

To account for seasonal variability in the observations we modified all profiles to represent late-winter (February–April) conditions, when the surface mixed layer is deepest and densest. Late-winter mixed-layer depths determined by Våge et al. (2015) and Brakstad et al. (2019) were used for the Iceland and Greenland Seas, respectively, while a density-difference criterion was employed to estimate the base of the mixed layer for the rest of the domain (Appendix B). The mean 2000–2019 mixed-layer distribution, with a $1/3^\circ$ longitude \times $1/8^\circ$ latitude resolution, is shown in Fig. B.1. The corresponding distributions of late-winter hydrographic and geochemical mixed-layer properties were then used to homogenize each profile from the mean local winter mixed-layer depth to the surface.

The final data set was interpolated onto a three-dimensional grid with a regular horizontal resolution of $1/3^\circ$ longitude (which ranges from 19 km at 58.5°N to 4 km at 84°N , Fig. 2) and $1/8^\circ$ latitude (approximately 14 km), and 46 vertical levels with intervals ranging from 10 m near the surface to 250 m at depth (Fig. C.1f). This equals the TMI resolution, which was chosen to resolve the complex bathymetry of the Nordic Seas and the overflow plumes through the deep gaps of the GSR (e.g., Figs. 5 and 13). The resolution is also sufficient to capture the upsloping isopycnals and water-mass properties associated with the narrow NIJ and IFSJ upstream of the sills (Semper et al., 2019, 2020). Since the inversion is observationally constrained and quantifies the net effect of advection and diffusion on the distribution of water masses, it is less prone to errors associated with the resolution compared to numerical simulations that need to parameterize subgrid-scale processes (Gebbie and Huybers, 2010). Details of the gridding procedure are provided in Appendix C. Grid cells without any measurements were kept empty, which implies that they were not used to constrain the inversion. The final gridded product represents the late-winter climatological conditions for the 2000–2019 period. Temporal variability in the observations was accounted for by allowing the TMI inversion to deviate from the climatology within the uncertainty limits of the observations. The uncertainty was estimated based on the number of observations included in each grid cell and their variance, which typically decreases with depth (Appendix C, Fig. C.1). Uncertainties related to the precision of the measurements are small compared to the temporal variability and were not included in our estimates.

3. Total Matrix Intercomparison

3.1. Description of the method

A regional version of the TMI method was developed for the domain 58.5 – 84°N and 45°W – 45°E with the resolution $1/3^\circ$ longitude, $1/8^\circ$

latitude, and 46 vertical levels (Section 2.2, Fig. 2). Apart from the higher resolution, the main difference between this and earlier global versions (Gebbie and Huybers, 2010; Gebbie, 2014) is that it considers both the surface and lateral boundary locations potential sources for the interior water masses in the Nordic Seas. For temperature and salinity we assume that all interior values can be described as some combination of the surface and lateral boundary properties, while oxygen, nitrate, and phosphate are in addition affected by remineralization. The value of any water-mass property c_i at location i in the ocean interior can, in general, be expressed as a linear combination of the properties in the neighboring grid cells plus any local sources or sinks (Gebbie and Huybers, 2010). That is:

$$c_i = \sum_{j=1}^N m_{ij} c_j + r q_i, \quad (1)$$

where $N = 6$ is the number of neighboring grid cells, m_{ij} is the fraction of water that originates from cell j with property c_j , and $\sum_{j=1}^N m_{ij} = 1$ to assure conservation of mass. Local sources and sinks for oxygen, nitrate, and phosphate are expressed as a product between the interior source term q_i and the stoichiometric ratio r ($\Delta P : 15.5\Delta N : -170\Delta O$, Anderson and Sarmiento, 1994; Gebbie and Huybers, 2010).

Following Gebbie and Huybers (2010) and Gebbie (2014), the conservation equation (Eq. (1)) is used to formulate an explicit model for each parameter c as:

$$Ac = d, \quad (2)$$

where c is a vector made from the three-dimensional property field in the Nordic Seas and d is a vector filled with the surface and lateral boundary properties, as well as $r q_i$ for the interior sources and sinks. The matrix A quantifies the strengths of the connections between each location i and its neighbors (the mass fractions m_{ij}). If the pathway matrix A , the boundary properties, and the interior source term q were known, it would be possible to predict the distribution of each parameter c by calculating the inverse of Eq. (2). The goal is to find the solution of A , q , and boundary properties that minimizes the difference between the predicted and observed distributions c . The initial boundary properties and the first guess of A and q are defined in Section 3.2, while Section 3.3 outlines how to solve the inverse problem. The resulting matrix A can be used to diagnose water-mass composition and pathways (Section 3.4), where the pathways represent the steady-state circulation that best fits the observations (i.e., the late-winter hydrographic and geochemical properties in the period 2000–2019). An evaluation of the inversion-to-observational misfits is given in Section 3.5.

3.2. Initial boundary conditions and first guess of pathway matrix A

The initial properties along the surface and lateral boundaries were obtained from the winter-mean gridded climatology described in Section 2.2. Potential modifications to these properties were constrained by the corresponding uncertainty estimated from the observational temporal variability. Measurements of the interior source term q and water-mass pathways A are not available. The interior source term is assumed and enforced to be positive (as a first guess q equals $10^{-3} \mu\text{mol kg}^{-1}$ everywhere, Gebbie, 2014). The magnitude of q relative to the first guess is also constrained such that larger values only occur if the observations demand it.

The first guess of the pathway matrix A used in previous global TMI inversions (e.g., Gebbie and Huybers, 2010; Gebbie, 2014) represents an isotropic exchange between all grid cells. This means that $m_{ij} = 1/6$ for all grid cells with 6 neighbors. In our regional inversion this first guess resulted in a circulation characterized by excessive diffusivity. Instead we constructed a first guess of A based on the assumption that water tends to flow and mix along geostrophic streamlines and isopycnals (Nøst and Isachsen, 2003). Potential density and geostrophic

velocity fields relative to the surface were derived from the late-winter gridded climatology. Absolute geostrophic velocities were then estimated using annual-mean (2000–2019) surface geostrophic velocity from satellite as reference (gridded altimeter data were obtained from Copernicus Marine Environmental Monitoring Service, <http://marine.copernicus.eu>). Half of the fraction of water from neighboring grid cells were determined by gradients in density, while the remaining half was determined by gradients in the geostrophic stream function (see Appendix D for details). This first guess substantially improved the solution, in particular the representation of the East Greenland Current.

The sensitivity of the solution to the first guess of A was investigated by altering the weights of the contributions (by $\pm 10\%$) determined by gradients in density versus gradients in the geostrophic stream function. We consider the resulting changes in water-mass composition and pathways, which were relatively minor, an approximate estimate of uncertainty (e.g., Figs. 4, 6, and 14). That is, the error bars of our estimates only represent the uncertainties related to the first guess of A . Uncertainties related to temporal variability in the observations were included as constraints in the inversion to obtain the optimal 2000–2019 winter mean solution.

3.3. Solving the inverse problem

The unknowns that we seek a solution for are the property distributions c (temperature, salinity, oxygen, nitrate, and phosphate), the mass fractions m (which form the pathway matrix A), and the interior source term q . The solution is required to follow the conservation equation (Eq. (1)) for each predicted parameter c and to conserve mass. The solution is then obtained by minimizing the sum of the squared inversion-to-observational misfits, using the method of Lagrange multipliers (Schlitzer, 2007; Gebbie, 2014). The Lagrange multiplier method is specifically designed to handle complex, nonlinear problems such as this, although there is no guarantee that the solution arrives at the overall minimum of the cost function (Köhl and Willebrand, 2002).

The Lagrangian cost function to be minimized is constrained by the conservation equations, the inversion-to-observational misfits weighted by the observational uncertainty, as well as other non-observational constraints on the predicted distributions c , such as a stably stratified water column, temperatures above freezing, and non-negative values for salinity and the geochemical parameters (see supplementary material in Gebbie, 2014, for details). The minimum of the Lagrangian function is found by setting the partial derivatives with respect to c , m , and q equal to zero. This results in a set of adjoint equations that yield information about how the Lagrangian function will change given a change in the pathway matrix A , the initial boundary conditions, and the interior source term q . This information is then used to iteratively improve the Lagrangian function by a quasi-Newton gradient descent method (Nocedal, 1980; Gilbert and Lemaréchal, 1989; Gebbie, 2014).

3.4. Diagnosing water-mass composition and pathways

The optimized pathway matrix A was used to diagnose the composition and upstream pathways of the overflow water at the GSR. Information about the fraction of water (g) sourced from a particular surface or lateral boundary location (b_i) can be obtained by releasing a passive dye at that boundary location. The three-dimensional distribution of dye concentrations equals g and is found directly from the inverse of Eq. (2) ($g = A^{-1}b$, Gebbie and Huybers, 2010), where b equals one at location i and zero elsewhere. The volume of overflow water originating from location i can then be estimated as the sum of the volume in each overflow water grid cell v multiplied by the fraction g :

$$V = v^T g. \quad (3)$$

Our ultimate goal is to determine the amount of overflow water originating from each boundary location, but it would be very inefficient to compute the distribution of g for every single boundary point.

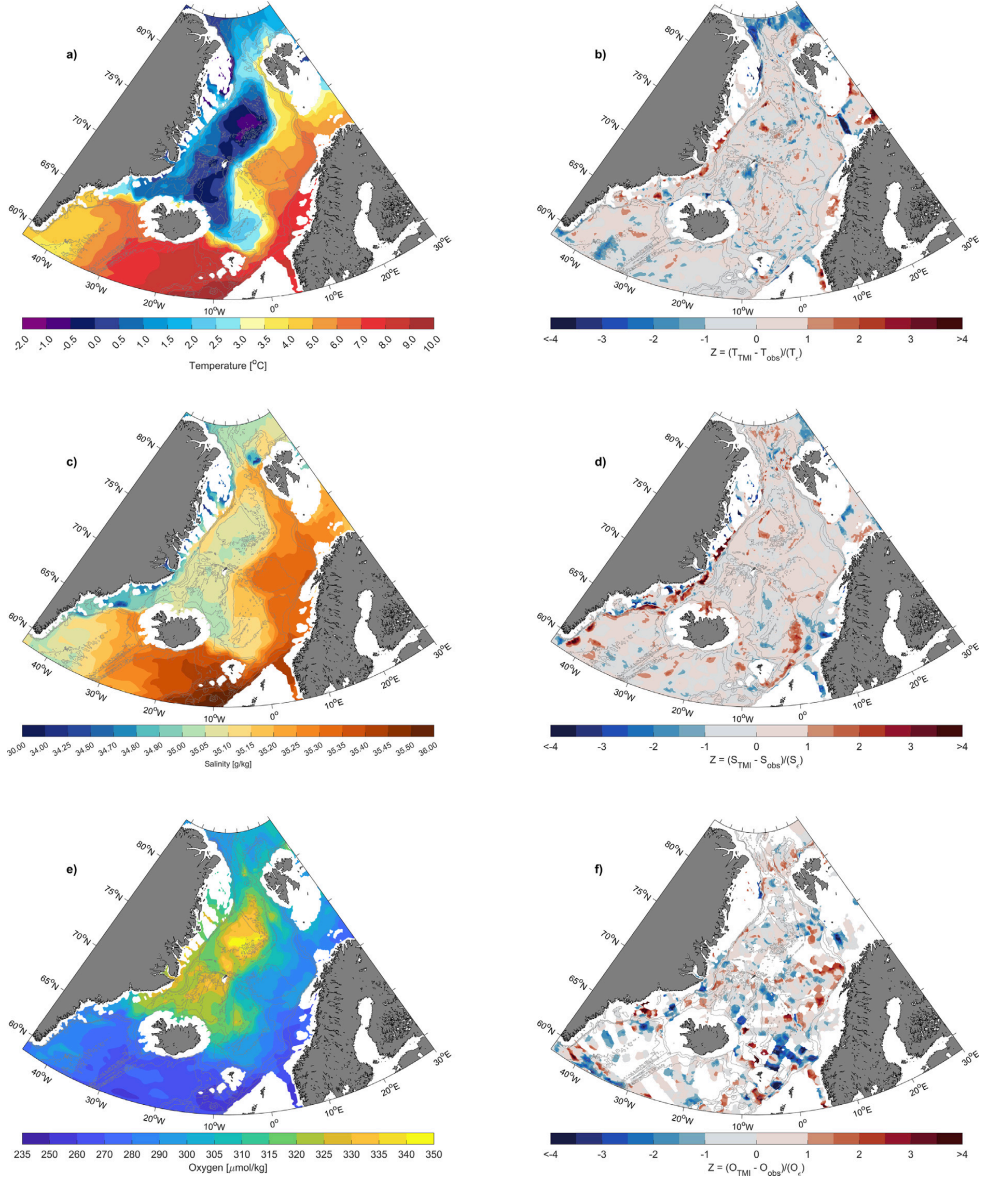


Fig. 3. Distribution of TMI temperature (T), salinity (S), and oxygen (O) at 250 m depth (left panels). The corresponding Z-score distribution for each parameter is shown in the panels to the right. The Z-score is defined as the difference between the inversion and observations divided by the observational uncertainty (ϵ). Positive values indicate that the TMI property is larger than the observed, while values between ± 1 indicate that the difference is smaller than the uncertainty. The 500-, 1000-, 1500-, and 3000-m isobaths are shown as thin gray contours.

Instead we combine Eqs. (2) and (3) following [Gebbie and Huybers \(2011\)](#) such that:

$$\frac{\partial V}{\partial b} = A^{-T} v, \quad (4)$$

which can be solved in one operation by calculating the inverse transpose of A . The partial derivative on the left side of Eq. (4) is a

vector that describes the sensitivity of V to changes in the boundary conditions b . At the surface and lateral boundaries the sensitivity vector equals the volume of overflow water originating from each boundary location, while the interior values of $\partial V / \partial b$ give information about the pathways (i.e., the amount of overflow water that has passed through each interior location).

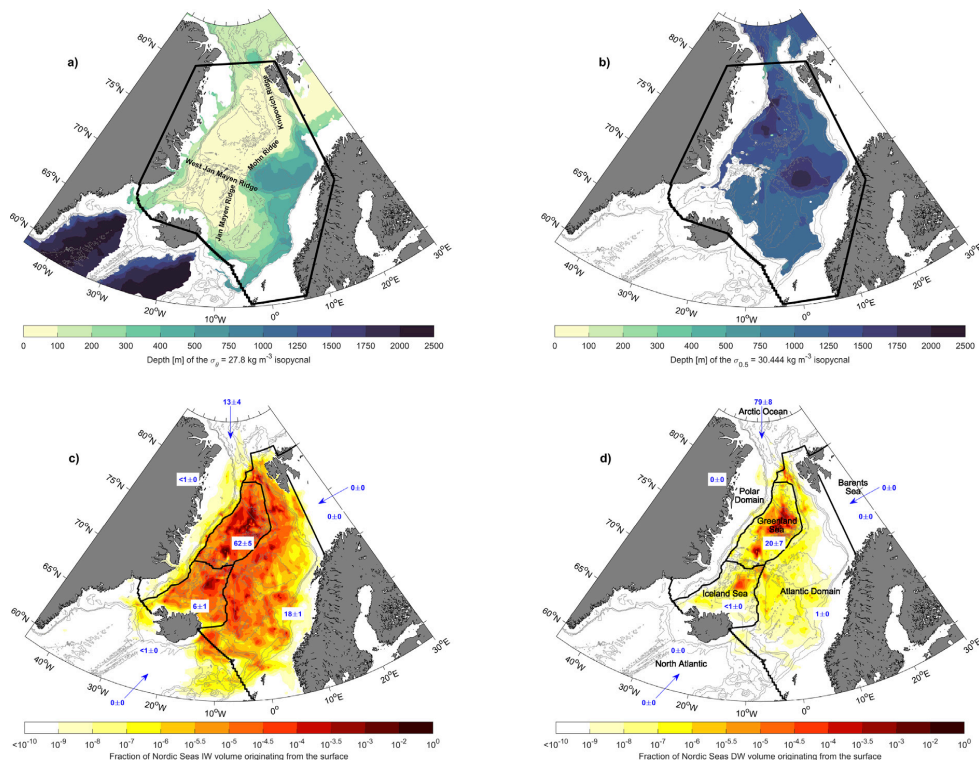


Fig. 4. Depths of the $\sigma_{\theta} = 27.8 \text{ kg m}^{-3}$ (a) and $\sigma_{0.5} = 30.444 \text{ kg m}^{-3}$ (b) isopycnals. The lower panels show the fraction of contribution from the surface to the intermediate (c) and deep (d) water inventories in the Nordic Seas (defined as the region within the black contour marked in a and b). Note that the color scale is logarithmic, with dark red colors indicating substantial contributions. The blue numbers are the total contribution (in percent) from each surface region outlined in black and the lateral boundaries, and the uncertainty represents the sensitivity to the first guess of A (Section 3.2). The 500-, 1000-, 1500-, and 3000-m isobaths are shown as thin gray contours.

Note that the terms *origin* and *source* refer to the surface locations where the water masses constituting the overflow plumes were last in contact with the atmosphere (or the lateral boundaries if the water-masses originate outside of the domain), which is not necessarily where the largest buoyancy loss occurs (Isachsen et al., 2007).

3.5. Evaluation of the Nordic Seas TMI solution

One way to quantify how well the steady-state pathways fit the observations is to compare the TMI and observed property distributions. By construction the fields should compare well, which is evident from the vertical distribution of the average misfit for each parameter (Fig. C.1). The magnitudes of the misfits are generally similar to (or below) the observational uncertainty. The misfits also have the same vertical shape, with the largest values in the upper 500 m.

The horizontal distributions of TMI temperature, salinity, and oxygen at 250 m depth are shown in Fig. 3 along with the corresponding misfits divided by the observational uncertainty (called Z-score, e.g., Glover et al., 2011). As expected, the differences between the inversion and observations are low. The Norwegian Sea is dominated by warm and saline AW with relatively low oxygen concentration, while the Iceland and Greenland Seas are cold, oxygen-rich, with intermediate salinity. Also visible are the temperature and salinity local maxima of the Atlantic-origin water in the East Greenland Current flowing southwards along the Greenland shelf break. The TMI fields are generally smoother than the observations, which results in a patchy structure of the Z-scores. Apart from these small-scale discrepancies, the majority

of the misfits are within the observational uncertainty (i.e., 82% of all Z-scores are between ± 1 , which indicates a slight overfit relative to the expected 67%).

4. Dense-water formation in the Nordic Seas

Before we investigate the origin and pathways of the overflow water at the GSR, we identified all areas that supply dense water to the Nordic Seas and their relative contributions. This was done by backtracking all intermediate and deep water masses within the Nordic Seas (thick black contour, Figs. 4a and b) to the surface and lateral boundaries (Section 3.4). Intermediate waters (IW) have potential densities between $\sigma_{\theta} = 27.8 \text{ kg m}^{-3}$ and $\sigma_{0.5} = 30.444 \text{ kg m}^{-3}$, while deep water (DW) is denser than $\sigma_{0.5} = 30.444 \text{ kg m}^{-3}$ (Rudels et al., 2005; Jeansson et al., 2008).

The upper 1500 m of the Nordic Seas water column are dominated by IW (Figs. 4a and b), in particular the western and northern areas where the IW extends to the surface during winter. These areas also supply most of the Nordic Seas IW inventory (Fig. 4c). The colors in Fig. 4c show the fraction of Nordic Seas IW volume originating from each surface grid point. All volume fractions (including those from the lateral boundaries, not shown) add up to 1. The blue numbers on the figures indicate the total contribution (in percent) from the different source regions outlined in black and the lateral boundaries. These regions were defined based on bathymetry and surface hydrography as described below, and are used throughout the paper for easier interpretation and comparison with earlier studies.

Approximately $6 \pm 1\%$ and $62 \pm 5\%$ of the IW volume originate in the Iceland and Greenland Seas, respectively. These surface source regions are separated from the Polar Domain by the Polar Front (defined by the 34.66 kg kg^{-1} surface isohaline, which corresponds to the practical salinity contour 34.50 used by Swift and Aagaard, 1981) and from the Atlantic Domain by the Arctic Front (here defined by the 2°C surface isotherm, which closely follows the Jan Mayen, Mohr, and Knipovich Ridges, Fig. 4a). The West Jan Mayen Ridge separates the Greenland and Iceland Seas. The North Atlantic is the source region south of the GSR, including the southern lateral boundary, while the Barents Sea is the region south of Svalbard and east of 19°E (which is the approximate longitude of the Barents Sea Opening transect, O'Dwyer et al., 2001). Because water modified in the Barents Sea largely continues into the Arctic Ocean before returning southwards through Fram Strait, water that was last at the surface in this area is accounted for in the inversion as a contribution from the northern lateral boundary along with other water masses flowing southwards from the Arctic Ocean. Combined, all water masses present at the northern lateral boundary, hereafter referred to as the Arctic Ocean, supply $13 \pm 4\%$ of the IW in the Nordic Seas. The remaining main contributor is the Atlantic Domain which accounts for approximately $18 \pm 1\%$.

The majority of the Nordic Seas DW stems from the Arctic Ocean ($79 \pm 8\%$, Fig. 4d). As the only source region where observations show densities greater than $\sigma_{0.5} = 30.444 \text{ kg m}^{-3}$ in the 2000–2019 period this was an expected result. However, the inversion also backtracks a substantial portion ($20 \pm 7\%$) of the DW to the Greenland Sea. The Nordic Seas DW is a mixture of DW formed in the Greenland Sea and the Arctic Ocean (Swift and Koltermann, 1988), but GSDW was not formed during the 2000–2019 period (e.g., Brakstad et al., 2019). To resolve the properties of the remaining GSDW at depth the inversion requires a surface contribution from the Greenland Sea. The impact of this modification on the DSOW (Section 5) is small, as only $6 \pm 2\%$ of the DSOW is supplied by DW ($4 \pm 1\%$ from the Greenland Sea and $2 \pm 1\%$ from the Arctic Ocean). Approximately $28 \pm 17\%$ of the FBCOW is supplied by DW from the Greenland Sea ($3 \pm 8\%$) and Arctic Ocean ($25 \pm 9\%$). These contributions will be discussed further in Section 6.

5. Origin and pathways of Denmark Strait Overflow Water

The hydrographic and geochemical properties in the inversion, and the corresponding Z-scores, across Denmark Strait are shown in Fig. 5. The overall distributions are well reproduced by the inversion, with the warm and saline North Icelandic Irminger Current on the Icelandic side of the strait and the cold and fresh PSW in the East Greenland Current on the Greenland side. The location as well as the properties of the DSOW plume (defined as water denser than $\sigma_\theta = 27.8 \text{ kg m}^{-3}$) are in good agreement with observations, with the exceptions of small negative biases in salinity and oxygen (Figs. 5d and f). At the interface between the overflow plume and the North Icelandic Irminger Current there is also a negative bias in both oxygen and nitrate (Fig. 5f and h, respectively), which suggests that the stoichiometric ratio may not be locally correct. This ratio is, however, known to vary spatially (Anderson and Sarmiento, 1994; Frigstad et al., 2014; Jeansson et al., 2015). We also note that large variability in DSOW volume transport and hydrographic properties are observed on short time scales (e.g., Jochumsen et al., 2017; Mastropole et al., 2017).

The origin of the DSOW plume was determined by backtracking all of the overflow water at Denmark Strait to the surface and lateral boundaries (Section 3.4). This reveals that most of the DSOW is produced in the Nordic Seas, with the largest contributions from the Greenland Sea ($39 \pm 2\%$), the Iceland Sea ($20 \pm 3\%$), and the Atlantic Domain ($19 \pm 2\%$, Fig. 6). The contribution from the Atlantic Domain stems almost entirely from the northern part near Fram Strait, in the West Spitsbergen Current. This is where the Atlantic-origin water has cooled sufficiently to leave the surface and flows beneath the fresh

PSW (Mauritzen, 1996). Most of the water from the Greenland Sea originates in the central basin, within the cyclonic gyre where the deepest convection is found (Fig. B.1, Brakstad et al., 2019). The deepest and densest convection in the Iceland Sea occurs in the north-western part, outside of the gyre (Våge et al., 2015), which also corresponds well with the elevated contributions to the DSOW (Fig. 6). The Polar Domain, mainly the region near the Polar Front, supplies $7 \pm 0\%$, while only $2 \pm 1\%$ originates in the Arctic Ocean. We also find a $12 \pm 1\%$ contribution from the North Atlantic, mainly from the region just south of Denmark Strait, which corroborates the numerical results of Saberi et al. (2020), although their simulated contribution was slightly higher (16%).

The hydrographic and geochemical properties at the boundary locations with significant DSOW contributions (fractions greater than $10^{-4.5}$, Fig. 6) vary substantially, even within each source region (Fig. 7). Hence, direct comparisons with results from earlier end-member analyses, which are sensitive to the predefined end-members, are not straightforward. One example is the temperature limit (0°C) used to separate Atlantic- from Arctic-origin waters (e.g., Rudels et al., 2005; Jeansson et al., 2008; Våge et al., 2011; Mastropole et al., 2017). Arctic-origin water masses, interpreted as IW originating in the Iceland and Greenland Seas, are typically defined as water colder than 0°C . From Fig. 7a we see that IW warmer than 0°C in the Iceland and Greenland Seas contribute to the DSOW, at least based on the 2000–2019 late-winter conditions. Distinguishing Arctic- and Atlantic-origin waters by the 0°C limit would thus lead to an overestimate of water originating from the Atlantic Domain and an underestimate of water from the Iceland (in particular) and Greenland Seas.

In accordance with Våge et al. (2022), we find that most of the water formed in the Iceland Sea in the 2000–2019 period was warmer than 0°C . We note that the warmest source water from the Iceland Sea ($>3^\circ\text{C}$, Fig. 7a) stems from the North Icelandic Irminger Current on the shelf northwest of Iceland. Garcia-Quintana et al. (2021) suggested, based on numerical simulations, that dense-water formation on the north-west Iceland shelf can supply up to 21% of the overflow water transported by the NIJ to Denmark Strait. This is incongruent with observations, which indicate that formation of overflow water on the shelf north of Iceland is rare (Semper et al., 2022). Our inversion confirms that result, we find that the total contribution from the north Iceland shelf to the DSOW is less than 1%. Larger contributions are found from the Iceland shelf south of Denmark Strait (within the North Atlantic domain, Fig. 6), but this water recirculates in and just north of Denmark Strait and does not supply the NIJ (Saberi et al., 2020; Garcia-Quintana et al., 2021).

Another instance where comparisons between end-member analyses may be challenging is that water originating in the Greenland Sea and the Arctic Ocean can have the same hydrographic properties, while their geochemical properties differ (Fig. 7). Dense waters formed in the Greenland Sea typically have higher oxygen and lower nitrate and phosphate concentrations, because they were ventilated more recently. Hence, only studies that include geochemical parameters can distinguish water masses originating in the Arctic Ocean and in the Greenland Sea. As a result, DSOW end-member analyses solely based on hydrographic properties typically have a higher contribution from the Iceland and Greenland Seas (e.g., Mastropole et al., 2017; Lin et al., 2020), while studies also including geochemical properties often have substantial contributions from the Arctic Ocean (e.g., Tanhua et al., 2005; Jeansson et al., 2008). The TMI solution is based on hydrographic as well as geochemical observations, yet our estimated contribution from the Arctic Ocean to the DSOW is much lower than suggested by Tanhua et al. (2005) and Jeansson et al. (2008). Our contribution from the Arctic Ocean is mainly classified as deep water, while Tanhua et al. (2005) and Jeansson et al. (2008) also found a large intermediate-water contribution. The TMI source properties available at the northern lateral boundary (i.e., the Arctic Ocean, Fig. 7) are slightly more saline compared to the source properties used by Jeansson et al. (2008).

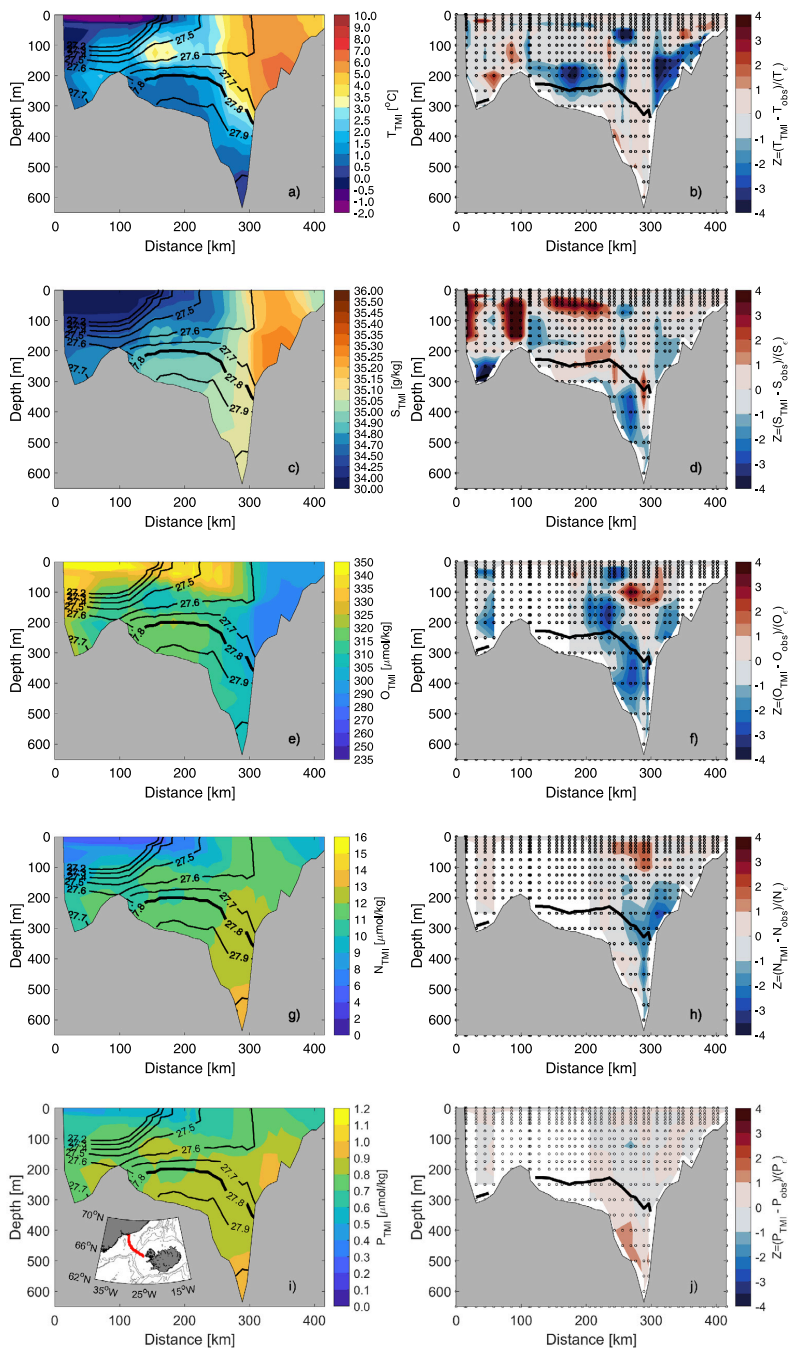


Fig. 5. TMI temperature (T), salinity (S), oxygen (O), nitrate (N), and phosphate (P) across Denmark Strait (left panels, the location of the section is indicated in red on the map inserted in panel i). The black contours show the potential density (σ_θ) field and the thick black line marks the $\sigma_\theta = 27.8 \text{ kg m}^{-3}$ isopycnal, which is the lower density limit of the overflow water. The corresponding observed overflow water limit is marked in the right panels along with the Z-score (Fig. 3) for each parameter. The TMI resolution is indicated by black circles. The x-axes show the distance along the section starting from Greenland.

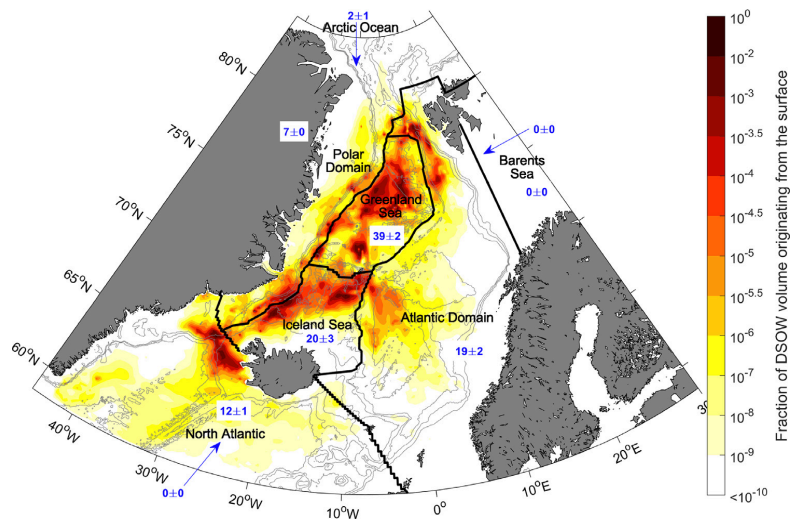


Fig. 6. Fraction of contribution from the surface to the Denmark Strait Overflow Water. Note that the color scale is logarithmic. The blue numbers indicate the total contribution (in percent) from each surface region outlined in black and the lateral boundaries, and the 500-, 1000-, 1500-, and 3000-m isobaths are shown as thin gray contours.

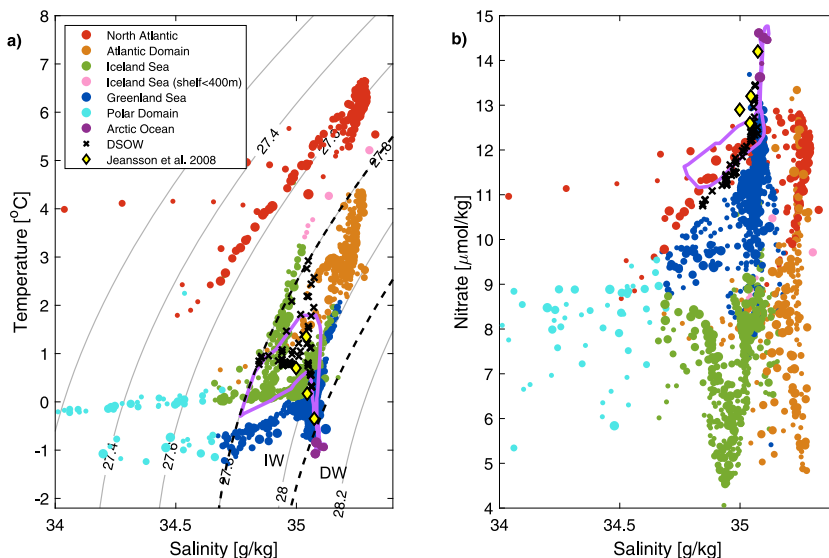


Fig. 7. Temperature and salinity (a), as well as nitrate (b) of the DSW (black crosses) and the source regions with fractional contributions exceeding $10^{-4.5}$ (Fig. 6). The source properties (circles) are color-coded by region, while the marker sizes are scaled by the magnitude of the contribution. The purple contour outlines all properties denser than $\sigma_\theta = 27.8 \text{ kg m}^{-3}$ that are present at the northern lateral boundary (i.e., Arctic Ocean), while the yellow diamonds show the source properties of the intermediate water from the Arctic Ocean as defined by Jeansson et al. (2008). The gray contours in (a) indicate potential density ($\sigma_\theta, \text{ kg m}^{-3}$), and the black dashed lines mark the $\sigma_\theta = 27.8 \text{ kg m}^{-3}$ and $\sigma_{0.5} = 30.444 \text{ kg m}^{-3}$ isopycnals.

The Atlantic-origin water ($>0 \text{ }^\circ\text{C}$) that has encircled the Arctic Ocean also has lower nitrate concentrations (compare the purple contour and yellow diamonds in Fig. 7). This could be due to temporal variability in the water masses, which is not properly accounted for in Tanhua et al. (2005) and Jeansson et al. (2008), as their estimates are based

on observations from single cruises, nor in the TMI solution, which is based on the 2000–2019 winter-mean conditions.

Although the DSW source properties vary substantially, they form separate clusters with nearly distinct hydrographic and geochemical properties when grouped geographically (Fig. 7). Each source region

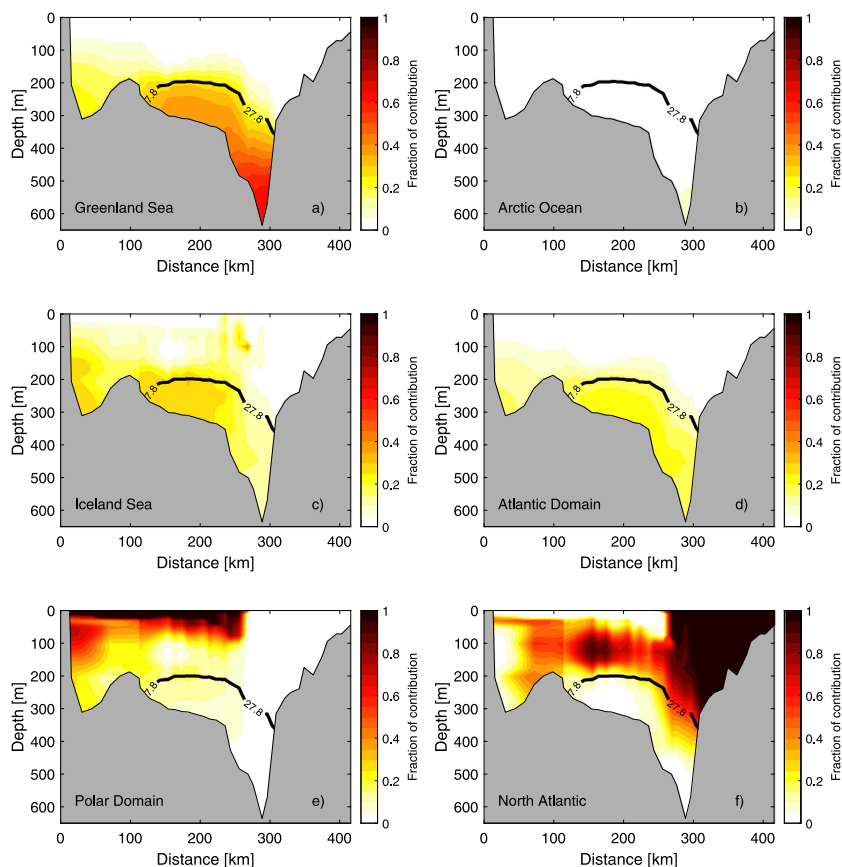


Fig. 8. Contributions from six different source regions to the transect across Denmark Strait (Fig. 5i). The lower density limit of the DSOW is indicated by the $\sigma_{\theta} = 27.8 \text{ kg m}^{-3}$ isopycnal (black contour). The x-axes show distance along the section starting from Greenland.

also contributes to distinct parts of the DSOW plume. To investigate this further, we traced water from each boundary source region to Denmark Strait using the inverse of Eq. (2) as described in Section 3.4. The densest portion of the DSOW filling most of the deep trough is dominated by water formed in the Greenland Sea (Fig. 8a), while the Iceland Sea and the Atlantic Domain contribute to the slightly less dense components near and on the Greenland shelf break (Figs. 8c and d, respectively). This distribution is in good agreement with previous studies (Mastropole et al., 2017; Lin et al., 2020). The small contribution from the Arctic Ocean (Fig. 8b) is primarily to the densest component of the DSOW, coinciding with elevated values of nitrate and phosphate (Fig. 5g and i). As Mastropole et al. (2017) and Lin et al. (2020), we find that the Polar Domain and the North Atlantic (via the North Icelandic Irminger Current) contribute to the lightest components of the DSOW plume (Figs. 8e and f). Some of the warm water from the North Atlantic recirculates north of Denmark Strait (Casanova-Masjoan et al., 2020), but most of this water is too light to supply the overflow plume (Fig. 8f).

A major advantage of the TMI method is the possibility to identify interior pathways (Section 3.4). By backtracking overflow water from the Denmark Strait sill, we can estimate the fraction of DSOW that passed through each interior grid cell upstream of the sill (Fig. 9). The most prominent pathway is the East Greenland Current along the Greenland shelf break, which can be traced back to Fram Strait where

most of the Atlantic-origin water transported by the current was last in contact with the atmosphere (Fig. 6). Another pathway, parallel to the East Greenland Current, traces DSOW back to the central Greenland Sea. The core of the pathway is centered at 550 m depth and located roughly 70 to 120 km offshore of the Greenland shelf break. The depth and location of this pathway coincide with the deep part of the outer East Greenland Current branch that Håvik et al. (2017) observed north of the West Jan Mayen Ridge near 71°N . As Håvik et al. (2017), we cannot identify a distinct outer branch south of this ridge, where the branch appears to have merged with the shelf break branch of the East Greenland Current. The NIJ flowing along the slope north of Iceland (e.g., Semper et al., 2019), is visible only to the west of Kolbeinsey Ridge in Fig. 9. From this figure the origin of the NIJ is unclear, this will be investigated further in the following sections.

The NIJ was further examined at the Hornbanki transect upstream of Denmark Strait, corresponding to the location of one of the regular hydrographic monitoring transects north of Iceland (Jónsson and Valdimarsson, 2012; Semper et al., 2019), where the overflow water in the NIJ can be readily separated from the overflow water transported by the East Greenland Current. The section (indicated in blue in Fig. 9) was extended northward across Blossville Basin, for complete coverage between the Iceland and Greenland shelves. The temperature and fraction of DSOW volume that has passed through the extended Hornbanki section are shown in Figs. 10a and b, respectively. From the fraction

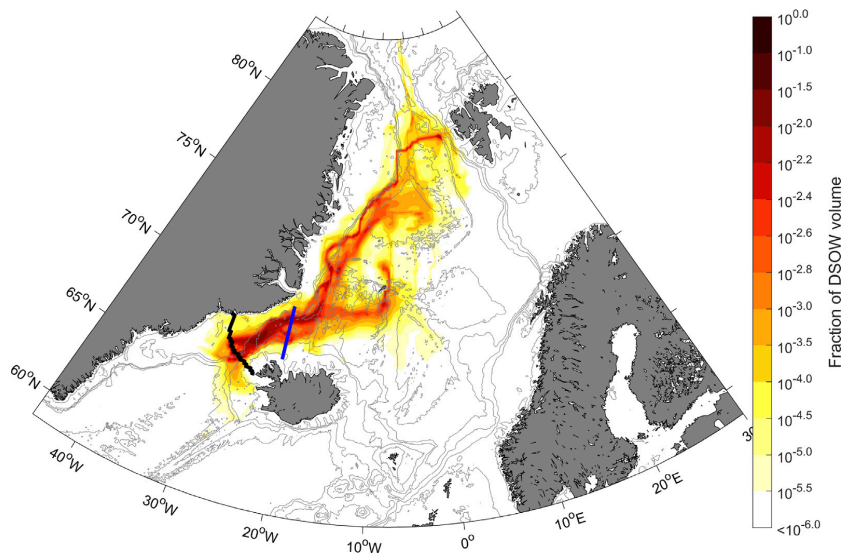


Fig. 9. Fraction of Denmark Strait Overflow Water that has passed through each horizontal location, integrated over the entire water column. Note that the color scale is logarithmic. The location of the Denmark Strait section is indicated in black, while the location of the extended Hornbanki section is marked in blue. The 500-, 1000-, 1500-, and 3000-m isobaths are shown as thin gray contours.

of DSOW volume (Fig. 10b), we identified three major local maxima that correspond to the NIJ and the separated and shelf break branches of the East Greenland Current (Våge et al., 2013; Harden et al., 2016; Semper et al., 2019). The NIJ is located between the 550 and 850 m isobaths, and is associated with a tongue of cold, dense water sloping up towards Iceland (Semper et al., 2019).

The origin and upstream pathways of the DSOW in the NIJ (black circles, Fig. 10b) are shown in Fig. 11. In accordance with Huang et al. (2020), we find that most of the overflow water in the NIJ originates in the Greenland Sea ($82 \pm 2\%$), while the remaining portion is supplied by the Arctic Ocean ($8 \pm 2\%$), the Iceland Sea ($5 \pm 1\%$), and the Atlantic Domain ($5 \pm 1\%$). The water originating in the Greenland Sea follows two main pathways towards Denmark Strait. One is the outer core of the East Greenland Current (Håvik et al., 2017), which is supported by RAFOS float tracks (de Jong et al., 2018) and an SF₆ tracer release experiment (Messias et al., 2008), but not among the pathways suggested by Huang et al. (2020). Based on hydrographic observations and surface geostrophic velocities from satellite, Huang et al. (2020) found two branches of dense water flowing southward along the submarine ridges surrounding the central Iceland Sea: one current east of the Kolbeinsey Ridge and another east of the Jan Mayen Ridge. Our inversion suggests that the southward flow along the Jan Mayen Ridge primarily supplies overflow water to the Faroe Bank Channel (Section 6), while the southward flow along the eastern side of the Kolbeinsey Ridge could be represented by our other main pathway from the Greenland Sea (Fig. 11). Following this pathway, dense water formed in the Greenland Sea flows through the Jan Mayen Channel in the Mohn Ridge, then enters the Iceland Sea across the sloping Jan Mayen Ridge just south of Jan Mayen. Across the ridge, the pathway is centered between the 400 and 600 m isobaths and associated with up sloping isopycnals similar to the NIJ along the slope north of Iceland (not shown). Observations on the Jan Mayen Ridge are sparse, but two years (2007–2009) of moored measurements from the 800 m isobath indicate a consistent westward flow across the ridge below 300 m depth (Mork et al., 2014a). The average westward velocity (increasing with depth to about 1.2 cm s^{-1} near the bottom) was relatively weak,

but the location of the mooring was on the outskirts of the pathway identified by the inversion, where the slope along the crest of the ridge is substantially reduced. Within the Iceland Sea the water follows the cyclonic gyre circulation, which leads to a southward flow east of the Kolbeinsey Ridge. The majority of the water crosses the Kolbeinsey Ridge near the Spar Fracture Zone at depths of 400–800 m and feeds the NIJ as it progresses westward along the Iceland slope from northeast of Iceland to Denmark Strait.

The origin of the shelf break and separated branches of the East Greenland Current (dark and light blue circles, Fig. 10b) were also determined similar to the NIJ. Combined, $20 \pm 1\%$ of the overflow water from the EGC system at Hornbanki stems from the Atlantic Domain, while the Greenland and Iceland Seas account for $50 \pm 2\%$ and $26 \pm 6\%$, respectively (not shown). This indicates that substantial mixing occurs between the East Greenland Current and the interior basins (Strass et al., 1993; Rudels et al., 2002; Jeansson et al., 2008; Håvik et al., 2019) or that the current is directly ventilated along the pathway (Våge et al., 2018; Moore et al., 2022; Våge et al., 2022). To investigate where the mixing takes place we applied a dye to the northern part of the Atlantic Domain and quantified how the dye was diluted from Fram Strait to Denmark Strait (Fig. 12). At each latitude, we identified the core of the Atlantic-origin water in the East Greenland Current by Atlantic Domain contributions $\geq 25\%$. Grid cells satisfying this criterion coincided with the subsurface temperature and salinity maxima in the current as illustrated at the extended Hornbanki section (Fig. 10a). The mean contribution from the Atlantic Domain to this core volume, as well as the contributions from the Greenland and Iceland Seas were then estimated for each latitude (Fig. 12b). In Fram Strait, outside the Atlantic Domain, we find that approximately 60% of the East Greenland Current core volume is Atlantic-origin water. As the water progresses southwards, it is increasingly influenced by water from the interior Iceland and Greenland Seas. There are two latitude bands where substantial mixing with the interior basins and dilution of the Atlantic-origin water occur. This is in the Greenland Sea between 76°N and 75°N , and in the Iceland Sea between 69.5°N and 68.5°N , which corroborates the results of Strass et al. (1993) and Håvik

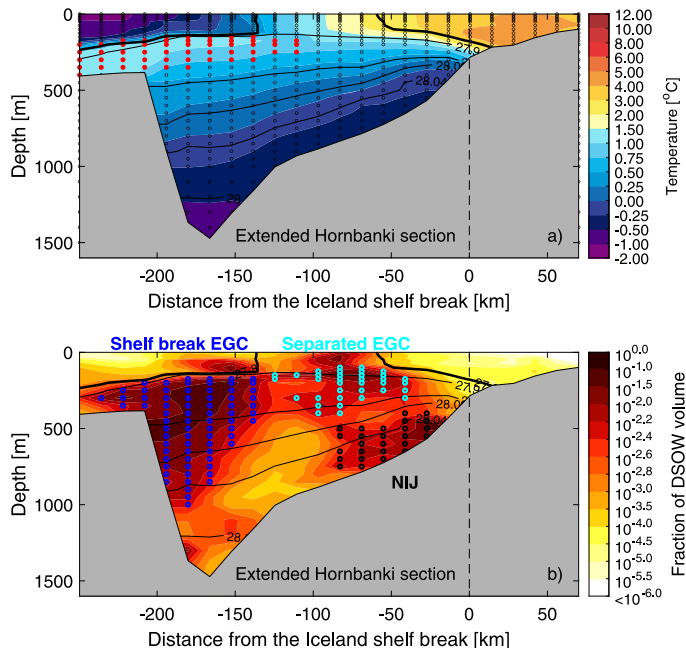


Fig. 10. Temperature (a) and fraction of DSO volume that has passed through the extended Hornbanki section (b). The location of the section is shown in Fig. 9. The black contours show potential density (σ_{θ} , kg m^{-3}). The black circles in (a) indicate the TMI resolution, while the red circles mark grid cells with a large ($\geq 25\%$) contribution from the Atlantic Domain. The colored circles in (b) mark grid cells identified as the NIJ (black), and as the shelf break (dark blue) and separated (light blue) East Greenland Current (EGC).

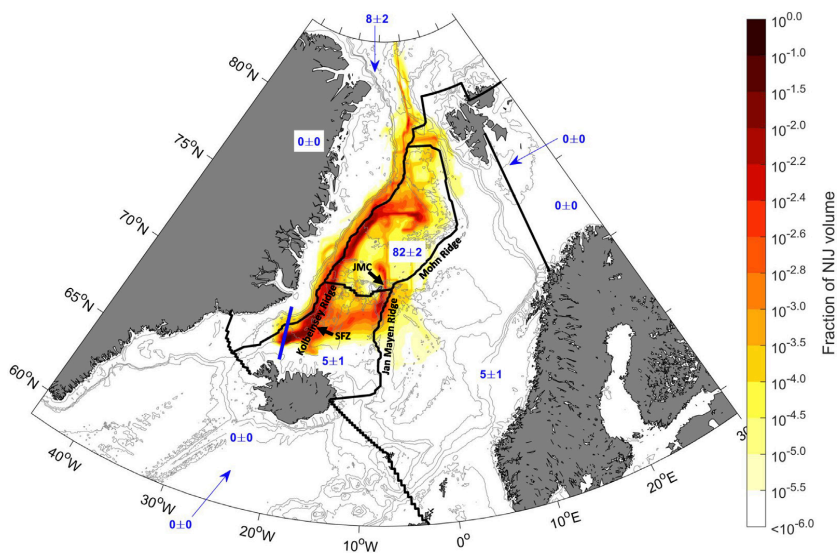


Fig. 11. Upstream pathways of the NIJ, shown as the fraction of NIJ volume that has passed through each horizontal location integrated over the entire water column. Note that the color scale is logarithmic. The blue numbers indicate the total contribution (in percent) from each surface region outlined in black and the lateral boundaries, and the uncertainty represents the sensitivity to the first guess of A (Section 3.2). The location of the extended Hornbanki section is indicated in blue, while the 500-, 1000-, 1500-, and 3000-m isobaths are shown as thin gray contours. The acronyms are: JMC=Jan Mayen Channel and SFZ=Spar Fracture Zone.

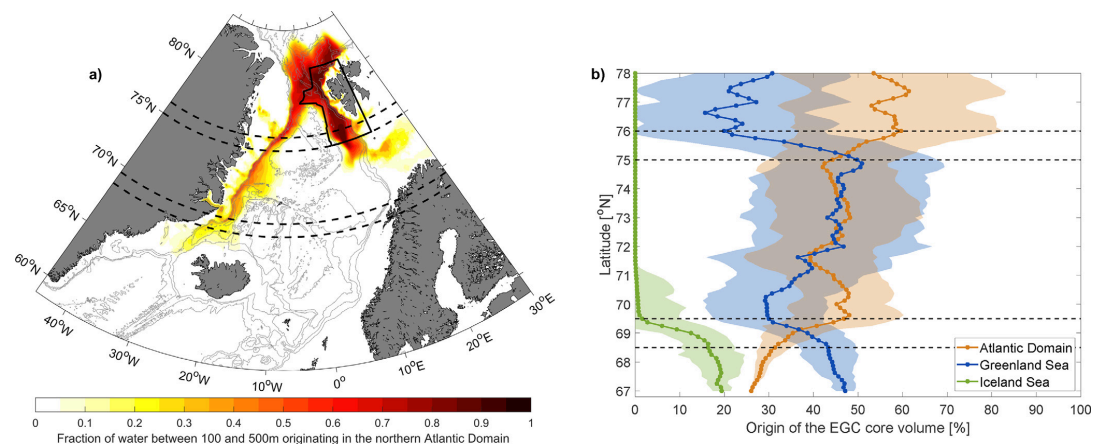


Fig. 12. Contribution from the northern part of the Atlantic Domain (solid black box) to the water column between 100 and 500 m depth (a) and along-stream contribution from the Atlantic Domain, Greenland Sea, and Iceland Sea to the East Greenland Current (EGC) core volume (b). The core volume was defined as all grid cells with $\geq 25\%$ contribution from the Atlantic Domain, which overlaps with the temperature and salinity maxima in the EGC as illustrated by red circles in Fig. 10a. The colored lines and shading in (b) represent the mean contribution from each source region and ± 1 standard deviation. The black dashed lines in both panels mark latitude bands where the EGC experiences significant mixing with ambient water masses, which dilutes the signal from the Atlantic Domain.

et al. (2019). Associated with these regions of enhanced mixing is a decline in Atlantic-origin water temperature (approaching -0.5 °C, not shown). Håvik et al. (2019) also found a strong decline in temperature around 69°N and attributed this to a local maximum in eddy activity and the bifurcation of the East Greenland Current into the separated and shelf break branches.

6. Origin and pathways of Faroe Bank Channel Overflow Water

A similar analysis was performed to determine the origin and pathways of the overflow water in the Faroe-Shetland Channel, upstream of the Faroe Bank Channel (Fig. 1). The Faroe-Shetland Channel section was chosen because the overflow water across the section is better represented with the TMI resolution due to the larger channel width. As the overflow water in the Faroe-Shetland Channel continues downstream into the Faroe Bank Channel, we will refer to it as Faroe Bank Channel Overflow Water (FBCOW). We note that there could be a slight dense bias in the FBCOW since the Faroe-Shetland Channel is nearly 200 m deeper than the Faroe Bank sill. The hydrographic and geochemical properties across the Faroe-Shetland Channel and the corresponding Z-scores are shown in Fig. 13. Warm, saline, low-oxygen AW dominates the upper part of the water column, while the deeper parts are occupied by cold and dense ($\sigma_\theta \geq 27.8$ kg m^{-3}) overflow water. Even though there is a positive salinity bias near the $\sigma_\theta = 27.8$ kg m^{-3} isopycnal (Fig. 13d), the depth of the isopycnal is well captured. There are substantial biases within the overflow water, at least relative to the uncertainty associated with temporal variability in the observations. The plume is slightly warmer than observed and the oxygen, nitrate, and phosphate concentrations are too large (Fig. 13b, f, h, j, respectively). It is important to note that the uncertainty related to temporal variability is low within the overflow plume, and the average TMI-to-observational differences are only 0.11 °C, 7.38 $\mu\text{mol kg}^{-1}$, 0.42 $\mu\text{mol kg}^{-1}$, and 0.06 $\mu\text{mol kg}^{-1}$ for temperature, oxygen, nitrate, and phosphate, respectively. The positive bias in both oxygen and nitrate/phosphate suggests that the stoichiometric ratio would need adjustment locally. As this is a local signal, using another stoichiometric ratio ($\Delta P : 16\Delta N : -138\Delta O$, Redfield et al., 1963) did not improve the

TMI solution. The results were similar both in terms of FBCOW biases and overflow water source contributions (not shown).

The origins of the FBCOW were determined by backtracking the overflow water in Faroe-Shetland Channel (Fig. 13) to the source regions. The contributions from the surface and lateral boundaries reveal that the two most important source regions of the FBCOW are the Greenland Sea ($46 \pm 8\%$) and the Arctic Ocean ($25 \pm 9\%$, Fig. 14). The FBCOW is denser than the DSOW (Figs. 7 and 15), hence a greater portion of the FBCOW originates in the Greenland Sea and Arctic Ocean, where the densest boundary conditions are located. Another difference between the origin of the FBCOW and the DSOW is the contribution from the Polar Domain. The majority of the fresh PSW is advected southwards by the East Greenland Current through Denmark Strait (Fig. 8e). Some of the PSW mixes with denser water and is entrained into the DSOW. Some PSW is also diverted into the interior basins of the Nordic Seas (Langehaug et al., 2022), but the amount is small and does not reach the Faroe-Shetland Channel. The Atlantic Domain accounts for $11 \pm 1\%$ of the FBCOW (Fig. 14), mainly from the southwestern part of the Norwegian Basin as suggested by Eldevik et al. (2009), while the Iceland Sea and the North Atlantic supply $10 \pm 1\%$ and $9 \pm 0\%$, respectively.

Based on the properties at the boundary locations with significant FBCOW contributions (fractions greater than $10^{-4.5}$, Fig. 14), we find that the overflow is composed of $28 \pm 1\%$ DW, $55 \pm 1\%$ IW, while the remaining $17 \pm 1\%$ was originally less dense than $\sigma_\theta = 27.8$ kg m^{-3} (Fig. 15). Of the DW, $3 \pm 8\%$ originates in the Greenland Sea (i.e., between 0 and 11%, as the contributions are always ≥ 0) and $25 \pm 9\%$ in the Arctic Ocean, while the IW contribution from the Greenland Sea and Arctic Ocean is $43 \pm 0\%$ and $0 \pm 0\%$, respectively. Fogelqvist et al. (2003) and McKenna et al. (2016) decomposed the FBCOW into Norwegian Sea IW and DW, and found that roughly 50% of the overflow is Norwegian Sea DW (which, in turn, stems from the Greenland Sea and the Arctic Ocean, Swift and Koltermann, 1988). According to Turrell et al. (1999) and Fogelqvist et al. (2003) the DW supply has decreased due to the cessation of very deep convection in the Greenland Sea. This could be one explanation for our overall lower DW and higher IW contributions in 2000–2019, which would imply

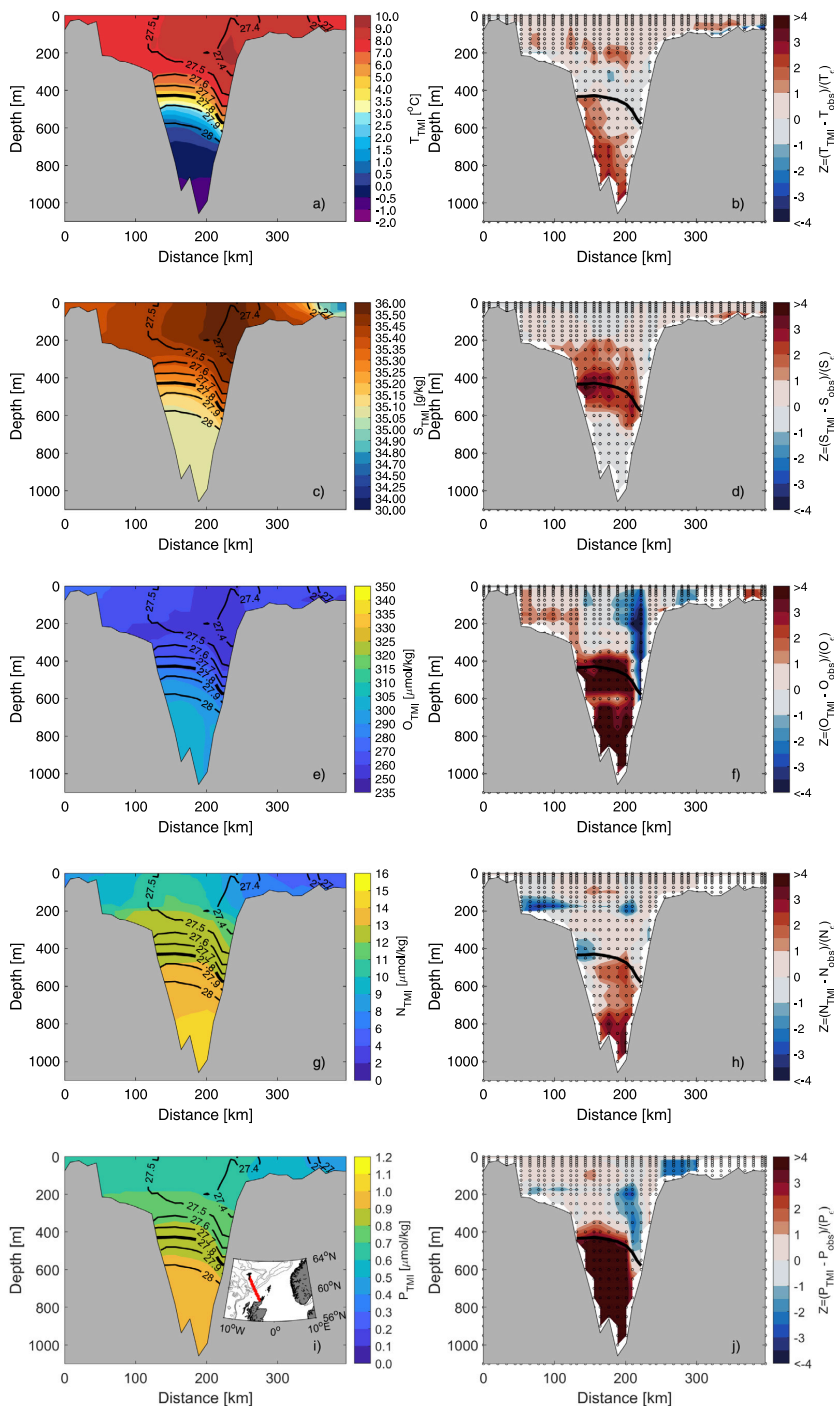


Fig. 13. TMI temperature (T), salinity (S), oxygen (O), nitrate (N), and phosphate (P) across the Faroe-Shetland Channel (left panels, the location of the section is indicated in red on the map inserted in panel i). The black contours show the potential density (σ_{θ}) field and the thick black line marks the $\sigma_{\theta} = 27.8 \text{ kg m}^{-3}$ isopycnal, which is the lower density limit of the overflow water. The corresponding observed overflow water limit is marked in the right panels along with the Z-score (Fig. 3) for each parameter. The TMI resolution is indicated by black circles. The x-axes show the distance along the section starting from the Faroe Islands.

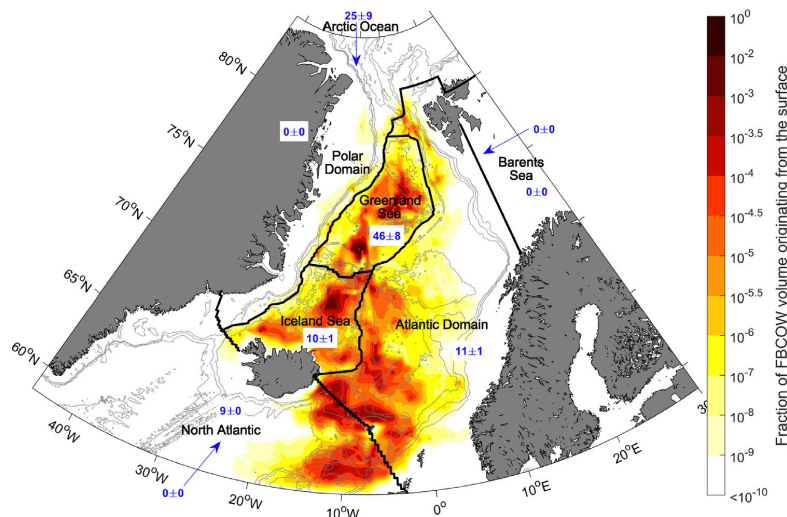


Fig. 14. Fraction of contribution from the surface to the Faroe Bank Channel Overflow Water. Note that the color scale is logarithmic. The blue numbers indicate the total contribution (in percent) from each surface region outlined in black and the lateral boundaries, and the uncertainty represents the sensitivity to the first guess of A (Section 3.2). The 500-, 1000-, 1500-, and 3000-m isobaths are shown as thin gray contours.

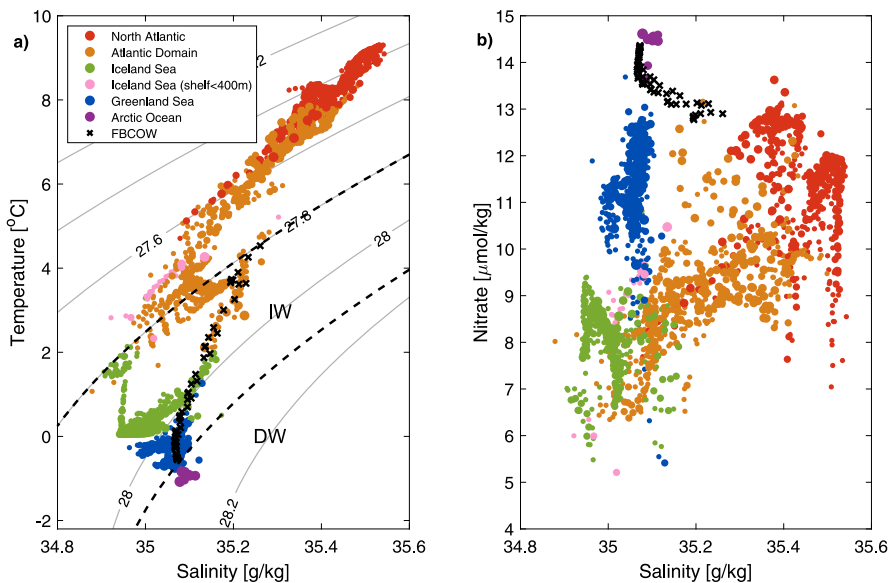


Fig. 15. Temperature and salinity (a), as well as nitrate (b) of the FBCOW (black crosses) and the source regions with fractional contributions exceeding $10^{-4.5}$ (Fig. 14). The source properties are color-coded by region, while the marker sizes are scaled by the magnitude of the contribution. The gray contours in (a) indicate potential density (σ_θ , kg m^{-3}), and the black dashed lines mark the $\sigma_\theta = 27.8 \text{ kg m}^{-3}$ and $\sigma_{0.5} = 30.444 \text{ kg m}^{-3}$ isopycnals.

that the entire FBCOW has become less dense. As for the DSOW, the contribution from the Arctic Ocean to the FBCOW is mainly classified as DW. This is incongruent with Jeansson et al. (2017), who determined a substantial intermediate-water contribution from the Arctic Ocean to the Norwegian Sea upstream of the Faroe-Shetland Channel.

The contribution from each geographical source region to the transect across the Faroe-Shetland Channel is shown in Fig. 16. The densest component of the overflow water is dominated by water formed in the Greenland Sea (above 40%) and the Arctic Ocean (approaching 60% in the deepest part of the trough), while the Iceland Sea and Atlantic Domain contribute to the less dense components (Fig. 16a, b,

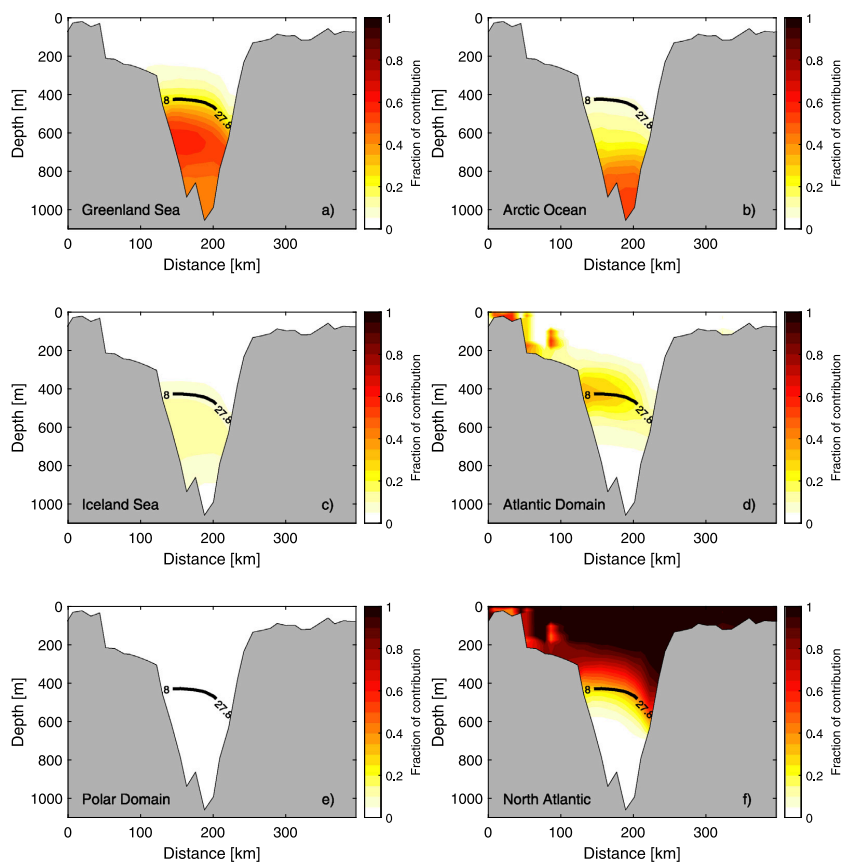


Fig. 16. Contributions from six different source regions to the transect across the Faroe-Shetland Channel (Fig. 13i). The lower density limit of the FBCOW is indicated by the $\sigma_\theta = 27.8 \text{ kg m}^{-3}$ isopycnal (black contour). The x-axes show distance along the section starting from the Faroe Islands.

c, and d, respectively). This is in agreement with Jeansson et al. (2017), who found that the primary sources of the lightest IW upstream in the Norwegian Sea were Atlantic-origin water and Arctic-origin water from the Iceland Sea, while the densest component mainly originated in the Greenland Sea and Arctic Ocean. The North Atlantic (Fig. 16f) dominates the supply of the AW in the upper part of the water column, and a small portion of this water is entrained into the overflow water.

The upstream pathways of the water masses constituting the FBCOW are visualized in Fig. 17. In accordance with Chafik et al. (2020) and Hátún et al. (2021), two main pathways of overflow water approach the Faroe-Shetland Channel, where they merge and continue toward the sill. One pathway approaches the channel from the northwest and the other from the northeast following the Norwegian continental slope. The FBCOW transported with the latter pathway also stems from the northwest farther upstream, as noted by Chafik et al. (2020). From Fig. 17 it is difficult to separate the individual pathways farther upstream. However, we can identify elevated FBCOW fractions along the GSR from northeast of Iceland toward the Faroe-Shetland Channel. This pathway corresponds to the recently documented IFSJ (Semper et al., 2020). Another major upstream pathway is visible all along the eastern side of the Jan Mayen Ridge. This is not a surprising result as

previous studies, both observational and numerical, show evidence of this southward-flowing current (e.g., Olsson et al., 2005; Voet et al., 2010; Serra et al., 2010; Köhl, 2010; Huang et al., 2020; Hátún et al., 2021). However, the contribution from this current to the FBCOW and how it connects water from the source regions to the Faroe Bank Channel are not well known.

To investigate the connection between the FBCOW, the various pathways, and the source regions, we constructed a section upstream of the Faroe-Shetland Channel (marked in blue in Fig. 17) where the two main pathways approaching the channel could easily be identified and distinguished. The fraction of FBCOW that has passed through this section is shown in Figs. 18a and b for the western and eastern legs of the section, respectively. In the western part of the section (Fig. 18a), there is a local maximum along the Faroe slope that we divided into the Faroe Current and the IFSJ by the $\sigma_\theta = 27.8 \text{ kg m}^{-3}$ isopycnal (Semper et al., 2020). The Faroe Current primarily consists of warm and saline AW from the North Atlantic ($39 \pm 2\%$) and the Atlantic Domain of the Nordic Seas ($50 \pm 1\%$), that recirculates around the Faroe Islands (Berk et al., 2013; Rossby et al., 2018). By the time this recirculating current reaches the Faroe-Shetland Channel, part of it is sufficiently dense to contribute to the lightest component of the FBCOW (Fig. 16d).

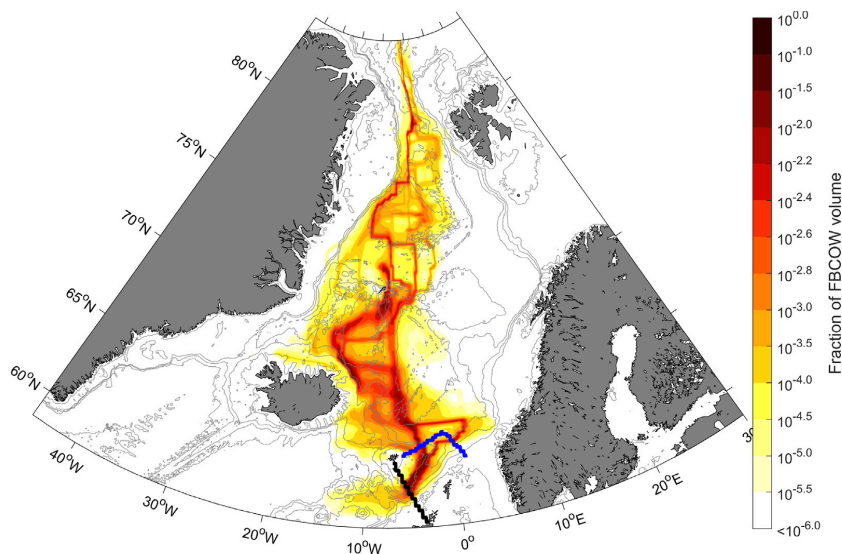


Fig. 17. Fraction of Faroe Bank Channel Overflow Water that has passed through each horizontal location, integrated over the entire water column. Note that the color scale is logarithmic. The location of the Faroe-Shetland Channel section is indicated in black, while the location of the section upstream of the Faroe-Shetland Channel is marked in blue. The 500-, 1000-, 1500-, and 3000-m isobaths are shown as thin gray contours.

The IFSJ was identified as water denser than $\sigma_\theta = 27.8 \text{ kg m}^{-3}$ (Fig. 18a). The maximum associated with this FBCOW core extends down to a density of $\sigma_\theta = 28.04 \text{ kg m}^{-3}$, which is lighter than the maximum density found by Semper et al. (2020) of $\sigma_\theta = 28.06 \text{ kg m}^{-3}$. Despite the light density bias, the upstream pathway of the core (Fig. 18c) closely resembles the IFSJ. Almost half of the IFSJ volume stems from the Greenland Sea ($48 \pm 3\%$), while $11 \pm 6\%$ originates in the Arctic Ocean. Water from both of these source regions exits the Greenland Sea through gaps in the Mohn Ridge (e.g., Shao et al., 2019; Wang et al., 2021). Then the majority of the water follows a similar route as that which supplies the NIJ (i.e., across the sloping Jan Mayen Ridge between the 400 and 600 m isobaths just south of Jan Mayen, then anticlockwise around the Iceland Sea, Fig. 11). Some of the water that exits the Greenland Sea deeper in the water column continues farther south along the Jan Mayen Ridge below 1000 m depth before entering the Iceland Sea through a deep gap in the ridge (Fig. 18c). The two pathways merge along the northeast Iceland slope approximately where the NIJ emerges (Semper et al., 2019). According to Semper et al. (2022), this is a region of enhanced eddy kinetic energy, which could be linked to the emergence of the NIJ as suggested by Våge et al. (2011), as well as the separation of the NIJ and IFSJ. Downstream from the region northeast of Iceland we observe several branches exiting the Iceland Sea. Semper et al. (2020) identified two cores of the IFSJ on the slope along the GSR, but the inversion suggests that several branches also exist farther offshore in line with Argo-float trajectories (Hátún et al., 2021). Mixing with ambient water along the pathways results in a $16 \pm 3\%$ and $18 \pm 1\%$ contribution from the Iceland Sea and Atlantic Domain, respectively, while the North Atlantic contributes $7 \pm 1\%$ to the IFSJ core.

Another pronounced FBCOW core was identified on the eastern side of the section upstream of the Faroe-Shetland Channel (Fig. 18b). This core is situated deep in the water column, between 1000 and 1300 m depth, and supplies the densest component of the FBCOW (corroborating the results of Chafik et al., 2020). Nearly all of the overflow

water following this pathway originates in the Arctic Ocean ($62 \pm 23\%$) and Greenland Sea ($36 \pm 23\%$). Dense water from the Arctic Ocean flows southward through Fram Strait and into the central Greenland Sea, where it continues southward across the Mohn Ridge along with water formed locally in the Greenland Sea (Fig. 18d). After exiting the Greenland Sea, the water follows the eastern side of the Jan Mayen Ridge towards the Faroe Islands, before turning eastwards with the cyclonic circulation in the Norwegian Basin (e.g., Hátún et al., 2021). When approaching the Norwegian slope and the Vøring Plateau, the overflow water is deflected south towards the Faroe-Shetland Channel. The total contribution from this deep pathway to the FBCOW was estimated to $24 \pm 3\%$, while the IFSJ and Faroe Current account for $58 \pm 3\%$ and $18 \pm 1\%$, respectively.

We note that several of these deep pathways appear very straight, with sharp edges (Fig. 18c). The TMI pathways are solely based on hydrographic and geochemical water-mass properties, and thus, they are not directly dynamically constrained. Weak or no gradients in water-mass properties, as typically observed at depth, may therefore result in non-physical straight pathways that sometimes cross isobaths to minimize distance. The contributions from the Greenland Sea and Arctic Ocean to the deep FBCOW pathway also have relatively high uncertainties (Fig. 18c). This is probably due to some GSDW, which was formed before the 2000–2019 period considered here, remaining at depth. As the inversion is not guided by strong data constraints to resolve this portion, the solution is more sensitive to the first guess of the pathway matrix A (Section 3.2).

7. Summary and conclusions

In this study we developed a regional version of the TMI inverse method to determine the origin, pathways, and final composition of the overflow water in Denmark Strait and the Faroe Bank Channel, the two main passages of dense water from the Nordic Seas to the

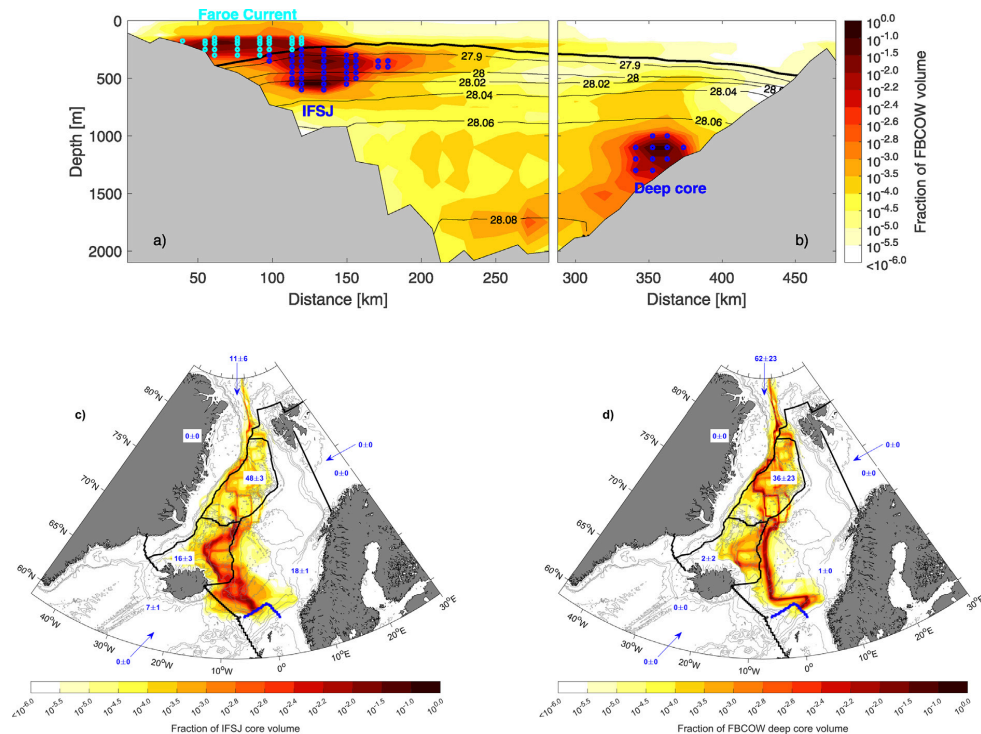


Fig. 18. Fraction of FBCOW volume that has passed through the section upstream of the Faroe-Shetland Channel (a and b). The black contours show potential density (σ_{θ} , kg m^{-3}). The colored circles in a) mark grid cells identified as the Faroe Current (light blue) and IFSJ (dark blue), while the dark blue circles in b) identify a deep FBCOW core. The upstream pathways of the identified IFSJ (c) and deep core (d) are shown as the fraction of volume that has passed through each horizontal location integrated over the entire water column. Note that the scale is logarithmic. The blue numbers in c) and d) indicate the total contribution (in percent) from each surface region outlined in black and the lateral boundaries, and the uncertainty represents the sensitivity to the first guess of A (Section 3.2).

deep North Atlantic (Østerhus et al., 2019). The TMI method includes both hydrographic and geochemical observations, as well as their geographical distributions, which is a major advantage compared to traditional decomposition methods (e.g., Mastropole et al., 2017; Tanhua et al., 2005; Jeansson et al., 2008) as it resolves also the pathways connecting the overflow plumes to their origins. The resulting overflow water compositions are not dependent on a few pre-defined end-members, but consider all surface and lateral boundary locations as potential sources. This is crucial to determine the importance of different source regions, as water-mass properties vary spatially, also within each source region (Figs. 7 and 15). Compared to earlier global TMI versions (Gebbie and Huybers, 2010; Gebbie, 2014), the regional high-resolution inversion was able to resolve the narrow overflow water pathways and complex bathymetry of the Nordic Seas, which gave a more realistic representation of the dense-water circulation. The pathways were also improved by implementing a more realistic first guess based on density and absolute geostrophic velocity estimated from hydrographic observations and satellite altimetry.

The majority of the DSOW originates in the Greenland Sea ($39 \pm 2\%$), the Iceland Sea ($20 \pm 3\%$), and the Atlantic Domain ($19 \pm 2\%$) of the Nordic Seas. Consistent with previous studies, we find that dense water from these source regions approaches Denmark Strait in the East Greenland Current and the North Icelandic Jet (Mauritzen, 1996; Våge et al., 2011; Harden et al., 2016). The East Greenland Current

transports warm and saline Atlantic-origin water from Fram Strait to Denmark Strait, but substantial mixing with the interior basins occurs along its path (Fig. 12, Strass et al., 1993; Rudels et al., 2002; Jeansson et al., 2008; Håvik et al., 2019). The mixing takes place primarily in the Greenland Sea between 75 and 76°N and in the Iceland Sea between 68.5 and 69.5°N , where the East Greenland Current bifurcates into the separated and shelf break branches (Våge et al., 2013; Håvik et al., 2019). At Hornbanki, 300 km upstream of Denmark Strait, only $20 \pm 1\%$ of the separated and shelf break East Greenland Current branches stem from the Atlantic Domain, while the Greenland and Iceland Seas account for $50 \pm 2\%$ and $26 \pm 6\%$, respectively. In agreement with Håvik et al. (2017), we also find an outer core of the East Greenland Current north of the West Jan Mayen Ridge. This outer core provides an important pathway for dense water formed in the central Greenland Sea towards Denmark Strait. The overflow water supplied by the NIJ originates primarily in the Greenland Sea ($82 \pm 2\%$), corroborating the results of Huang et al. (2020). This water follows two distinct pathways from the Greenland Sea to the slope north of Iceland: the outer core of the East Greenland Current and another, previously unknown, pathway across the Jan Mayen Ridge into the Iceland Sea. Within the Iceland Sea the water follows the cyclonic gyre, which leads to a southward flow along Kolbeinsey Ridge to the slope north of Iceland.

Although the upstream sources of the DSOW are in broad agreement with previous studies, we find a substantially lower contribution from

the Arctic Ocean than indicated by [Tanhua et al. \(2005\)](#) and [Jeansson et al. \(2008\)](#), who also included both hydrographic and geochemical observations. In addition to uncertainty in their contributions related to the spatial variability of water masses, the discrepancy is likely a result of temporal variability. Neither [Tanhua et al. \(2005\)](#) and [Jeansson et al. \(2008\)](#) nor the TMI solution properly account for temporal variability in water-mass properties. Substantial short-term variability is observed in both volume transport and hydrographic properties of the DSO (e.g., [Jochumsen et al., 2017](#); [Mastropole et al., 2017](#); [Lin et al., 2020](#)) and the production and hydrographic properties of the source water masses vary inter-annually ([Våge et al., 2015](#); [Lauvset et al., 2018](#); [Jeansson et al., 2017](#); [Brakstad et al., 2019](#); [Mork et al., 2019](#)). Both [Tanhua et al. \(2005\)](#) and [Jeansson et al. \(2008\)](#) performed sensitivity simulations, where the end-member properties were allowed to vary within the variance of each parameter, to validate the effect of temporal variability in their source water compositions. This indicated relative mean errors of 30%–40%, and higher for some of the Arctic Ocean end-members ([Jeansson et al., 2008](#)). Similar sensitivity simulations with the TMI inversion would be computationally demanding, which is the reason our uncertainty estimates represent only the uncertainty related to the first guess of the pathway matrix and not temporal variability (Section 3.2). It is important to note that uncertainties related to temporal variability in hydrographic and geochemical properties were included as constraints in the inversion when optimizing the 2000–2019 winter-mean solution.

The two main contributors to the FBCOW is dense water formed in the Greenland Sea ($46 \pm 8\%$) and the Arctic Ocean ($25 \pm 9\%$). These source regions also supply the densest part of the overflow, while the less dense components stem from the Iceland Sea ($10 \pm 1\%$), the Atlantic Domain ($11 \pm 1\%$), and the North Atlantic ($9 \pm 0\%$). Dense water formed in the Greenland Sea and Arctic Ocean flows southward from the Greenland Sea along two distinct pathways. One corresponds to the recently documented IFSJ ([Semper et al., 2020](#)) and one follows the eastern side of the Jan Mayen Ridge (in accordance with e.g., [Olsson et al., 2005](#); [Voet et al., 2010](#); [Serra et al., 2010](#); [Huang et al., 2020](#); [Hátún et al., 2021](#)). Half ($48 \pm 3\%$) of the FBCOW transported with the IFSJ originates in the Greenland Sea, while $11 \pm 6\%$ stems from the Arctic Ocean. The majority of these dense waters flow across the sloping Jan Mayen Ridge and cyclonically around the Iceland Sea, similar to the dense water that supplies the NIJ. Some mixing occurs along the IFSJ path, which results in a $16 \pm 3\%$ contribution from the Iceland Sea, $18 \pm 1\%$ from the Atlantic Domain, and $7 \pm 1\%$ from the North Atlantic. The pathway along the Jan Mayen Ridge turns east and crosses over to the Norwegian continental slope, where it follows the eastern margin southwards to the Faroe-Shetland Channel. In agreement with [Chafik et al. \(2020\)](#), we find that this pathway is situated deep (>1000 m) in the water column and supplies the densest component of the FBCOW. In total, this pathway accounts for $24 \pm 3\%$ of the FBCOW, while the IFSJ supplies $58 \pm 3\%$. The remaining portion is AW that is densified in the Faroe Current and recirculates around the Faroe Islands ($18 \pm 1\%$).

The fractional contributions from the Greenland Sea and Arctic Ocean to the overflow water transported by the IFSJ may be underestimated due to the light density bias in the IFSJ core. [Semper et al. \(2020\)](#) used one survey of high-resolution (2.5–10 km) hydrographic transects following the IFSJ to document its structure and properties. Based on 30 years of repeat hydrographic transects north of the Faroe Islands, they found that only 38 of the 120 surveys captured the upsloping dense water associated with the current due to the lower horizontal resolution (20 km). Hence, the densest water in the IFSJ is not well captured north of the Faroe Islands in the observations, which in turn impacts the TMI solution. Nevertheless, the TMI solution can help identify key locations where high-resolution observations are needed to properly resolve the currents feeding the overflows, such as north of the Faroe Islands and along the Jan Mayen Ridge.

The overflow water pathways resolved by the inversion represent the steady-state circulation that best fits the late-winter hydrographic and geochemical properties in the Nordic Seas between 2000 and 2019. Although water-mass properties vary within this period, it is considered sufficiently stable in terms of dense-water formation and water column structure (i.e., [Brakstad et al., 2019](#); [Somavilla, 2019](#)). Considering the last 50 years, substantial changes have been observed in water-mass production and properties in the Nordic Seas (e.g., [Eldevik et al., 2009](#); [Våge et al., 2015](#); [Lauvset et al., 2018](#); [Brakstad et al., 2019](#); [Smedsrud et al., 2022](#); [Våge et al., 2022](#)). Multiple inversions covering different decades or the inclusion of an age tracer similar to [Schlitzer \(2007\)](#) or [Gebbie and Huybers \(2012\)](#) are needed to determine how the time-evolving source regions and flow structure have influenced the overflows. The inclusion of an age tracer would also make it possible to estimate the residence times and the rate of exchange between water masses, which could be used to diagnose the propagation of heat or anthropogenic carbon into the deep ocean as demonstrated by [Davila et al. \(2022\)](#) with a global version of the TMI method. As opposed to numerical simulations, the TMI method observationally constrains and quantifies the net effect of advection and diffusion on the distribution of water masses ([Gebbie and Huybers, 2010](#)). Our results provide a step toward understanding how the dense overflow waters are supplied at present. This is crucial to better understand the impact of climate-driven changes, such as global warming and sea-ice retreat, which are projected to reduce dense-water formation in the interior of the Nordic Seas in the future ([Moore et al., 2015, 2022](#); [Bretonet et al., 2022](#)).

Declaration of competing interest

The authors declare that they have no known competing financial interests or personal relationships that could have appeared to influence the work reported in this paper.

Data availability

Access to the individual hydrographic and geochemical data sources are listed in [Table 1](#). The combined and quality-controlled data set, covering the period 1950–2019, is available at the Norwegian Marine Data Centre (NMDC; <https://doi.org/10.21335/NMDC-1271328906>). The late-winter (February to April) climatology for the period 2000–2019 is available at <https://doi.org/10.21335/NMDC-1518531676>. Sea-ice concentrations were obtained from [Walsh et al. \(2015\)](#), while surface geostrophic velocities from satellite were obtained from the Copernicus Marine Environment Monitoring Service (<http://marine.copernicus.eu>).

Acknowledgments

Support for this work was provided by the Trond Mohn Foundation under grant agreement BFS2016REK01 (AB and KV) and the Office of Naval Research Global (award number N62909-22-1-2023, AB and KV). GG was supported by NASA project 80NSSC20K0419 and U.S. NSF OCE-1850753.

Appendix A. Observational quality control

All hydrographic profiles were required to include both temperature and salinity measurements within the range -2 – 30 °C and 0 – 36 g kg $^{-1}$, respectively. Profiles with density inversions exceeding 0.05 kg m $^{-3}$ were excluded unless the inversion was associated with a single data spike, in which case the spike was removed. We also required positive concentrations for the geochemical parameters and that all profiles had a minimum length of 3 data points. The same data are often stored in multiple archives. In many cases, however, the profiles are not exact duplicates. They can be interpolated to different vertical resolutions, truncated to different depths, or be ship-board CTD measurements and

bottle data recorded at the same cast (e.g., Behrendt et al., 2018). The position, time, and data can also vary slightly if they are rounded to different decimals. To detect these duplicates we compared each profile (position, time, and hydrography) to all other profiles within 1° longitude/latitude and ± 5 days. Each profile pair that was compared was truncated to the depth range shared by both profiles and interpolated to the same vertical resolution. Profiles were considered duplicates if they were acquired less than 0.5 days and 1 km apart or if the temperature and salinity profiles matched to the second and third decimal, respectively. Several of the duplicates were visually inspected. This was necessary to detect, for example, truncated duplicates (or bottle data) that had been linearly interpolated to higher resolution. In general, we kept the profile with most information and excluded truncated and hydrographic bottle data. If a profile pair had similar resolution we retained the profile from the most original source. We also prioritized data from UDASH (Behrendt et al., 2018), which have already gone through a thorough quality control.

After erroneous and duplicate data were removed, we divided the dataset into three different periods (1950–1979, 1980–1999, and 2000–2019) that were inspected for outliers separately. Each hydrographic profile was compared to all other profiles from the same period within a radius of 110 km (approximately 1° of latitude, Våge et al., 2013). In the Nordic Seas water-mass properties tend to vary more across than along topographic gradients because of the close alignment between currents and bathymetry (Nøst and Isachsen, 2003). This was accounted for by adjusting the distance to the other profiles (r) according to Davis (1998), Skagseth and Mork (2012), and Våge et al. (2013) as:

$$r^2 = |x_g - x_o|^2 + \left| 3\lambda \frac{H_g - H_o}{H_g + H_o} \right|^2, \quad (\text{A.1})$$

where $x_g(x_o)$ is the geographical position of the profile in question (all other profiles) and $H_g(H_o)$ is the corresponding depth based on ETOPO1 (Amante and Eakins, 2009). The topographic parameter $\lambda = 100$ km (Lavender et al., 2005; Voet et al., 2010; Skagseth and Mork, 2012; Våge et al., 2013). The difference in bottom depth determines the magnitude of the adjustment, and the result is an effective radius that is increased along isobaths. All profiles within an effective radius of 110 km were then interpolated onto a common vertical coordinate with 5-m resolution. Profiles that differed from the mean, at any depth, by more than six standard deviations were considered outliers and removed.

A slightly different procedure was used for the geochemical data due to the generally lower vertical and horizontal resolution. All geochemical profiles were interpolated onto 46 depth levels with intervals ranging from 10 m near the surface to 250 m at depth (same as the TMI resolution, Fig. C.1f), before the mean and standard deviation in each time period were calculated. Profiles were then identified as outliers and removed if they differed from the mean by more than six standard deviations.

Appendix B. Mixed-layer depths

For the Iceland and Greenland Seas we used late-winter (February–April) mixed-layer depths from Våge et al. (2015) and Brakstad et al. (2019), respectively. These were determined by a procedure involving two independent automated routines: one based on a density-difference criterion (Nilsen and Falck, 2006) and one based on the curvature of the temperature profile (Lorbacher et al., 2006). If neither of the automated routines accurately identified the base of the mixed layer, which was verified by visual inspection of each hydrographic profile, it was determined by a manual procedure developed by Pickart et al. (2002). This manual procedure was used for 44% (Våge et al., 2015) and 39% (Brakstad et al., 2019) of the profiles in the Iceland and Greenland Seas, respectively. The automated routines performed well for profiles having a pronounced density gradient below the base of the mixed layer, but this is often not the case during winter in the Iceland

and Greenland Seas where the entire water column is weakly stratified. The same semi-automatic procedure was employed here to update the Iceland and Greenland Seas mixed-layer databases such that the entire 2000–2019 period was covered.

For the rest of the domain, where the density stratification is stronger, late-winter mixed-layer depths were estimated based on the density-difference criterion (Nilsen and Falck, 2006). That is, the base of the mixed layer was identified as the depth where the increase in potential density from the surface reached $\Delta\rho = \rho(T_0 - \Delta T, S_0) - \rho(T_0, S_0)$. The density difference $\Delta\rho$ varies with measured surface temperature (T_0) and salinity (S_0), which provides more accurate results than using a constant value (de Boyer Montégut et al., 2004; Nilsen and Falck, 2006). As de Boyer Montégut et al. (2004), Våge et al. (2015), and Brakstad et al. (2019) we used $\Delta T = 0.2$ °C.

The late-winter mixed-layer properties were interpolated onto a regular 1/3° longitude by 1/8° latitude grid as described in Appendix C (Eq. (C.1)). Only the 75% deepest mixed layers were included in each grid cell to remove re-stratified profiles and profiles taken prior to the onset of convection. Changing this limit by $\pm 10\%$ had an impact almost exclusively on the Greenland Sea gyre and the average difference within the gyre was ± 50 m, which is small compared to the total mean mixed-layer depth (555 m, within the white contour in Fig. B.1). For polar, ice-covered regions where winter data are scarce, we used the available data to estimate mean mixed-layer properties. These were then applied to the entire sea-ice-covered area (north of the annual-mean 50% sea-ice concentration contour marked in blue in Fig. B.1). The sea-ice concentration data were obtained from the National Snow and Ice Data Center (Walsh et al., 2015, 2017). The final gridded mixed-layer product shown in Fig. B.1 was smoothed by convolution with a Gaussian window of size $9 \times (1/3^\circ$ longitude and $1/8^\circ$ latitude).

Appendix C. Gridding and uncertainty estimates

All 2000–2019 observations of temperature, salinity, oxygen, nitrate, and phosphate were modified to represent late-winter conditions (Section 2.2) and used to construct the three-dimensional fields included in the TMI inversion. The value in each grid cell was computed from all measurements within an effective radius of 50 km. As in Appendix A (Eq. (A.1)), the effective radius was increased along isobaths to account for the greater correlation length scales along topography. The effective radius and the topographic parameter λ were modified to 120 km and 300 km, respectively, in the sea-ice covered area (north of the annual mean 50% sea-ice concentration contour, Fig. B.1). This was done to improve the representation of the East Greenland Current in the inversion, which was generally not well constrained due to the sparse data coverage in this region (Fig. 2). The result of both increased radius and λ was that more observations were included in each grid cell, but only from along the bathymetry.

The average value \bar{x}_i in each grid cell i was weighted by the inverse distance as:

$$\bar{x}_i = \frac{\sum_{t=1}^{N_i} \omega_{it} x_{it}}{\sum_{t=1}^{N_i} \omega_{it}} = \sum_{t=1}^{N_i} \omega'_{it} x_{it}, \quad (\text{C.1})$$

where x_{it} is measurement number t and N_i is the total number of observations contributing to the weighted average. ω_{it} is the inverse distance to each observation and $\omega'_{it} = \omega_{it} / \sum_{t=1}^{N_i} \omega_{it}$.

The uncertainty of the final gridded product representing the climatological winter conditions between 2000 and 2019 depends on the amount of observations included in the estimate and their variance. In general, the uncertainty decreases with depth due to the lower variance at depth and with increased number of observations. For each grid cell we estimated the variance $\hat{\sigma}_i^2$ as:

$$\hat{\sigma}_i^2 = \frac{1}{N - m} \sum_{l=1}^m \sum_{t=1}^{N_l} (x_{it} - \bar{x}_i)^2, \quad (\text{C.2})$$

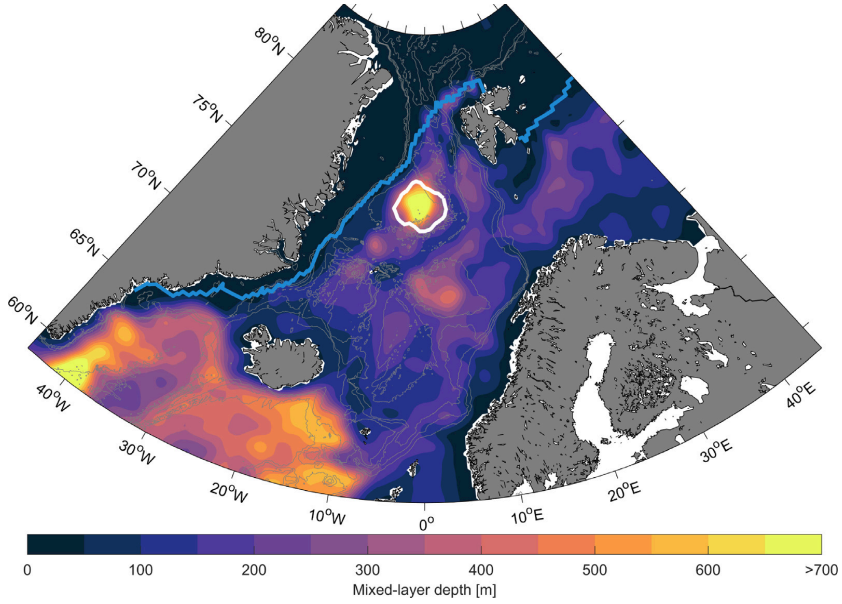


Fig. B.1. Late-winter (February–April) mixed-layer depth between 2000 and 2019. The blue line marks the annual-mean (2000–2013) 50% sea-ice concentration contour from Walsh et al. (2015), while the white contour outlines the Greenland Sea gyre (Moore et al., 2015). The 500-, 1000-, 1500-, and 3000-m isobaths are shown as thin gray contours.

where N is the total number of observations and m is the total number of ocean grid cells at the corresponding depth level. That is, all observations across the entire domain at each depth level were used to estimate the expected variance for each grid cell at the same level. The uncertainty ε_i was then defined as:

$$\varepsilon_i = \hat{\sigma}_i \sqrt{\sum_{t=1}^{N_i} (\omega_{it})^2}, \quad (\text{C.3})$$

which decreases with number of observations (weighted according to distance to the grid cell in question). The resulting uncertainty profiles (overall means and standard deviations) are shown in Fig. C.1.

Appendix D. First guess of the pathway matrix A

The first guess of the mass fractions m that form the pathway matrix A was constructed based on gradients in potential density and the geostrophic stream function. To obtain absolute geostrophic velocities we used surface geostrophic velocity from satellite altimeter data as reference (Section 3.2, Fig. D.1). The surface geostrophic velocity is very patchy in sea-ice covered areas due to large uncertainty. The hydrographic data coverage is also very sparse in the same region (Fig. 2). As a consequence, we decided to keep the isotropic first guess (Gebbie and Huybers, 2010; Gebbie, 2014) in areas with annual-mean sea-ice concentration exceeding 80% (north of the blue line in Fig. D.1). In the open ocean we assumed that large gradients in potential density and the geostrophic stream function lead to weak exchange between neighboring grid cells (i.e. small mass fractions).

Half of the mass fractions were determined by gradients in potential density (σ_θ), while the remaining half was determined by gradients in the geostrophic stream function (ψ). For each interior grid cell i , the

sum of the mass fractions m_{ij} from the neighboring grid cells j can be expressed as:

$$\sum_{j=1}^N m_{ij} = \frac{1}{2} \sum_{j=1}^N m_{ij}^{\Delta\sigma_\theta} + \frac{1}{2} \sum_{j=1}^N m_{ij}^{\Delta\psi} = 1, \quad (\text{D.1})$$

where $m_{ij}^{\Delta\sigma_\theta}$ and $m_{ij}^{\Delta\psi}$ are the mass fractions determined by gradients in σ_θ and ψ , respectively. Below the mixed layer, $m_{ij}^{\Delta\sigma_\theta}$ was calculated based on gradients in σ_θ as:

$$m_{ij}^{\Delta\sigma_\theta} = \frac{|\Delta\sigma_{\theta ij, \max}| - |\Delta\sigma_{\theta ij}| + 10^{-4}}{\sum_{j=1}^N (|\Delta\sigma_{\theta ij, \max}| - |\Delta\sigma_{\theta ij}| + 10^{-4})}, \quad (\text{D.2})$$

where $\Delta\sigma_{\theta ij}$ is the density difference between the grid cell in question (i) and its neighbor j . $\Delta\sigma_{\theta ij, \max}$ is the density difference to the neighbor with the largest difference. That is, a larger gradient leads to a smaller mass fraction and weaker exchange. The constant 10^{-4} is added for regularization. Vertical mixing dominates within the mixed layer, where the density is homogeneous. Hence, we prescribed $m_{ij}^{\Delta\sigma_\theta}$ to represent exchange with the neighbor located vertically above the grid cell in question.

The mass fractions $m_{ij}^{\Delta\psi}$ based on the geostrophic stream function only include horizontal contributions in the direction of the geostrophic flow. That is, if the geostrophic flow was from the north-east, the only non-zero mass fractions $m_{ij}^{\Delta\psi}$ would be the mass fractions from the northern and eastern neighbors. The magnitude of the non-zero mass fractions was calculated as:

$$m_{ij}^{\Delta\psi_{x(y)}} = \frac{|\Delta\psi_{x(y)}|}{\sum_{j=1}^N (|\Delta\psi_{xy}|)}, \quad (\text{D.3})$$

where $\Delta\psi_x$ and $\Delta\psi_y$ are the longitudinal and latitudinal differences in the geostrophic stream function, respectively. This means that if $\Delta\psi_x > 0$ (southward geostrophic flow component), the neighbor to the north

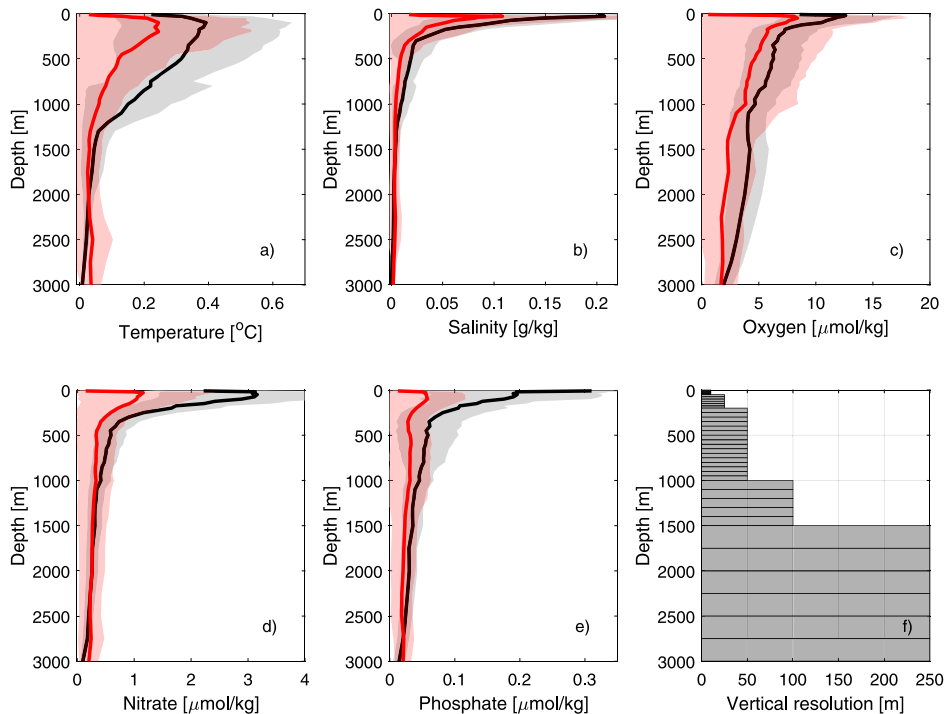


Fig. C.1. Mean observational uncertainty (black) and mean misfit (red) between the TMI and observed temperature (a), salinity (b), oxygen (c), nitrate (d), and phosphate (e) in the upper 3000 m of the water column. The shading indicates ± 1 standard deviation. The TMI vertical resolution is shown by the gray bars in f).

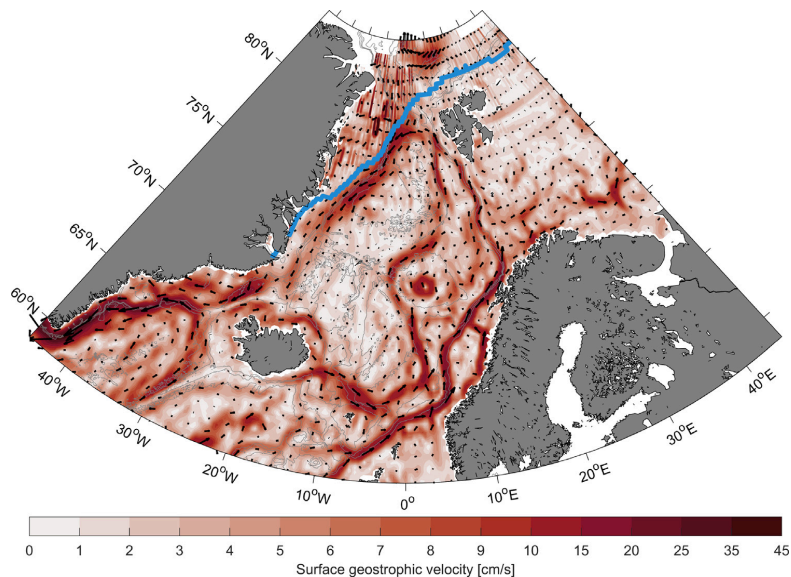


Fig. D.1. Annual-mean surface geostrophic velocity between 2000 and 2019 from the gridded satellite altimeter product. The blue line indicates the mean (2000–2013) 80% sea-ice concentration contour from Walsh et al. (2015). The 500-, 1000-, 1500-, and 3000-m isobaths are shown as thin gray contours.

contributes with a non-zero mass fraction with the magnitude m_{ij}^{dw} . The first guess of the pathway matrix A based on $m_{ij}^{d\sigma\theta}$ and m_{ij}^{dw} resulted in more advective pathways and a better (less diffuse) representation of the ocean state. The running time of the inversion was also significantly reduced.

References

- Aagaard, K., Swift, J.H., Carmack, E.C., 1985. Thermohaline circulation in the Arctic Mediterranean Seas. *J. Geophys. Res.* 90 (NC3), 4833–4846. <http://dx.doi.org/10.1029/JC090iC03p04833>.
- Amante, C., Eakins, B.W., 2009. ETOPO1 1 Arc-Minute Global Relief Model: Procedures, Data Sources, and Analysis. Technical Report, National Geophysical Data Center, NOAA. <http://dx.doi.org/10.7289/V5C8Z276M>, NOAA Technical Memorandum NESDIS NGDC-24.
- Anderson, L.A., Sarmiento, J.L., 1994. Redfield ratios of remineralization determined by nutrient data analysis. *Glob. Biogeochem. Cycles* 8 (1), 65–80. <http://dx.doi.org/10.1029/93GB03318>.
- Behrendt, A., Sumata, H., Rabe, B., Schauer, U., 2018. UDASH—unified database for Arctic and Subarctic hydrography. *Earth Syst. Sci. Data* 10 (2), 1119–1138. <http://dx.doi.org/10.5194/essd-10-1119-2018>.
- Berx, B., Hansen, B., Østerhus, S., Larsen, K.M., Sherwin, T., Jochumsen, K., 2013. Combining in situ measurements and altimetry to estimate volume, heat and salt transport variability through the Færoe-Shetland Channel. *Ocean Sci.* 9 (4), 639–654. <http://dx.doi.org/10.5194/os-9-639-2013>.
- Brakstad, A., Våge, K., Håvik, L., Moore, G.W.K., 2019. Water mass transformation in the Greenland Sea during the period 1986–2016. *J. Phys. Oceanogr.* 49 (1), 121–140. <http://dx.doi.org/10.1175/JPO-D-17-0273.1>.
- Bretones, A., Nisancioglu, K.H., Jensen, M.F., Brakstad, A., Yang, S., 2022. Transient increase in Arctic deep-water formation and ocean circulation under sea ice retreat. *J. Clim.* 35 (1), 109–124. <http://dx.doi.org/10.1175/JCLI-D-21-0152.1>.
- Casanova-Masjoan, M., Pérez-Hernández, M.D., Pickart, R.S., Valdimarsson, H., Ólafsdóttir, S.R., Macrander, A., Grisolia-Santos, D., Torres, D.J., Jónsson, S., Våge, K., Lin, P., Hernández-Guerra, A., 2020. Along-stream, seasonal, and interannual variability of the North Icelandic Irminger Current and East Icelandic Current around Iceland. *J. Geophys. Res.: Oceans* 125 (9), e2020JC016283. <http://dx.doi.org/10.1029/2020JC016283>.
- Chafik, L., Hátún, H., Kjellsson, J., Larsen, K.M.H., Rossby, T., Berx, B., 2020. Discovery of an unrecognized pathway carrying overflow waters toward the Færoe Bank Channel. *Nature Commun.* 11 (1), 1–10. <http://dx.doi.org/10.1038/s41467-020-17426-8>.
- Chafik, L., Rossby, T., 2019. Volume, heat, and freshwater divergences in the subpolar North Atlantic suggest the Nordic Seas as key to the state of the meridional overturning circulation. *Geophys. Res. Lett.* 46, 4799–4808. <http://dx.doi.org/10.1029/2019GL082110>.
- Davila, X., Gebbie, G., Brakstad, A., Lauvset, S.K., McDonagh, E.L., Schwinger, J., Olsen, A., 2022. How is the ocean anthropogenic carbon reservoir filled? *Glob. Biogeochem. Cycles* 36 (5), e2021GB007055. <http://dx.doi.org/10.1029/2021GB007055>.
- Davis, R.E., 1998. Preliminary results from directly measuring middepth circulation in the tropical and South Pacific. *J. Geophys. Res.* 103 (C11), 24619–24639. <http://dx.doi.org/10.1029/98JC01913>.
- de Boyer Montégut, C., Madec, G., Fischer, A.S., Lazar, A., Iudicone, D., 2004. Mixed layer depth over the global ocean: an examination of profile data and a profile-based climatology. *J. Geophys. Res.: Oceans* 109 (C12), <http://dx.doi.org/10.1029/2004JC002378>.
- de Jong, M.F., Søiland, H., Bower, A.S., Furey, H.H., 2018. The subsurface circulation of the Iceland sea observed with RAFOS floats. *Deep-Sea Res.* 141, 1–10. <http://dx.doi.org/10.1016/j.dsr.2018.07.008>.
- Dickson, R.R., Brown, J., 1994. The production of North Atlantic deep water: sources, rates, and pathways. *J. Geophys. Res.* 99 (C6), 12319–12341. <http://dx.doi.org/10.1029/94JC00530>.
- Eldevik, T., Nilsen, J.E.Ø., Iovino, D., Olsson, K.A., Sandø, A.B., Drange, H., 2009. Observed sources and variability of Nordic Seas overflow. *Nat. Geosci.* 2 (6), 405–409. <http://dx.doi.org/10.1038/ngeo518>.
- Fogelqvist, E., Blindheim, J., Tanhua, T., Østerhus, S., Buch, E., Rey, F., 2003. Greenland - Scotland overflow studied by hydro-chemical multivariate analysis. *Deep-Sea Res.* 50 (1), 73–102. [http://dx.doi.org/10.1016/S0967-0637\(02\)00131-0](http://dx.doi.org/10.1016/S0967-0637(02)00131-0).
- Frigstad, H., Andersen, T., Bellerby, R.G.J., Silyakova, A., Hessen, D.O., 2014. Variation in the seston C:N ratio of the Arctic Ocean and pan-Arctic shelves. *J. Mar. Syst.* 129, 214–223. <http://dx.doi.org/10.1016/j.jmarsys.2013.06.004>.
- García-Quintana, Y., Grivault, N., Hu, X., Myers, P.G., 2021. Dense water formation on the Icelandic shelf and its contribution to the North Icelandic Jet. *J. Geophys. Res.: Oceans* 126 (8), e2020JC016951. <http://dx.doi.org/10.1029/2020JC016951>.
- Gebbie, G., 2014. How much did Glacial North Atlantic Water shoal? *Paleoceanography* 29 (3), 190–209. <http://dx.doi.org/10.1002/2013PA002557>.
- Gebbie, G., Huybers, P., 2010. Total matrix intercomparison: a method for determining the geometry of water-mass pathways. *J. Phys. Oceanogr.* 40 (8), 1710–1728. <http://dx.doi.org/10.1175/2010JPO4272.1>.
- Gebbie, G., Huybers, P., 2011. How is the ocean filled? *Geophys. Res. Lett.* 38 (6), <http://dx.doi.org/10.1029/2011GL046769>.
- Gebbie, G., Huybers, P., 2012. The mean age of ocean waters inferred from radiocarbon observations: sensitivity to surface sources and accounting for mixing histories. *J. Phys. Oceanogr.* 42 (2), 291–305. <http://dx.doi.org/10.1175/JPO-D-11-043.1>.
- Gilbert, J.C., Lemaréchal, C., 1989. Some numerical experiments with variable-storage quasi-Newton algorithms. *Math. Program.* 45 (1), 407–435. <http://dx.doi.org/10.1007/BF01589113>.
- Glover, D.M., Jenkins, W.J., Doney, S.C., 2011. *Modeling Methods for Marine Science*. Cambridge University Press.
- Hansen, B., Østerhus, S., 2000. North Atlantic-Nordic Seas exchanges. *Prog. Oceanogr.* 45 (2), 109–208. [http://dx.doi.org/10.1016/S0079-6611\(99\)00052-X](http://dx.doi.org/10.1016/S0079-6611(99)00052-X).
- Harden, B.E., Pickart, R.S., Valdimarsson, H., Våge, K., de Steur, L., Richards, C., Bahr, F., Torres, D., Børve, E., Jónsson, S., Macrander, A., Østerhus, S., Håvik, L., Hattermann, T., 2016. Upstream sources of the Denmark Strait overflow: observations from a high-resolution mooring array. *Deep-Sea Res.* 112, 94–112. <http://dx.doi.org/10.1016/j.dsr.2016.02.007>.
- Hátún, H., Chafik, L., Larsen, K.M.H., 2021. The Norwegian Sea Gyre – a regulator of Iceland–Scotland Ridge exchanges. *Front. Mar. Sci.* 8 (694614), <http://dx.doi.org/10.3389/fmars.2021.694614>.
- Håvik, L., Almansi, M., Våge, K., Haine, T.W.N., 2019. Atlantic-origin overflow water in the East Greenland Current. *J. Phys. Oceanogr.* 49 (9), 2255–2269. <http://dx.doi.org/10.1175/JPO-D-18-0216.1>.
- Håvik, L., Pickart, R.S., Våge, K., Torres, D., Thurnherr, A.M., Beszczynska-Möller, A., Walczowski, W., von Appen, W.-J., 2017. Evolution of the East Greenland Current from Fram Strait to Denmark Strait: synoptic measurements from summer 2012. *J. Geophys. Res.: Oceans* 122 (3), 1974–1994. <http://dx.doi.org/10.1002/2016JC012228>.
- Helland-Hansen, B., Nansen, F., 1909. The Norwegian Sea: its physical oceanography based upon the Norwegian researches 1900–1904. *Rep. Nor. Fish. Mar. Investig.* 2 (2), 1–390.
- Huang, J., Pickart, R.S., Huang, R.X., Lin, P., Brakstad, A., Xu, F., 2020. Sources and upstream pathways of the densest overflow water in the Nordic Seas. *Nature Commun.* 11 (5389), <http://dx.doi.org/10.1038/s41467-020-19050-y>.
- IOC, SCOR, IAPSO, 2010. The international thermodynamic equation of seawater - 2010: calculation and use of thermodynamic properties. In: *Intergovernmental Oceanographic Commission, Manuals and Guides No. 56*. UNESCO.
- Isachsen, P.E., Mauritzen, C., Svendsen, H., 2007. Dense water formation in the Nordic Seas diagnosed from sea surface buoyancy fluxes. *Deep-Sea Res.* 54 (1), 22–41. <http://dx.doi.org/10.1016/j.dsr.2006.09.008>.
- Jeansson, E., Bellerby, R.G.J., Skjelvan, I., Frigstad, H., Ólafsdóttir, S.R., Ólafsson, J., 2015. Fluxes of carbon and nutrients to the Iceland Sea surface layer and inferred primary productivity and stoichiometry. *Biogeosciences* 12 (3), 875–885. <http://dx.doi.org/10.5194/bg-12-875-2015>.
- Jeansson, E., Jutterström, S., Rudels, B., Anderson, L.G., Olsson, K.A., Jones, E.P., Smethie, W.M., Swift, J.H., 2008. Sources to the East Greenland Current and its contribution to the Denmark Strait overflow. *Prog. Oceanogr.* 78 (1), 12–28. <http://dx.doi.org/10.1016/j.pocean.2007.08.031>.
- Jeansson, E., Olsen, A., Jutterström, S., 2017. Arctic intermediate water in the Nordic Seas, 1991–2009. *Deep-Sea Res.* 128, 82–97. <http://dx.doi.org/10.1016/j.dsr.2017.08.013>.
- Jochumsen, K., Moritz, M., Nunes, N., Quadfasel, D., Larsen, K.M., Hansen, B., Valdimarsson, H., Jónsson, S., 2017. Revised transport estimates of the Denmark Strait overflow. *J. Geophys. Res.* 122, 3434–3450. <http://dx.doi.org/10.1002/2017JC012803>.
- Jónsson, S., Valdimarsson, H., 2012. Water mass transport variability to the north Icelandic shelf, 1994–2010. *ICES J. Mar. Sci.* 69 (5), 809–815. <http://dx.doi.org/10.1093/icesjms/ifs024>.
- Karstensen, J., Schlosser, P., Wallace, D.W.R., Bullister, J.L., Blindheim, J., 2005. Water mass transformation in the Greenland Sea during the 1990s. *J. Geophys. Res.* 110 (C7), <http://dx.doi.org/10.1029/2004JC002510>.
- Köhl, A., 2010. Variable source regions of Denmark Strait and Færoe Bank Channel overflow waters. *Tellus A* 62 (4), 551–568. <http://dx.doi.org/10.1111/j.1600-0870.2010.00454.x>.
- Köhl, A., Willebrand, J., 2002. An adjoint method for the assimilation of statistical characteristics into eddy-resolving ocean models. *Tellus A* 54 (4), 406–425. <http://dx.doi.org/10.3402/tellusa.v54i4.12150>.
- Langehaug, H.R., Brakstad, A., Våge, K., Jeansson, E., Ilicak, M., Katsman, C.A., 2022. Drivers of surface salinity changes in the Greenland–Iceland Seas on seasonal and interannual time scales - a climate model study. *Earth Space Sci. Open Arch.* <http://dx.doi.org/10.1002/essoar.10511221.1>.
- Langehaug, H.R., Falck, E., 2012. Changes in the properties and distribution of the intermediate and deep waters in the Fram Strait. *Prog. Oceanogr.* 96 (1), 57–76. <http://dx.doi.org/10.1016/j.pocean.2011.10.002>.
- Latarius, K., Quadfasel, D., 2010. Seasonal to inter-annual variability of temperature and salinity in the Greenland Sea Gyre: heat and freshwater budgets. *Tellus A* 62 (4), 497–515. <http://dx.doi.org/10.1111/j.1600-0870.2010.00453.x>.

- Lauvet, S.K., Brakstad, A., Våge, K., Olsen, A., Jeansson, E., Mork, K.A., 2018. Continued warming, salinification and oxygenation of the Greenland Sea gyre. *Tellus A* 70 (1), 1–9. <http://dx.doi.org/10.1080/16000870.2018.1476434>.
- Lavender, K.L., Owens, W.B., Davis, R.E., 2005. The mid-depth circulation of the subpolar North Atlantic Ocean as measured by subsurface floats. *Deep-Sea Res.* 52 (5), 767–785. <http://dx.doi.org/10.1016/j.dsr.2004.12.007>.
- Lin, P., Pickart, R.S., Jochumsen, K., Moore, G.W.K., Valdimarsson, H., Fristedt, T., Pratt, L.J., 2020. Kinematic structure and dynamics of the Denmark Strait overflow from ship-based observations. *J. Phys. Oceanogr.* 50 (11), 3235–3251. <http://dx.doi.org/10.1175/JPO-D-20-0095.1>.
- Lorbacher, K., Dommenget, D., Niiler, P.P., Köhl, A., 2006. Ocean mixed layer depth: A subsurface proxy of ocean - atmosphere variability. *J. Geophys. Res.* 111 (C7), <http://dx.doi.org/10.1029/2003JC002157>.
- Lozier, S.M., Li, F., Bacon, S., Bahr, F., Bower, A.S., Cunningham, S.A., de Jong, F.M., de Steur, L., deYoung, B., Fischer, J., Gary, S.F., Greenan, B.J.W., Holliday, N.P., Houk, A., Houpert, I., Inall, M.E., Johns, W.E., Johnson, H.L., Johnson, C., Karstensen, J., Koman, G., Le Bras, I.A., Lin, X., Mackay, N., Marshall, D.P., Mercier, H., Oltmanns, M., Pickart, R.S., Ramsey, A.L., Rayner, D., Straneo, F., Thierry, V., Torres, D.J., Williams, R.G., Wilson, C., Yang, J., Yashayev, I., Zhao, J., 2019. A sea change in our view of overturning in the subpolar North Atlantic. *Science* 363, 516–521. <http://dx.doi.org/10.1126/science.aau6592>.
- Malmberg, S.A., 1983. Hydrographic Investigations in the Iceland and Greenland Seas in Late Winter 1971 - "Deep Water Project". Vol. 33. Jökull.
- Marshall, J., Schott, F., 1999. Open - ocean convection: observations, theory, and models. *Rev. Geophys.* 37 (1), 1–64. <http://dx.doi.org/10.1029/98RG02739>.
- Mastropole, D., Pickart, R.S., Valdimarsson, H., Våge, K., Jochumsen, K., Girtin, J., 2017. On the hydrography of Denmark Strait. *J. Geophys. Res.* 122 (1), 306–321. <http://dx.doi.org/10.1002/2016JC012007>.
- Mauritzen, C., 1996. Production of dense overflow waters feeding the North Atlantic across the Greenland–Scotland Ridge. Part 1: Evidence for a revised circulation scheme. *Deep-Sea Res.* 43 (6), 769–806. [http://dx.doi.org/10.1016/0967-0637\(96\)00037-4](http://dx.doi.org/10.1016/0967-0637(96)00037-4).
- McKenna, C., Berc, B., Austin, W.E.N., 2016. The decomposition of the Faroese–Shetland Channel water masses using parametric optimum multi-parameter analysis. *Deep-Sea Res.* 1107, 9–21. <http://dx.doi.org/10.1016/j.dsr.2015.10.013>.
- Meincke, J., Jónsson, S., Swift, J.H., 1992. Variability of convective conditions in the Greenland Sea. *ICES Mar. Sci. Symp.* 195, 32–39.
- Meincke, J., Rudels, B., 1996. *Greenland Sea Deep Water: A Balance Between Convection and Advection*. World Meteorological Organization, pp. 436–440.
- Messias, M.J., Watson, A.J., Johannessen, T., Oliver, K.I.C., Olsson, K.A., Fogelqvist, E., Olafsson, J., Bacon, S., Balle, J., Bergman, N., Budéus, G., Danielsen, M., Gascard, J.C., Jeansson, E., Olafsdottir, S.R., Simonsen, K., Tanhua, T., Van Scoy, K., Ledwell, J.R., 2008. The Greenland Sea tracer experiment 1996–2002: Horizontal mixing and transport of Greenland Sea Intermediate Water. *Prog. Oceanogr.* 78 (1), 85–105. <http://dx.doi.org/10.1016/j.pocean.2007.06.005>.
- Moore, G.W.K., Våge, K., Pickart, R.S., Renfrew, I.A., 2015. Decreasing intensity of open-ocean convection in the Greenland and Iceland seas. *Nature Clim. Change* 5 (9), 877–882. <http://dx.doi.org/10.1038/nclimate2688>.
- Moore, G.W.K., Våge, K., Renfrew, I.A., Pickart, R.S., 2022. Sea-ice retreat suggests reorganization of water mass transformation in the Nordic and Barents Seas. *Nature Commun.* 13 (1), 1–8. <http://dx.doi.org/10.1038/s41467-021-27641-6>.
- Mork, K.A., Drinkwater, K.F., Jónsson, S., Valdimarsson, H., Ostrowski, M., 2014a. Water mass exchanges between the Norwegian and Iceland seas over the Jan Mayen Ridge using in-situ current measurements. *J. Mar. Syst.* 139, 227–240. <http://dx.doi.org/10.1016/j.jmarsys.2014.06.008>.
- Mork, K.A., Skagseth, Ø., Ivshin, V., Ozhigin, V., Hughes, S.L., Valdimarsson, H., 2014b. Advective and atmospheric forcing changes in heat and fresh water content in the Norwegian Sea, 1951–2010. *Geophys. Res. Lett.* 41 (17), 6221–6228. <http://dx.doi.org/10.1002/2014GL061038>.
- Mork, K.A., Skagseth, Ø., Søiland, H., 2019. Recent warming and freshening of the Norwegian Sea observed by Argo data. *J. Clim.* 32 (12), 3695–3705. <http://dx.doi.org/10.1175/JCLI-D-18-0591.1>.
- Nilsen, J.E.Ø., Falck, E., 2006. Variations of mixed layer properties in the Norwegian Sea for the period 1948–1999. *Prog. Oceanogr.* 70 (1), 58–90. <http://dx.doi.org/10.1016/j.pocean.2006.03.014>.
- Nilsen, J.E.Ø., Hátún, H., Mork, K.A., Valdimarsson, H., 2008. *The NISE Dataset, No. 08–01*. Technical Report, Faroese Fisheries Laboratory, Box 3051, Tórshavn, Faroese Islands.
- Nocedal, J., 1980. Updating quasi-Newton matrices with limited storage. *Math. Comp.* 35 (151), 773–782. <http://dx.doi.org/10.1090/S0025-5718-1980-0572855-7>.
- Nøst, O.A., Isachsen, P.E., 2003. The large-scale time-mean ocean circulation in the Nordic Seas and Arctic Ocean estimated from simplified dynamics. *J. Mar. Res.* 61 (2), 175–210. <http://dx.doi.org/10.1357/00224003322005069>.
- O'Dwyer, J., Kasajima, Y., Nøst, O.A., 2001. North Atlantic water in the Barents Sea opening, 1997 to 1999. *Polar Res.* 20 (2), 209–216. <http://dx.doi.org/10.3402/polar.v20i2.6519>.
- Olsen, A., Key, R.M., van Heuven, S., Lauvet, S.K., Velo, A., Lin, X., Schirnick, C., Kozyr, A., Tanhua, T., Hoppema, M., Jutterström, S., Steinfeldt, R., Jeansson, E., Ishii, M., Pérez, F.F., Suzuki, T., 2016. The global ocean data analysis project version 2 (GLODAPv2) - an internally consistent data product for the world ocean. *Earth Syst. Sci. Data* 8, 297–323. <http://dx.doi.org/10.5194/essd-8-297-2016>.
- Olsen, A., Lange, N., Key, R.M., Tanhua, T., Álvarez, M., Becker, S., Bittig, H.C., Carter, B.R., Cotrim da Cunha, L., Feely, R.A., van Heuven, S., Hoppema, M., Ishii, M., Jeansson, E., Jones, S.D., Jutterström, S., Karlsen, M.K., Kozyr, A., Lauvet, S.K., Lo Monaco, C., Murata, A., Pérez, F.F., Peil, B., Schirnick, C., Steinfeldt, R., Suzuki, T., Telszewski, M., Tilbrook, B., Velo, A., Wanninkhof, R., 2019. GLODAPv2.2019 - an update of GLODAPv2. *Earth Syst. Sci. Data* 11, 1437–1461. <http://dx.doi.org/10.5194/essd-11-1437-2019>.
- Olsson, K.A., Jeansson, E., Anderson, L.G., Hansen, B., Eldevik, T., Kristiansen, R., Messias, M.-J., Johannessen, T., Watson, A.J., 2005. Intermediate water from the Greenland Sea in the Faroer Bank Channel: spreading of released sulphur hexafluoride. *Deep-Sea Res.* 52 (2), 279–294. <http://dx.doi.org/10.1016/j.dsr.2004.09.009>.
- Østerhus, S., Gammelsrød, T., 1999. The abyss of the Nordic Seas is warming. *J. Clim.* 12 (11), 3297–3304. [http://dx.doi.org/10.1175/1520-0442\(1999\)012<3297:TAOTNS>2.0.CO;2](http://dx.doi.org/10.1175/1520-0442(1999)012<3297:TAOTNS>2.0.CO;2).
- Østerhus, S., Woodgate, R., Valdimarsson, H., Turrell, B., de Steur, L., Quadfasel, D., Olsen, S.M., Moritz, M., Lee, C.M., Larsen, K.M.H., Jonsson, S., Johnson, C., Jochumsen, K., Hansen, B., Curry, B., Cunningham, S., Berc, B., 2019. Arctic Mediterranean exchanges: a consistent volume budget and trends in transports from two decades of observations. *Ocean Sci.* 15 (2), 379–399. <http://dx.doi.org/10.5194/os-15-379-2019>.
- Pickart, R.S., Torres, D.J., Clarke, R.A., 2002. Hydrography of the Labrador Sea during active convection. *J. Phys. Oceanogr.* 32 (2), 428–457. [http://dx.doi.org/10.1175/1520-0485\(2002\)032<0428:hotltd>2.0.co;2](http://dx.doi.org/10.1175/1520-0485(2002)032<0428:hotltd>2.0.co;2).
- Redfield, A.C., Ketchum, B.H., Richards, F.A., 1963. *The influence of organisms on the composition of seawater*. In: Hill, M.N. (Ed.), *In the Sea, Vol. 2*. Interscience, New York, pp. 26–77.
- Renfrew, I.A., Pickart, R.S., Våge, K., Moore, G.W.K., Braccigirdi, T.J., Elvidge, A.D., Jeansson, E., Lachlan-Cope, T., McRaven, L., Papritz, L., Reuder, J., Sodemann, H., Terpstra, A., Waterman, S., Valdimarsson, H., Weiss, A., Almansi, M., Bahr, F., Brakstad, A., Barrell, C., Broeke, J.K., Brooks, B.J., Brooks, I.M., Brooks, M.E., Bruvik, E.M., Dusch, C., Fer, I., Golid, H.M., Hallerstig, M., Hessevik, I., Huang, J., Houghton, L., Jónsson, S., Jonasson, M., Jackson, K., Kvalsund, K., Kolstad, E.W., Konstali, K., Kristiansen, J., Larkin, R., Lin, P., Macrander, A., Mitchell, A., Olafson, H., Pacini, A., Payne, C., Palmason, B., Pérez-Hernández, M.D., Peterson, A.K., Petersen, G.N., Pisarova, M.N., Pope, J.O., Seidl, A., Semper, S., Sergeev, D., Skjelsvik, S., Søiland, H., Smith, D., Spall, M.A., Spengler, T., Touzeau, A., Tupper, G., Weng, Y., Williams, K.D., Yang, X., Zhou, S., 2019. The Iceland Greenland Sea project. *Bull. Am. Meteorol. Soc.* 100 (9), 1795–1817. <http://dx.doi.org/10.1175/BAMS-D-18-0217.1>.
- Ronski, S., Budéus, G., 2005. Time series of winter convection in the Greenland Sea. *J. Geophys. Res.* 110 (C4), <http://dx.doi.org/10.1029/2004jc002318>.
- Rosby, T., Flagg, C., Chafik, L., Harden, B., Søiland, H., 2018. A direct estimate of volume, heat, and freshwater exchange across the Greenland–Iceland–Faroese–Scotland Ridge. *J. Geophys. Res.: Oceans* 123 (10), 7139–7153. <http://dx.doi.org/10.1029/2018JC014250>.
- Rudels, B., Björk, G., Nilsson, J., Winsor, P., Lake, I., Nohr, C., 2005. The interaction between waters from the Arctic Ocean and the Nordic Seas north of Fram Strait and along the East Greenland Current: results from the Arctic Ocean-02 Oden expedition. *J. Mar. Syst.* 55 (1–2), 1–30. <http://dx.doi.org/10.1016/j.jmarsys.2004.06.008>.
- Rudels, B., Fahrback, E., Meincke, J., Budéus, G., Eriksson, P., 2002. The East Greenland Current and its contribution to the Denmark Strait overflow. *ICES J. Mar. Sci.* 59 (6), 1133–1154. <http://dx.doi.org/10.1006/jmsc.2002.1284>.
- Rudels, B., Friedrich, H.J., Quadfasel, D., 1999. The Arctic circumpolar boundary current. *Deep-Sea Res.* 46 (6–7), 1023–1062. [http://dx.doi.org/10.1016/S0967-0645\(99\)00015-6](http://dx.doi.org/10.1016/S0967-0645(99)00015-6).
- Saberi, A., Haine, T.W.N., Gelderloos, R., Femke de Jong, M., Furey, H., Bower, A., 2020. Lagrangian perspective on the origins of Denmark Strait Overflow. *J. Phys. Oceanogr.* 50 (8), 2393–2414. <http://dx.doi.org/10.1175/JPO-D-19-0210.1>.
- Schlitzer, R., 2007. Assimilation of radiocarbon and chlorofluorocarbon data to constrain deep and bottom water transports in the world ocean. *J. Phys. Oceanogr.* 37 (2), 259–276. <http://dx.doi.org/10.1175/JPO3011.1>.
- Schlosser, P., Bönisch, G., Rhein, M., Bayer, R., 1991. Reduction of deepwater formation in the Greenland Sea during the 1980s: Evidence from tracer data. *Science* 251 (4997), 1054–1056. <http://dx.doi.org/10.1126/science.251.4997.1054>.
- Semper, S., Pickart, R.S., Våge, K., Larsen, K.M.H., Hansen, B., Hátún, H., 2020. The Iceland-Faroer Slope Jet: a conduit for dense water toward the Faroer Bank Channel overflow. *Nature Commun.* 11 (5390), <http://dx.doi.org/10.1038/s41467-020-19049-5>.
- Semper, S., Våge, K., Pickart, R.S., Jónsson, S., Valdimarsson, H., 2022. Evolution and transformation of the North Icelandic Irminger Current along the north Iceland shelf. *J. Geophys. Res.: Oceans* 127 (3), e2021JC017700. <http://dx.doi.org/10.1029/2021JC017700>.
- Semper, S., Våge, K., Pickart, R.S., Valdimarsson, H., Torres, D.J., Jónsson, S., 2019. The emergence of the North Icelandic Jet and its evolution from northeast Iceland to Denmark Strait. *J. Phys. Oceanogr.* (2019), <http://dx.doi.org/10.1175/JPO-D-19-0088.1>.
- Serra, N., Käse, R.H., Köhl, A., Stammer, D., Quadfasel, D., 2010. On the low-frequency phase relation between the Denmark Strait and the Faroer-Bank Channel overflows. *Tellus A* 62 (4), 530–550. <http://dx.doi.org/10.1111/j.1600-0870.2009.00445.x>.

- Shao, Q., Zhao, J., Drinkwater, K.F., Wang, X., Cao, Y., 2019. Internal overflow in the Nordic Seas and the cold reservoir in the northern Norwegian Basin. *Deep-Sea Res. I* 148, 67–79. <http://dx.doi.org/10.1016/j.dsr.2019.04.012>.
- Skagseth, Ø., Mork, K.A., 2012. Heat content in the Norwegian Sea, 1995 - 2010. *ICES J. Mar. Sci.* 69 (5), 826–832. <http://dx.doi.org/10.1093/icesjms/fss026>.
- Smedsrud, L.H., Muijwijk, M., Brakstad, A., Madonna, E., Lauvset, S.K., Spensberger, C., Born, A., Eldevik, T., Drange, H., Jeansson, E., Li, C., Olsen, A., Skagseth, Ø., Slater, D.A., Straneo, F., Våge, K., Årthun, M., 2022. Nordic Seas heat loss, Atlantic inflow, and Arctic sea ice cover over the last century. *Rev. Geophys.* 60 (1), e2020RG000725. <http://dx.doi.org/10.1029/2020RG000725>.
- Somavilla, R., 2019. Draining and upwelling of Greenland Sea deep waters. *J. Geophys. Res.: Oceans* 124, 2842–2860. <http://dx.doi.org/10.1029/2018JC014249>.
- Somavilla, R., Schauer, U., Budeus, G., 2013. Increasing amount of Arctic Ocean deep waters in the Greenland Sea. *Geophys. Res. Lett.* 40 (16), 4361–4366. <http://dx.doi.org/10.1002/grl.50775>.
- Strass, V.H., Fahrback, E., Schauer, U., Sellmann, L., 1993. Formation of Denmark Strait overflow water by mixing in the East Greenland Current. *J. Geophys. Res.* 98 (C4), 6907–6919. <http://dx.doi.org/10.1029/92JC02732>.
- Swift, J.H., Aagaard, K., 1981. Seasonal transitions and water mass formation in the Iceland and Greenland seas. *Deep-Sea Res. A* 28 (10), 1107–1129. [http://dx.doi.org/10.1016/0198-0149\(81\)90050-9](http://dx.doi.org/10.1016/0198-0149(81)90050-9).
- Swift, J.H., Aagaard, K., Malmberg, S.A., 1980. The contribution of the Denmark Strait overflow to the deep North Atlantic. *Deep-Sea Res. A* 27 (1), 29–42. [http://dx.doi.org/10.1016/0198-0149\(80\)90070-9](http://dx.doi.org/10.1016/0198-0149(80)90070-9).
- Swift, J.H., Koltermann, K.P., 1988. The origin of Norwegian Sea deep water. *J. Geophys. Res.: Oceans* 93 (C4), 3563–3569. <http://dx.doi.org/10.1029/JC093iC04p03563>.
- Tanhua, T., Olsson, K.A., Jeansson, E., 2005. Formation of Denmark Strait overflow water and its hydro-chemical composition. *J. Mar. Syst.* 57 (3–4), 264–288. <http://dx.doi.org/10.1016/j.jmarsys.2005.05.003>.
- Tsubouchi, T., Våge, K., Hansen, B., Larsen, K.M.H., Østerhus, S., Johnson, C., Jónsson, S., Valdimarsson, H., 2021. Increased ocean heat transport into the Nordic Seas and Arctic Ocean over the period 1993–2016. *Nature Clim. Change* 11, 21–26. <http://dx.doi.org/10.1038/s41558-020-00941-3>.
- Turrell, W.R., Slessor, G., Adams, R.D., Payne, R., Gillibrand, P.A., 1999. Decadal variability in the composition of Faroe Shetland Channel bottom water. *Deep-Sea Res. I* 46 (1), 1–25. [http://dx.doi.org/10.1016/S0967-0637\(98\)00067-3](http://dx.doi.org/10.1016/S0967-0637(98)00067-3).
- Våge, K., Moore, G.W.K., Jónsson, S., Valdimarsson, H., 2015. Water mass transformation in the Iceland Sea. *Deep-Sea Res. I* 101, 98–109. <http://dx.doi.org/10.1016/j.dsr.2015.04.001>.
- Våge, K., Papritz, L., Håvik, L., Spall, M.A., Moore, G.W.K., 2018. Ocean convection linked to the recent ice edge retreat along east Greenland. *Nature Commun.* 9, 1287. <http://dx.doi.org/10.1038/s41467-018-03468-6>.
- Våge, K., Pickart, R.S., Spall, M.A., Moore, G.W.K., Valdimarsson, H., Torres, D.J., Erofeeva, S.Y., Nilsen, J.E.Ø., 2013. Revised circulation scheme north of the Denmark Strait. *Deep-Sea Res. I* 79, 20–39. <http://dx.doi.org/10.1016/j.dsr.2013.05.007>.
- Våge, K., Pickart, R.S., Spall, M.A., Valdimarsson, H., Jónsson, S., Torres, D.J., Østerhus, S., Eldevik, T., 2011. Significant role of the North Icelandic Jet in the formation of Denmark Strait overflow water. *Nat. Geosci.* 4 (10), 723–727. <http://dx.doi.org/10.1038/ngeo1234>.
- Våge, K., Semper, S., Valdimarsson, H., Jónsson, S., Pickart, R.S., Moore, G.W.K., 2022. Water mass transformation in the Iceland Sea: Contrasting two winters separated by four decades. *Deep-Sea Res. I* 186, 103824. <http://dx.doi.org/10.1016/j.dsr.2022.103824>.
- Voet, G., Quadfasel, D., Mork, K.A., Søiland, H., 2010. The mid - depth circulation of the Nordic Seas derived from profiling float observations. *Tellus A* 62 (4), 516–529. <http://dx.doi.org/10.1111/j.1600-0870.2009.00444.x>.
- Walsh, J.E., Chapman, W.L., Fetterer, F., 2015. Gridded Monthly Sea Ice Extent and Concentration, 1850 Onwards, Version 1. National Snow and Ice Data Center, Boulder, Colorado USA. <http://dx.doi.org/10.7265/N5833PZ5>.
- Walsh, J.E., Fetterer, F., Stewart, J.S., Chapman, W.L., 2017. A database for depicting Arctic sea ice variations back to 1850. *Geogr. Rev.* 107 (1), 89–107. <http://dx.doi.org/10.1111/j.1931-0846.2016.12195.x>.
- Wang, X., Zhao, J., Hattermann, T., Lin, L., Chen, P., 2021. Transports and accumulations of Greenland Sea intermediate waters in the Norwegian Sea. *J. Geophys. Res.: Oceans* 126 (4), e2020JC016582. <http://dx.doi.org/10.1029/2020JC016582>.

6 Concluding discussion

Overturning in the Nordic Seas is an integral part of the large-scale circulation and climate system in the North Atlantic. Based on a multitude of observational data covering the period 1950–2019, a one dimensional mixed-layer model, and a regional water-mass inversion, this thesis provides novel insights into the formation and pathways of dense water within the Nordic Seas and their variability, which are critical for our understanding of the overturning in the Nordic Seas and the supply of dense water to the lower limb of the AMOC. In Chapter 1, we posed the following research questions:

- I) What determines the interannual and long-term variability in dense-water formation in the Greenland Sea?
- II) How do cold-air outbreaks and lateral fluxes of heat and salt impact dense-water formation in the Greenland Sea?
- III) Where do the overflow waters originate and how do they propagate toward the Greenland-Scotland Ridge?
- IV) How have the dense-water reservoir and the overflows from the Nordic Seas changed over the observational record and why?

These questions were addressed in Papers I-IV, respectively, which constitute this thesis (Chapter 5). While the results presented here provide a step forward in our understanding of the Nordic Seas overturning at present, they also raise several new questions that will be discussed in the following sections.

6.1 Surface origin of the overflows and density transformation

In Paper III, we found that the FBCOW primarily consists of dense water originating in the Greenland Sea ($46\pm 8\%$) and the Arctic Ocean ($25\pm 9\%$), while the DSOW is composed of dense water originating in the Greenland Sea ($39\pm 2\%$), the Iceland Sea ($20\pm 3\%$), and in the Atlantic Domain ($19\pm 2\%$) of the Nordic Seas. These fractional contributions reflect where the different components of the overflow plumes were last in contact with the atmosphere. That is, where they were last modified by the atmosphere and finally left the surface layer. Assuming that the water-mass properties are conservative, further modifications will only take place by interior mixing, which is quantified in the TMI inversion. As such, the surface origin of the dense-water mixture that supplies the overflow plumes is crucial for determining their final water properties. The surface origins do not necessarily coincide with the locations of greatest density transformation (or buoyancy loss, *Isachsen et al.*, 2007). Consider, for instance, the contribution from the Atlantic Domain to the DSOW, which stems almost entirely from the northern part near Fram Strait (Paper III). This is where the Atow leaves the surface and flows beneath the fresh PSW from the Arctic Ocean (e.g., *Mauritzen*, 1996), but substantial densification took place farther south in the Lofoten and Norwegian basins (Section 2.3.2, *Isachsen et al.*, 2007; *Bosse et al.*, 2018). The densification of the AW as it propagates northward with the Norwegian Atlantic Current also impacts the preconditioning of the Greenland Sea gyre (*Lawset et al.*, 2018, Paper I, Paper II, Paper IV). According

to *Isachsen et al.* (2007) and *Árthun* (submitted), the largest densification in the Nordic Seas takes place in the eastern basins. Thus, the eastern basins of the Nordic Seas are considered most important in terms of the total density transformation. Regions where the dense water leaves the surface layer are important for the final transformation and properties that are transported into the deep ocean, including the uptake of anthropogenic heat and carbon. They also impact the final density and the vertical extent of the overturning. Hence, it is important to understand the variability in the surface origin regions of the overflows, as well as in the upstream preconditioning/densification, in order to determine the variability in the overturning and overflows from the Nordic Seas.

6.2 Overflow-water pathways

Although our knowledge about the upstream pathways of the Nordic Seas' overflows have increased substantially over the past 2-3 decades (Sections 2.4.1 and 2.4.2), some major gaps remained, particularly regarding the upstream pathways of the FBCOW and how dense water formed in the Greenland Sea propagates toward the overflows and supplies the NIJ and IFSJ (e.g., *Huang et al.*, 2020; *Semper et al.*, 2020; *Chafik et al.*, 2020). Results from the regional water-mass inversion revealed that dense water from the Greenland Sea feeds the NIJ through two distinct pathways: an outer core of the East Greenland Current and along a previously unknown pathway that crosses the sloping Jan Mayen Ridge just south of Jan Mayen (Paper III). The latter pathway also supplies dense water from the Greenland Sea to the IFSJ. Furthermore, the inversion showed that dense water originating in the Greenland Sea and Arctic Ocean propagate southward along the eastern boundary of the Jan Mayen Ridge and feed the Faroe-Shetland Channel Jet identified by *Chafik et al.* (2020) that follows the continental slope of Norway southward through the Faroe-Shetland Channel. This pathway can account for $24\pm 3\%$ of the FBCOW, while the IFSJ supplies $58\pm 3\%$ (Paper III), which agrees well with transport estimates of the IFSJ (*Semper et al.*, 2020). The pathways identified by the water-mass inversion are remarkably consistent with previous literature and the additional information provided regarding the dense-water pathways from the Greenland Sea and how the FBCOW approaches the Faroe-Shetland Channel have significantly advanced our understanding on the upstream pathways of the overflows. We note, however, that since the inversion is constrained by observations, the identified pathways may be more uncertain in areas of sparse data coverage, such as the area surrounding Jan Mayen. Hence, further studies are needed to examine the transport and structure of the Jan Mayen Ridge boundary current and the branch crossing the ridge south of Jan Mayen to confirm their contribution to the overflows. The representation of the narrow NIJ and IFSJ in the water-mass inversion were also impacted by the data coverage and resolution. In particular, only a small portion of the NIJ were traced back along the slope of Iceland east of the Kolbeinsey Ridge and the IFSJ had a light density bias (Paper III, *Semper et al.*, 2019, 2020). While part of this could be due to the resolution of the inversion itself, which was around 14 km for both longitude and latitude north of Iceland, it is also impacted by the resolution of the observations. *Semper et al.* (2019) and *Semper et al.* (2020) used a few high-resolution (2.5–10 km) transects to quantify the transport and structure of the NIJ and IFSJ, respectively. The standard repeat hydrographic transects around Iceland and the Faroe Islands, however, have lower resolution (approximately 20 km) and *Semper et al.* (2020) found that only 32% of the surveys performed north of the Faroe Islands over 30 years, captured the the upsloping

dense water associated with the IFSJ. Hence, the densest water in the IFSJ is not well captured north of the Faroe Islands in the climatological mean, which, in turn, impacts the representation of the current in the inversion. The new insights from the regional water-mass inversion provide a guide as to where we should focus future observational sampling, as well as where high-resolution observations are needed, to further improve our understanding of the upstream pathways of the two main overflows from the Nordic Seas.

6.3 Strengths and weaknesses of the regional water-mass inversion

Compared to traditional water-mass decomposition methods (e.g., *Eldevik et al.*, 2009; *Mastropole et al.*, 2017; *Tanhua et al.*, 2005; *Jeansson et al.*, 2008, 2017), the TMI water-mass inversion has two major advantages. First, it takes the spatial distribution of water masses into account, which makes it possible to resolve the pathways that connect the overflow plumes to their origins. Second, it is not dependent on a few pre-defined end-members, but considers all surface and lateral boundary locations potential overflow water sources. In Paper III, we showed that this is crucial to determine the importance of different source regions, as the water-mass properties vary spatially, also within each source region. Compared to earlier global TMI versions with lower resolution (*Gebbie and Huybers*, 2010; *Gebbie*, 2014), the regional water-mass inversion better resolved the complex bathymetry of the Nordic Seas and the main features of the water-mass distribution, which gave a more realistic representation of the pathways feeding the overflows and how the water mixed along the pathways. We also implemented a more realistic first guess of the pathways based on density and absolute geostrophic velocity, which led to further improvements of the advective pathways. Compared to numerical simulations that need to parameterize subgrid-scale processes, the TMI inversion takes the combined effect of advection and diffusion into account when solving for the pathways that best fit the observed water-mass distribution (*Gebbie and Huybers*, 2010, Paper III). As such, the inversion is less prone to errors associated with insufficient resolution.

While the spatial variability in water-mass properties is accounted for in the TMI, it assumes that the observations constraining the solution represent a steady ocean state. Although we divided the observational dataset into different periods that align with the observed long-term variability in the inflowing AW (e.g., *Holliday et al.*, 2008; *Glessmer et al.*, 2014, Paper IV), changes in Greenland Sea convection (Paper I, *Somavilla*, 2019; *Strehl et al.*, submitted), and changes in the Nordic Seas dense-water reservoir (Paper IV), there is still considerable variability in both the overflow water properties and dense-water formation on interannual and shorter time scales (*Eldevik et al.*, 2009; *Mastropole et al.*, 2017, Paper I, Paper II, Paper IV). The steady-state assumption is, thus, the main weakness of the TMI water-mass inversion. Temporal variability was partly accounted for by focusing on late-winter properties and allowing the TMI inversion to deviate from the climatological mean conditions within the uncertainty limits of the observations (which represent the temporal variability of the observed properties within each period). However, the final optimized solutions still represent climatological mean conditions for the different periods 1950-1979 and 2000-2019 (Paper III and IV) and the contribution from each source region to the overflows are expected to vary within each period.

Another related aspect that was not included in our regional water-mass inversion, is the rate of exchange between water masses (i.e., the inversion does not contain direct velocity information). This means that our estimated overflow water compositions

in Denmark Strait and the Faroe-Shetland Channel represent the volume occupied by each water-mass component, which may not be proportional to the transport across the ridge because of non-uniform velocity distributions (e.g., *Lin et al.*, 2020; *Chafik et al.*, 2020). While it is difficult to estimate how different the contributions from the various source regions to the overflow-water transports would be, it is likely that the water masses transported within the boundary currents with higher velocity (such as the Atow) would have a higher weight. We would like to emphasize, though, that the distribution of water-mass properties includes the effect of both advection and diffusion, and similar properties along the pathways of ocean currents results in larger exchange of mass between neighboring grid cells in the inversion. The advective pathways, in particular the East Greenland Current, were further improved in the regional inversion by using gradients in density and absolute geostrophic velocity to estimate the first guess of the water-mass pathways, instead of assuming an isotropic first guess as in previous global TMI versions (*Gebbie and Huybers*, 2010; *Gebbie*, 2014, Paper III).

The rate of exchange between water masses could be estimated by including an age tracer in the inversion similar to *Schlitzer* (2007) or *Gebbie and Huybers* (2012). A regional water-mass inversion for the Nordic Seas based on the work performed in this thesis that includes age tracers is currently under development (*Davila et al.*, in prep.). The resulting transport matrix from this inversion will make it possible to estimate residence times and to determine how the flow structure and time-evolving source regions have influenced the overflow water compositions and transports. The transport matrix can also be used to diagnose the propagation of heat or anthropogenic carbon into the deep ocean as demonstrated by *Davila et al.* (2022) with a global version of the TMI method. While the results from this transient inversion is expected to shed light on several of the concerns raised above, the transport matrix itself will not be time evolving. One way to solve this challenge could be to include time as a fourth dimension in the inversion.

6.4 Contribution from the Greenland Sea to the overflows

Based on the 2000–2019 water-mass inversion developed in Paper III, we found that dense water formed the Greenland Sea is important for the overflows both east and west of Iceland. In terms of volume contribution it accounts for $39\pm 2\%$ and $46\pm 8\%$ of the Denmark Strait and Faroe Bank Channel overflows, respectively. Out of these fractions, $4\pm 1\%$ and $3\pm 8\%$ were classified as deep water, which was formed in the Greenland Sea prior to the 1980s. If we focus on the remaining intermediate water fraction and use the mean overflow water transports from *Østerhus et al.* (2019) of 3.2 Sv in Denmark Strait and 2.0 Sv in the Faroe Bank Channel, then the production of GSAIW should account for 1.12 ± 0.10 Sv and 0.81 ± 0.27 Sv of the overflow transports, respectively. In total, this amounts to 1.93 ± 0.37 Sv, which is significantly larger than the estimated mean (1994–2014) GSAIW export rate of 0.9 ± 0.7 Sv (Paper I). This export estimate was based on the GSAIW volume change within the gyre over the summer and on the assumption that the export is constant throughout the year, which is probably not the case. It also only accounts for the export from the gyre to its surroundings, and not the total export from the entire Greenland Sea. Water sufficiently dense to contribute to the overflows are also formed in the vicinity of the gyre and contributes to the overflows (Paper I, Paper III). The results in Paper III indicate that the areas surrounding the gyre as defined in Paper I can account for more than half of the overflow water supply from

the Greenland Sea. *Messias et al.* (2008) also inferred a higher export rate of 1–1.85 Sv based on the amount of SF₆ tracer leaving the Greenland Sea over the period 1998–2002. The tracer was released at the $\sigma_0=28.05$ kg m⁻³ isopycnal in the Greenland Sea gyre, which corresponds to GSAIW. Hence, our GSAIW export estimate in Paper I is probably biased low and does not properly represent the contribution from the Greenland Sea to the overflows. We also note that the rates of GSAIW export and production within the gyre are highly variable and the largest summertime exports generally follow winters with deep convection (Paper I).

Another source of uncertainty in these estimates is the non-uniform distribution of velocity/transport across the overflow plumes (*Lin et al.*, 2020; *Chafik et al.*, 2020), which in Denmark Strait also vary substantially on short time scales (*Mastropole et al.*, 2017), and the fact that the contribution from the Greenland Sea is most important for the densest components of the overflows (*Huang et al.*, 2020, Paper I, Paper III). The results from including age tracers in the water-mass inversion is expected to shed more light on some of these aspects (*Davila et al.*, in prep.). Furthermore, our analyses of the long-term variability in overflow water composition and properties revealed that the regime shift in the Greenland Sea (from the formation of GSDW to formation of GSAIW), has led to reduced contributions to the FBCOW, while the contribution to the DSOW has increased (Paper IV).

6.5 Mechanisms governing the variability in Greenland Sea convection

Both Paper I and II highlight the importance of the interplay between air-sea heat fluxes and oceanic lateral advection for the Greenland Sea mixed-layer development. Lateral advection generally leads to an input of heat into the gyre that acts to increase the gyre stratification and an input of salt that decreases the stratification. The combined effect is a reduction in the end-of-winter mixed-layer depth, which implies that the temperature effect dominates (Paper II). By contrast, the lateral input of salt seems to dominate in terms of interannual variability in stratification and, in turn, the mixed-layer depth (Paper I). Years with anomalously fresh near-surface conditions in fall typically have shallow convection the following winter. While there has been several shorter periods of fresh conditions and relatively shallow convection in the Greenland Sea (Paper I), only the fresh period that lasted from the 80s into the early 90s was sufficiently severe to cause the regime shift from GSDW formation to GSAIW formation (*Strehl et al.*, submitted). While the East Greenland Current transports a substantial amount of freshwater and sea ice that potentially can be diverted into the interior Greenland Sea and impact the salinity variability (e.g., *Dodd et al.*, 2009; *Spall et al.*, 2021; *Langehaug et al.*, 2022), *Glessmer et al.* (2014) and *Lauvset et al.* (2018) argue that variability in the AW inflow is more important. Our results in Paper IV focusing on multidecadal and long-term variability corroborates these results, but further studies are needed to better understand where and how the lateral advection takes place (Paper II). Recent evidence also indicate that the AW salinity decline in the past decade (*Mork et al.*, 2019, , Paper IV) has resulted in reduced Greenland Sea convection since 2014 (*Abot et al.*, 2023; *Almeida et al.*, submitted). If this freshening will be sufficiently severe to result in a new regime shift in the Greenland Sea remains to be determined. The anomalously fresh period in the 1980s (starting in the mid-1970s for the AW) was related to a Great Salinity Anomaly event that propagated around the North Atlantic (*Dickson et al.*, 1988; *Belkin*

et al., 1998). A new such event could occur if the substantial amounts of freshwater stored in the Beaufort Gyre in the Arctic Ocean are released.

During years with more saline conditions in the Greenland Sea, the integrated atmospheric heat loss during the winter determines the end-of winter mixed-layer depth (Paper I). The integrated heat loss in winter is closely related to the frequency and intensity of CAOs, and their temporal distribution determines when the active convection phase (i.e., the deepening phase) starts (Paper II). Sea-ice formation rarely occurred within the Greenland Sea gyre during the period considered here, and was therefore not a main driver for the convective variability in the Greenland Sea over the period 1986–2016 (Paper I). However, the sea-ice retreat has important implications for the winter atmospheric heat loss. While *Strehl et al.* (submitted) found that the total air-sea heat loss over the Greenland Sea has increased since 1950 due to a larger open-ocean area, *Moore et al.* (2015) found a 20% decline in the magnitude of the heat fluxes over the Greenland Sea gyre since the end of the 1970s. The reduced heat fluxes over the gyre were primarily a result of increased distance to the sea-ice edge and decreased winter air-sea temperature differences (Section 2.2.2, *Moore et al.*, 2015). These changes have also resulted in reduced intensity of cold-air outbreaks (i.e., the strongest heat-flux events, *Somavilla*, 2019; *Dahlke et al.*, 2022; *Strehl et al.*, submitted). According to *Moore et al.* (2015, 2022), the trend toward weaker atmospheric heat fluxes is expected to continue in a warming climate with continued sea-ice retreat, which could have substantial ramifications for the water-mass transformation in the Greenland Sea gyre.

6.6 Future perspectives and the impacts of climate change

The temperature of the AW has increased over the last 25 years, and since 2000 this has resulted in a decreased AW density (Paper IV). This trend of warmer and less dense AW inflow is expected to continue in the future (e.g., *Árthun et al.*, 2019; *Shu et al.*, 2022; *Árthun et al.*, 2023; *Asbjørnsen and Árthun*, submitted). As convection in the Greenland Sea and the size of the Nordic Seas dense-water reservoir are closely connected to changes in the AW inflow (Papers I, II, and IV), we expect that also the trend toward a warmer and less dense Nordic Seas reservoir will continue in the future. This implies a less dense overturning in the Nordic Seas, which will ultimately impact the properties of the overflows and the lower limb of the AMOC. However, as the ocean and atmosphere are warming, reduced sea-ice extent will lead to regions previously insulated by the sea ice becoming ice free and in direct contact with the atmosphere (*Moore et al.*, 2015; *Våge et al.*, 2018; *Moore et al.*, 2022). Recent studies suggest that formation of dense water masses can take place in these newly ice-free areas and may compensate for some of the predicted decline in the interior basins of the Nordic Seas (*Våge et al.*, 2018; *Pérez-Hernández et al.*, 2019; *Athanase et al.*, 2020; *Lique et al.*, 2018; *Bretones et al.*, 2022; *Moore et al.*, 2022). To which extent these new dense-water formation areas can compensate for the decline in density in the Nordic Seas remains uncertain and needs to be investigated more thoroughly to understand how it will impact the lower limb of the AMOC. *Shu et al.* (2022) suggested that although the larger open-ocean area will increase the integrated heat loss, particularly in the Arctic Ocean, it may not be sufficient to overcome the effect of increased northward AW heat transport, which implies a sustained warming and density decrease.

While the hydrographic properties and composition of the overflows have changed over the observational record (Paper IV), the overflow water transport has remained

remarkably stable (*Hansen et al.*, 2016; *Jochumsen et al.*, 2017; *Østerhus et al.*, 2019). Two recent studies even indicate that the maximum overturning strength in the Nordic Seas and Arctic Ocean may increase in the 21st century (*Bretones et al.*, 2022; *Árthun et al.*, 2023). While *Bretones et al.* (2022) pointed to the northwestward shift in sea ice and dense-water formation as the main reason for this strengthening, *Árthun et al.* (2023) found that changes in AW density and surface buoyancy forcing will increase the zonal density gradient in the Nordic Seas, resulting in enhanced horizontal circulation and overturning. *Árthun et al.* (2023) further showed that changes in the Nordic Seas overturning impact the lower limb of the overturning circulation in the subpolar North Atlantic and could provide a stabilizing factor in the future AMOC, which is predicted to weaken in most models (*Weijer et al.*, 2020; *Bretones et al.*, 2022; *Árthun et al.*, 2023). The predicted increased importance of the overturning in the Nordic Seas (and Arctic Ocean), suggests that increased efforts should be made to understand their overturning variability and downstream implications.

Although *Bretones et al.* (2022) and *Árthun et al.* (2023) predict a strengthening of the maximum overturning in the Nordic Seas and Arctic Ocean, both studies indicate that the overturning will become less dense, which is supported by our results in Paper IV given that the AW warming trend continues. While it is unclear to which extent this will impact the lower limb of the AMOC, one could speculate that it may reduce the depth of the lower limb (i.e. reduce the vertical extent of overturning). If this is the case, it would result in reduced ventilation of the deepest layers similar to what we already have observed in the central Greenland Sea and the Nordic Seas (Papers I, II, and IV). This could potentially have major ramifications for the ocean uptake and storage of anthropogenic carbon.

6.7 Summary

The four papers that constitute this thesis have significantly advanced our understanding of the formation and pathways of dense water in the Nordic Seas, their variability, and the contributions to the overflow waters across the Greenland-Scotland Ridge. In particular, the development of the observation-based, regional water-mass inversion revealed unprecedented details about the origin and upstream pathways of the overflows that have not previously been quantified using observations (Papers III and IV). For Denmark Strait, we found that most of the overflow water originates within the Nordic Seas. Dense water from the Greenland Sea, which supplied the largest fraction, propagates southward along two distinct pathways: an outer core of the East Greenland Current and along a previously unknown pathway across the Jan Mayen Ridge. Both of these pathways supply the NIJ (Paper III). Most of the Faroe Bank Channel overflow originates in the Greenland Sea and Arctic Ocean. Dense water from these regions approaches the channel in the IFSJ and along the eastern boundary of the Jan Mayen Ridge (Paper III). The convection and production of dense water in the Greenland Sea have changed substantially over the observational record (Papers I, II, and IV). In particular, there was a transition from bottom-reaching convection forming GSDW prior to the 1980s, via predominantly shallow convection between the mid-1980s and mid-1990s, to intermediate-depth convection forming the GSAIW after the mid-1990s. This long-term variability was largely controlled by the hydrographic conditions and changes in the inflowing AW to the Nordic Seas (Papers I and IV). Combined, the AW changes and the ceased GSDW formation have resulted in a warmer and less dense Nordic Seas reservoir

(Paper IV). The transition from formation of GSDW to GSAIW has also reduced the density and supply from the Greenland Sea to the FBCOW, while the contribution of the less dense intermediate water to the DSOW has increased (Paper IV). Essential for the interannual variability in Greenland Sea convection was variability in air-sea heat exchange, which is dominated by the frequency, intensity, and distribution of cold-air outbreaks (Papers I and II). Using a unique 10-year hydrographic record from moored profilers, the direct impact of these events on the wintertime mixed layer in the Greenland Sea was quantified for the first time (Paper II). This has not previously been possible because of sparse temporal data coverage and the short duration of these events. Both Paper I and Paper II highlight the importance of the combined effect of air-sea heat fluxes and oceanic lateral fluxes of heat and salt for the Greenland Sea mixed-layer development. Collectively, this thesis provide a step forward in our understanding of the overturning in the Nordic Seas and its variability, from an observational point of view.

Bibliography

- Aagaard, K., J. H. Swift, and E. C. Carmack (1985), Thermohaline circulation in the Arctic Mediterranean Seas, *Journal of Geophysical Research*, *90*(NC3), 4833–4846, doi:10.1029/JC090iC03p04833. 1, 13, 16, 19, 22
- Abot, L., C. Provost, and L. Poli (2023), Recent convection decline in the Greenland Sea: Insights from the Mercator Ocean System over 2008–2020, *Journal of Geophysical Research: Oceans*, *128*(6), e2022JC019,320, doi:10.1029/2022JC019320. 151
- Almeida, L., N. Kolodziejczyk, and C. Lique (submitted), Open ocean winter convection weakened in the Greenland Sea during 2014–2020, *Geophysical Research Letters*. 151
- Amante, C., and B. W. Eakins (2009), ETOPO1 1 arc-minute global relief model: procedures, data sources, and analysis, *Tech. rep.*, National Geophysical Data Center, NOAA, doi:10.7289/V5C8276M, NOAA Technical Memorandum NESDIS NGDC-24. 5
- Anderson, L. A., and J. L. Sarmiento (1994), Redfield ratios of remineralization determined by nutrient data analysis, *Global Biogeochemical Cycles*, *8*(1), 65–80, doi:10.1029/93GB03318. 31
- Årthun, M. (submitted), Surface-forced multidecadal variability in Nordic Seas overturning circulation and overflows, *Geophysical Research Letters*. 148
- Årthun, M., T. Eldevik, and L. H. Smedsrud (2019), The role of Atlantic heat transport in future Arctic winter sea ice loss, *Journal of Climate*, *32*(11), 3327–3341, doi:10.1175/JCLI-D-18-0750.1. 152
- Årthun, M., H. Asbjørnsen, L. Chafik, H. L. Johnson, and K. Våge (2023), Future strengthening of the Nordic Seas overturning circulation, *Nature Communications*, *14*(1), 2065, doi:10.1038/s41467-023-37846-6. 1, 3, 152, 153
- Asbjørnsen, H., and M. Årthun (submitted), Deconstructing future amoc decline at 26.5°N, *Geophysical Research Letters*, *2023*. 152
- Asbjørnsen, H., M. Årthun, Ø. Skagseth, and T. Eldevik (2019), Mechanisms of ocean heat anomalies in the Norwegian Sea, *Journal of Geophysical Research: Oceans*, *124*(4), 2908–2923, doi:10.1029/2018JC014649. 1
- Athanase, M., C. Provost, M. D. Pérez-Hernández, N. Sennéchaël, C. Bertosio, C. Artana, G. Garric, and J. Lellouche (2020), Atlantic Water modification north of Svalbard in the Mercator physical system from 2007 to 2020, *Journal of Geophysical Research: Oceans*, *125*(10), e2020JC016,463, doi:10.1029/2020JC016463. 2, 7, 152
- Backhaus, J. O., H. Fohrmann, J. Kämpf, and A. Rubino (1997), Formation and export of water masses produced in Arctic shelf polynyas—Process studies of oceanic convection, *ICES Journal of Marine Science*, *54*(3), 366–382, doi:10.1006/jmsc.1997.0230. 19

- Bauch, D., P. Schlosser, and R. G. Fairbanks (1995), Freshwater balance and the sources of deep and bottom waters in the Arctic Ocean inferred from the distribution of H_2^{18}O , *Progress in Oceanography*, 35(1), 53–80, doi:10.1016/0079-6611(95)00005-2. 19
- Belkin, I. M., S. Levitus, J. Antonov, and S.-A. Malmberg (1998), “Great salinity anomalies” in the North Atlantic, *Progress in Oceanography*, 41(1), 1–68, doi:10.1016/S0079-6611(98)00015-9. 151
- Berx, B., B. Hansen, S. Østerhus, K. M. Larsen, T. Sherwin, and K. Jochumsen (2013), Combining in situ measurements and altimetry to estimate volume, heat and salt transport variability through the Faroe–Shetland Channel, *Ocean Science*, 9(4), 639–654, doi:10.5194/os-9-639-2013. 8
- Bönisch, G., and P. Schlosser (1995), Deep water formation and exchange rates in the Greenland/Norwegian Seas and the Eurasian Basin of the Arctic Ocean derived from tracer balances, *Progress in Oceanography*, 35(1), 29–52, doi:10.1016/0079-6611(95)00004-Z. 16
- Bönisch, G., J. Blindheim, J. L. Bullister, P. Schlosser, and D. W. R. Wallace (1997), Long-term trends of temperature, salinity, density, and transient tracers in the central Greenland Sea, *Journal of Geophysical Research: Oceans*, 102(C8), 18,553–18,571, doi:10.1029/97JC00740. 16
- Bosse, A., and I. Fer (2019), Mean structure and seasonality of the Norwegian Atlantic Front Current along the Mohn Ridge from repeated glider transects, *Geophysical Research Letters*, 46, 13,170–13,179, doi:10.1029/2019GL084723. 13, 19
- Bosse, A., I. Fer, H. Søyland, and T. Rossby (2018), Atlantic Water transformation along its poleward pathway across the Nordic Seas, *Journal of Geophysical Research: Oceans*, 123(9), 6428–6448, doi:10.1029/2018JC014147. 13, 16, 147
- Bourke, R. H., R. G. Paquette, and R. F. Blythe (1992), The Jan Mayen Current of the Greenland Sea, *Journal of Geophysical Research*, 97(C5), 7241–7250. 10, 19
- Brakstad, A. (2016), Water mass transformation in the Greenland Sea, Master’s thesis, University of Bergen. 35
- Brakstad, A., K. Våge, L. Håvik, and G. W. K. Moore (2019), Water mass transformation in the Greenland Sea during the period 1986–2016, *Journal of Physical Oceanography*, 49(1), 121–140, doi:10.1175/JPO-D-17-0273.1. 18, 21
- Brakstad, A., G. Gebbie, K. Våge, E. Jeansson, and S. R. Ólafsdóttir (2023), Formation and pathways of dense water in the Nordic Seas based on a regional inversion, *Progress in Oceanography*, 212, doi:10.1016/j.pocean.2023.102981. 22
- Bretones, A., K. H. Nisancioglu, M. F. Jensen, A. Brakstad, and S. Yang (2022), Transient increase in Arctic deep-water formation and ocean circulation under sea ice retreat, *Journal of Climate*, 35(1), 109–124, doi:10.1175/JCLI-D-21-0152.1. 3, 152, 153
- Bringedal, C., T. Eldevik, Ø. Skagseth, M. A. Spall, and S. Østerhus (2018), Structure and forcing of observed exchanges across the Greenland–Scotland Ridge, *Journal of Climate*, 31(24), 9881–9901, doi:10.1175/JCLI-D-17-0889.1. 6

- Buckley, M. W., and J. Marshall (2016), Observations, inferences, and mechanisms of the Atlantic Meridional Overturning Circulation: A review, *Reviews of Geophysics*, *54*(1), 5–63, doi:10.1002/2015RG000493. 3
- Budéus, G. (2009), Autonomous daily CTD profiles between 3,700 meters and the ocean surface, *Sea Technology*, (October 2009), 45–48. 27
- Budéus, G., and S. Ronski (2009), An integral view of the hydrographic development in the Greenland Sea over a decade, *The Open Oceanography Journal*, *3*, 8 – 39. 17
- Budéus, G., K. Ohm, M. Damm, and R. Plugge (2005), The externally powered, compressibility compensated Jojo mooring: A mechanical solution to autonomous deep sea profiling, *Deep-Sea Research Part I: Oceanographic Research Papers*, *52*(10), 1964–1973, doi:10.1016/j.dsr.2005.05.005. 27
- Carmack, E., and K. Aagaard (1973), On the Deep Water of the Greenland Sea, *Deep-Sea Research*, *20*(8), 687–715, doi:10.1016/0011-7471(73)90086-7. 16
- Casanova-Masjoan, M., M. D. Pérez-Hernández, R. S. Pickart, H. Valdimarsson, S. R. Ólafsdóttir, A. Macrander, D. Grisolia-Santos, D. J. Torres, S. Jónsson, K. Våge, P. Lin, and A. Hernández-Guerra (2020), Along-stream, seasonal, and interannual variability of the North Icelandic Irminger Current and East Icelandic Current around Iceland, *Journal of Geophysical Research: Oceans*, *125*(9), e2020JC016283, doi:10.1029/2020JC016283. 8, 21
- Cavaliere, D. J., and S. Martin (1994), The contribution of Alaskan, Siberian, and Canadian coastal polynyas to the cold halocline layer of the Arctic Ocean, *Journal of Geophysical Research*, *99*(C9), 18,343–18,362, doi:10.1029/94JC01169. 30
- Chafik, L., and T. Rossby (2019), Volume, heat, and freshwater divergences in the subpolar north atlantic suggest the nordic seas as key to the state of the meridional overturning circulation, *Geophysical Research Letters*, *46*, 4799–4808, doi:10.1029/2019GL082110. 1, 3
- Chafik, L., H. Hátún, J. Kjellsson, K. M. H. Larsen, T. Rossby, and B. Berx (2020), Discovery of an unrecognized pathway carrying overflow waters toward the Faroe Bank Channel, *Nature Communications*, *11*(1), 1–10, doi:10.1038/s41467-020-17426-8. 23, 148, 150, 151
- Dahlke, S., A. Solbès, and M. Maturilli (2022), Cold air outbreaks in Fram Strait: Climatology, trends, and observations during an extreme season in 2020, *Journal of Geophysical Research: Atmospheres*, *127*, e2021JD035741, doi:10.1029/2021JD035741. 2, 17, 152
- Davila, X., G. Gebbie, A. Brakstad, S. K. Lauvset, E. L. McDonagh, J. Schwinger, and A. Olsen (2022), How is the ocean anthropogenic carbon reservoir filled?, *Global Biogeochemical Cycles*, *36*(5), e2021GB007055, doi:10.1029/2021GB007055. 1, 3, 150
- Davila, X., G. Gebbie, A. Brakstad, S. K. Lauvset, E. L. McDonagh, E. Jeansson, and A. Olsen (in prep.), Water-mass ages and ventilation timescales of the Nordic Seas inferred from transient tracers, *Manuscript in preparation*, 2023. 150, 151

- de Boyer Montégut, C., G. Madec, A. S. Fischer, A. Lazar, and D. Iudicone (2004), Mixed layer depth over the global ocean: an examination of profile data and a profile-based climatology, *Journal of Geophysical Research: Oceans*, *109*(C12), doi:10.1029/2004JC002378. 28, 29
- de Jong, M. F., H. Søyland, A. S. Bower, and H. H. Furey (2018), The subsurface circulation of the Iceland Sea observed with RAFOS floats, *Deep Sea Research Part I: Oceanographic Research Papers*, *141*, 1–10, doi:10.1016/j.dsr.2018.07.008. 10
- Dee, D. P., S. M. Uppala, A. J. Simmons, P. Berrisford, P. Poli, S. Kobayashi, U. Andrae, M. A. Balmaseda, G. Balsamo, P. Bauer, P. Bechtold, A. C. M. Beljaars, L. Van de Berg, J. Bidlot, N. Bormann, C. Delsol, R. Dragani, M. Fuentes, A. J. Geer, L. Haimberger, S. B. Healy, H. Hersbach, E. V. Hólm, L. Isaksen, P. Kållberg, M. Köhler, M. Matricardi, A. P. McNally, B. M. Monge-Sanz, J. J. Morcrette, B. K. Park, C. Peubey, P. De Rosnay, C. Tavolato, J. N. Thépaut, and F. Vitart (2011), The ERA - Interim reanalysis: configuration and performance of the data assimilation system, *Quarterly Journal of the Royal Meteorological Society*, *137*(656), 553–597, doi:10.1002/qj.828. 28
- Dickson, R. R., and J. Brown (1994), The production of North Atlantic Deep Water: sources, rates, and pathways, *Journal of Geophysical Research*, *99*(C6), 12,319–12,341, doi:10.1029/94jc00530. 3, 9, 10, 20
- Dickson, R. R., J. Meincke, S.-A. Malmberg, and A. J. Lee (1988), The “great salinity anomaly” in the northern North Atlantic 1968 - 1982, *Progress in Oceanography*, *20*(2), 103–151. 151
- Dickson, R. R., T. J. Osborn, J. W. Hurrell, J. Meincke, J. Blindheim, B. Adlandsvik, T. Vinje, G. Alekseev, and W. Maslowski (2000), The Arctic ocean response to the North Atlantic oscillation, *Journal of Climate*, *13*(15), 2671–2696, doi:10.1175/1520-0442(2000)013<2671:TAORTT>2.0.CO;2. 6
- Dodd, P. A., K. J. Heywood, M. P. Meredith, A. C. Naveira-Garabato, A. D. Marca, and K. K. Falkner (2009), Sources and fate of freshwater exported in the East Greenland Current, *Geophysical Research Letters*, *36*(19), doi:10.1029/2009GL039663. 10, 20, 151
- Drange, H., T. Dokken, T. Furevik, R. Gerdes, W. Berger, A. Nesje, K. A. Orvik, Ø. Skagseth, I. Skjelvan, and S. Østerhus (2005), *The Nordic Seas: an overview*, Wiley Online Library. 1, 4
- Dugstad, J., I. Fer, J. LaCasce, M. Sanchez de La Lama, and M. Trodahl (2019), Lateral heat transport in the Lofoten Basin: Near-surface pathways and subsurface exchange, *Journal of Geophysical Research: Oceans*, *124*(5), 2992–3006, doi:10.1029/2018JC014774. 13, 19
- Eldevik, T., and J. E. Ø. Nilsen (2013), The Arctic–Atlantic Thermohaline Circulation, *Journal of Climate*, *26*(21), 8698–8705, doi:10.1175/JCLI-D-13-00305.1. 7
- Eldevik, T., J. E. Ø. Nilsen, D. Iovino, K. A. Olsson, A. B. Sandø, and H. Drange (2009), Observed sources and variability of Nordic Seas overflow, *Nature Geoscience*, *2*(6), 405–409, doi:10.1038/ngeo518. 1, 11, 13, 14, 21, 22, 31, 149

- Fer, I., A. Bosse, and J. Dugstad (2020), Norwegian Atlantic Slope Current along the Lofoten Escarpment, *Ocean Science*, 16(3), 685–701, doi:10.5194/os-16-685-2020. 19
- Fogelqvist, E., J. Blindheim, T. Tanhua, S. Østerhus, E. Buch, and F. Rey (2003), Greenland - Scotland overflow studied by hydro-chemical multivariate analysis, *Deep-Sea Research Part 1*, 50(1), 73–102, doi:10.1016/s0967-0637(02)00131-0. 2, 22
- Frajka-Williams, E., I. J. Ansorge, J. Baehr, H. L. Bryden, M. P. Chidichimo, S. A. Cunningham, G. Danabasoglu, S. Dong, K. A. Donohue, S. Elipot, P. Heimbach, N. P. Holliday, R. Hummels, L. C. Jackson, J. Karstensen, M. Lankhorst, I. A. Le Bras, M. S. Lozier, E. L. McDonagh, C. S. Meinen, H. Mercier, B. I. Moat, R. C. Perez, C. G. Piecuch, M. Rhein, M. A. Srokosz, K. E. Trenberth, S. Bacon, G. Forget, G. Goni, D. Kieke, J. Koelling, T. Lamont, G. D. McCarthy, C. Mertens, U. Send, D. A. Smeed, S. Speich, M. van den Berg, D. Volkov, and C. Wilson (2019), Atlantic Meridional Overturning Circulation: Observed transport and variability, *Frontiers in Marine Science*, p. 260, doi:10.3389/fmars.2019.00260. 3
- Furevik, T., and J. E. Ø. Nilsen (2005), Large-scale atmospheric circulation variability and its impacts on the Nordic Seas ocean climate - a review, *Geophysical Monograph-American Geophysical Union*, 158, 105, doi:10.1029/158GM09. 5, 6, 7
- Garcia-Quintana, Y., N. Grivault, X. Hu, and P. G. Myers (2021), Dense water formation on the Icelandic shelf and its contribution to the North Icelandic Jet, *Journal of Geophysical Research: Oceans*, 126(8), e2020JC016,951, doi:10.1029/2020JC016951. 21
- Gascard, J.-C., A. J. Watson, M.-J. Messias, K. A. Olsson, T. Johannessen, and K. Simonsen (2002), Long-lived vortices as a mode of deep ventilation in the Greenland Sea, *Nature*, 416(6880), 525–527. 15
- Gebbie, G. (2014), How much did Glacial North Atlantic Water shoal?, *Paleoceanography*, 29(3), 190–209, doi:10.1002/2013PA002557. 22, 31, 32, 33, 149, 150
- Gebbie, G., and P. Huybers (2010), Total Matrix Intercomparison: a method for determining the geometry of water-mass pathways, *Journal of Physical Oceanography*, 40(8), 1710–1728, doi:10.1175/2010JPO4272.1. 22, 31, 32, 149, 150
- Gebbie, G., and P. Huybers (2011), How is the ocean filled?, *Geophysical Research Letters*, 38(6), doi:10.1029/2011GL046769. 1, 32
- Gebbie, G., and P. Huybers (2012), The mean age of ocean waters inferred from radiocarbon observations: sensitivity to surface sources and accounting for mixing histories, *Journal of Physical Oceanography*, 42(2), 291–305, doi:10.1175/JPO-D-11-043.1. 32, 150
- Glessmer, M. S., T. Eldevik, K. Våge, J. E. Ø. Nilsen, and E. Behrens (2014), Atlantic origin of observed and modelled freshwater anomalies in the Nordic Seas, *Nature Geoscience*, 7(11), 801–805, doi:10.1038/ngeo2259. 1, 20, 149, 151
- Haine, T. W. N., B. Curry, R. Gerdes, E. Hansen, M. Karcher, C. Lee, B. Rudels, G. Spreen, L. de Steur, K. D. Stewart, and R. Woodgate (2015), Arctic freshwater export: Status, mechanisms, and prospects, *Global and Planetary Change*, 125, 13–35, doi:10.1016/j.gloplacha.2014.11.013. 1, 9

- Hansen, B., and S. Østerhus (2000), North Atlantic-Nordic Seas exchanges, *Progress in Oceanography*, 45(2), 109–208, doi:10.1016/s0079-6611(99)00052-x. 5, 8, 22
- Hansen, B., K. Larsen, H. Hátún, R. Kristiansen, E. Mortensen, and S. Østerhus (2015), Transport of volume, heat, and salt towards the Arctic in the Faroe Current 1993–2013, *Ocean Science*, 11(5), 743–757, doi:10.5194/os-11-743-2015. 8
- Hansen, B., K. M. Larsen, H. Hátún, and S. Østerhus (2016), A stable Faroe Bank Channel overflow 1995–2015, *Ocean Science*, 12(6), 1205–1220, doi:10.5194/os-12-1205-2016. 20, 153
- Harden, B. E., R. S. Pickart, H. Valdimarsson, K. Våge, L. de Steur, C. Richards, F. Bahr, D. Torres, E. Børve, S. Jónsson, A. Macrander, S. Østerhus, L. Håvik, and T. Hattermann (2016), Upstream sources of the Denmark Strait Overflow: observations from a high-resolution mooring array, *Deep Sea Research I*, 112, 94–112, doi:10.1016/j.dsr.2016.02.007. 10, 21
- Hattermann, T., P. E. Isachsen, W. von Appen, J. Albreetsen, and A. Sundfjord (2016), Eddy-driven recirculation of Atlantic water in Fram Strait, *Geophysical Research Letters*, 43(7), 3406–3414, doi:10.1002/2016GL068323. 20
- Hátún, H., L. Chafik, and K. M. H. Larsen (2021), The Norwegian Sea Gyre – a regulator of Iceland-Scotland Ridge exchanges, *Frontiers in Marine Science*, 8(694614), doi:10.3389/fmars.2021.694614. 22
- Håvik, L., R. S. Pickart, K. Våge, D. Torres, A. M. Thurnherr, A. Beszczynska-Möller, W. Walczowski, and W. von Appen (2017a), Evolution of the East Greenland Current from Fram Strait to Denmark Strait: synoptic measurements from summer 2012, *Journal of Geophysical Research: Oceans*, 122(3), 1974–1994, doi:10.1002/2016JC012228. 9, 10, 15, 20
- Håvik, L., K. Våge, R. S. Pickart, B. Harden, W.-J. von Appen, S. Jónsson, and S. Østerhus (2017b), Structure and Variability of the Shelfbreak East Greenland Current North of Denmark Strait, *Journal of Physical Oceanography*, 47(10), 2631–2646, doi:10.1175/JPO-D-17-0062.1. 19
- Håvik, L., M. Almansi, K. Våge, and T. W. N. Haine (2019), Atlantic-origin overflow water in the East Greenland Current, *Journal of Physical Oceanography*, 49(9), 2255–2269, doi:10.1175/JPO-D-18-0216.1. 20
- Helland-Hansen, B., and F. Nansen (1909), The Norwegian Sea: its physical oceanography based upon the Norwegian researches 1900–1904, *Report on Norwegian fishery and marine investigations*, 2(2), 1–390. 8, 10, 16
- Hersbach, H., B. Bell, P. Berrisford, S. Hirahara, A. Horányi, J. Muñoz-Sabater, J. Nicolas, C. Peubey, R. Radu, D. Schepers, A. Simmons, C. Soci, S. Abdalla, X. Abellan, G. Balsamo, P. Bechtold, G. Biavati, J. Bidlot, M. Bonavita, G. De Chiara, P. Dahlgren, D. Dee, M. Diamantakis, R. Dragani, J. Flemming, R. Forbes, M. Fuentes, A. Geer, L. Haimberger, S. Healy, R. J. Hogan, E. Hólm, M. Janisková, S. Keeley, P. Laloyaux, P. Lopez, C. Lupu, G. Radnoti, P. de Rosnay,

- I. Rozum, F. Vamborg, S. Villaume, and J.-N. Thépaut (2020), The ERA5 global re-analysis, *Quarterly Journal of the Royal Meteorological Society*, *146*(730), 1999–2049, doi:10.1002/qj.3803. 6, 28
- Holliday, N. P., S. L. Hughes, S. Bacon, A. Beszczynska-Möller, B. Hansen, A. Lavin, H. Loeng, K. A. Mork, S. Østerhus, and T. Sherwin (2008), Reversal of the 1960s to 1990s freshening trend in the northeast North Atlantic and Nordic Seas, *Geophysical Research Letters*, *35*(3). 149
- Huang, J., R. S. Pickart, R. X. Huang, P. Lin, A. Brakstad, and F. Xu (2020), Sources and upstream pathways of the densest overflow water in the Nordic Seas, *Nature Communications*, *11*(5389), doi:10.1038/s41467-020-19050-y. 2, 21, 22, 148, 151
- Huang, J., R. S. Pickart, Z. Chen, and R. X. Huang (2023), Role of air-sea heat flux on the transformation of Atlantic Water encircling the Nordic Seas, *Nature Communications*, *14*(1), 141, doi:10.1038/s41467-023-35889-3. 13, 20
- ICES, SCOR, and IAPSO (1981), *Tenth Report of the Joint Panel on Oceanographic Tables and Standards (The Practical Salinity Scale 1978 and the International Equation of State of Seawater 1980)*, UNESCO Technical Papers in Marine Science No. 36, 25 pp. 26
- IOC, SCOR, and IAPSO (2010), *The international thermodynamic equation of seawater - 2010: calculation and use of thermodynamic properties*, intergovernmental Oceanographic Commission, Manuals and Guides No. 56, UNESCO. 11, 26
- Isachsen, P. E., C. Mauritzen, and H. Svendsen (2007), Dense water formation in the Nordic Seas diagnosed from sea surface buoyancy fluxes, *Deep Sea Research Part I: Oceanographic Research Papers*, *54*(1), 22–41, doi:10.1016/j.dsr.2006.09.008. 7, 13, 147, 148
- Isachsen, P. E., S. R. Sørli, C. Mauritzen, C. Lydersen, P. Dodd, and K. M. Kovacs (2014), Upper-ocean hydrography of the Nordic Seas during the International Polar Year (2007 - 2008) as observed by instrumented seals and Argo floats, *Deep Sea Research I*, *93*, 41–59, doi:10.1016/j.dsr.2014.06.012. 25
- Ivanov, V. V., G. I. Shapiro, J. M. Huthnance, D. L. Aleynik, and P. N. Golovin (2004), Cascades of dense water around the world ocean, *Progress in oceanography*, *60*(1), 47–98, doi:10.1016/j.pocean.2003.12.002. 19
- Jeansson, E., S. Jutterström, B. Rudels, L. G. Anderson, K. A. Olsson, E. P. Jones, W. M. Smethie, and J. H. Swift (2008), Sources to the East Greenland Current and its contribution to the Denmark Strait Overflow, *Progress in Oceanography*, *78*(1), 12–28, doi:10.1016/j.pocean.2007.08.031. 2, 11, 12, 13, 15, 17, 19, 20, 21, 22, 31, 149
- Jeansson, E., A. Olsen, T. Eldevik, I. Skjelvan, A. M. Omar, S. K. Lauvset, J. E. O. Nilsen, R. G. J. Bellerby, T. Johannessen, and E. Falck (2011), The Nordic Seas carbon budget: Sources, sinks, and uncertainties, *Global Biogeochemical Cycles*, *25*(4), doi:10.1029/2010GB003961. 1
- Jeansson, E., A. Olsen, and S. Jutterström (2017), Arctic Intermediate Water in the Nordic Seas, 1991-2009, *Deep Sea Research I*, *128*, 82–97, doi:10.1016/j.dsr.2017.08.013. 11, 13, 19, 22, 31, 149

- Jochumsen, K., M. Moritz, N. Nunes, D. Quadfasel, K. M. Larsen, B. Hansen, H. Valdimarsson, and S. Jónsson (2017), Revised transport estimates of the Denmark Strait overflow, *Journal of Geophysical Research*, *122*, 3434–3450, doi:10.1002/2017JC012803. 20, 153
- Jónsson, S. (1991), Seasonal and interannual variability of wind stress curl over the Nordic Seas, *Journal of Geophysical Research: Oceans*, *96*(C2), 2649–2659, doi:10.1029/90JC02230. 6
- Jónsson, S. (1999), The circulation in the northern part of the Denmark Strait and its variability, *ICES report CM*, *50*, 06. 21
- Jónsson, S., and H. Valdimarsson (2004), A new path for the Denmark strait overflow water from the Iceland Sea to Denmark Strait, *Geophysical Research Letters*, *31*(3), doi:10.1029/2003gl019214. 10, 21
- Jónsson, S., and H. Valdimarsson (2012), Water mass transport variability to the north Icelandic shelf, 1994–2010, *ICES Journal of Marine Science*, *69*(5), 809–815, doi:10.1093/icesjms/fss024. 8
- Karstensen, J., and M. Tomczak (1998), Age determination of mixed water masses using CFC and oxygen data, *Journal of Geophysical Research: Oceans*, *103*(C9), 18,599–18,609, doi:10.1029/98JC00889. 31
- Karstensen, J., P. Schlosser, D. W. R. Wallace, J. L. Bullister, and J. Blindheim (2005), Water mass transformation in the Greenland Sea during the 1990s, *Journal of Geophysical Research*, *110*(C7), doi:10.1029/2004jc002510. 2, 17
- Köhl, A. (2007), Generation and stability of a quasi-permanent vortex in the Lofoten Basin, *Journal of Physical Oceanography*, *37*(11), 2637–2651, doi:10.1175/2007JPO3694.1. 13, 19, 21
- Köhl, A. (2010), Variable source regions of Denmark Strait and Faroe Bank Channel overflow waters, *Tellus A: Dynamic Meteorology and Oceanography*, *62*(4), 551–568, doi:10.1111/j.1600-0870.2010.00454.x. 22
- Köhl, A., and J. Willebrand (2002), An adjoint method for the assimilation of statistical characteristics into eddy-resolving ocean models, *Tellus A: Dynamic Meteorology and Oceanography*, *54*(4), 406–425, doi:10.3402/tellusa.v54i4.12150. 33
- Kuhlbrodt, T., A. Griesel, M. Montoya, A. Levermann, M. Hofmann, and S. Rahmstorf (2007), On the driving processes of the Atlantic meridional overturning circulation, *Reviews of Geophysics*, *45*(2). 3
- Lambert, E., T. Eldevik, and P. M. Haugan (2016), How northern freshwater input can stabilise thermohaline circulation, *Tellus A: Dynamic Meteorology and Oceanography*, *68*(1), 31,051, doi:10.3402/tellusa.v68.31051. 6, 7
- Langehaug, H. R., and E. Falck (2012), Changes in the properties and distribution of the intermediate and deep waters in the Fram Strait, *Progress in Oceanography*, *96*(1), 57–76, doi:10.1016/j.pocean.2011.10.002. 4, 19

- Langehaug, H. R., A. Brakstad, K. Våge, E. Jeansson, M. Ilicak, and C. A. Katsman (2022), Drivers of surface salinity changes in the Greenland-Iceland Seas on seasonal and interannual time scales - a climate model study, *Earth and Space Science Open Archive*, doi:10.1002/essoar.10511221.1. 10, 20, 151
- Latarius, K., and D. Quadfasel (2010), Seasonal to inter-annual variability of temperature and salinity in the Greenland Sea Gyre: heat and freshwater budgets, *Tellus A*, *62*(4), 497–515, doi:10.1111/j.1600-0870.2010.00453.x. 2, 17
- Latarius, K., and D. Quadfasel (2016), Water mass transformation in the deep basins of the Nordic Seas: Analyses of heat and freshwater budgets, *Deep-Sea Research I*, *114*, 23–42, doi:10.1016/j.dsr.2016.04.012. 17, 18, 29
- Lauvset, S. K., A. Brakstad, K. Våge, A. Olsen, E. Jeansson, and K. A. Mork (2018), Continued warming, salinification and oxygenation of the Greenland Sea gyre., *Tellus A*, *70*(1), 1–9, doi:10.1080/16000870.2018.1476434. 1, 2, 17, 20, 147, 151
- Lin, P., R. S. Pickart, K. Jochumsen, G. W. K. Moore, H. Valdimarsson, T. Fristedt, and L. J. Pratt (2020), Kinematic structure and dynamics of the Denmark Strait overflow from ship-based observations, *Journal of Physical Oceanography*, *50*(11), 3235–3251, doi:10.1175/JPO-D-20-0095.1. 22, 31, 150, 151
- Lique, C., H. L. Johnson, and Y. Plancherel (2018), Emergence of deep convection in the Arctic Ocean under a warming climate, *Climate Dynamics*, *50*(9-10), 3833–3847, doi:10.1007/s00382-017-3849-9. 152
- Lorbacher, K., D. Dommenges, P. P. Niiler, and A. Köhl (2006), Ocean mixed layer depth: A subsurface proxy of ocean - atmosphere variability, *Journal of Geophysical Research*, *111*(C7), doi:10.1029/2003JC002157. 28
- Lozier, S. M., S. Bacon, A. S. Bower, S. A. Cunningham, F. M. de Jong, L. de Steur, B. deYoung, J. Fischer, S. F. Gary, B. J. W. Greenan, P. Heimbach, N. P. Holliday, L. Houpert, M. E. Inall, W. E. Johns, H. L. Johnson, J. Karstensen, F. Li, X. Lin, N. Mackay, D. P. Marshall, H. Mercier, P. G. Myers, R. S. Pickart, H. R. Pillar, F. Straneo, V. Thierry, R. A. Weller, R. G. Williams, C. Wilson, J. Yang, J. Zhao, and J. D. Zika (2017), Overturning in the Subpolar North Atlantic Program: A new international ocean observing system, *Bulletin of the American Meteorological Society*, *98*(4), 737–752, doi:10.1175/BAMS-D-16-0057.1. 3
- Lozier, S. M., F. Li, S. Bacon, F. Bahr, A. S. Bower, S. A. Cunningham, F. M. de Jong, L. de Steur, B. deYoung, J. Fischer, S. F. Gary, B. J. W. Greenan, N. P. Holliday, A. Houk, L. Houpert, M. E. Inall, W. E. Johns, H. L. Johnson, C. Johnson, J. Karstensen, G. Koman, I. A. Le Bras, X. Lin, N. Mackay, D. P. Marshall, H. Mercier, M. Oltmanns, R. S. Pickart, A. L. Ramsey, D. Rayner, F. Straneo, V. Thierry, D. J. Torres, R. G. Williams, C. Wilson, J. Yang, I. Yashayaev, and J. Zhao (2019), A sea change in our view of overturning in the subpolar north atlantic, *Science*, *363*, 516–521, doi:10.1126/science.aau6592. 1, 3
- Macrander, A., H. Valdimarsson, and S. Jónsson (2014), Improved transport estimate of the East Icelandic Current 2002–2012, *Journal of Geophysical Research: Oceans*, *119*(6), 3407–3424, doi:10.1002/2013JC009517. 10, 19

- Malmberg, S.-A. (1983), *Hydrographic investigations in the Iceland and Greenland seas in late winter 1971 - "Deep water project"*, vol. 33, Jökull. 16
- Malmberg, S.-A., and S. Jónsson (1997), Timing of deep convection in the Greenland and Iceland Seas, *ICES Journal of Marine Science*, 54(3), 300–309, doi:10.1006/jmsc.1997.0221. 16
- Marnela, M., B. Rudels, I. Goszczko, A. Beszczynska Möller, and U. Schauer (2016), Fram Strait and Greenland Sea transports, water masses, and water mass transformations 1999 - 2010 (and beyond), *Journal of Geophysical Research*, 121(4), 2314–2346, doi:10.1002/2015JC011312. 25
- Marshall, J., and F. Schott (1999), Open - ocean convection: observations, theory, and models, *Reviews of Geophysics*, 37(1), 1–64, doi:10.1029/98RG02739. 15, 16, 30
- Marshall, J., and K. Speer (2012), Closure of the meridional overturning circulation through Southern Ocean upwelling, *Nature geoscience*, 5(3), 171–180, doi:10.1038/ngeo1391. 3
- Mastropole, D., R. S. Pickart, H. Valdimarsson, K. Våge, K. Jochumsen, and J. Girton (2017), On the hydrography of Denmark Strait, *Journal of Geophysical Research*, 122(1), 306–321, doi:10.1002/2016JC012007. 11, 21, 22, 31, 149, 151
- Mauritzen, C. (1996), Production of dense overflow waters feeding the North Atlantic across the Greenland-Scotland Ridge. Part 1: Evidence for a revised circulation scheme, *Deep-Sea Research I*, 43(6), 769–806, doi:10.1016/0967-0637(96)00037-4. 1, 8, 9, 13, 15, 20, 21, 147
- McKenna, C., B. Berx, and W. E. N. Austin (2016), The decomposition of the Faroe-Shetland Channel water masses using Parametric Optimum Multi-Parameter analysis, *Deep Sea Research Part I: Oceanographic Research Papers*, 107, 9–21, doi:10.1016/j.dsr.2015.10.013. 22
- Meincke, J., and B. Rudels (1996), Greenland Sea Deep Water: A balance between convection and advection, *World Meteorological Organization*, pp. 436–440. 19
- Meincke, J., S. Jónsson, and J. H. Swift (1992), Variability of convective conditions in the Greenland Sea, *ICES Mar. Sci. Symp*, 195, 32–39. 2, 16, 17
- Meincke, J., B. Rudels, and H. J. Friedrich (1997), The Arctic Ocean - Nordic Seas thermohaline system, *ICES Journal of Marine Science*, 54(3), 283–299, doi:10.1006/jmsc.1997.0229. 17
- Messias, M. J., A. J. Watson, T. Johannessen, K. I. C. Oliver, K. A. Olsson, E. Fogelqvist, J. Olafsson, S. Bacon, J. Balle, N. Bergman, G. Budéus, M. Danielsen, J. C. Gascard, E. Jeansson, S. R. Olafsdottir, K. Simonsen, T. Tanhua, K. Van Scoy, and J. R. Ledwell (2008), The Greenland Sea tracer experiment 1996-2002: Horizontal mixing and transport of Greenland Sea Intermediate Water, *Progress in Oceanography*, 78(1), 85–105, doi:10.1016/j.pocean.2007.06.005. 21, 22, 151
- Moore, G. W. K., K. Våge, R. S. Pickart, and I. A. Renfrew (2015), Decreasing intensity of open-ocean convection in the Greenland and Iceland seas, *Nature Climate Change*, 5(9), 877–882, doi:10.1038/nclimate2688. 1, 2, 7, 17, 18, 29, 152

- Moore, G. W. K., K. Våge, I. A. Renfrew, and R. S. Pickart (2022), Sea-ice retreat suggests re-organization of water mass transformation in the Nordic and Barents Seas, *Nature communications*, *13*(1), 1–8, doi:10.1038/s41467-021-27641-6. 1, 2, 7, 14, 15, 17, 18, 152
- Mork, K. A., Ø. Skagseth, V. Ivshin, V. Ozhigin, S. L. Hughes, and H. Valdimarsson (2014a), Advective and atmospheric forced changes in heat and fresh water content in the Norwegian Sea, 1951–2010, *Geophysical Research Letters*, *41*(17), 6221–6228, doi:10.1002/2014GL061038. 1
- Mork, K. A., K. F. Drinkwater, S. Jónsson, H. Valdimarsson, and M. Ostrowski (2014b), Water mass exchanges between the Norwegian and Iceland seas over the Jan Mayen Ridge using in-situ current measurements, *Journal of Marine Systems*, *139*, 227–240, doi:10.1016/j.jmarsys.2014.06.008. 8
- Mork, K. A., Ø. Skagseth, and H. Sjøland (2019), Recent warming and freshening of the Norwegian Sea observed by Argo data, *Journal of Climate*, *32*(12), 3695–3705, doi:10.1175/JCLI-D-18-0591.1. 151
- Muilwijk, M., L. H. Smedsrud, M. Ilicak, and H. Drange (2018), Atlantic Water heat transport variability in the 20th century Arctic Ocean from a global ocean model and observations, *Journal of Geophysical Research: Oceans*, *123*(11), 8159–8179, doi:10.1029/2018JC014327. 6
- Nilsen, J. E. Ø., and E. Falck (2006), Variations of mixed layer properties in the Norwegian Sea for the period 1948–1999, *Progress in Oceanography*, *70*(1), 58–90, doi:10.1016/j.pocean.2006.03.014. 28, 29
- Nøst, O. A., and P. E. Isachsen (2003), The large-scale time-mean ocean circulation in the Nordic Seas and Arctic Ocean estimated from simplified dynamics, *Journal of Marine Research*, *61*(2), 175–210, doi:10.1357/002224003322005069. 5, 6, 32
- Olsson, K. A., E. Jeansson, L. G. Anderson, B. Hansen, T. Eldevik, R. Kristiansen, M.-J. Messias, T. Johannessen, and A. J. Watson (2005), Intermediate water from the Greenland Sea in the Faroe Bank Channel: spreading of released sulphur hexafluoride, *Deep Sea Research Part I: Oceanographic Research Papers*, *52*(2), 279–294, doi:10.1016/j.dsr.2004.09.009. 22
- Onarheim, I. H., T. Eldevik, L. H. Smedsrud, and J. C. Stroeve (2018), Seasonal and regional manifestation of Arctic sea ice loss, *Journal of Climate*, *31*(12), 4917–4932, doi:10.1175/JCLI-D-17-0427.1. 1, 7
- Orvik, K. A., and P. Niiler (2002), Major pathways of Atlantic Water in the northern North Atlantic and Nordic Seas toward Arctic, *Geophysical Research Letters*, *29*(19), 2–1–2–4, doi:10.1029/2002GL015002. 8
- Østerhus, S., and T. Gammelsrød (1999), The abyss of the Nordic Seas is warming, *Journal of Climate*, *12*(11), 3297–3304, doi:10.1175/1520-0442(1999)012<3297:TAOTNS>2.0.CO;2. 17, 19, 22

- Østerhus, S., R. Woodgate, H. Valdimarsson, B. Turrell, L. de Steur, D. Quadfasel, S. M. Olsen, M. Moritz, C. M. Lee, K. M. H. Larsen, S. Jonsson, C. Johnson, K. Jochumsen, B. Hansen, B. Curry, S. Cunningham, and B. Berx (2019), Arctic mediterranean exchanges: a consistent volume budget and trends in transports from two decades of observations, *Ocean Science*, *15*(2), 379–399, doi:10.5194/os-15-379-2019. 8, 10, 20, 150, 153
- Papritz, L., and T. Spengler (2017), A Lagrangian Climatology of Wintertime Cold Air Outbreaks in the Irminger and Nordic Seas and Their Role in Shaping Air-Sea Heat Fluxes, *Journal of Climate*, *30*(8), 2717–2737, doi:10.1175/JCLI-D-16-0605.1. 1, 7
- Pérez-Hernández, M. D., R. S. Pickart, D. J. Torres, F. Bahr, A. Sundfjord, R. Ingvaldsen, A. H. H. Renner, A. Beszczynska-Möller, W. von Appen, and V. Pavlov (2019), Structure, transport, and seasonality of the Atlantic Water boundary current north of Svalbard: Results from a yearlong mooring array, *Journal of Geophysical Research: Oceans*, *124*(3), 1679–1698, doi:10.1029/2018JC014759. 1, 7, 12
- Petit, T., M. S. Lozier, S. A. Josey, and S. A. Cunningham (2020), Atlantic deep water formation occurs primarily in the Iceland Basin and Irminger Sea by local buoyancy forcing, *Geophysical Research Letters*, *47*(22), e2020GL091028, doi:10.1029/2020GL091028. 1, 3
- Pickart, R. S., D. J. Torres, and R. A. Clarke (2002), Hydrography of the Labrador Sea during active convection, *Journal of Physical Oceanography*, *32*(2), 428–457, doi:10.1175/1520-0485(2002)032<0428:hotlsd>2.0.co;2. 28, 29
- Pickart, R. S., G. W. K. Moore, C. Mao, F. Bahr, C. Nobre, and T. J. Weingartner (2016), Circulation of winter water on the Chukchi shelf in early Summer, *Deep Sea Research II*, *130*, 56–75, doi:10.1016/j.dsr2.2016.05.001. 30
- Poole, R., and M. Tomczak (1999), Optimum multiparameter analysis of the water mass structure in the Atlantic Ocean thermocline, *Deep Sea Research Part I: Oceanographic Research Papers*, *46*(11), 1895–1921, doi:10.1016/S0967-0637(99)00025-4. 31
- Pope, J. O., T. J. Bracegirdle, I. A. Renfrew, and A. D. Elvidge (2020), The impact of wintertime sea-ice anomalies on high surface heat flux events in the Iceland and Greenland Seas, *Climate Dynamics*, *54*, 1937–1952, doi:10.1007/s00382-019-05095-3. 7
- Poulain, P., A. Warn-Varnas, and P. P. Niiler (1996), Near-surface circulation of the Nordic seas as measured by Lagrangian drifters, *Journal of Geophysical Research: Oceans*, *101*(C8), 18,237–18,258, doi:10.1029/96JC00506. 8, 13
- Price, J. F., R. A. Weller, and R. Pinkel (1986), Diurnal cycling: observations and models of the upper-ocean response to diurnal heating, cooling, and wind mixing, *Journal of Geophysical Research*, *91*(C7), 8411–8427, doi:10.1029/JC091iC07p08411. 29, 30
- Raj, R. P., J. A. Johannessen, T. Eldevik, J. E. Ø. Nilsen, and I. Halo (2016), Quantifying mesoscale eddies in the Lofoten Basin, *Journal of Geophysical Research: Oceans*, *121*(7), 4503–4521, doi:10.1002/2016JC011637. 13, 19

- Read, J. F., and R. T. Pollard (1992), Water masses in the region of the Iceland–Faroes Front, *Journal of Physical Oceanography*, *22*(11), 1365–1378, doi:10.1175/1520-0485(1992)022<1365:WMITRO>2.0.CO;2. 14
- Redfield, A. C., B. H. Ketchum, and F. A. Richards (1963), The influence of organisms on the composition of seawater, in *The Sea, vol. 2, edited by M. N. Hill, pp. 26-77, Interscience, New York.* 31
- Rhein, M. (1996), Convection in the Greenland Sea, 1982-1993, *Journal of Geophysical Research*, *101*(C8), 18,183–18,192, doi:10.1029/96jc01295. 17
- Ronski, S., and G. Budéus (2005), Time series of winter convection in the Greenland Sea, *Journal of Geophysical Research*, *110*(C4), doi:10.1029/2004jc002318. 2, 17
- Rudels, B., D. Quadfasel, H. Friedrich, and M. N. Houssais (1989), Greenland Sea convection in the winter of 1987-1988, *Journal of Geophysical Research*, *94*(C3), 3223–3227, doi:10.1029/JC094iC03p03223. 15
- Rudels, B., H. J. Friedrich, and D. Quadfasel (1999), The Arctic Circumpolar Boundary Current, *Deep Sea Research Part II: Topical Studies in Oceanography*, *46*(6-7), 1023–1062, doi:10.1016/S0967-0645(99)00015-6. 1, 15, 19
- Rudels, B., E. Fahrbach, J. Meincke, G. Budéus, and P. Eriksson (2002), The East Greenland Current and its contribution to the Denmark Strait overflow, *ICES Journal of Marine Science*, *59*(6), 1133–1154, doi:10.1006/jmsc.2002.1284. 10, 11, 13, 15, 20, 21
- Rudels, B., E. P. Jones, U. Schauer, and P. Eriksson (2004), Atlantic sources of the Arctic Ocean surface and halocline waters, *Polar Research*, *23*(2), 181–208, doi:10.1111/j.1751-8369.2004.tb00007.x. 15
- Rudels, B., G. Björk, J. Nilsson, P. Winsor, I. Lake, and C. Nohr (2005), The interaction between waters from the Arctic Ocean and the Nordic Seas north of Fram Strait and along the East Greenland Current: results from the Arctic Ocean-02 Oden expedition, *Journal of Marine Systems*, *55*(1-2), 1–30, doi:10.1016/j.jmarsys.2004.06.008. 11, 13, 15, 17, 18, 19, 20
- Saberi, A., T. W. N. Haine, R. Gelderloos, M. Femke de Jong, H. Furey, and A. Bower (2020), Lagrangian perspective on the origins of Denmark Strait Overflow, *Journal of Physical Oceanography*, *50*(8), 2393–2414, doi:10.1175/JPO-D-19-0210.1. 21
- Schauer, U., H. Loeng, B. Rudels, V. K. Ozhigin, and W. Dieck (2002), Atlantic Water flow through the Barents and Kara Seas, *Deep Sea Research Part I: Oceanographic Research Papers*, *49*(12), 2281–2298, doi:10.1016/S0967-0637(02)00125-5. 14
- Schlitzer, R. (2007), Assimilation of radiocarbon and chlorofluorocarbon data to constrain deep and bottom water transports in the world ocean, *Journal of Physical Oceanography*, *37*(2), 259–276, doi:10.1175/JPO3011.1. 33, 150
- Schlosser, P., G. Bönisch, M. Rhein, and R. Bayer (1991), Reduction of deepwater formation in the Greenland Sea during the 1980s: Evidence from tracer data, *Science*, *251*(4997), 1054–1056, doi:10.1126/science.251.4997.1054. 2, 16

- Segtnan, O. H., T. Furevik, and A. D. Jenkins (2011), Heat and freshwater budgets of the Nordic Seas computed from atmospheric reanalysis and ocean observations, *Journal of Geophysical Research: Oceans*, *116*(C11), doi:10.1029/2011JC006939. 6, 19
- Selyuzhenok, V., I. Bashmachnikov, R. Ricker, A. Vesman, and L. Bobylev (2020), Sea ice volume variability and water temperature in the Greenland Sea, *The Cryosphere*, *14*(2), 477–495, doi:10.5194/tc-14-477-2020. 1, 7
- Semper, S. (2020), Circulation along the northern slope of the Greenland-Scotland Ridge, Ph.D. thesis, University of Bergen. 11
- Semper, S., K. Våge, R. S. Pickart, H. Valdimarsson, D. J. Torres, and S. Jónsson (2019), The emergence of the North Icelandic Jet and its evolution from northeast Iceland to Denmark Strait, *Journal of Physical Oceanography*, (2019), doi:10.1175/JPO-D-19-0088.1. 10, 21, 148
- Semper, S., R. S. Pickart, K. Våge, K. M. H. Larsen, B. Hansen, and H. Hátún (2020), The Iceland-Faroe Slope Jet: a conduit for dense water toward the Faroe Bank Channel overflow, *Nature Communications*, *11*(5390), doi:10.1038/s41467-020-19049-5. 10, 22, 148
- Semper, S., K. Våge, R. S. Pickart, S. Jónsson, and H. Valdimarsson (2022), Evolution and transformation of the North Icelandic Irminger Current along the north Iceland shelf, *Journal of Geophysical Research: Oceans*, *127*(3), e2021JC017,700, doi:10.1029/2021JC017700. 8, 21
- Serra, N., R. H. Käse, A. Kähl, D. Stammer, and D. Quadfasel (2010), On the low-frequency phase relation between the Denmark Strait and the Faroe-Bank Channel overflows, *Tellus A: Dynamic Meteorology and Oceanography*, *62*(4), 530–550, doi:10.1111/j.1600-0870.2009.00445.x. 22
- Serreze, M. C., A. P. Barrett, A. G. Slater, M. Steele, J. Zhang, and K. E. Trenberth (2007), The large-scale energy budget of the Arctic, *Journal of Geophysical Research: Atmospheres*, *112*(D11), doi:10.1029/2006JD008230. 6, 7
- Shao, Q., J. Zhao, K. F. Drinkwater, X. Wang, and Y. Cao (2019), Internal overflow in the Nordic Seas and the cold reservoir in the northern Norwegian Basin, *Deep Sea Research Part I: Oceanographic Research Papers*, *148*, 67–79, doi:10.1016/j.dsr.2019.04.012. 22
- Shu, Q., Q. Wang, M. Årthun, S. Wang, Z. Song, M. Zhang, and F. Qiao (2022), Arctic Ocean Amplification in a warming climate in CMIP6 models, *Science Advances*, *8*(30), eabn9755, doi:10.1126/sciadv.abn9755. 1, 152
- Skagseth, Ø., and K. A. Mork (2012), Heat content in the Norwegian Sea, 1995 - 2010, *ICES Journal of Marine Science*, *69*(5), 826–832, doi:10.1093/icesjms/fss026. 1, 26
- Skagseth, Ø., T. Eldevik, M. Årthun, H. Asbjørnsen, V. S. Lien, and L. H. Smedsrud (2020), Reduced efficiency of the Barents Sea cooling machine, *Nature Climate Change*, *10*(7), 661–666, doi:10.1038/s41558-020-0772-6. 14

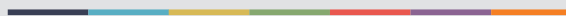
- Smedsrud, L. H., M. Muilwijk, A. Brakstad, E. Madonna, S. K. Lauvset, C. Spensberger, A. Born, T. Eldevik, H. Drange, E. Jeansson, C. Li, A. Olsen, Ø. Skagseth, D. A. Slater, F. Straneo, K. Våge, and M. Årthun (2022), Nordic Seas heat loss, Atlantic inflow, and Arctic sea ice cover over the last century, *Reviews of Geophysics*, *60*(1), e2020RG000,725, doi:10.1029/2020RG000725. 1, 6, 7, 13, 14
- Somavilla, R. (2019), Draining and upwelling of Greenland Sea deep waters, *Journal of Geophysical Research: Oceans*, *124*, 2842–2860, doi:10.1029/2018JC014249. 2, 17, 22, 149, 152
- Somavilla, R., U. Schauer, and G. Budeus (2013), Increasing amount of Arctic Ocean deep waters in the Greenland Sea, *Geophysical Research Letters*, *40*(16), 4361–4366, doi:10.1002/grl.50775. 17, 19
- Spall, M. A. (2010), Non-local topographic influences on deep convection: An idealized model for the Nordic Seas, *Ocean Modelling*, *32*(1-2), 72–85, doi:10.1016/j.ocemod.2009.10.009. 19
- Spall, M. A., M. Almansi, J. Huang, T. W. Haine, and R. S. Pickart (2021), Lateral redistribution of heat and salt in the Nordic Seas, *Progress in Oceanography*, *196*(102609), doi:10.1016/1087j.pcean.2021.102609. 1, 10, 19, 20, 151
- Spensberger, C., and T. Spengler (2021), Sensitivity of Air-Sea Heat Exchange in Cold-Air Outbreaks to Model Resolution and Sea-Ice Distribution, *Journal of Geophysical Research: Atmospheres*, *126*(5), e2020JD033,610, doi:10.1029/2020JD033610. 1, 7
- Straneo, F. (2006), Heat and freshwater transport through the central Labrador Sea*, *Journal of Physical Oceanography*, *36*(4), 606–628. 15
- Strass, V. H., E. Fahrbach, U. Schauer, and L. Sellmann (1993), Formation of Denmark Strait overflow water by mixing in the East Greenland Current, *Journal of Geophysical Research*, *98*(C4), 6907–6919, doi:10.1029/92JC02732. 1, 19, 20, 21
- Strehl, A.-M., K. Våge, and L. H. Smedsrud (submitted), A 70-year perspective on convection in the Greenland Sea, *2023*. 2, 7, 16, 17, 29, 149, 151, 152
- Svingen, K. (2019), Dense water formation in the Greenland Sea between 1999 and 2009, Master’s thesis, University of Bergen. 36
- Svingen, K., A. Brakstad, K. Våge, W.-J. von Appen, and L. Papritz (2023), The impact of cold-air outbreaks and oceanic lateral fluxes on dense-water formation in the Greenland Sea from a ten-year moored record (1999–2009), *Journal of Physical Oceanography*, *53*(6), 1499–1517, doi:10.1175/JPO-D-22-0160.1. 18, 21
- Swift, J. H., and K. Aagaard (1981), Seasonal transitions and water mass formation in the Iceland and Greenland seas, *Deep-Sea Research A*, *28*(10), 1107–1129, doi:10.1016/0198-0149(81)90050-9. 1, 2, 8, 9, 10, 13, 18, 21
- Swift, J. H., and K. P. Koltermann (1988), The origin of Norwegian Sea deep water, *Journal of Geophysical Research: Oceans*, *93*(C4), 3563–3569, doi:10.1029/JC093iC04p03563. 13, 22

- Swift, J. H., K. Aagaard, and S. A. Malmberg (1980), The contribution of the Denmark Strait overflow to the deep North Atlantic, *Deep-Sea Research A*, *27*(1), 29–42, doi:10.1016/0198-0149(80)90070-9. 1, 2, 10, 13, 21
- Tanhua, T., K. A. Olsson, and E. Jeansson (2005), Formation of Denmark Strait overflow water and its hydro-chemical composition, *Journal of Marine Systems*, *57*(3-4), 264–288, doi:10.1016/j.jmarsys.2005.05.003. 11, 21, 22, 31, 149
- Terpstra, A., I. A. Renfrew, and D. E. Sergeev (2021), Characteristics of cold-air outbreak events and associated polar mesoscale cyclogenesis over the North Atlantic region, *Journal of Climate*, *34*(11), 4567–4584, doi:10.1175/JCLI-D-20-0595.1. 2, 7, 27
- Timmermans, M., and J. Marshall (2020), Understanding Arctic Ocean circulation: a review of ocean dynamics in a changing climate, *Journal of Geophysical Research: Oceans*, *125*(4), doi:10.1029/2018JC014378. 7
- Tomczak, M., and D. G. B. Large (1989), Optimum multiparameter analysis of mixing in the thermocline of the eastern Indian Ocean, *Journal of Geophysical Research: Oceans*, *94*(C11), 16,141–16,149, doi:10.1029/JC094iC11p16141. 31
- Trenberth, K. E., and J. T. Fasullo (2008), An observational estimate of inferred ocean energy divergence, *Journal of Physical Oceanography*, *38*(5), 984–999, doi:10.1175/2007JPO3833.1. 3
- Tsubouchi, T., K. Våge, B. Hansen, K. M. H. Larsen, S. Østerhus, C. Johnson, S. Jónsson, and H. Valdimarsson (2021), Increased ocean heat transport into the Nordic Seas and Arctic Ocean over the period 1993–2016, *Nature Climate Change*, *11*, 21–26, doi:10.1038/s41558-020-00941-3. 1
- Våge, K., R. S. Pickart, V. Thierry, G. Reverdin, C. M. Lee, B. Petrie, T. A. Agnew, A. Wong, and M. H. Ribergaard (2009), Surprising return of deep convection to the subpolar North Atlantic Ocean in winter 2007–2008, *Nature Geoscience*, *2*(1), 67–72, doi:10.1038/ngeo382. 29
- Våge, K., R. S. Pickart, M. A. Spall, H. Valdimarsson, S. Jónsson, D. J. Torres, S. Østerhus, and T. Eldevik (2011), Significant role of the North Icelandic Jet in the formation of Denmark Strait overflow water, *Nature Geoscience*, *4*(10), 723–727, doi:10.1038/ngeo1234. 10, 11, 13, 18, 21
- Våge, K., R. S. Pickart, M. A. Spall, G. W. K. Moore, H. Valdimarsson, D. J. Torres, S. Y. Erofeeva, and J. E. Ø. Nilsen (2013), Revised circulation scheme north of the Denmark Strait, *Deep-Sea Research I*, *79*, 20–39, doi:10.1016/j.dsr.2013.05.007. 10, 19, 20, 26
- Våge, K., G. W. K. Moore, S. Jónsson, and H. Valdimarsson (2015), Water mass transformation in the Iceland Sea, *Deep-Sea Research I*, *101*, 98–109, doi:10.1016/j.dsr.2015.04.001. 18, 21, 25, 26, 28, 29
- Våge, K., L. Papritz, L. Håvik, M. A. Spall, and G. W. K. Moore (2018), Ocean convection linked to the recent ice edge retreat along east Greenland, *Nature Communications*, *9*, 1287, doi:10.1038/s41467-018-03468-6. 1, 7, 10, 15, 18, 152

- Våge, K., S. Semper, H. Valdimarsson, S. Jónsson, R. S. Pickart, and G. W. K. Moore (2022), Water mass transformation in the Iceland Sea: Contrasting two winters separated by four decades, *Deep Sea Research Part I: Oceanographic Research Papers*, *186*, 103,824, doi:10.1016/j.dsr.2022.103824. 18, 21
- van Aken, H. M., G. Budéus, and M. Hähnel (1995), The anatomy of the Arctic frontal zone in the Greenland Sea, *Journal of Geophysical Research: Oceans*, *100*(C8), 15,999–16,014, doi:10.1029/95JC01176. 19
- Visbeck, M., J. Fischer, and F. Schott (1995), Preconditioning the Greenland Sea for deep convection: Ice formation and ice drift, *Journal of Geophysical Research*, *100*, 18,489–18,502, doi:10.1029/95JC01611. 2, 30
- Voet, G., D. Quadfasel, K. A. Mork, and H. Søyland (2010), The mid - depth circulation of the Nordic Seas derived from profiling float observations, *Tellus A*, *62*(4), 516–529, doi:10.1111/j.1600-0870.2009.00444.x. 22
- Wadhams, P., J. Holfort, E. Hansen, and J. P. Wilkinson (2002), A deep convective chimney in the winter Greenland Sea, *Geophysical Research Letters*, *29*(10), doi:10.1029/2001gl014306. 15
- Walsh, J. E., W. L. Chapman, and F. Fetterer (2015), Gridded monthly sea ice extent and concentration, 1850 onwards, version 1. National Snow and Ice Data Center, Boulder, Colorado USA., doi:https://doi.org/10.7265/N5833PZ5. 28
- Walsh, J. E., F. Fetterer, J. S. Stewart, and W. L. Chapman (2017), A database for depicting Arctic sea ice variations back to 1850, *Geographical Review*, *107*(1), 89–107, doi:10.1111/j.1931-0846.2016.12195.x. 6, 28
- Wang, X., J. Zhao, T. Hattermann, L. Lin, and P. Chen (2021), Transports and accumulations of Greenland Sea intermediate waters in the Norwegian Sea, *Journal of Geophysical Research: Oceans*, *126*(4), e2020JC016,582, doi:10.1029/2020JC016582. 22
- Weijer, W., W. Cheng, O. A. Garuba, A. Hu, and B. T. Nadiga (2020), CMIP6 models predict significant 21st century decline of the Atlantic Meridional Overturning Circulation, *Geophysical Research Letters*, *47*(12), e2019GL086,075, doi:10.1029/2019GL086075. 153
- Yashayaev, I., and D. Seidov (2015), The role of the Atlantic Water in multidecadal ocean variability in the Nordic and Barents Seas, *Progress in Oceanography*, *132*, 68–127, doi:10.1016/j.pocean.2014.11.009. 1
- Ypma, S. L., S. Georgiou, J. S. Dugstad, J. D. Pietrzak, and C. A. Katsman (2020), Pathways and water mass transformation along and across the Mohn-Knipovich Ridge in the Nordic Seas, *Journal of Geophysical Research*, *125*(9), doi:10.1029/2020JC016075. 19, 20



Graphic design: Communication Division, UIB / Print: Skjipes Kommunikasjon AS



uib.no

ISBN: 9788230842706 (print)
9788230853245 (PDF)